Ph.D. in Physics and Nanosciences

cycle XXXV

"The Cryogenic AntiCoincidence detector for Athena X-IFU"

Lorenzo Ferrari Barusso

Referees:
Dr. Caroline Anne Kilbourne
NASA / Goddard Space Flight Center

Prof. Enectali Figueroa-Feliciano
Department of Physics and Astronomy Northwestern University

Advisor:
Prof. Flavio Gatti
Dipartimento di Fisica
Università di Genova

How I did it

Dr. Victor Frankenstein

Thanks Dad, I love you

Acknowledgements

I would like to thank my supervisor Flavio Gatti. He was able to push me beyond my limits and make me face a huge amount of different aspects achieving important results and developing awareness about this world.

Then I would like to thank my referees Dr. Caroline Anne Kilbourne and prof. Enectali Figueroa-Feliciano for their corrections on this thesis.

I would also like to thank all my colleagues from the INAF-IAPS group in Rome. Matteo, Claudio, Gabriele, Andrea and Guido from the CNR. They have done a lot of work, from the organization to the measurement point of view, and have helped me to follow the purpose of this thesis.

I have to thank CNR-SPIN for the possibility of doing this Ph.D., I would not have had this oppurtunity without their financial support.

Now I would like to thank the whole Genoa laboratory group, from Matteo for his light and critical speeches to Adriano, Mariia, Luigi, Daniele, Manuela, Giovanni, Edvige and Fabio for their work and help. I would also like to thank Michele, who helped me at the beginning of my work and still shapes my point of view, and Beatrice, who is a good friend, was a fantastic colleague and anchor, we shared all our goals.

Finally, all the other students I worked with: Matteo, Vilson, Silvia, Pietro and Stefano. You helped me with your work and gave me the opportunity to grow following you in your MScs thesis.

Contents

Acknowledgements **v**

Contents **vii**

Introduction **1**

1 The Athena X-ray observatory **7**

The Athena X-ray observatory **7**
1.1 Scientific Goals 7
1.1.1 Compact objects and accretion physics 8
1.1.2 Cosmic Feedback 10
1.1.3 Hot plasma physics 16
1.1.4 Gamma Ray Bursts (GRBs), multi-messenger physics with Gravitational Waves (GW) 18
1.2 The Advance Telescope for High ENergy Astrophysics 21
1.2.1 The service module 22
1.2.2 The mirror housing module 22
1.2.3 The instrumental focal plane 23

2 The Cryogenic AntiCoincidence Detector - CryoAC **31**

The Cryogenic AntiCoincidence Detector - CryoAC **31**
2.1 The Anticoincidence detector 31
2.2 The Transition Edge Sensor microcalorimeter 34
2.2.1 Thermo-electric response 37
2.2.2 Energy resolution 42
2.3 The phonon mediated TES detector 43
2.3.1 Signal generation 43
2.3.2 Signal model of the CryoAC 45
2.3.3 The a-thermal phonon hot-spot 52
2.4 The CryoAC design 60
2.4.1 Absorber Geometry configurations 62
2.4.2 Demonstration Model 64

3 Fabrication of the CryoAC **67**

Fabrication of the CryoAC **67**
3.1 Photo-lithography 67
3.1.1 Positive photo-lithography 67
3.1.2 Negative photo-lithography 68
3.2 Silicon chip preparation 68
3.3 Ir/Au TES bilayer 70
3.3.1 Ir/Au film growing 71
3.3.2 Ir/Au etching 74
3.3.3 The splashing issue 76
3.3.4 Thickness uniformity 76
3.3.5 Iridium films critical temperature distortions 77
3.4 Pt Heaters 88
3.5 Au thermalizing frame 88
3.6 Nb superimposed striplines 90
3.6.1 First layer of electrical connections 90
3.6.2 SiO insulating layer 91
3.6.3 Second layer of electrical connections 92
3.6.4 The current dependant parasitic resistance 93
3.7 Absorber and silicon bridges Etching 95

4 The CryoAC structural model **99**

The CryoAC structural model **99**
4.1 The SM0 manufacturing process 100
4.2 Sample preparation 101
4.2.1 The optical diffusivity of the samples 102
4.2.2 Bonding the samples to the interface flange 104
4.3 Experimental setup for vibration 106
4.3.1 Electrodynamic shaker 106
4.3.2 Doppler effect Laser vibrometry 107
4.4 Vibration test 108
4.4.1 Test procedure 109
4.5 Test results 114

5 Measurements on the CryoAC models **117**

Measurements on the CryoAC models **117**
5.1 The measurement setup in Genoa LTD lab 117
5.1.1 Dilution Cryostat 117
5.1.2 Instrumental apparatus 122
5.2 Operating the Demonstration Model 127
5.2.1 Demonstration Model characterization 127
5.2.2 Joint tests of AC-S10 and the NASA TES-array DM . . 132
5.2.3 DM measurements conclusions 136
5.3 Measurements of the detector thermal properties 137
5.3.1 Review of TES-substrate thermal coupling measurements 137

5.3.2 Pure thermal detector measurements 138
5.4 Measurement of the a-thermal phonon hotspot 143

Conclusion **147**

A Manufacturing report **149**

Bibliography **211**

Introduction

The purpose of my Ph.D. thesis was to develop a laboratory model of the cryogenic anticoincidence detector for the future focal plane of the X-ray space telescope of the Athena mission. The objective of the work was to study a large area detector operating at 50 mK with TES superconducting sensors in support of the NASA GSFC TES microcalorimeter array detector for X-ray spectroscopy to demonstrate the required Technology Readiness Level (TRL-5).

Early studies prior to my work had shown the need for active background rejection of charged particles in order to access a large part of Athena's science. In addition, based on the group's experience studying some early prototypes, it was recognized that the principles of signal generation needed to be consolidated. In addition, the manufacturing processes and material selection had to be studied and defined with regard to the requirements of a space mission.

My work has begun with the fabrication of the first Demonstration Model samples, one of which has been integrated into the SRON Facility for joint testing with a prototype TES microcalorimeter array. Unfortunately, the pandemic denied me direct participation in testing and to carry on the work in efficient manners between 2020 and 2021. Upon full resumption of activities, I devoted myself in parallel to the study of fabrication processes, tests and measurements on detectors, and the production and testing of structural models. The fabrication processes revealed several unexpected effects, mainly due to the interaction between fabrication processes and detector performance. Much of the work done to understand the causes led to the establishment of a plan for process modifications and fabrication facility upgrades. I also participated in the simulation study of the propagation and slowing-down of the phonon hot-spot in the detector and the definition of a setup to measure its effective size.

In short, my work shows that it is possible to:

1. build cryogenic anticoincidence prototypes, based on Ir/Au TES, with energy thresholds of keV and resolution of 160 eV FWHM at 6 keV and 0.9 keV at 60 keV,

2. build final size prototypes that will withstand mechanical vibration tests,

3. operate the CryoAc coupled to the TES microcalorimeter array, simulating a plausible final configuration without significant interference.

Outline

The main arguments of my work are presented in the following order:

1. In Chapter 1, some of the scientific goals of Athena, focusing on the observational capabilities and the opportunities for multi-messenger physics, giving an overview of the telescope with focus on the parts involved in my Ph.D project.

2. In Chapter 2, the working principles of the cryogenic anticoincidence detector, starting with the theory of Transition Edge Sensor (TES) microcalorimeters, and the generation and evolution of signals in the detector. The electro-thermal and a phonon models of the device are also presented in this chapter.

3. In Chapter 3, the development of the manufacturing process of the detector, analyzing: problems, solutions and their impact on the performance of the detector.

4. In Chapter 4, the first structural model of the detector: its fabrication and vibration load tests to understand the structural properties of the device.

5. In Chapter 5, the performance characterization of the anticoincidence detector, with emphasis on measurements of the thermal and a-thermal contributions to the signal generation.

X-Ray Astrophysics

The study of the universe and celestial bodies has always been of great importance in human life, but in ancient times our eye was the only instrument to study the sky. However, thanks to the scientific and technological progress, several methods of studying the cosmos have been developed and nowadays, in addition to the study of visible light, every region of the electromagnetic spectrum is studied together with astroparticles.
The beginning of X-ray astronomy is fixed in 1962, when a group led by Riccardo Giacconi observed for the first time an extra-solar X-ray source [1]: Scorpius X-1, a low-mass X-ray binary consisting of a blue star and a neutron star. Photons between 0.1 and 100 keV, which constitute the X-band, are able to penetrate the gas columns of entire galaxies and reach the Earth's atmosphere from distances comparable to the radius of the entire Universe. This makes it possible to study radiation from objects billions of light-years away. The study of hot or energetic events such as: supernovae, emissions from active galactic nuclei (AGN), high-temperature plasmas, gamma-ray bursts (GRBs) have major implications in astronomy, and X-rays are essential to their understanding.

Figure 1 shows how X-rays are completely absorbed by the atmosphere. For this reason, during the last 50 years, numerous missions have carried detectors

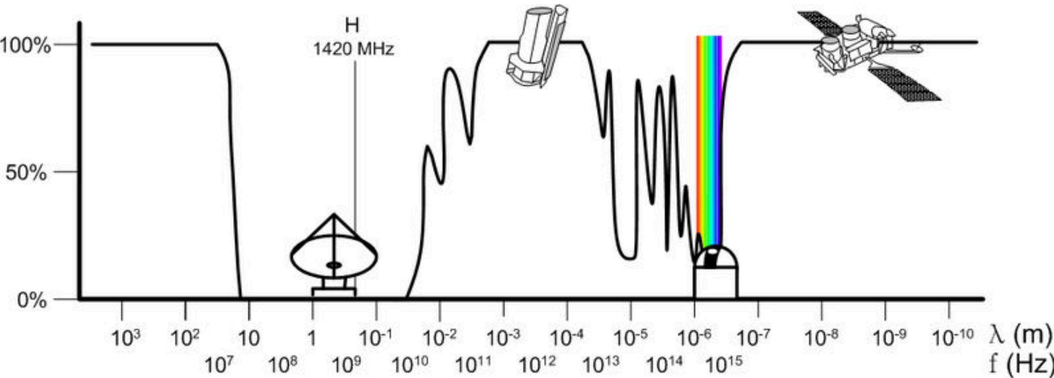

Figure 1: Opacity of the atmosphere as a function of the spectrum electromagnetic spectrum. From haade, AtmosphereEMSpectrum, CC BY-SA 3.0.

outside our atmosphere via balloons or rockets to detect X-rays. During this period, the sensitivity of the detectors of the various missions, expressed in $erg\ cm^2\ s$, has improved by more than 9 orders of magnitude, as shown in Figure 2. Such an improvement is comparable to that obtained by observing stars with the naked eye or with the current generation of $8-10\ m$ telescopes, and all celestial objects have been observed, from planets to stars, galaxies, and quasars. It has also been possible to observe the energy released by matter in the accretion disks of neutron stars or black holes, and to increase the amount of baryonic matter observable through the Warm Hot Intergalactic Medium (WHIM) [2]. There are currently two large X-ray telescopes in orbit around the Earth: Chandra and XMM-Newton, both launched in 1999. These two missions have now reached the end of their lifetimes, and new technologies have been developed that will enable a new generation of space telescopes for X-ray astrophysics. Thus, the Athena space observatory shown in figure 3, with its improved sensitivity and performance, will allow deeper observations of objects of great astrophysical interest.

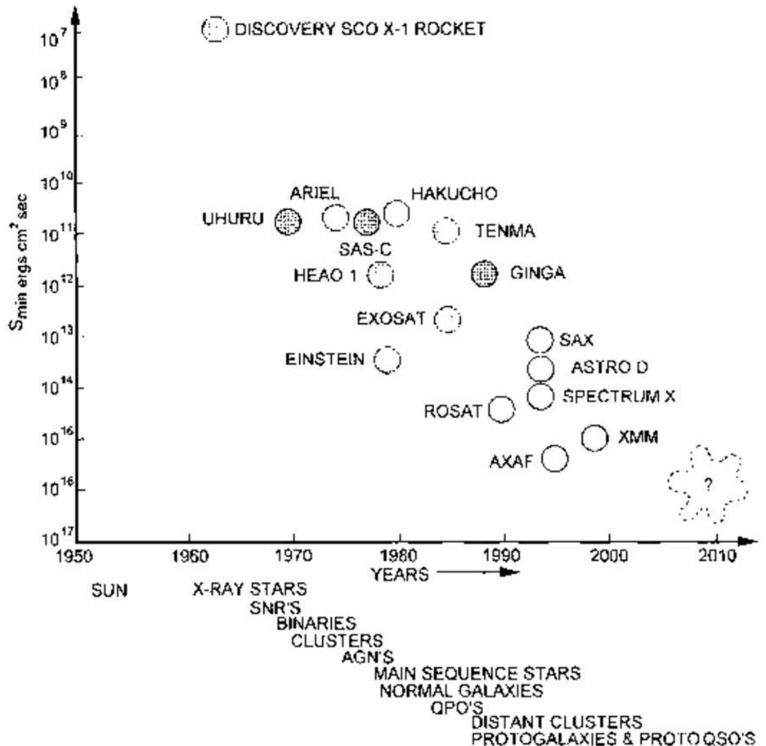

Figure 2: Sensitivity of various space missions from 1962 to 2000, expressed in $erg\ cm^2\ s$. The question mark is used to identify the area in which the Athena sensitivity should go. Illustration from [3]

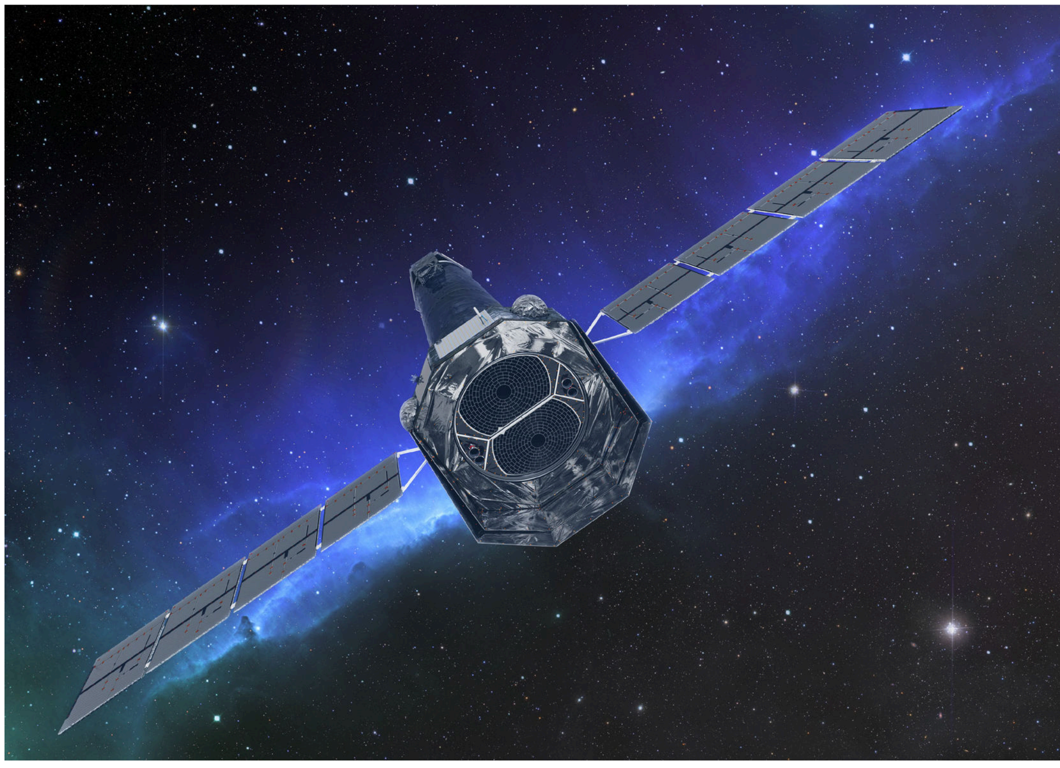

Figure 3: Artistic view of the future space observatory Athena in flight. Credits ESA

Chapter 1

The Athena X-ray observatory

Athena stands for Advanced Telescope for High ENergy Astrophysics. It is a project to build a telescope to study the universe in the X-band of the electromagnetic spectrum. Commissioned by the European Space Agency (ESA), the observatory will be placed in orbit around the Lagrange point L-1[1] in the late 2030s. The project is currently undergoing a redefinition phase. [4, 5, 6, 7]

1.1 Scientific Goals

The scientific goal of the mission is to study the Universe in its hot and energetic parts. This requires observations in the X-band. The importance of such studies is related to the fact that most of the baryonic matter in the Universe is trapped in hot gases at temperatures around a million degrees, or because processes near the event horizon of a black hole occur at high energies. The Athena telescope will have special features. One of them is the presence for the first time of cryogenic X-ray detectors operating at 50 mK. In particular, the scientific objectives require: spatial resolution, broad dynamics and X-ray spectral resolution up to two orders of magnitude better than those of current orbiting observatories such as XMM-Newton [8] and Chandra [9].
By observing the evolution of baryonic matter in different objects. Some possibilities are:

- Compact objects in high gravity environments, such as black holes. To determine how matter accumulates in them.
- Super-massive black holes, to unravel the mechanisms of so-called cosmic feedback and show how their growth is linked to the evolution of galaxies.

[1]The Lagrange point L1 is one of the five points where, in the three-body problem, the gravitational forces of two large bodies, such as the Sun and the Earth, balance the centrifugal force felt by a smaller object, such as a satellite or spacecraft. At this point, the gravitational pull of the two bodies is equal and opposite, creating a saddle point of equilibrium that provides long-term stability for objects orbiting around it. The L1 point is placed along the Earth-Sun axis as L2 and L3. L1 and L2 are the two points closest to Earth, 1.5×10^6 km, and are commonly used for space missions and scientific observations.

- Warm baryon gases to observe the formation and evolution of large-scale structures such as the Warm-Hot Intergalactic Medium (WHIM), which should be structured as plasma between clusters of galaxies.

- Warm plasma in all astronomical environments, from planets to stars, to determine their formation mechanisms.

- Gamma-ray bursts (GRBs), focusing on their emission, as tools in multi-messenger astronomy. GRBs have recently been identified as the electromagnetic counterpart of gravitational waves in some coalescence events.

In what follows I will present more deeply the scientific goals, some comparisons with telescopes currently in orbit to enhance the improvements, and a summary of the performance techniques of Athena's instruments, as in Figure 1.1.

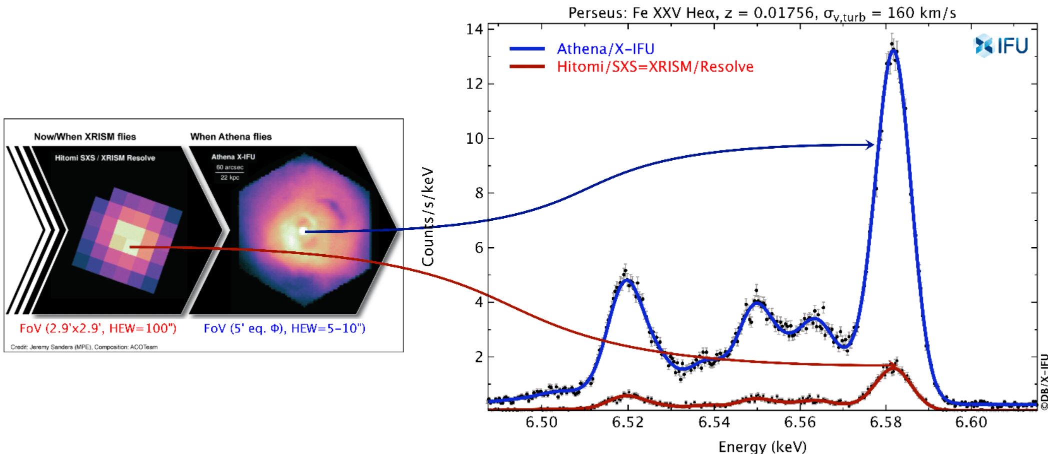

Figure 1.1: The figure shows the imaging and spectral resolving improvements with comparable field of view and same exposure time between the Hitomi/SXS=XRISM/Resolve and X-IFU images and spectra of Perseus cluster. From [6] (2021 X-IFU design).

1.1.1 Compact objects and accretion physics

Some of the most extreme conditions in the universe are found in and around compact objects. Among them, black holes produce the strongest gravitational fields, while neutron stars, or pulsars, are the densest clusters of matter observable. Matter trapped in these extreme gravitational fields is compressed and heated to millions of Kelvins, producing X-band radiation. Thus, observations in X-rays are a unique tool for studying the regions closest to black holes and pulsars. We can study how the laws of general relativity apply in these fields, and how matter behaves under conditions of such high density and intense gravity.
Black hole accretion processes are the largest sources of energy in the Universe, second only to nuclear fusion reactions in stars. However, compared to

nuclear fusion, accretion is an order of magnitude more efficient at releasing energy. In addition, the accretion process of a supermassive black hole has a feedback effect on the galaxy in which it is located, which is reflected back to the black hole itself. This phenomenon is described in the next section 1.1.2. These effects can be very important on galactic and cosmological scales and can be revealed thanks to the very high spectral resolution of X-IFU and the high temporal and spatial resolution of WFI (X-IFU and WFI are the two instruments in the Athena focal plane and will be briefly explained in section 1.2.3).

Black holes

The X-rays emitted by matter just before it crosses the event horizon have specific spectral and temporal properties that depend on the strongly gravitational environment, the type of accretion, and the spin of the black hole. X-IFU and WFI will make it possible to map the flux in the strong gravity regime for both stellar-mass objects and supermassive black holes found in the cores of galaxies. In addition, the space-time around the black hole depends directly on the spin, so that a change in the spectral lines directly reveals a measure of the spin. In this way, it will be possible to determine whether the black hole under observation has spin and, if so, to proceed to measure it. With current observatories it is not possible to distinguish between non-rotating and counter-rotating black holes with respect to their accretion disks [10], see Figure 1.2. The high spectral resolution of Athena will overcome the actual possibilities and observe all different black hole spins. In addition, Athena's angular resolution will be sufficient to distinguish X-ray emission from Sagittarius A*, the never-before-observed supermassive black hole at the center of the Milky Way.

Accretion physics

Athena's properties will give us new insights into the phenomena of accretion in the presence of strong gravity. For example, accreting neutron stars have slightly open spectral lines that are virtually identical to those of accreting black holes. In principle, these would be two indistinguishable phenomena, the only difference is the presence of a solid surface in the case of neutron stars. This fundamental difference should give rise to some observable effects (such as X-ray bursts or magnetic field pulsations) using high-resolution spectroscopy. Another example of an application to the study of accretion can be found in the ultra-luminous X-ray sources, the latter having an observed luminosity above the Eddington limit[2]: the idea to explain this violation is based on

[2]The Eddington limit represents the maximum luminosity of a celestial body. It is determined by the balance between the radiation pressure and the gravitational force of the object. The ratio of the maximum luminosity of an object to its mass is 10^4 times the luminosity/mass ratio of the Sun. $\frac{L_{max}}{M_{oggetto}} = 3.2 \times 10^4 \frac{L_\odot}{M_\odot}$.

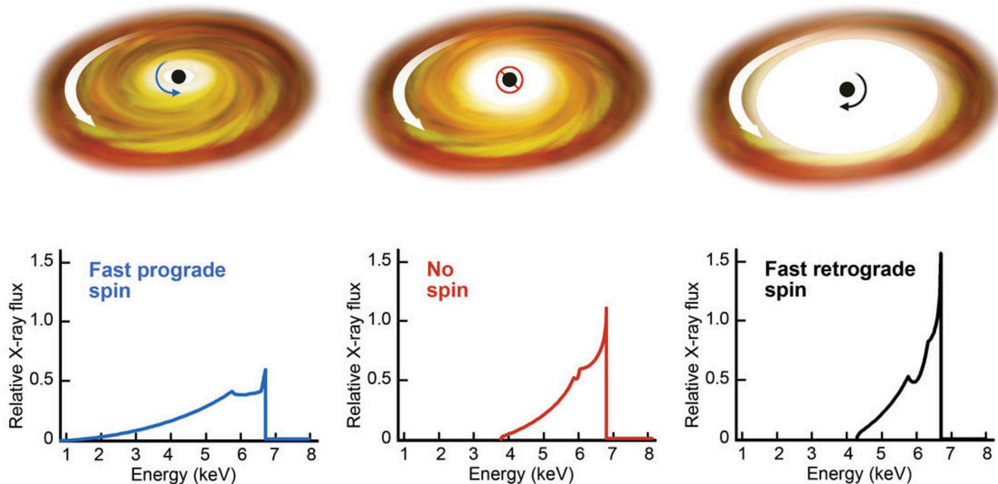

Figure 1.2: Artist's impression of different spin black holes with a rotating accretion disk. Three possibilities are presented: maximally BH-disk co-rotating: spin=1 (left), no rotating black hole, spin=0 (centre), and maximally BH-disk counter-rotating, spin=-1 (right). The inner disk radius varies as a function of spin and can therefore be measured through the emission line profiles as affected by strong gravity. From [4], credits Sky and Telescope.

the possibility that it is the accretion material of such sources that emits so violently, and not the object itself.

Determining the equation of state of ultra-dense matter in neutron stars

Of astrophysical interest will also be the mapping of the accretion flux of neutrons, focusing on the radius both in physical units and in terms of the gravitational radius. In this case, a mass-radius relation and thus an equation of state can be found for the core of the neutron star, with many implications for chromodynamics.

These goals can be summarized as follows:

1. Determine how black holes work and measure their spin.

2. To study the physics of accretion in all types of compact objects.

1.1.2 Cosmic Feedback

Supermassive black holes (SMBH) at the center of galaxies play a crucial role in the stellar mass of the galaxy itself. The process by which this happens is called cosmic feedback, and it occurs when the energy and radiation emitted by the accretion process of the active galactic nucleus (AGN) interacts with the gas present in its host galaxy. As a result, the intense photon and particle

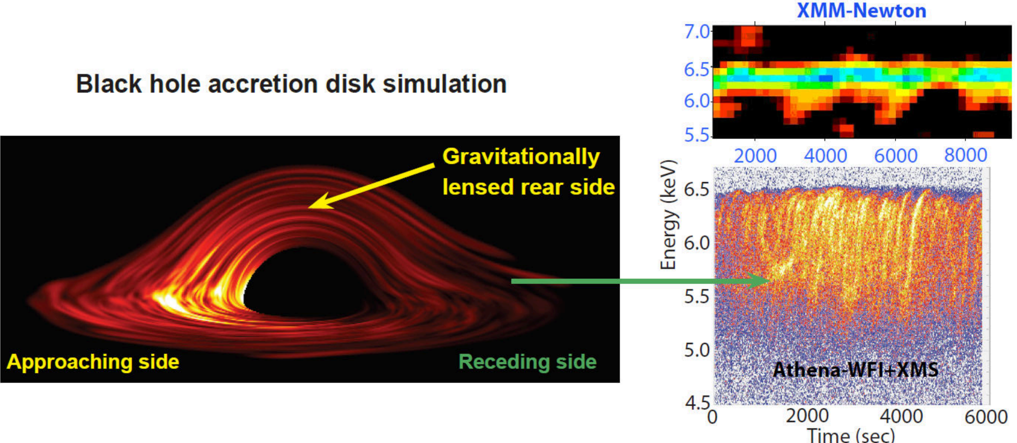

Figure 1.3: Graphical representation of a black hole accretion disk and comparison between the data observable by XMM-Newton and those observable by Athena, where it is clear how it will be possible to observe in greater detail the hot matter that makes up the accretion disk of a black hole. From [4].

fluxes produced by the AGN sweep away the interstellar gas within the galaxy, see Figure 1.4. These jets suppress star formation and thus the black hole accretion process, which in turn reduces the matter feeding the AGN itself. This process operates on scales much larger than the size of the black hole, which is $8-9$ orders of magnitude smaller than the host galaxy.

This feedback mechanism is a key point in models of galaxy formation and evolution. The heating and ejection of cold gas from galaxies by active galactic nuclei could govern the downsizing process; according to this hypothesis, smaller galaxies form successively into larger ones. Star formation also acts as a feedback mechanism through the supernovae; this is particularly important in starbust galaxies, galaxies in which the star formation process is exceptionally violent compared to that in the vast majority of other galaxies, and where jets from large supernovae eject a large amount of matter out of the galaxy. Despite their importance, these feedback processes are not fully understood.

The AGN flux energy and the feedback physics

Athena will greatly improve our chances of understanding the cosmic feedback phenomenon. By combining the high spectral and spatial resolution of X-IFU, it should be possible to reveal the mechanical and radiative influences in the galactic nuclei and the properties of the winds produced by the active galactic nuclei, and how jets and radiative pressure trigger the mechanism. This will be achieved by measuring the gas drift velocities and spectral line broadening of cold core galaxies, and by observing the coupling of AGNs to: the gases within the clusters, the energy content, and the time scales. In addition, the outgoing flux properties of active galactic nuclei will also be studied in detail,

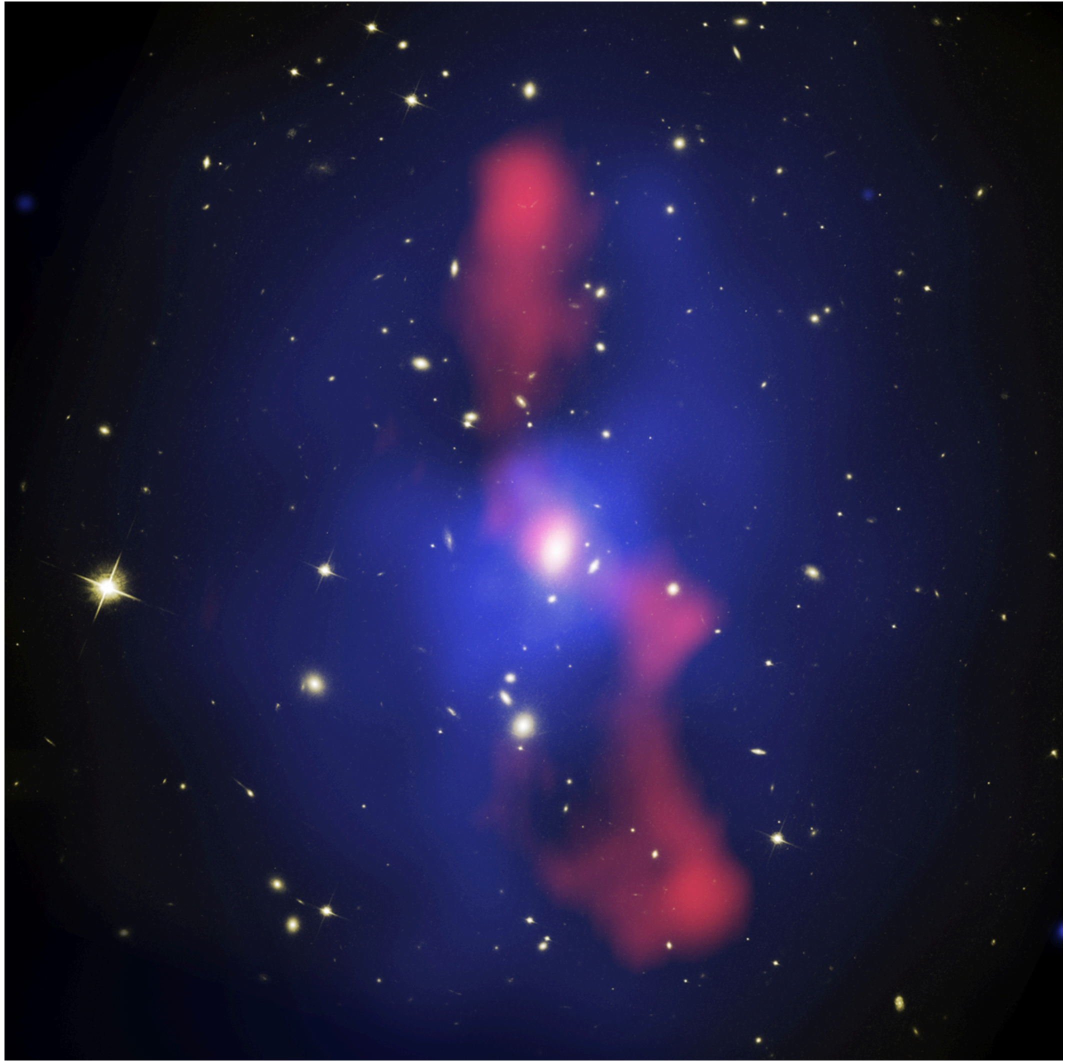

Figure 1.4: This figure shows that AGN can affect structures at galaxy and cluster scales: giant cavities of 200 *kpc* are being excavated by the AGN with the mechanical energy of its jets. The image is a composite of a Hubble optical image of the z=0.21 cluster MS0735.6+7421 were is visible in blue the X-ray emission obtained with Chandra and in red the 320 MHz radio emission acquired with NRAO. From [11], Credit: X-ray: NASA/CXC/Univ. Waterloo/B.McNamara; Optical: NASA/ESA/STScI/Univ. Waterloo/B.McNamara; Radio: NRAO/Ohio Univ./L. Birzan et al.

as a consequence of the accretion processes in the innermost regions from which the feedback power is derived.

SMBH growth and galactic nuclei darkening

With the field amplitude of WFI, it will be possible to do a census of galaxies to determine which are in the feedback phase. Instead, thanks to the high

spectral quality of X-IFU, it will be possible to observe many of the obscured active galactic nuclei that we are currently unable to detect. These will include the first galaxies to form after the Big Bang. With such a database, it will be possible to study the complete evolution of galaxies.

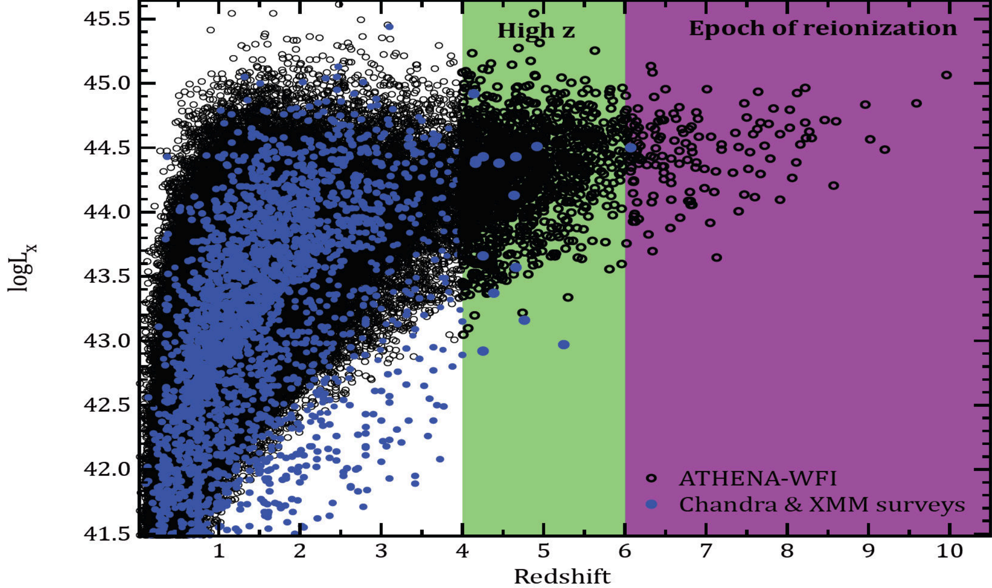

Figure 1.5: Simulation of the luminosity distribution on the redshift plane of the active galactic nuclei that Athena should observe compared to those already observed by Chandra and XMM-Newton. It is clearly visible the increment of the number of supermassive black holes observable, particularly the older ones at high Z. From [4].

Metallicity flux

Finally, the metallic enrichment of the intergalactic medium will be studied thanks to the accurate spectroscopy carried out with the X-IFU instrument. By measuring the flux rate and the amount of elements ejected by a supernova, a detailed map of the metallicity[3] of the intergalactic medium will be obtained, as shown in Figure 1.6. This is done to understand the evolution of the Universe.

In summary, with respect to cosmic feedback Athena will work on:

1. The flux energy due to supermassive black holes measurement.
2. The growth of supermassive black holes study.
3. The velocity and metallicity flux due to winds in starbust galaxies measurement.

[3] abundance of elements with atomic number greater than 2

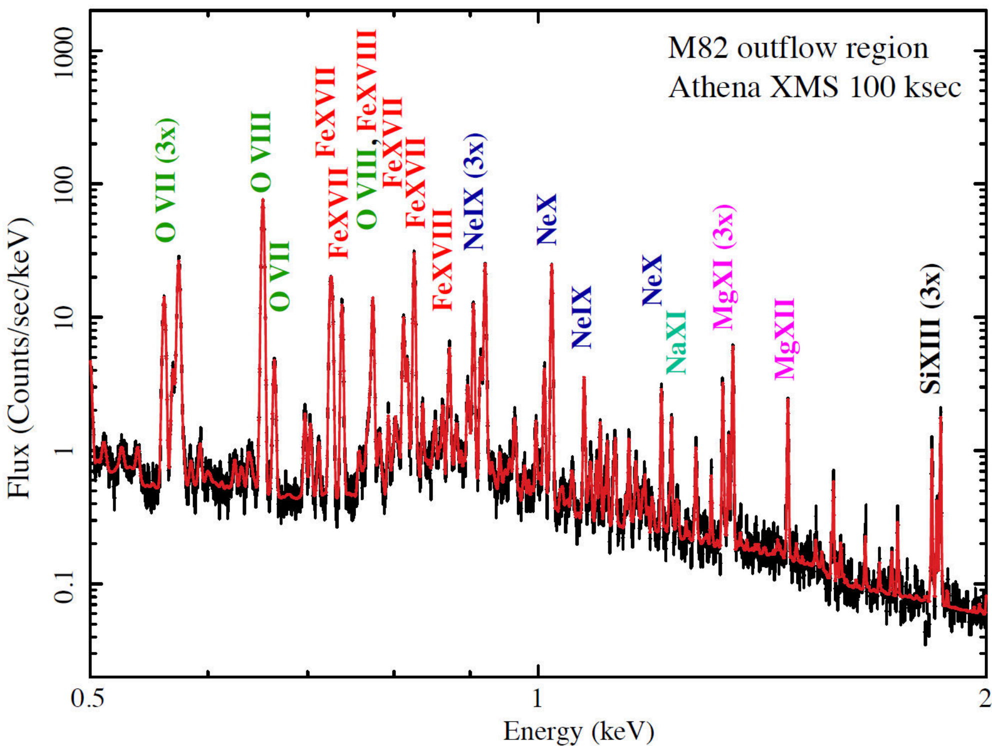

Figure 1.6: The spectral and imaging capabilities of X-IFU will be able to determine the abundance of the various elements in the intergalactic medium. The mass, temperature, and state of ionization of many elements will be able to be determined using the diagnostic Iron L-shell, and H-like and He-like lines. From [4].

The history of the formation, on cosmological timescales, of large-scale structures in the Universe is encapsulated in the hot baryons that are organized into groups, such as clusters of galaxies and moaning structures in the Universe. These objects have temperatures of about 10^7 K, so they emit radiation in the X-band. Thanks to the spatially resolved high-resolution spectroscopy of the X-IFU, it will be possible to measure the velocity of galaxy clusters, look for turbulence in the gas within them, and find out when excess energy was formed. It will also map the evolution of the abundance of chemical elements by studying the metallicity of the gases within the clusters.

The Warm Hot Intergalactic Medium (WHIM)

By making X-IFU and WFI work in pairs, it will be possible to reduce systematic errors in the cluster masses and make accurate measurements of the fraction of baryons trapped in them. At low redshifts, most of the baryons in the Universe (about 40 percent) are found in the hot gas clouds that connect galaxy clusters, the so-called Warm and Hot Intergalactic Medium (WHIM), as shown in the Figure 1.7. These gases have much lower densities than intra-cluster gases and temperatures ranging from 10^5 to 10^7 K. A clear indication

of the existence of these gases first occurred in 2017. Their detection required a long period of observation by XMM-Newton (430 hours over 2 years, 2015 to 2017). [2]. With the characteristics of Athena it will be possible to characterize the WHIM, studying its spatial distribution, ionization state and abundance of chemical elements.

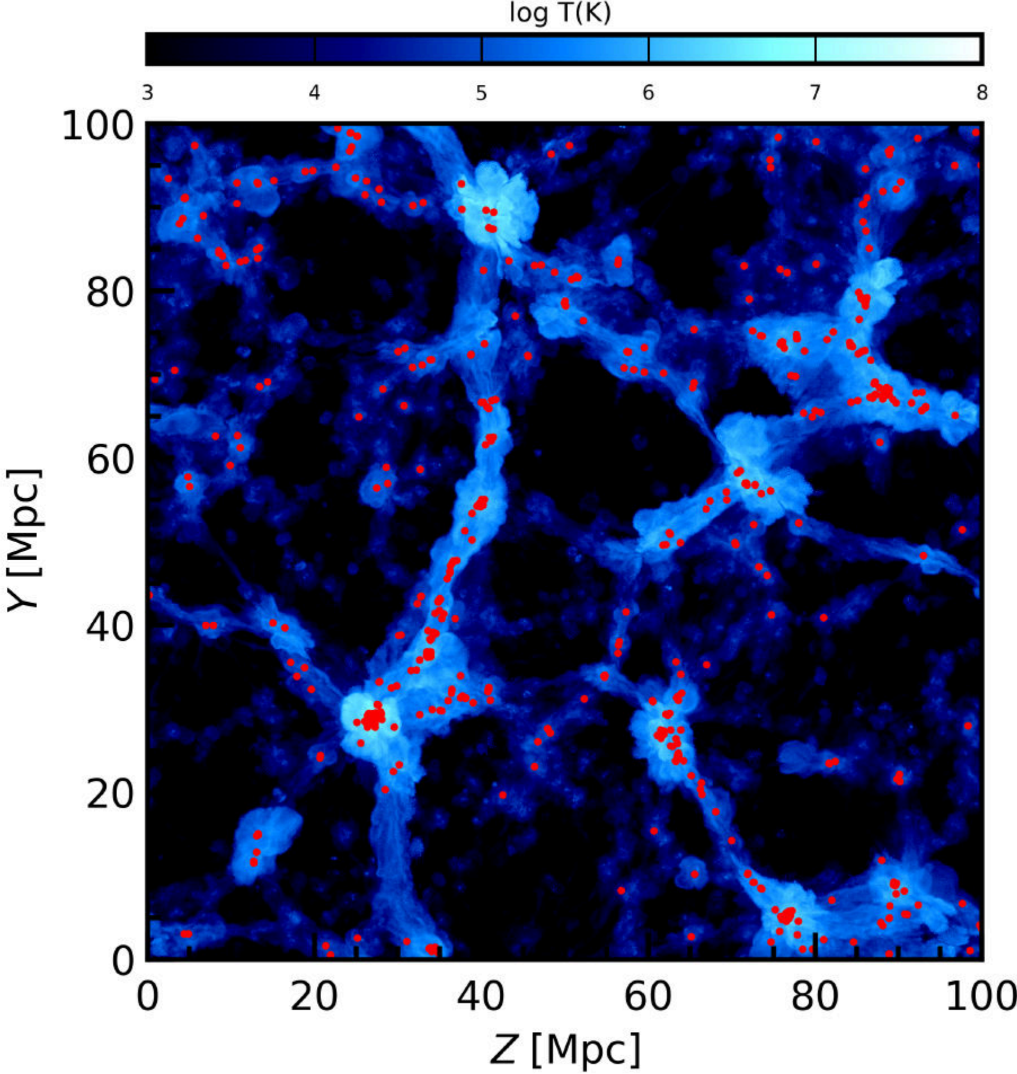

Figure 1.7: Simulation of the temperature distribution of intergalactic gas within the large-scale structure. The red dots indicate the position of the most brilliant galaxies. From and credits [12].

Dark matter and dark energy

It will also have important cosmological implications: for example, studies of dark energy, since evolutionary models of the baryonic structure give great importance to the study of dark matter and dark energy. Based on most theories, it seems that the WHIM filaments are confined around a dark matter

skeleton. In fact, it is possible that by going to study these walls it could be found spectral lines that identify a decay of unknown dark matter particles. In particular, a good candidate in this regard is an X-photon peak at 3 keV, which has not been possible to characterize from parts of XMM-Newton [13] due to insufficient spectral resolution. Another candidate for the indirect search for dark matter are spheroidal dwarf galaxies, an example of a system dominated by the presence of dark matter. Simulations carried out in March 2021 have verified how Athena will be able to detect the X-ray emission of dark matter decay present in the Draco and Ursa Major II galaxies [14].

Standard cosmological model

The organization of matter into large-scale structures within the Universe is also a powerful tool for studying the Standard Model of cosmology. The structure and evolution of the Universe is described by a set of cosmological parameters, including the densities of objects in the Universe and the rate at which it is expanding. These parameters have been determined with great precision by ESA's recent Planck mission, which studied the cosmic microwave background radiation (CMB) [15, 16]. With the XMM-Newton Space Telescope, a massive census of galaxy clusters was made, and the observations were compared with data from the Standard Model of cosmology using the parameters found with Planck. The result was a distribution of clusters and AGN compatible with the model data, but fewer clusters were observed than predicted. [17] The Athena space mission, will make it possible to observe a greater number of galaxy clusters, even so far from Earth as to observe the light emitted during their formation, so that their evolution can be best studied.

Thus, the specific studies will be:

1. The study of the chemical, dynamical and thermodynamic evolution of hot baryons.

2. The study of dark energy and dark matter through observations of galaxy clusters and spheroidal dwarf galaxies.

3. The testing of cosmological models with a complete census of baryons and their properties in the local Universe.

1.1.3 Hot plasma physics

Thanks to wide-field imaging and ultra-high resolution spectroscopy, Athena will also be able to explore a large portion of the parameters needed to understand the nature of many celestial objects, from those closest to us to intracluster objects. By highlighting possible case studies, it becomes clear how Athena can effectively study in depth the physics of hot plasma at different astrophysical scales.

Solar System bodies

Athena will be able to study how the space plasma interacts with the magnetic fields produced by the planets, while also taking a deeper look at the physics that drives the magnetosphere and planetary exosphere. The study of X-rays from the solar system has become particularly important in recent years thanks to Chandra and XMM-Newton, whose high sensitivity has allowed us to observe extremely interesting processes. Jupiter, for example, shows numerous X-emission processes, see Figure 1.8 through its atmosphere (via a process of interaction between ions from cosmic rays and the planet's magnetosphere) [18]. On the other hand, according to the observations of previous telescopes, Saturn doesn't show the same phenomena [19]. X-IFU, due to the improved performance, will again subject these planets to a careful observational campaign to determine what are the characteristics that lead to a different behavior in the X-emission domain.

Exoplanets

The atmospheric conditions and eventual habitability of a planet are intimately linked and regulated by the emission of the host star. In fact, intense X-rays during the early period of a star and the associated strong UV emission will ionize molecules in the planet's atmosphere. In addition, such intense radiation, as it penetrates into the interior of the atmosphere, would certainly interfere with the evolution of a possible life form. Therefore, the study of the star's X-rays, thanks to Athena, combined with models of each planet's atmosphere, will be able to provide a fairly clear picture of the planet's evolution and potential habitability.

Supernovae and supernova remnants

Supernovae are the major sources of heavy elements in the Universe. Such explosions are among the most important energy inputs to the interstellar medium, both from a thermal and a kinetic point of view, in the form of cosmic rays. Thanks to the X-IFU, Athena will be able to map the abundance of elements released by supernovae in order to obtain a complete picture of the conditions that give rise to nucleosynthesis. By studying radiation from the innermost region of the Galaxy, Athena will be able to study the environment at the center of the Galaxy and the accretion processes surrounding the supermassive black hole at its center, Sagittarius A* (Sgr A*). As mentioned in section 1.1.1. The wide field of view of the WFI offers the possibility of simultaneously observing the space around Sgr A*, one of the richest regions in terms of the presence of X-ray binaries, supernova remnants, diffuse emission.

Athena will study the hot plasma physics at different scale in objects like:

1. Solar system bodies.

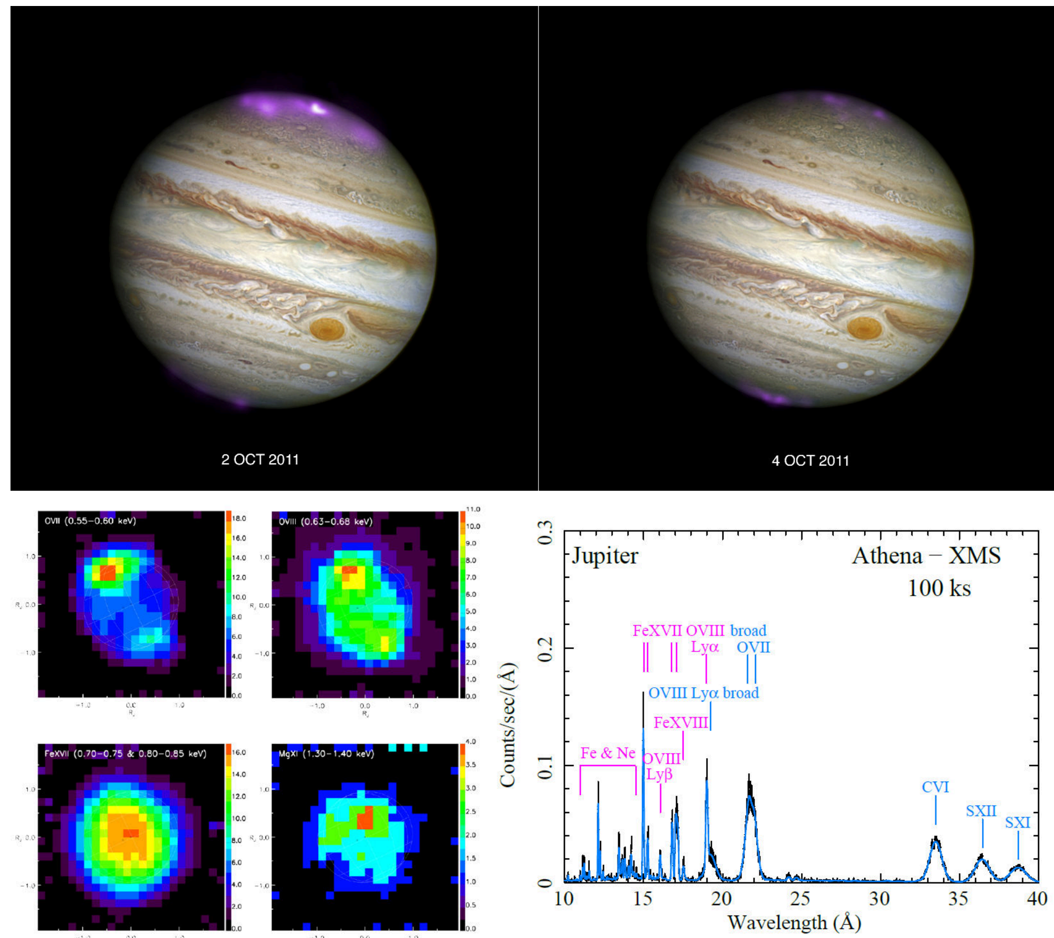

Figure 1.8: Top): Composite images of Jupiter and its aurora during (left) and after (right) the arrival of a solar coronal mass ejection at Jupiter in October 2011. X-ray data from Chandra on purple are superimposed on a Hubble Space Telescope optical. From [20], credits: X-ray: NASA/CXC/UCL/W.Dunn et al, Optical: NASA/STScI.
Bottom): Images of Jupiter taken by XMM-Newton in a narrow energy band show the aurora (top) and disk contributions (bottom). (right) Only thanks to X-IFU and its high resolution will it be possible to determine the ion species that interact with the upper region of the Jovian atmosphere and give rise to the auroral phenomenon. From [4].

2. Stars.

3. Supernova remnants.

1.1.4 Gamma Ray Bursts (GRBs), multi-messenger physics with Gravitational Waves (GW)

The possibility of multi-messenger physics with Athena and: GW, neutrinos and gamma-ray observatories is discussed in detail in [21]. GRBs, are intense

flashes of gamma rays that can last from a few milliseconds to several tens of minutes. They constitute the most energetic phenomenon observed in the universe and associated with them there is a residual emission in all spectral bands. According to the current theories, these powerful gamma-ray emissions are generated by the accretion of matter onto a black hole, the coalescence of two neutron stars or a neutron star and a black hole. Observing the X-ray part of GRBs, as in Figure 1.9 with Athena and all the other emissions associated with them such as: Gravitational Waves, neutrinos, and the gamma itself; using observatories like LIGO, Virgo, the future LISA, IceCube, KM3NeT, and CTA a new era of multi-messenger physics on these event will be possible.

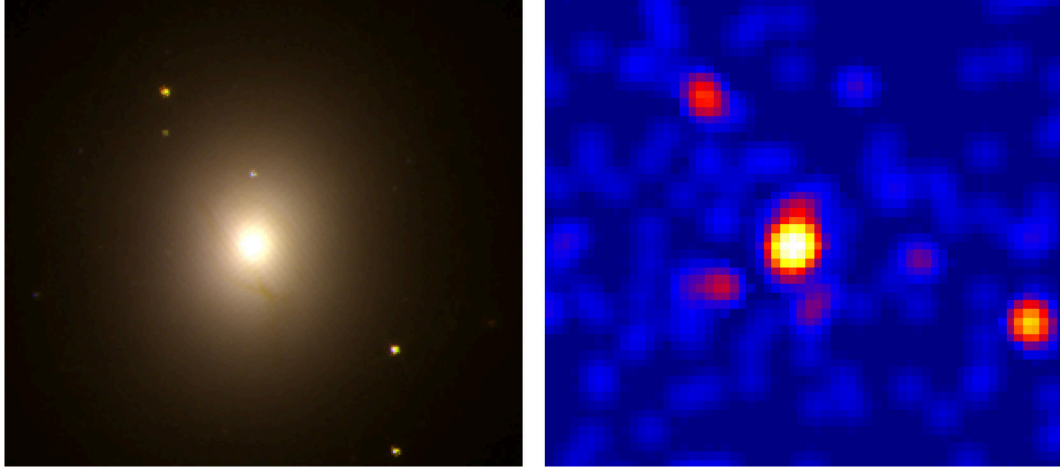

Figure 1.9: Images in: the optical and infrared (left), and in the X spectrum (right) of the electromagnetic counterpart of GW170817. (Left) Observations from the Hubble Space Telescope show a bright transient (kilonova) within the galaxy NGC 4993. (Right) At the same spot, with the CHANDRA space observatory. it was possible to observe a faint X-ray source. From [22].

GRBs as electromagnetic counterpart of GW

According to the most widely accepted models, in astrophysics at the collision or coalescence of two neutron stars should be followed by the emission of collimated streams of matter (jets) that give rise to short gamma ray bursts lasting less than two seconds. So far, the observations supporting these models have all been indirect, but it appears that these GRBs are the electromagnetic counterpart of gravitational waves, produced by the same events. In 2017 [22] it was observed the radiation emitted at the occasion of the coalescence of two neutron stars, that have product gravitational waves GW170817 [23], measured by LIGO in July of the same year and researchers were able to establish the link between gravitational waves and short-lived GRBs. This was possible by observing the products of this event: a kilonova peaking in the infrared given by neutrons, a kilonova peaking in the optical region of the electromagnetic spectrum given by neutron-free winds, and a synchrotron radiation visible at

radio, X-ray and optical wavelengths. This emission is not isotropic and the view of the event changes as the observation angle changes, as better explained in the Figure 1.10 and relative caption. With the new observational capabilities

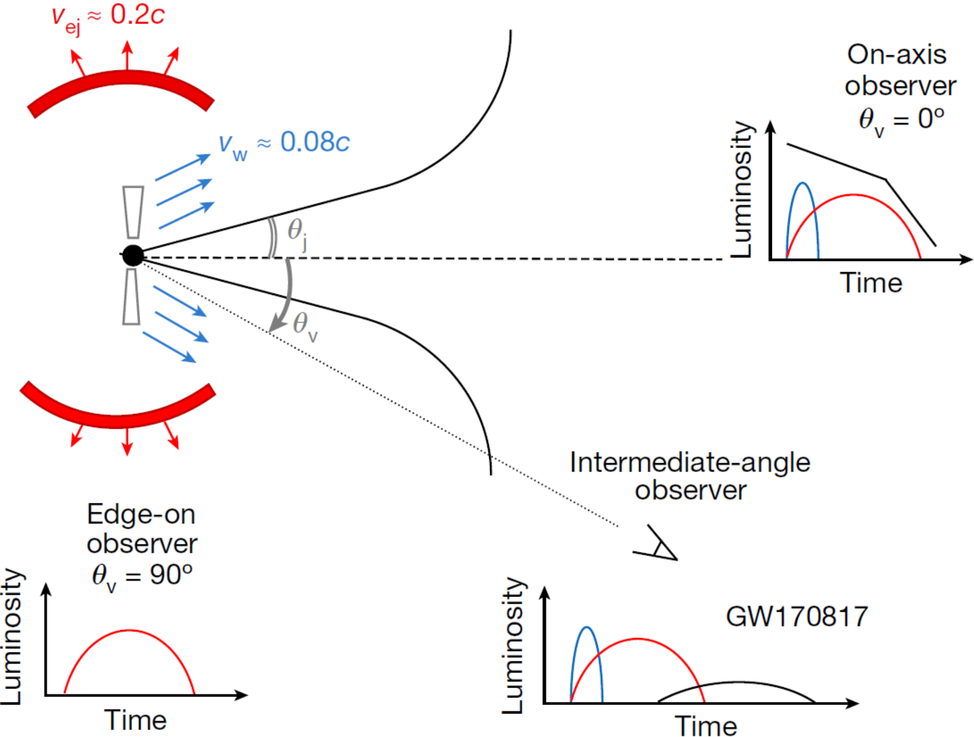

Figure 1.10: Schematic of the coalescence products of the two neutron stars in the GW170817 event. Neutrons were emitted at 0.2 times the speed of light in vacuum (red arrows), corresponding to an isotropic kilonova peaking in the infrared. Simultaneously, neutron-free particle winds are emitted along the polar axis (blue arrows), corresponding to a kilonova emission in the optical region of the electromagnetic spectrum. In addition, a synchrotron radiation is also emitted in the radio, X and optical regions of the electromagnetic spectrum (the cone in black).
Observing the coalescence from three different positions the event manifests itself in three very different ways: Along the polar axis ($\theta_v = 0$) the emission of synchrotron radiation is much brighter than the other two. On the other hand, perpendicular to the polar axis ($\theta_v = 90$) only the emitted neutrons can be observed. At an angle in between the previous two, but where it is possible to see the synchrotron emission, it turns out that the synchrotron afterglow, i.e. the most intense radiation at $\theta_v = 0$, is much weaker than the others, and is detected on timescales of even several weeks after the event. From [22].

that Athena and the next generation of interferometers will provide, it is hoped that the development of models that take all these aspects into account will resolve the inconsistencies in models of neutron star coalescence when the

production of gravitational waves and electromagnetic radiation are considered separately.

Neutrinos

Another possibility for multi-messenger studies with gamma-ray bursts is the observation of muon neutrinos produced during the emission GRB's. A study at the neutrino observatory IceCube at the South Pole [24], showed that GRBs are not the main source of high-energy cosmic Neutrinos. However, they remain very important as they would constitute evidence for Ultra-High Energy Cosmic Ray (UHECR) production in GRBs. This would be provoked by interactions between accelerated protons and the prompt γ-ray field produced during gamma-ray burst emissions. In addition the collection of neutrinos can derive from particle decays due to other events already treated, such as: active galactic nuclei jets, supernova remnants, and pulsar wind nebulae; that are involved in non-thermal X-ray emissions.

1.2 The Advance Telescope for High ENergy Astrophysics

The Athena telescope have been designed to study the scientific themes presented in the previous sections with performance far superior to that of current X-ray missions. Offering wide-field spectral imaging and spatially resolved high-resolution spectroscopy. To do this, the Athena spacecraft will consist of three modules: the mirror block to place the optics that will focus the X-rays on the instruments, the service module i.e. the body of the telescope, and the focal plane where the sensing instruments will be assembled as in Figure 1.11.

The mission development concluded the System Required Review (SRR) in the preliminary definition phase of the project (B-1), but is currently under a redefinition process called by ESA to re modulate costs in order to adopt the mission with the (Laser Interferometer Space Antenna LISA) mission. Leading to launch the observatory in late 2030s with an Ariane 6. It will operate in a large halo orbit, of about 106 km radius, around L1, one of the Lagrange point in the Sun-Earth system. Initially, the halo orbit was planned around L2, but has been changed as L1 has a more known environment that helps in making more representative predictions about the non X-ray background level[4]. The position at a Lagrangian point, at a distance of more than 1.5 million of km from the Earth, is another difference with Chandra and XMM-Newton that work in a Highly Elliptical Orbit around the Earth. Since the L1 orbit provides a constant good sky visibility and a very stable thermal environment, ensuring

[4]The the Galactic Cosmic Rays (GCR) contribution is expected to be the same in L1 and L2. Instead the Soft Solar Protons one is well studied in L1 from previous missions, but not as well known in L2

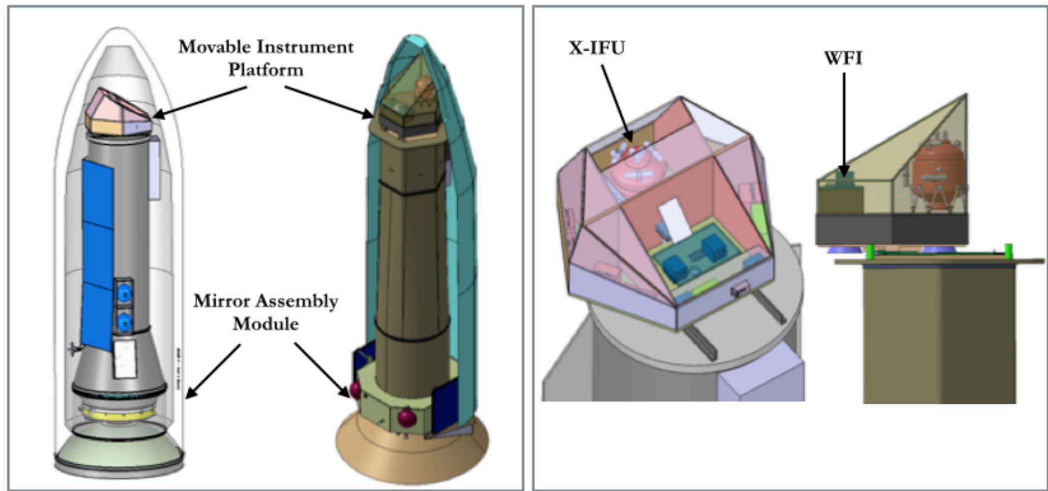

Figure 1.11: Illustrative model of the whole telescope with detail on the focal plane with the two instruments X-IFU and WFI. From [5]

a higher observing efficiency.

1.2.1 The service module

The service module consists of a fixed structure between the housing of the mirrors and the focal plane. This structure should give a fixed focal length of 12 m. It is optimized to have a low moment of inertia, so as to have a rapid response to mechanisms of pointing. Inside it are housed all the standard functions of the satellite, from the orbit control system to thermal control, telemetry, and data management, and on it will also be mounted the solar panels that will provide power to the satellite.

1.2.2 The mirror housing module

The mirrors will be housed at one end of the telescope and will focus the X-photons to the other end of the telescope where the focal plane lays. It will exploit a new technology developed by ESA and based on. on the SPO (Silicon Pore Optics). SPO is composed of highly luminescent silicon wafers mounted together through a self-supporting structure. The single mirror, which forms a monolithic mono-crystalline silicon structure, is assembled with the others to produce a matricial modular structure. By thus, assembling a matrix of mirrors, it is possible to achieve a very low weight (350 kg per single matrix): this aspect is fundamental, especially dealing with a telescope of this size. The architecture is visible in Figure 1.12 and together with the fixed focal length of 12 m they will contribute to obtain a large effective area[5] of 1.4 m^2 at 1 keV [25]. The only way to focus X photons is to use a telescope with Wolter

[5]Because of of riemission, diffraction, and other effects, the geometric area of the telescope results reduced to an effective area that that is the real observational one.

configuration, taking advantage of grazing incidence; in fact, X-rays can be deflected by the optics only for angles of incidence less than 2. The mirrors used are essentially one paraboloid and one hyperboloid in series, to increase the number of photons captured is exploited the nesting, a series of concentric Wolter optics.

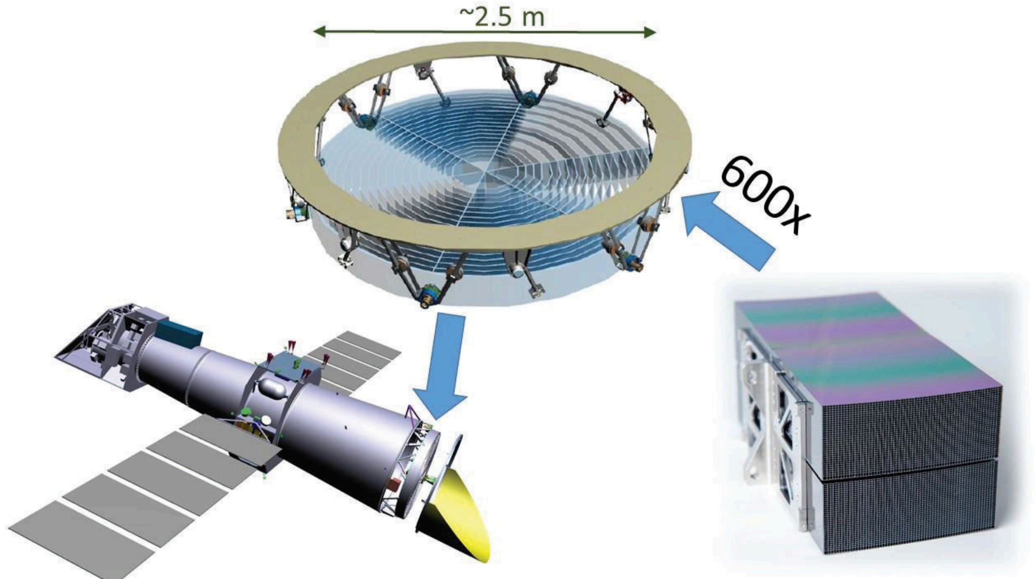

Figure 1.12: Right) single SPO module. Top) the entire configuration of the mirrors once assembled, where there are 972 SPOs assembled into 19 rings and 6 sectors in a ring. Left) Mirrors allocation in the telescope. From [25].

1.2.3 The instrumental focal plane

The telescope alternately focuses X-photons in two instruments: the innovative X-ray Integral Field Unit (X-IFU) [6], based on cryogenic detectors, characterized by a very high spectral resolution and moderate temporal and spatial resolution, and the Wide Field Imager (WFI) [7], based on Silicon detectors, field of effect transistors working in depletion through p-channel, DEpleted Pchannel Field Effect Transistors (DEPFETs) with high spatial and temporal resolution and moderate spectral resolution. These two instruments, together, combining their characteristics can provide for the scientific objectives, and also taking into account the characteristics of the lenses, a spectral bandwidth from 0.5 to 15 keV.

WFI - Wide Field Imager [7]

The Wide Field Imager, shown in its block diagram in Figure 1.13, will combine a wide field of view of 40×40 $arcmin$ with an excellent, 1 $Crab$[6], count rate.

[6]The $Crab$ is a commonly used unit to measure the intensity of astrophysical X-ray sources. It is defined as the intensity of the Crab Nebula at the corresponding X-ray pho-

The required performances, summarized in Table 1.1 , will be met using two detectors: a detector, with a large area, comprising 4 sensors for a total of 1024×1024 pixels and a fast detector, optimized for observations at high count rates. The detectors will be surrounded by a multilayer screen with several Zs, which will specifically eliminate lines of fluorescence that would contribute to the background. These are produced by the interaction of high-energy charged particles, cosmic rays, with the materials in the telescope. This interaction in fact generates electrons with energies equal to X-rays. In addition, because of the combination between the high count rate and the large number of pixels, the analysis of first-level and event identification will have to be done on-board and in real time, because the primary data transfer rate will be much higher than the capacity of the transmission channel.

Parameter	Characteristics
Energy Range	0.2-15 keV
Pixel Size	130 $\mu m \times$ 130 μm (2.2” $\times$ 2.2”)
Operating Mode	rolling shutter (min. power consumption)
	full frame mode
	optional: window mode
High-count rate detector	64 $\times$ 64 pixel, mounted defocused
	split full frame readout
	time resolution: $80\mu s$
	1 $Crab$: >90% throughput and <1% pile-up
Large-area DEPFET	4 quadrants, each with 512 $\times$ 512 pixel (total FOV $40' \times 40'$)
	time resolution: < 5 ms
Quantum efficiency incl. external filter	>20% @ 277 eV
	>80% @ 1 keV
	>90% @ 10 keV
	transmissivity for optical photons: 3×10^{-7}
	transmissivity for UV photons: $< 10^{-9}$
Energy resolution	FWHM(7 keV) ≤ 170 eV
Non-X-ray Background (L2 orbit)	$< 5 \times 10^{-3}$ $ctcm^{-2}s^{-1}keV^{-1}$

Table 1.1: WFI top level performance requirements. From [7].

X-IFU - X-ray Integral Field Unit [6]

To achieve the required performance, of 2.5 eV FWHM, summarized in Table 1.2, the X-ray Integral Field Unit, shown in its block diagram in Figure 1.14, will be based on cryogenic microcalorimeters with sensors that exploit the superconducting transition characteristics(Transition Edge Sensors, TES). These can provide the resolution in energy needed, working with incredibly better efficiency than the spectrometers mounted on current X-ray observatories [9]. It has already been demonstrated that TES technology is able to provide the required spectral resolution (2.5 eV FWHM)[26], however, what is still on under development is the capability to provide this resolution over a wide field of view (50 of arc). To obtain the cited performances the instrument

ton energy. Because of its well-known spectrum and its stable and intense emission, the Crab Nebula is commonly used as a standard candle for in-flight calibration of instruments response. In the $2 - 10$ keV range, 1 $Crab$ is 2.4×10^{8} erg $cm^{-2}s^{-1}$

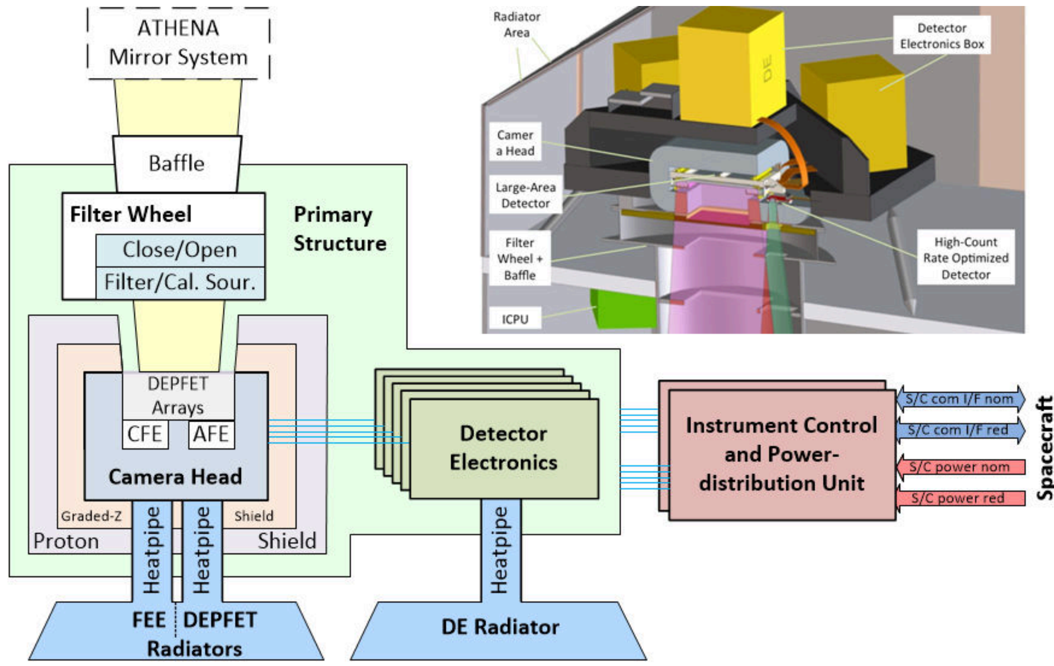

Figure 1.13: WFI block diagram and sectional drawing that show the subsystems of the instrument, the photons arrive from the telescope mirrors and are focused on the DEPFET detector, surrounded by the screens, the baffle, and a system of filters. The detector then interfaces with an electronic composed of six modules, which in turn interfaces with the instrument control system for recognition of events and an initial analysis of the data. From [7].

will consist of two detectors: the TES array developed by NASA Goddard [26], and the Cryogenic AntiCoincidence (CryoAC) to reduce by almost two orders of magnitude the non X signal background due to charged particles from cosmic rays. Very important to achieve the scientific goals on weak or very distant sources.

I will now present the two detectors, their functioning and the readout system. The non X-background, the CryoAC and the TES functioning will be examined even if they will be treated in depth in the following Chapters.

TES array

TESs are superconducting thin film thermistors operated in the sharp transition region between the superconducting and normal states. The X-IFU TESs consist of a 50 μm^2 Mo/Au bilayer voltage biased at a superconducting-to-normal transition temperature of $\sim 90\ mK$. The TES, visible in Figure 1.15, is deposited atop a 0.5 μm thick silicon-nitride membrane, which forms a weak thermal link to the heat sink. TESs are coupled to an electroplated $Au/Bi/Au$ absorber, which provides the X-ray stopping power. Its composition (Bi to Au ratio) is chosen to provide the desired pixel heat capacity (optimized for energy resolution and dynamic range), while simultaneously achieving the de-

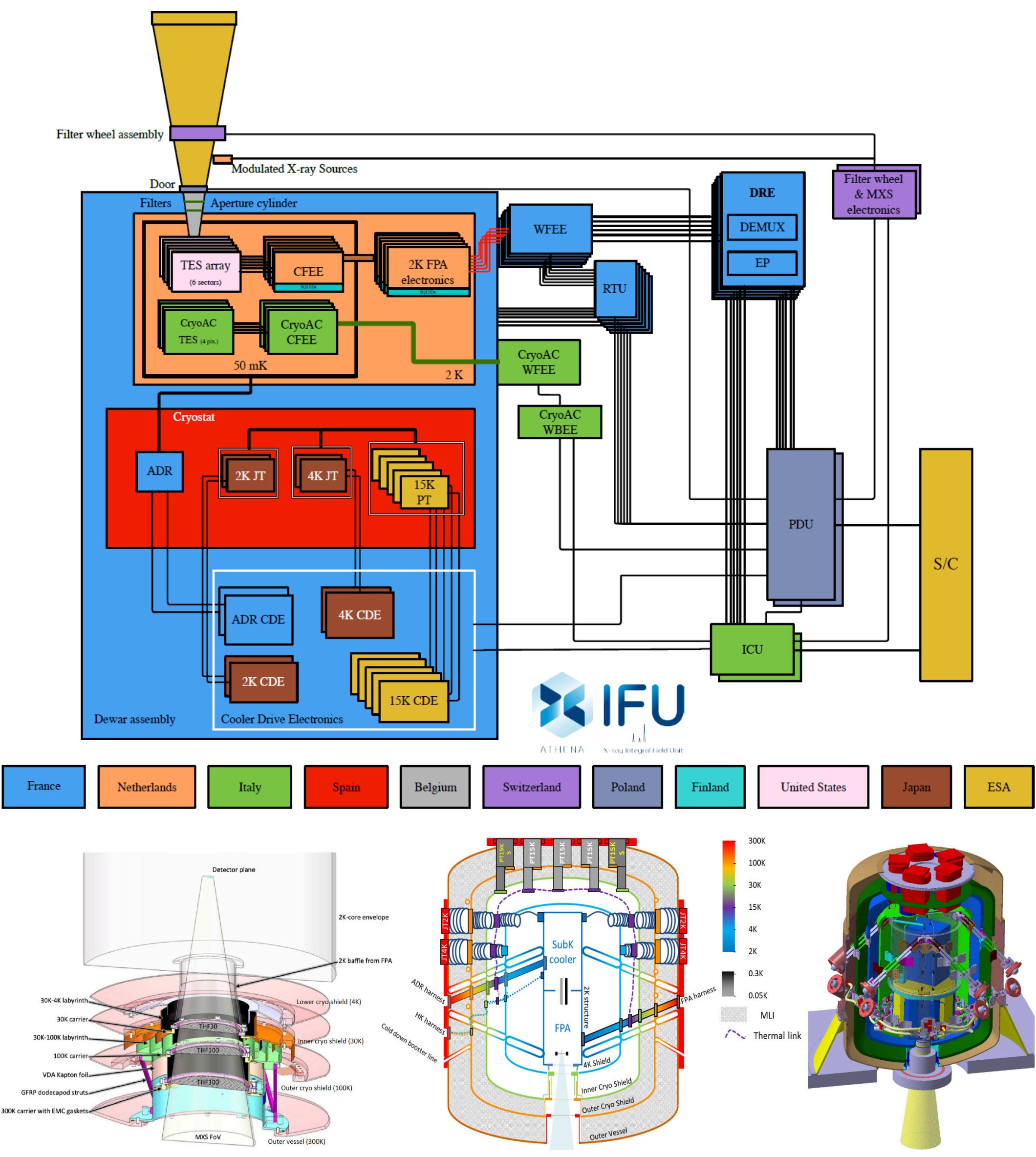

Figure 1.14: Top) X-IFU block diagram highlighting its main components, as well as the country responsible for the procurement. It is also shown how photons focused by the SPO lens pass through a system of filters on the TES array main sensor and thus on the anticoincidence. The detectors are maintained at the working condition by a thermal bath at 50 mK with a cryostat. Each component has its own electronics stage controlled by a interface control unit (ICU) that also performs interfacing with the rest of the satellite. From [6].
Bottom) Drawing of the instrument on the focal plane of X-IFU, which focuses attention on the interior of the cryostat that houses the sensors, showing the screens and the housing of the parts on the focal plane. From [6].

Key performance parameter	Value
Energy range	0.2-12 keV
Spectral resolution	< 2.5 eV up to 7 keV
Energy scale calibration	0.4 eV in the 0.2-7 keV range
Field of view	5' (equivalent diameter)
Instrument efficiency at 0.35, 1.0, 7.0, 10 keV	$> 13\%$, $> 57\%$, $> 63\%$, $> 42\%$
Non X-ray background	$< 5 \times 10^{-3}$ $counts/s/cm^2/keV$ (E > 2 keV)
Relative time resolution	10 μs
2.5 eV throughput (broadband, point source)	80% at 1 $mCrab$ (goal of 10 $mCrab$)
10 eV throughput (5-8 keV, point source)	50% at 1 $Crab$
2.5 eV throughput (broadband, extended source)	80% at 2×10^{-11} $ergs/s/cm^2/arcmin^2$
Continuous cool time / regeneration time	Up to 28.5 hours (75% duty cycle)

Table 1.2: X-IFU top level performance requirements. From [6].

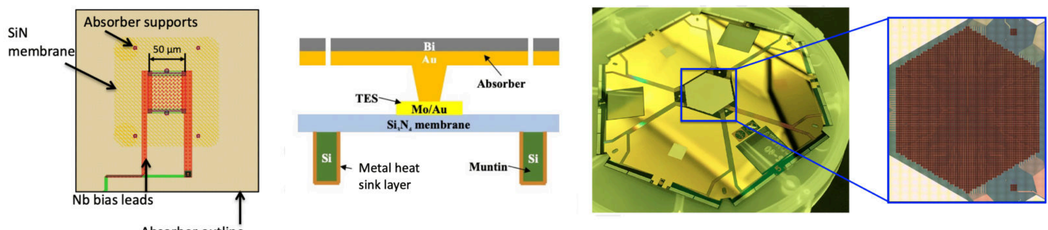

Figure 1.15: Left) Top-down view of pixel design. Center) Cross-section cartoon view of pixel layout. Right) Photograph of a X-IFU prototype hexagonal detector with more than 3000 pixels.

sired pixel quantum efficiency. This optimization has a limit, as a minimal layer of gold is required for intra-pixel heat diffusion. A small gold cap is deposited on top of the absorber to optimize infrared reflectivity and protect the porous bismuth from humidity. For the baseline 317 μm pitch pixels, a target of $\sim 91\%$ intrinsic stopping power at 7 keV is achieved with a total gold thickness of 1.09 μm (of which 40 nm are used for the capping) and bismuth thickness of 5.51 μm. The spacing between the pixels further introduces a flat multiplicative factor in the instrument efficiency. State of the art fabrication processes allow reaching an average gap of 6.34 μm, leading to a 96 % filling factor.

The absorption of an X-ray in the absorber leads to a temperature increase of the TES/absorber couple and thus of the TES resistance (see Figure 1.16). Under an (almost) constant bias voltage, the current going through the TES then shows a sharp decrease. Overall, each X-ray photon will create a current pulse, whose amplitude (and shape) depends on its energy. It is reconstructed on board to provide a precise measurement of the photon energy and arrival time. The combination of the TES/absorber heat capacity, the thermal conductance to the cold bath, and the electrical properties of the TES circuit, including the detector set point, define the temporal shape of the pulse. These are optimized to match the X-IFU 0.2 to 12 keV operating range and allow a multiplexed readout with minimal resolution degradation [6].

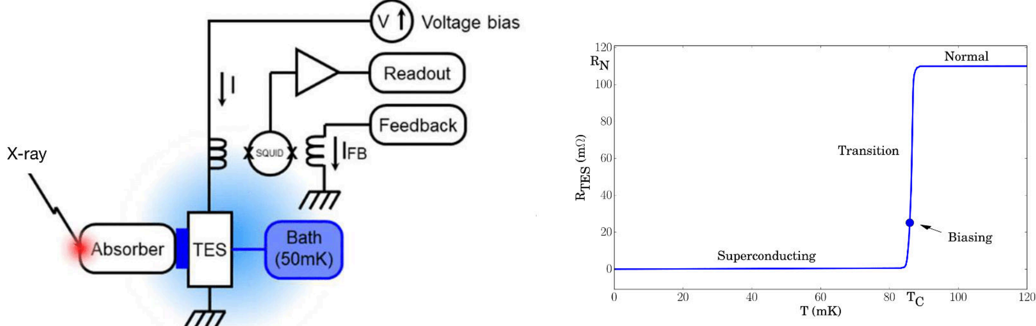

Figure 1.16: Left) The schematic of a TES. Right) The resistance variation as a function of the temperature, showing a sharp rise in the transition region between the superconducting and normal states[27].

The cold front end electronics

The amplification of the signal generated by the TES relies on SQUIDs (Superconducting QUantum Interference Devices), split in two stages and referred to as MUX SQUIDs (also called SQ1) for the first stage, and as the AMP SQUIDs for the second SQUID series array amplifier. SQUIDs are extremely sensitive magnetometers, operating at cryogenic temperatures. The current flowing through the TES is converted into a magnetic field by an input coil. To linearize the near-sinusoidal MUX SQUID response, and increase its dynamic range, the digital readout electronics generates a current for a feedback coil to null the magnetic field sensed by the SQUID (see Figure 1.17). This error signal is then read out by the AMP SQUID, operated at 2 K, to be amplified in order to increase the signal robustness against down-stream and external noise sources. The output voltage is then delivered to the low-noise amplifier of the warm front end electronics operated at room temperature.

Because resources are limited on the spacecraft, multiplexing is required and the baseline adopted for X-IFU is Time Division Multiplexing (TDM[28]), see Figure 1.17 for a description of the TDM principles. In TDM, each DC-biased TES is associated with a MUX SQUID. Those are activated sequentially via a flux-actuated superconducting switch, so the TESs in each readout column are measured sequentially. Every SQ1 activation is called a row and a full set of samples of a column constitutes a readout frame. TDM columns are read out in parallel: the SQ1 of the same row number of each column are activated synchronously. The row addressing is performed in the Digital Readout Electronic (DRE). In order to limit the number of row address lines, two levels of switches are used: instead of having 34 pairs of command lines to command the ON/OFF state of the MUX SQUID, a command matrix of 9×4 is implemented, thus requiring only 13 pairs. Another possible readout technology is based on Frequency Domain Multiplexing (FDM) [29], where each channel have its own resonant frequency, and it have been used for first joint measurements between the NASA TES array and CryoAC detectors [30].

In its present configuration, the total number of pixels of the detector array

of X-IFU is 2376, divided in 6 groups of 396 pixels each. Each group of 396 pixels is read out by independent electronics, so that a failure would not lead to a loss larger than one sixth of the whole detector. One group of 396 pixels is thus made of 12 columns of 33(+1) pixels (33 rows with sensitive pixels × 12 columns = 396 pixels, plus one "dark row" with a pure resistor attached, that monitors the drift in the gain of the readout electronics).

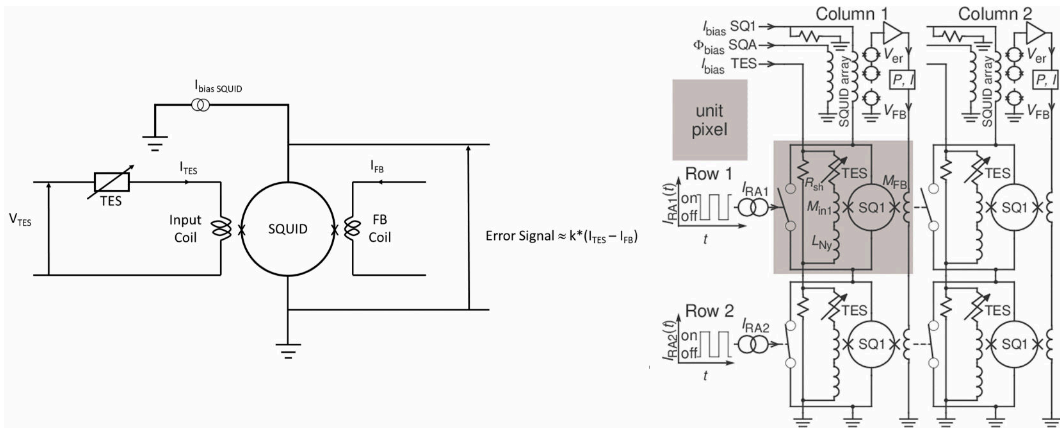

Figure 1.17: Left) Illustration of the feedback loop used to null out the magnetic field sensed by the SQUID[31]. Right) Schematic[28] of 2-column × 2-row TDM. Each dc-biased TES is read out by a first stage SQUID amplifier (SQ1) via inductive coupling (M_{in1}). A row of SQ1s is turned on by applying a row address current (I_{RA}) to the corresponding row address line, opening the row's flux actuated switches. During TDM operation, rows are opened sequentially, reading out one TES per column at a time. Each column's SQ1 signals are passed to a SQUID series array amplifier, whose voltage (V_{er}) is read out by room temperature electronics.

The cryogenic anti-coincidence (CryoAC) detector and associated electronics

Background will be generated by primary and secondary particles hitting the prime TES array and depositing energy in the science energy range of the X-IFU. A second cryogenic detector is accommodated just underneath the prime array (at a distance less than 1 mm, see Figure 1.18), so that events depositing energies both in the micro-calorimeter array and the CryoAC can be flagged out, and removed from the count stream from the observed source (see [32] and Figure 2.3 for a recent review of the particle background of the X-IFU). The CryoAC is made of Si suspended absorbers sensed by a network of Ir/Au TES. Time coincident multiple events (generated primarily by secondary particles generated in the metallic parts close to the detector) can also be flagged out, although not necessarily having a time coincident event in the CryoAC. The CryoAC detector is segmented in four quadrants, each associated with its own readout electronics. Each quadrant of the warm front end electronics provides

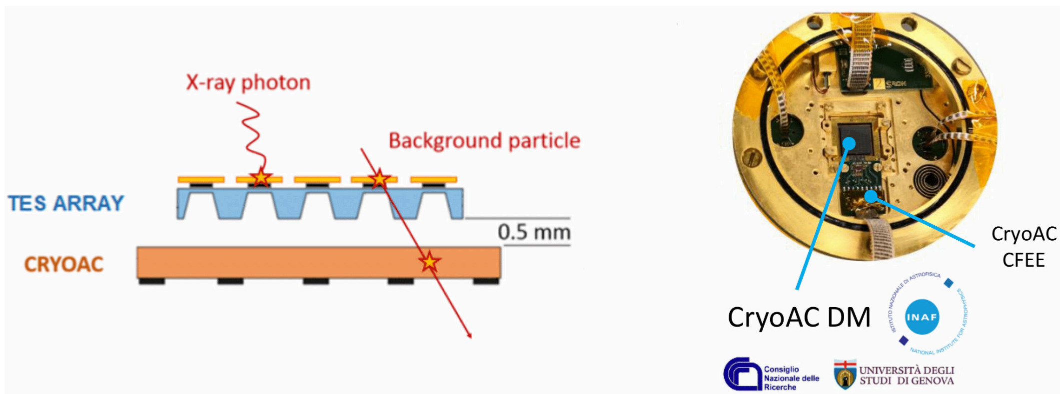

Figure 1.18: Left) Working principle of the CryoAC. Right) The CryoAC demonstration model and its cold front end electronics as used for the coupled test with prime micro-calorimeter array[30].

bias to TES and SQUID for a single pixel and producing the analog scientific signal and housekeeping. Then the CryoAC warm back end electronic performs the digital processing, detecting, and time stamping cosmic ray events by applying a proper trigger logic algorithm ([33]), and generating the associated telemetry. The function is implemented in two identical independent units operated in cold redundancy. Both units can operate the 4 anti-coincidence detection chains. Failure in one readout chain would mean that approximately one fourth of the prime array would have a higher background, though not leading to a complete loss as the pointing of the telescope could be offset so to avoid that particular quadrant.

Chapter 2

The Cryogenic AntiCoincidence Detector - CryoAC

5 E 'l duca che mi vide tanto atteso,

In this chapter the detector physics is presented with respect to the Transition Edge Sensor theory and the working principle of the anticoincidence detector with its thermal and a-thermal model and its design.

2.1 The Anticoincidence detector

The anti-coincidence detector is essential inside X-IFU as the spectrometer is sensitive to all particles which deposit energy in the absorbers and the mission working point, L1 is blasted by a stream of energetic charged particles, see Figure 2.1. Those particles constitute the non-X-ray background that can be decomposed as follows [32]:

1. High energy Galactic Cosmic Ray (GCR) particles. Their flux is modulated below 10 GeV by the solar activity along the solar 11-year cycle. The higher the solar activity, the lower the flux below 10 GeV. The applied spectrum used for background assessment corresponds to 80 % of the Pamela expected flux at solar minimum. Given the presence of the X-IFU cryostat, it is expected that only particles having energies > 150 MeV (TBC) can reach the FPA depositing energies in the TES-array.

2. Secondary particles showers (including fluorescence) created by GCR when interacting with the instrument and the spacecraft. The nature and distribution in energy of these secondary particles are obtained as Geant4 by-product result using the expected GCR spectrum in orbit.

3. High energy solar events, i.e. the high energy tail of the Solar Energetic Particles (SEP) at E$>$ 150 MeV. SEP flux in the Earth neighborhood varies with the solar activity, both with the phase in the solar cycle, and

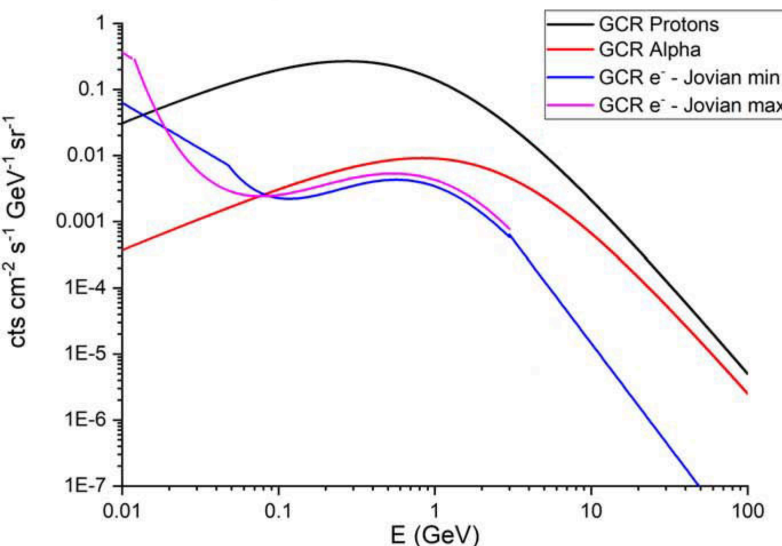

Figure 2.1: Spectra of GCR protons, GCR alpha particles, and electrons (both GCR and Jovian contribution) in L1. From [32].

the random occurrence of solar flares. These events are not accounted in the background budget since the instrument will be in close position in this case.

Since from the main detector point of view the signals produced by those particles are indistinguishable from the x-Ray photons to be studied, this background would significantly reduce the X-IFU capabilities, especially when studying distant or faint objects. Therefore, the acceptable non-X-ray background on the instrument key requirement is specified as:

- $\leq 5 \times 10^{-3}$ $cps/cm^2/keV$ in the 2-10 keV energy band,

this assuming the input spectra provided by the spacecraft at the Aperture Cylinder. The model shall include a 20% uncertainty to exclude fluorescence photons from Au material. An active anti-coincidence is then exploited to achieve this background level, the working principle is simple and can be schematized as in Figure 2.2. Particles will pass through the X-IFU main detector and will deposit energy also on the underneath anti-coincidence detector. On the other hand, soft X-photons will be absorbed by photoelectric effect [34] on the first detector, therefore any coincidence signal between the CryoAC and the spectrometer will be a signal to be rejected. The X-IFU background rejection efficiency depends: on the geometrical configuration of the cryoAC and main detector array related to the classical concept of the anti-coincidence solid angle coverage, and on the capability of the main array to discriminate background events on its own, relying on the energy deposited and on the pixel pattern activated by the impacting particles, i.e the detector rejection efficiency. Therefore, two different screening strategies are applied to the flux incident on the X-IFU:

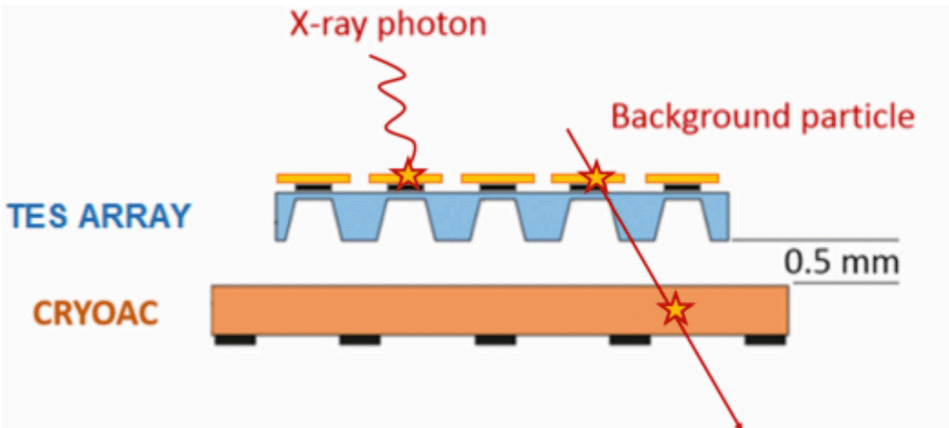

Figure 2.2: Soft X-rays that interact with the TES array are absorbed by photoelectric effect [34]. On the other hand, background particles will pass through the X-IFU main detector and will also deposit energy on the underneath anti-coincidence detector. Therefore, any coincidence signal between the CryoAC and the spectrometer will be a signal to be rejected.

1. Time coincidence with the cryoAC: photons are not expected to produce a coincidence signal in the cryoAC, so we can assume that every event that is detected simultaneously in both the cryoAC and the main detector can be rejected as particle-induced one.

2. Pattern recognition: due to the detector features (pixel physically separated, then no correlated signal among contiguous pixels , like CCD based detectors) photons will not produce complicated pixel patterns to reconstruct. Instead, we can assume that all the events that activate more than one pixel can be rejected as induced by particles with skewed trajectories intersecting more than one pixel, or by simultaneous impacts by multiple particles.

Extensive Monte Carlo simulations have been performed using the Geant4 software to assess the X-IFU background level for different geometrical configurations [32]. Special care was taken to incorporate the most representative mass model of the FPA. These simulations have shown the need for a low Z material coating (e.g. Kapton) inside the FPA Nb shield to limit the secondary electron production in close proximity of the detector, see Figure 2.3. Since, after the rejection processes are applied, the number of background events remains above requirements. It is due to the fact that metallic parts in the vicinity of the main detector array (mainly the niobium shield) generate secondary electrons that hit the main detector absorbers, but not the cryoAC, and deposit energy in the 2-10 keV band. Anyway, the low Z shield alone is not sufficient to get the right performance, thus we need to further reduce the fluorescence photons generated by the interaction of primaries and secondaries with the niobium shield, not fully stopped by the Kapton. One solution consists in coating the Kapton shield with $\sim 10\mu$m gold, which is thick enough to

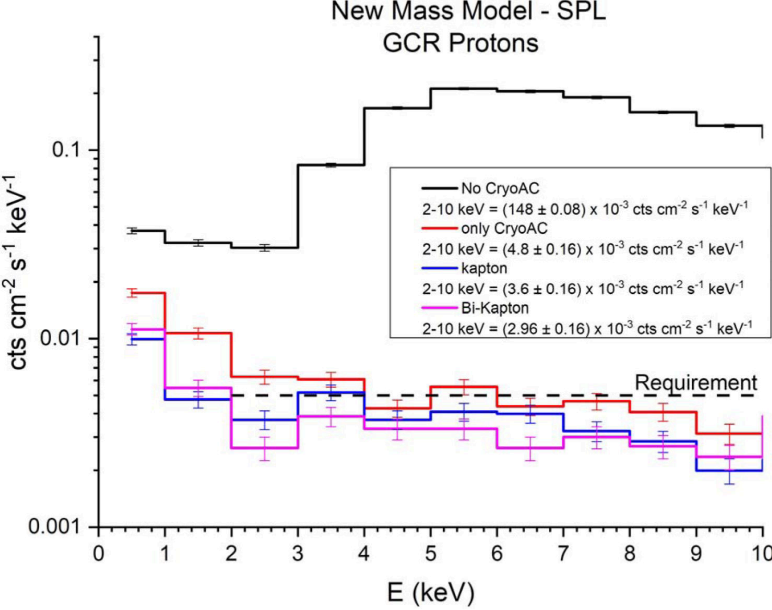

Figure 2.3: Background levels in different FPA configurations. The active anti-coincidence reduces the background level by more than one order of magnitude. Anyway, to achieve the required *cps* filtering with a low Z material is needed. From [32].

suppress the Nb fluorescence at $> 90\%$ level. Of course, gold have their own fluorescence (9.7 keV), but it is in the higher end of the energy range of the main detector and also not to be accounted for as from the original requirement.

The CryoAC will be less than 1 mm apart from the TES-array and at the same base temperature, 50 mK, thus it will work with the same technology of the spectrometer exploiting the transition edge sensor capabilities. The theory of TESs, of the CryoAC detector and its design are presented in the following sections.

2.2 The Transition Edge Sensor microcalorimeter

A Transition-Edge Sensor (TES) is a metal film of superconducting material, maintained at a working point on its normal-superconducting phase transition. A simple and generic detector based on TES would consists of four elements, visible in Figure 2.5:

1. an energy absorber in strong thermal contact with:
2. a TES,
3. a thermal bath,

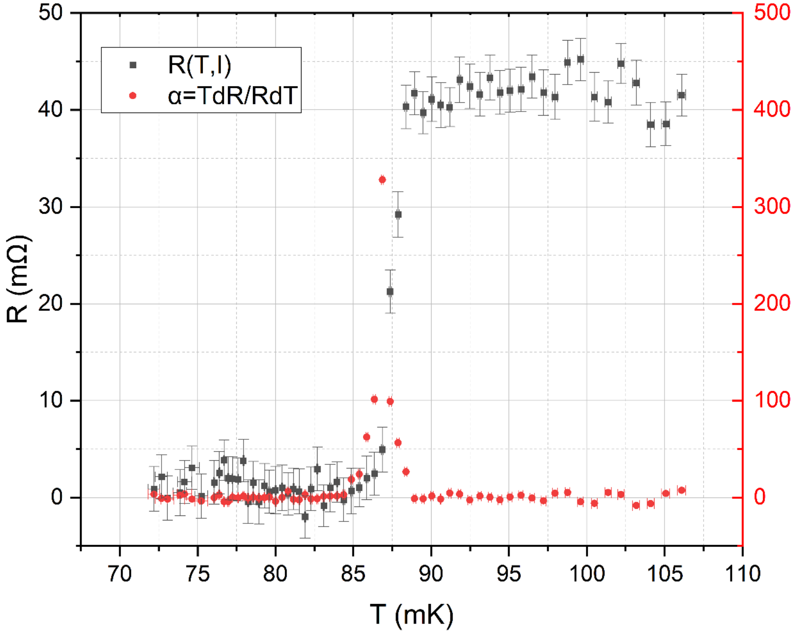

Figure 2.4: Example of the transition curve of a TES (dots and line) to which the sensitivity of the thermometer is superimposed (circles).

4. a weak link between the thermal bath and the TES-absorber.

Radiation incident on the absorber would release energy, causing a local temperature rise and consequently a transition of the film to normal metal, see Figure 2.4. The thermal bath allows the system to return to working temperature after a characteristic time, which will be the detector dead time, this be fast enough to avoid signal overlap phenomena, but still long enough for the readout electronics to measure the change in resistance of the thermometer.

Such a detector can be operated in two types of regime: full and linear, depending by their design and incident signals. In the full regime TES are in saturation, as the working point of the TES is kept below the critical temperature and the incident signal cause a full transition. In this case, the TES works as a counter, since the change in resistance cannot be used as an index of the energy incident on the absorber. In the linear regime, the sensor is kept at the beginning of the transition and the incident signal will keep the TES resistance inside the linear region of the transition. In this regime, it is possible to do spectroscopy by properly calibrating the thermometer, as the linear resistance increment depends on the amount of energy deposited, operating the TES as a micro-calorimeter.

TES based detectors allow excellent energy resolutions, up to 2 eV at 6 keV [26] and fast response time, anyway, is difficult to find the correct working point because the TES can be driven to instability, due to the narrow transition region which ranges from fractions to a few milliKelvin. Typically working temperatures are from tens to hundreds of mK and can be engineered by

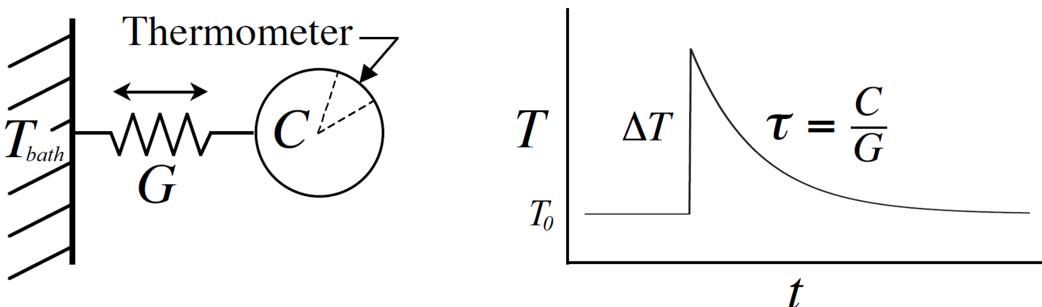

Figure 2.5: Left: Simplified thermodynamic model of a TES. Right: Thermal response. From [38].

the chose of the superconducting metal and exploiting the proximity effect [35], to tune the critical temperature as needed by the specific application. Absorbers must be designed according to the incident radiation to be studied, e.g. X-ray could be absorbed with a good efficiency by $5 - \mu m$-thick Gold absorbers [34]. Other possible issues could be related to Joule heating that can cause thermal drifts and fluctuations in working temperature that, although small, can significantly degrade their performance. In addition, self-heating can cause separations between superconducting and normal regions within the film. For example, if parallel segments have different temperatures, the hotter one will have greater resistance, so current will tend to pass into the other, leading the system to stability; on the other hand, if the segments with different temperatures are in series, the hotter one will receive more heat through the Joule effect, resulting in a detector with a temperature gradient within it and instabilities which lead to the transition to the normal state. The shape of the transition itself is heavily influenced by sensor geometry and edge effects, such as imperfections in the contours and within the films. Some of these problems can be solved by exploiting the Electro-Thermal Feedback (ETF) [36], thus biasing the TES with a constant voltage and reading the output signal with a current amplifier: in this configuration, as will be seen, the TES is stable. It is then necessary to make sure that the films have a very low degree of impurities, since their superconducting properties, e.g. transition temperature, can be greatly affected. This requires that their production take place under low contamination and high vacuum conditions. In addition, since these films are grown on a substrate, it is important to ensure that such growth is homogeneous.

TES, first introduced in 1940s [37], have been widely used since the 1990s, after the intuition of readout techniques with Superconducting QUantum Interference Devices (SQUIDs) [36]. Their functioning has been thoroughly investigated, and the basic TES calorimeters have been described in [38] and [31].

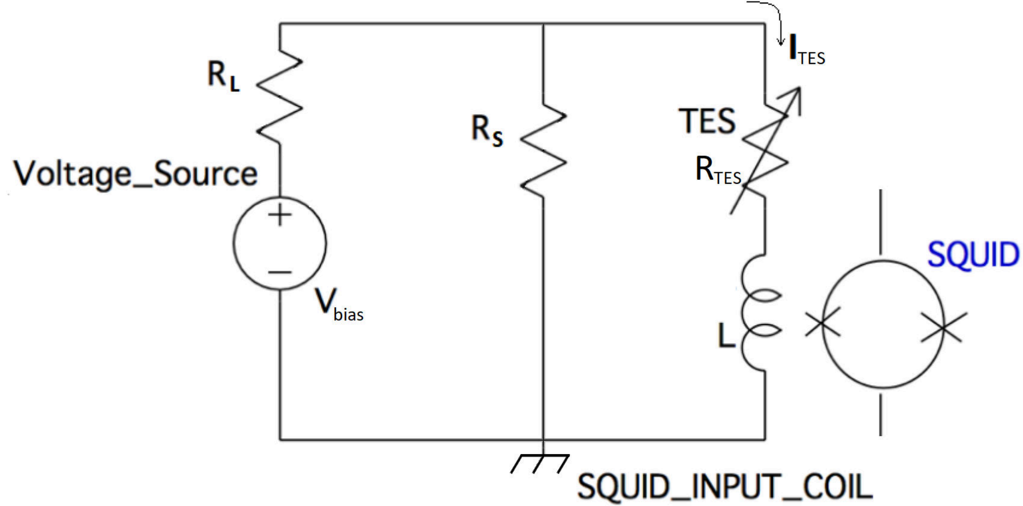

Figure 2.6: Typical circuit diagram for reading a TES.

2.2.1 Thermo-electric response

The simplest thermal TES detector have been already described and schematized and will now be retrieved by discussing the equations governing its dynamic and signal generation. Analyzing this configuration, at the equilibrium, we have a power P_{bath} dissipated toward the thermal bath describe by a power law:

$$P_{bath} = k(T^n - T^n_{bath}). \tag{2.1}$$

Thus, thermal conductance can be defined as:

$$G \equiv \frac{P_{bath}}{dT} = nkT^{n-1} \tag{2.2}$$

and the total power balance of the system is:

$$C\frac{dT}{dt} + P_{bath} = P_{in} + P_J(T), \tag{2.3}$$

that can be rewritten as:

$$C\frac{dT}{dt} + \int_{T_{bath}}^{T} G(T')dT' = P_{in} + I^2_{TES}R_{TES}, \tag{2.4}$$

whose terms are respectively: the power stored in the absorber through its thermal capacity and temperature, the power dissipated to the thermal bath, the incident power and the joule dissipated power by the TES reading. P and T are function of time and R_{TES} is a function of T and I_{TES}, thus functions of time.

Regarding electrical response of the TES, the electrical readout, see Figure 2.6, ignoring noise, is described by the following equations:

$$\begin{cases} V_{bias} = I_{bias}R_L + I_{TES}R_{TES} + L\dfrac{dI_{TES}}{dt} \\ I_{bias} = I_S + I_{TES} \\ I_S R_S = I_{TES}R_{TES} + L\dfrac{dI_{TES}}{dt} \end{cases} \tag{2.5}$$

obtaining:

$$V_{bias}\frac{R_S}{R_L + R_S} = I_{TES}\left(\frac{R_{TES}R_L + R_{TES}R_S + R_L R_S}{R_L + R_S}\right) + L\frac{dI_{TES}}{dt}, \tag{2.6}$$

where, again, R_{TES} is a function of T and I_{TES}. Thus, the electro-thermal model from Equations 2.4 and 2.6 of this simple configuration is complicated, but it could be resolved with some approximation from some simple considerations.

Linear response

It is possible to simplify the discussion in the small signal regime, considering to remain in the linear part of $R_{TES}(T, I_{TES})$ near the working point at $R_0 = R_{TES}(T_0, I_0)$. It is possible to define the TES sensitivity [39], as seen in Figure 2.4 as:

$$\alpha \equiv \frac{\partial log R_{TES}}{\partial log T} = \frac{T_0 \partial R_{TES}}{R_0 \partial T} = \frac{2\alpha_I + \frac{G_0 T_0}{P_{J0}}\beta_I}{2 + \beta_I}, \tag{2.7}$$

where the non linear behavior of TES is considered, for which the resistance is a function of temperature and current, α_I and β_I are:

$$\alpha_I = \left.\frac{T_0 \partial R_{TES}}{R_0 \partial T}\right|_{I_0} \qquad \beta_I = \left.\frac{I_0 \partial R_{TES}}{R_0 \partial I}\right|_{T_0}. \tag{2.8}$$

Following the procedure of ref. [38] it is possible to calculate the TES current change due to stationary incident power P_{in} at a constant voltage bias $V_{TES} = R_0 I_0$, as:

$$\frac{dI_{TES}}{dP_{in}} = \frac{dT}{dP_{in}}\frac{dR}{dT}\frac{dI}{dR}, \tag{2.9}$$

and thanks to Equations 2.2, 2.7 and Thevenin theorem applied to the Bias circuit in Figure 2.6 ($V_{Th} = V_{bias}\frac{R_S + R_L}{R_S}$ and $R_{Th} = \frac{R_S R_L}{R_S + R_L}$), we obtain:

$$\frac{dI_{TES}}{dP_{in}} = -\frac{1}{G}\frac{R_0}{T}\alpha\left(\frac{I_0}{R_{Th} + R_{TES}}\right) = -\frac{\mathscr{L}}{V_{TES}}\frac{R_{TES}}{R_{Th} + R_{TES}}, \tag{2.10}$$

where $\mathscr{L}$ is the D.C. loop gain:

$$\mathscr{L} = \frac{\alpha P_J}{GT}. \tag{2.11}$$

On the other hand, focusing on the thermal model, is possible to rewrite the Joule power dissipated inside the TES. The resistance can be expanded as:

$$R_{TES}(T, I_{TES}) \approx R_0 + \frac{\partial R_{TES}}{\partial T}\delta T + \frac{\partial R_{TES}}{\partial I}\delta I \tag{2.12}$$

and from Equations 2.8 we obtain

$$dR_{TES} = \alpha_I \frac{R_0}{T_0} dT + \beta_I \frac{R_0}{I_0}\, dI_{TES}. \tag{2.13}$$

At the same time from bias circuit we know that:

$$dI_{TES} = -\frac{I_{TES}}{R_{TES} + R_{Th}}\, dR_{TES}, \tag{2.14}$$

then, it is possible to write

$$dR_{TES} = \alpha_I \frac{R_{TES}}{T} \frac{R_{Th} + R_{TES}}{R_{Th} + R_{TES}(1+\beta_I)}\, dT \tag{2.15}$$

from which we find a relation for α and α_I, β_I and the circuit resistances

$$\alpha = \alpha_I \frac{R_{Th} + R_{TES}}{R_{Th} + R_{TES}(1+\beta_I)}, \tag{2.16}$$

and

$$\begin{aligned} dI_{TES} &= -\alpha_I \frac{R_{TES}}{T} \frac{I_{TES}}{R_{Th} + R_{TES}(1+\beta_I)}\, dT = \\ &= -\alpha \frac{R_{TES}}{T} \frac{I_{TES}}{R_{Th} + R_{TES}}\, dT. \end{aligned} \tag{2.17}$$

Thus, expanding linearly the Joule power:

$$\begin{aligned} dP_J &= I_0^2 dR_{TES} + 2 I_0 R_0 dI_{TES} = \\ &= \alpha \frac{P_J}{T} dT - 2\alpha \frac{P_J}{T} \frac{R_{TES}}{R_{Th} + R_{TES}} dT = \\ &= -\alpha \frac{P_J}{T} \left(\frac{R_{TES} - R_{Th}}{R_{Th} + R_{TES}} \right) dT \end{aligned} \tag{2.18}$$

is possible to define the Joule power thermal conductance:

$$G_{ETF} \equiv -\frac{dP_J}{dT} = \mathscr{L} G \left(\frac{R_{TES} - R_{Th}}{R_{Th} + R_{TES}} \right). \tag{2.19}$$

This term is really important as it define how the Joule power acts on the TES from a thermal point of view. This effect is called Electro-Thermal Feedback (ETF) [36] because a change in temperature will lead to a change in P_J, thus in a different thermal load on the TES acting as a positive or negative feedback, depending on the bias conditions and on the α value. For TES negative electro-thermal feedback is generally used because of the high positive value of α, then using a constant voltage bias, with $R_L \gg R_{TES} \gg R_S$, $L \to 0$, and a current amplifier to make the read-out, e.g. a SQUID, as in our case. This allows the TES to self-regulate and remain stable inside the linear regime due to the increase of the total thermal conductance of the TES.

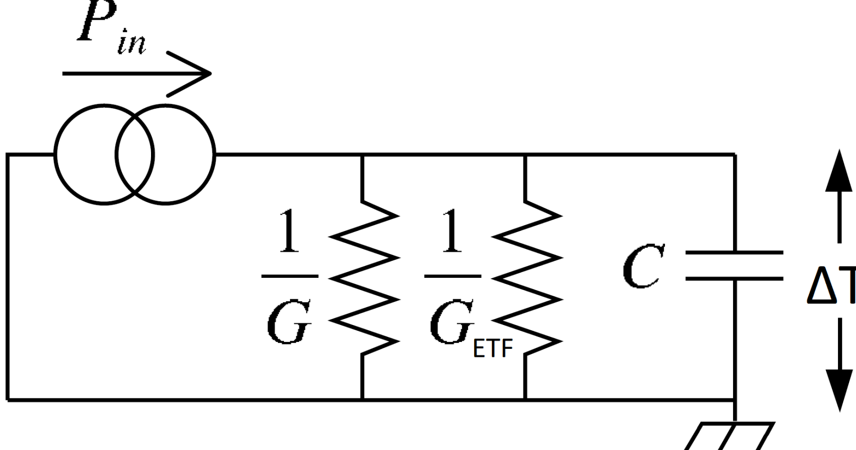

Figure 2.7: Equivalent thermal circuit of the TES electro-thermal model.

The thermal differential equation of the system, Equation 2.4, can now be represented through a simple circuit as in Figure 2.7 and solved as the net current onto the TES-absorber capacity C is: $P_{in} - (G + G_{ETF})T$:

$$\frac{dT}{dt} = \frac{P_{in} - G_{eq}T}{C}. \tag{2.20}$$

In case of impulsive Power input, like in single photon detection, we could model P_{in} as a delta function $E_\gamma \delta(t)$, and ignoring the inductance L, we obtain the pulse of Figure 2.5:

$$T(t) = \frac{E_\gamma}{C}\, e^{-\frac{t}{\tau_{eq}}}. \tag{2.21}$$

The system relaxes towards T_0 thanks to power dissipation to the thermal bath through G and the load of the Joule power, with a constant thermal time:

$$\tau_{eq} = \frac{C}{G + G_{ETF}}. \tag{2.22}$$

Taking into account the inductance we would have found also a pulse rise time $\tau_R = L/(R_{Th} + R_{TES}(1+\beta_I))$. Now, it is possible to find the relationship between $G_{eq} = G + G_{ETF}$ and G in order to find a correcting factor by exploiting the Equation 2.19:

$$F \equiv \frac{G_{eq}}{G} = 1 + \mathscr{L}\left(\frac{R_{TES} - R_{Th}}{R_{Th} + R_{TES}}\right), \tag{2.23}$$

to re-scale the quantities that do not take into account the electro-thermal feedback effect. In the end, we can study the TES response in frequency domain to obtain a general A.C. response. The thermal conductance in the frequency domain is:

$$\frac{dP_{in}(\omega)}{dT(\omega)} = GF(1 + i\omega\frac{\tau}{F}), \tag{2.24}$$

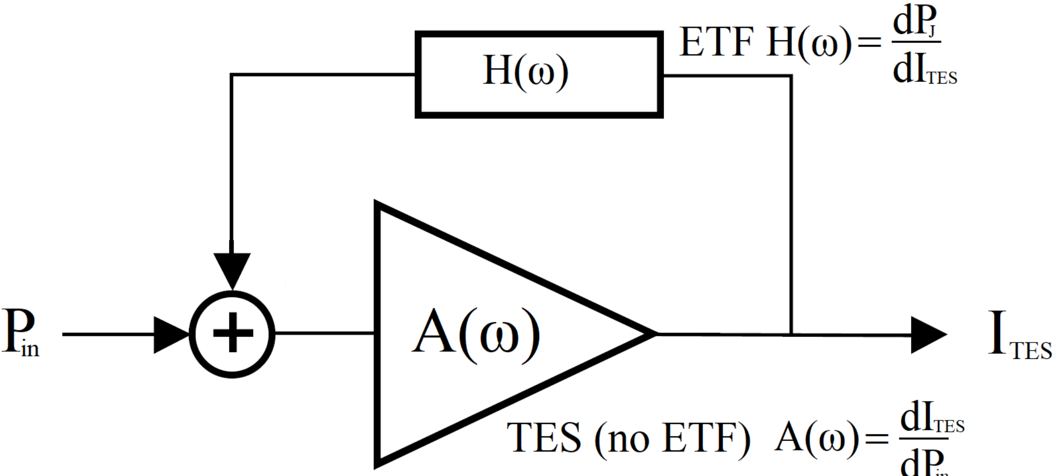

Figure 2.8: Equivalent circuit of the current response to the incident power on the TES to highlight the electro-thermal feedback effect.

thus from Equation 2.9 we obtain:

$$\frac{dI_{TES}(\omega)}{dP_{in}(\omega)} \equiv S_I(\omega) = -\frac{\mathscr{L}}{FV_{TES}}\frac{1}{1+i\omega\frac{\tau}{F}}\left(\frac{R_{TES}}{R_{Th}+R_{TES}}\right), \tag{2.25}$$

that is the TES responsivity. To better understand the role of ETF it is possible to derive $S_I(\omega)$ not from the circuit of Figure 2.7, but by considering the Joule power from the electrical point of view, showing the feedback nature of the effect. The system can then be modeled as in Figure 2.8. From this scheme we know that the TES current output is:

$$I_{TES} = P_{in}A(\omega) + P_{in}A(\omega)H(\omega) \tag{2.26}$$

Thus, the TES responsivity is:

$$S_I(\omega) = \frac{dI_{TES}}{dP_{in}} = \frac{A(\omega)}{1 - A(\omega)H(\omega)} \tag{2.27}$$

where $A(\omega)$ comes from Equation 2.25 with $G_{ETF} = 0$, thus $F = 1$. On the other hand, from Equation 2.27 it is possible to study the stability of the system, the root of $1 - A(\omega)H(\omega)$, considering $L \to 0$, is:

$$i\omega = \tau(1 + \mathscr{L}), \tag{2.28}$$

where $H(\omega) = \frac{dP_J}{dI} = I\frac{dV}{dI} + V = V(\frac{R_{TES}-R_H}{R_{TES}})$. Therefore, the electro-thermal feedback contribution for TES ($\alpha > 0$) can be:

- Negative in case of Voltage bias $H(\omega) = \frac{dP_J}{dI_{TES}} < 0$,
- Positive in case of Current bias $H(\omega) = \frac{dP_J}{dI_{TES}} > 0$.

Then the system is stable for $G_{ETF} > -G$, this is always satisfied in case of negative ETF where $G_{ETF} > 0$, but in case of positive ETF, $G_{ETF} < 0$ thus it is module must be lower than G. From Equation 2.19 its clear that positive feedback for high gain thermometers, like TES, would led to instability.

2.2.2 Energy resolution

In this section I will introduce the main noise sources in a TES microcalorimeter. The responsivity has been calculated as if it were independent of noise, but ETF has also implications on the Noise Equivalent Power (NEP), thus on the energy resolution. This is the result of the linear expansion of the equations, details of which can be found in [38]. Now, following the formalism of the same paper, the major noise sources are calculated considering them uncorrelated, thus finding the total NEP by simply adding their squares.

Thermodynamic fluctuation noise

The fluctuation of the thermal power flowing towards the thermal bath due to the random exchange of phonon between the absorber and the bath through G, writing the thermal link properties, $T > T_{bath}$, and non linearity of TES as Φ, is:

$$p^2_{TFN} = 4k_B T_{bath} G\Phi. \tag{2.29}$$

Then, the phonon noise observed at the output has current spectral density $(A/\sqrt{Hz})$:

$$e_n(\omega) = p^2_{TFN} \cdot S_I(\omega) = -\frac{\mathscr{L}}{FV_{TES}} \frac{4k_B T_{bath} G\Phi}{1 + i\omega\frac{\tau}{F}} \left(\frac{R_{TES}}{R_{Th} + R_{TES}} \right). \tag{2.30}$$

TES Johnson noise

The Johnson noise is due to the random transport of charge over a resistor. It manifests as a voltage fluctuation per square root Hz across the TES:

$$v_{Jh} = \sqrt{4k_B T R_{TES}} \tag{2.31}$$

Then the related NEP is:

$$p_{Jh} = \frac{\sqrt{4k_B T R_{TES}}}{V_{TES}(R_{TES} + R_{Th})} \mathscr{L}(1 + i\omega\tau) \tag{2.32}$$

and the related current spectral density is:

$$i_{Jh} = -\frac{\sqrt{4k_B T R_{TES}}}{F(R_{TES} + R_{Th})} \frac{1 + i\omega\tau}{1 + i\omega\frac{\tau}{F}} \left(\frac{R_{TES}}{R_{TES} + R_{Th}} \right) \tag{2.33}$$

Shunt Johnson noise

Johnson noise also manifests itself as a voltage fluctuation across the shunt resistor. So far we have always considered R_{Th}, but the circuit of Figure 2.6 has usually R_L at room temperature and R_S inside the cryostat at T_{bath}, using $R_L \gg R_S$, to evaluate the noise from the circuit we could neglect the

contribution from outside the cryostat as: $\frac{R_S}{R_L+R_S} \ll 1$ and consider only the Johnson noise from R_S. Then, $v_s = \sqrt{4k_B T_{bath} R_S}$, its NEP is:

$$p_{Jh_S} = \frac{\sqrt{4K_B T_{bath} R_S}}{V_{TES}} \frac{R_{TES}}{F R_S} \mathscr{L}(1 + \mathscr{L} + i\omega\tau) \tag{2.34}$$

and the output current spectral density is:

$$i_{Jh_S} = -\sqrt{4K_B T_{bath} R_S} \frac{R_{TES}}{R_S} \frac{1 + \mathscr{L} + i\omega\tau}{1 + i\omega\frac{\tau}{F}} \frac{R_{TES}}{R_{TES} + R_{Th}} \tag{2.35}$$

The theoretical energy resolution of a TES microcalorimeter can be then evaluated from NEPs and written:

$$\Delta E(FWHM) = \frac{2.36}{\sqrt{\int_0^\infty \frac{4df}{\Sigma\ NEP^2}}} \approx 2.36\sqrt{k_B T_{bath}^2 C \cdot \xi(t, \alpha_I, \beta_I, \gamma)}, \tag{2.36}$$

in case of strong electro-thermal feedback, where the function ξ for high $\mathscr{L}$ such as TES is proportional to $\frac{1}{\alpha_I}$. Therefore, in a real calorimeter, the energy resolution is dependent also on TES sensitivity and heat capacity scaling factor γ of the material.

2.3 The phonon mediated TES detector

Signal generation in real TES based detector is much more complex than the simple electro-thermal model just described. This is due to the decoupling of the TES and the absorber, the decoupling of electrons and phonons of the TES itself [40], and the specific detector configuration; a first model for the CryoAC have been proposed in [41].

The CryoAC detector has TESs grown on silicon, which is substrate and absorber. To understand the actual properties of the detector we started to study the excitation process that occur in silicon due to interactions with high energy particles or photons.

2.3.1 Signal generation

The high energy (GeV) primary cosmic protons and secondary particles passing through the satellite, and focused 10–20 keV X-rays are the main sources of signals for the anticoincidence. Energetic protons and electrons produce slightly different energy absorption dynamics, both due to the different tracks inside the detector and the number and types of primary excitation in silicon. Unfortunately, the signature of the two types of events is not so clear, due to the mixing of the components, except for the overall energy released: few hundreds of keV for protons against 10–20 keV for photo-electrons. The difference in deposited energy is a valid starting point, but it should be accompanied by

further signatures from intrinsic features related to signal generation in order to enhance the spectral capabilities.

Such energy deposition inside silicon gives rise to non-thermal phonons as a product of the energy relaxation of excited carriers, electrons, and holes. This process can be divided into two parts:

1. the distribution in space, time, and frequency of acoustic phonons radiating from the excitation volume, i.e., the phonons source,
2. the subsequent propagation and decay to lower energy phonons in the bulk of the silicon absorber.

In general, since isotopic or bulk defect scattering is highly dependent on frequency, the instantaneous diffusion constant increases with time as the phonons decay into lower energy ones. This process is called quasi-diffusion. Therefore, high-frequency sources lead to "quasi-diffusive" heat transport, while low-frequency sources emit phonons that propagate ballistically [42]. At low temperature, intrinsic silicon contains a low density of free carriers with a balanced density of electrons and holes. Ionization is the main process for generating a high local density of energetic electrons and holes along the particle track. Direct interactions of protons with Si nuclei, which generate energetic phonons and secondarily ionization by the recoiled nuclei, are only few events per track. This energy transfer channel is negligible. Finally, at first glance, primary event simulations suggest that the phonons source is dominated by electron-hole pairs that lose most of their kinetic energy in the sub-picosecond time scale by emitting non-thermal optical and acoustic phonons. The mechanism of phonons emission should be completed with the final electron-hole recombination.

Analytical calculations of the average parameters are very useful for consistency checks of the numerical solutions. Therefore, we will briefly mention the basics of the gas phonon model, which can be studied in more detail with the Boltzmann equations. As already mentioned, the generation of phonons is due to electronic relaxations via the longitudinal optical (LO) phonons. After losing their excess of kinetic energy in this channel, the carriers eventually recombine mainly in a non-radiative way, generating more phonons. The LO phonons decay into acoustic phonons in ps time scale. In turn, the acoustic phonons spilt into lower energy ones by "anharmonic" decays with a rate that has a very strong frequency dependence:

$$\tau_a^{-1} = C_a \nu^5. \tag{2.37}$$

This means that each successive generation of phonons has about half the frequency and about 2-5 times the lifetime of its predecessors. This strong dependence on frequency gives us the time evolution of the down-conversion process. We have considered longitudinal phonon with velocity equal to 9 km/s and $Ca = 1.2 \times 10^{-55} s^{-1}$.

In conjunction with anharmonic decay, there is elastic scattering, which affects the spatial evolution of thermal energy after the primary proton event. The elastic decay rate also has a sharp frequency dependence:

$$\tau_e^{-1} = C_e \nu^4. \tag{2.38}$$

Once a phonon is generated, at each successive generation the mean free path $\Lambda = \nu\tau_e$ increases considerably. As the phonon bifurcates in two phonons of half the energy, the elastic scattering time increases by a factor 2^4. The distance that phonons will cover with elastic scattering within the anharmonic lifetime is a measure of the scattering length associated with one generation of phonon of fixed frequency.

The approximate analytic approach is based on a model of phonon gas expansion. Here, we present the simplest arguments. In the standard kinetic theory of gas, the diffusion volume has a radius:

$$R = \sqrt{Dt}, \tag{2.39}$$

where

$$D = \frac{\nu^2\tau}{3}. \tag{2.40}$$

In the decaying phonon gas, the average frequency at time t is:

$$\nu = (C_a t)^{-\frac{1}{5}}, \tag{2.41}$$

so that the average elastic scattering time is

$$\tau_e = \frac{\nu^{-4}}{C_e} = \frac{(C_a t)^{\frac{4}{5}}}{C_e}. \tag{2.42}$$

The radius of the expanding phonon cloud is at first approximation given by:

$$R = \sqrt{\frac{\nu^2\tau_e}{3}t} = \sqrt{\frac{\nu^2 C_a^{\frac{4}{5}}}{3C_e}t^{\frac{9}{10}}} \tag{2.43}$$

which is approximately linear with time. The phonon gas quasi-diffusion is faster than in the standard kinetic theory of gas. By following the evolution of the radius and the temperature of this expanding phonon gas, we can predict the average energy and distribution of phonon hitting the crystal surface and the TES sensors.

2.3.2 Signal model of the CryoAC

The research group in which I did my thesis work developed a simulator of phonon dynamics in Cryo-AC-like detectors. The design of the simulator was led by Prof. C. Boragno and was adapted to the characteristics of our detector. The simulator was qualified with simulations of published phonon transport experiments in silicon. In this way we verified that the simulator calculates

with sufficient accuracy, from a few percent to better than 10 percent, phonon polarization, times of flight, decay times, over-all reflectivity of surfaces, etc.

The goal is to understand the mechanisms of a-thermal signal generation observed in TESs with an "ab initio" simulation of the dynamics of phonon transport of the primary energy of the charged particle released with local ionization along the track [43]. The basis of this work is strongly inspired by the simulation tools and methods developed by the cryogenic Dark Matter experiment groups [44]. The model is described below. Here I anticipate some results to support a semi-quantitative description of the phenomena that are important for the design of CryoAC. Suppose a particle passes through a silicon section releasing a known amount of kinetic energy. The modeling of these primary interactions is well known and it is easy to estimate the released energy density, the effective volume where energy deposition is significant, the nature of the primary excitations and the de-excitations with phonon emissions. Starting from these data, the simulator sets up a primary phonon spectrum in a defined volume around the trace. A typical output for a silicon absorber of large area and small thickness is summarily given in Figure 2.9. It can be stated that, lattice excitation begins with the production of high-energy phonons that quickly become quasi-diffusive with an equivalent temperature of 60 K after 1 μs, but at 3 μs they start having diffusive behavior with an equivalent temperature of about 20 K. The temperature is obtained by fitting the phonon frequency distribution with a Planckian distribution. Thus, with time, the substrate thermalize to equilibrium, and the TES will thermalize with substrate after a transient dependant by the distance from the phonon generation point. Since the first phonons that strike the electrons of the TES are very energetic, with an equivalent temperature of several tens of Kelvin, a fraction of them are raised to highly excited states compared to thermal states. The relaxation of these "hot electrons" with other electrons is typically much faster than the thermal relaxation time between electrons and phonons. This results in an effect more similar to direct electron excitation than heating by thermal phonons across the conductance between silicon and TES. The simulator calculates the a-thermal phonon flux hitting the TES as a function of time indicating high instantaneous powers even for short times in the first instants of the event. Thus, because of the hot electrons produced in the first moments, the signal has a much higher and faster initial spike than that one generated by a thermal heat flux. If the TES is close enough to be reached in the first μs by a-thermal phonons, pulse shapes very similar to those measured and shown in Figure 2.10a are calculated. If the event is far away, the TES will be hit by much smaller a-thermal power and will generate a signal with fast rise-time with small a-thermal spike as in those shown 2.10b. It is also known that the a-thermal spike is highly variable in amplitude, as can be observed in Figure 2.11 where a few pulses from gamma source of ^{241}Am, illuminating the whole detector, are superimposed. As we will see in the next section, this is explained by the strong dependence of the a-thermal phonon flux on the position of the primary event in the absorber, i.e. lateral distance and depth.

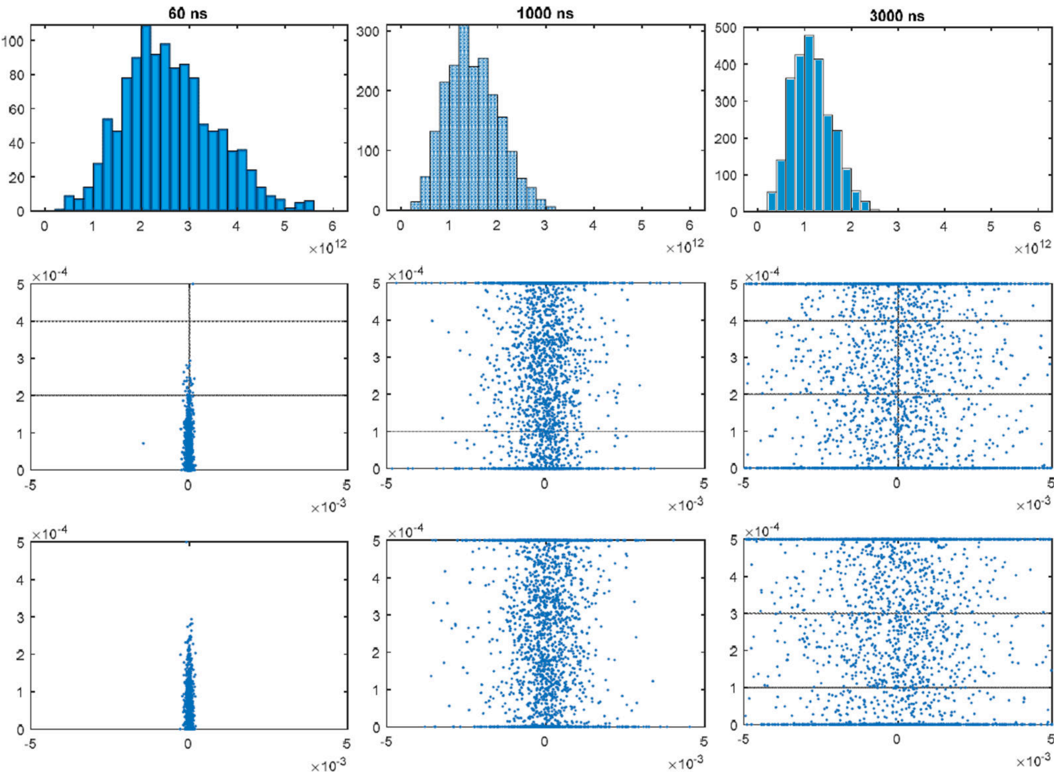

Figure 2.9: Top): phonon frequency distribution after 0.06, 1.00 and 3.00 μs. Center): High energetic phonon distribution inside Si in a X-Z section of the absorber. Bottom): High energetic phonon distribution inside Si in a Y-Z section of the absorber.

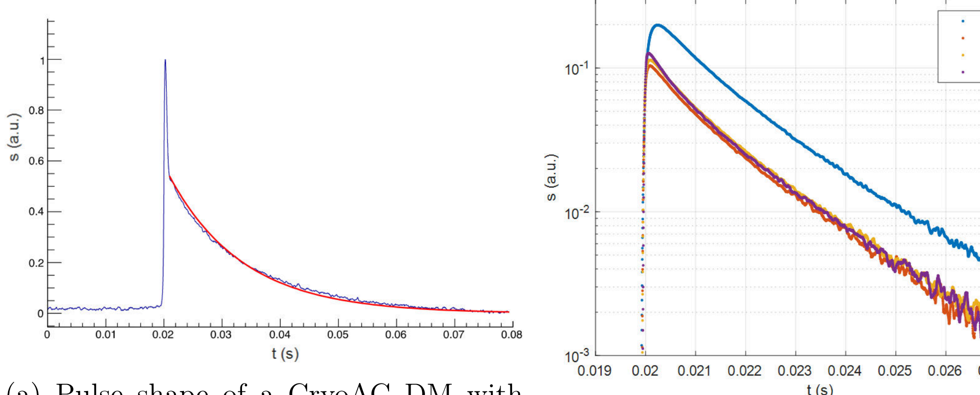

(a) Pulse shape of a CryoAC DM with signal generation point at $< 1\ mm$ from TES.

(b) Pulse shape of a prototype with signal generation point at $\sim 5\ mm$ from TES.

Figure 2.10: a): Pulse shape of a CryoAC demonstration model in which the a-thermal component, the fast spike, is clearly visible on top of the exponential decaying thermal pulse. The red curve fits the decay with single exponential function related to the conductance toward thermal sink. (Axis unit are arbitrary). (b): Pulse shape of a CryoAC prototype where the signal generation point is far from the TES ($\sim 5\ mm$). The rise-time is faster than a pure thermal equilibrium one, the a-thermal spike is present, but greatly attenuated.

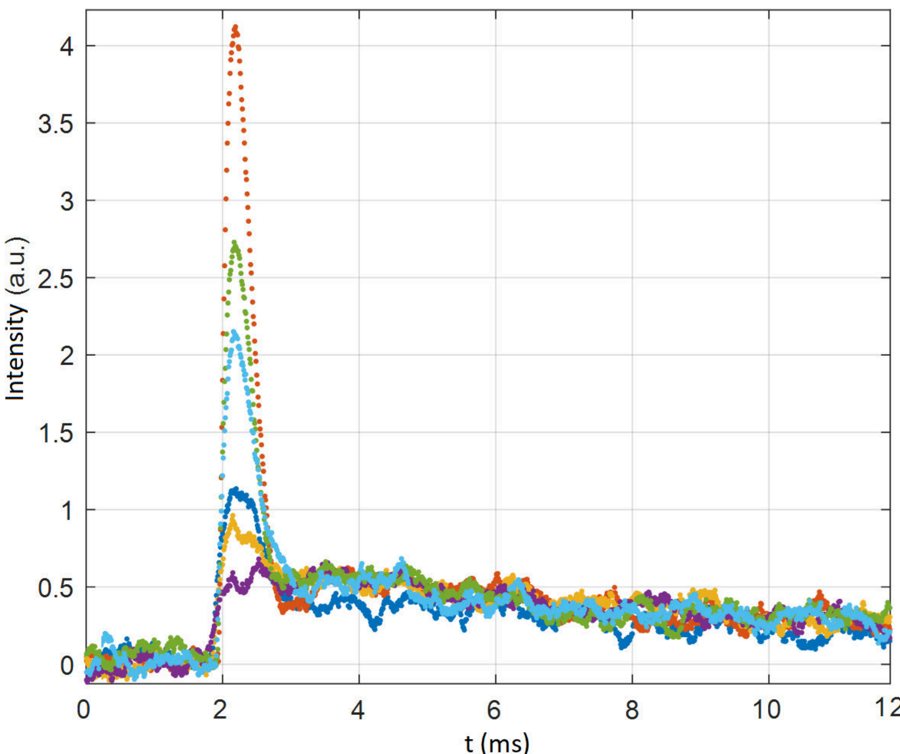

Figure 2.11: First 12 ms of the signal of different events at 60 keV in a CryoAC DM. The peak is due to the a-thermal component, which is strongly dependent on the position of the primary event in the absorber.

Then, to describe the TES response, the detector was modeled with the scheme shown in Figure 2.12. The conversion of the kinetic energy of the particle takes place inside the Si absorber, then is transferred to the TES Ir/Au lattice through a thermal conductance G_K, that represents the thermal decoupling between the TES and its substrate. Inside the TES, electrons and phonon are also decoupled and then a electron-phonon thermal conductance G_{e-p} is added. The electrons, in turn, can enter an excited state due to the high energy flux of a-thermal phonons; thus electrons are modelled in two state e and e^* (hot electrons) with a constant decay time τ_{ee} from the excited to thermal state. Finally, electron relaxation of the excited state within the TES and then thermal conductance G to the thermal sink restore equilibrium.

It is considered that the temporary excited state of the electrons justifies a rapid increase in the temperature of the TES electrons due to an injection of energy inside the absorber. To quantify the dynamics we choose to approximate the electron system in TES as consisting of 2 subsystems and the associated energy balance equations. This description appears to us to be sufficiently close to the observations, although several measurements need to be made to measure the parameters.

The energy balance equations, using an approach similar to that of [45], considering the energy of the a-thermal phonons $E_{ath}(t)$, the solid angle described by the TES area with respect to the phonon generation point $\Delta\Omega$, and the phonon excitation probability of the TES metal lattice, P_K, defined by the Kapitza resistance. Therefore, it is possible to write:

$$\begin{cases} E_{ath}(t)\Delta\Omega P_K = \langle\varepsilon_l\rangle N_l(t) \\ \\ \langle\varepsilon_l\rangle N_l(t) = \langle\varepsilon_{e^*}\rangle N_{e^*}(t) \\ \\ \dfrac{dN_{e^*}(t)}{dt} = \dfrac{N_l(t)}{\tau_{l-e}} - \dfrac{N_{e^*}(t)}{\tau_{e-e}} \end{cases} \tag{2.44}$$

where $\langle\varepsilon_x\rangle$ is the average energy and $N_x(t)$ the number of carrier in the state x, and τ_{x-y} the constant decay time between the state x and the state y; the energy is transferred from the Si absorber to the TES electrons. The typical a-thermal phonon has an energy $\langle\varepsilon_{ath}\rangle = \frac{E_{ath}}{N_{ph(Si)}}$, which decreases with a power law: as described in the next section due to intrinsic processes. Consequently, the number of $N_{ph(Si)}$ phonons will also increase. Therefore, assuming conservation of energy the conditions of Equations 2.44 are obtained from the continuity equation.

The first of Equations 2.44 states that a fraction of the a-thermal phonons in silicon impacting the TES interface generate N_l phonons of average energy $\langle\varepsilon_l\rangle$ in the TES.

The second equation states that, due to the high-energy phonon-electron cross section, the energy of the N_l TES phonons put N_{e^*} electrons in the excited state with average energy $\langle\varepsilon_{e^*}\rangle$.

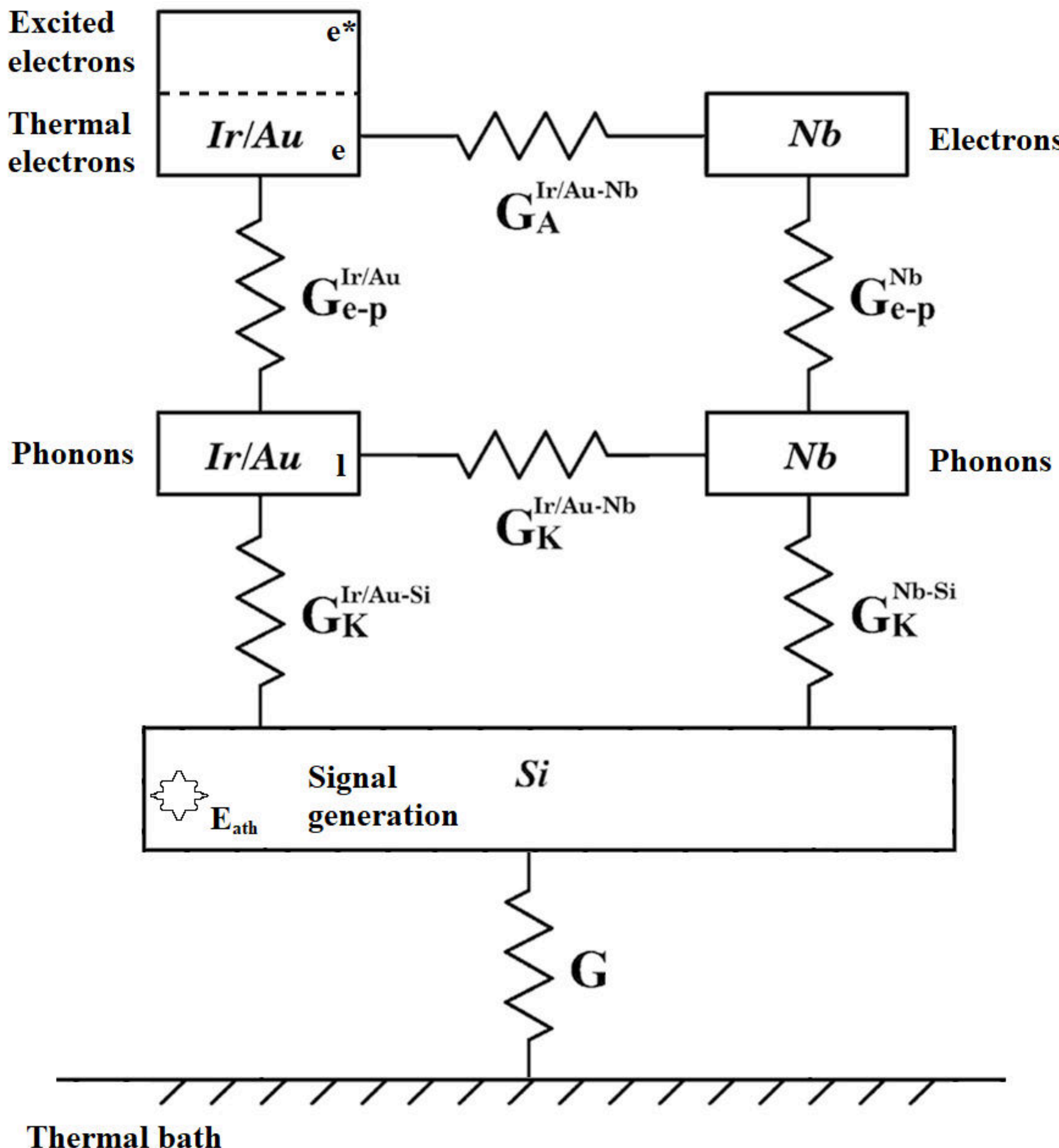

Figure 2.12: The Ir/Au TES Signal is generated inside the Si absorber, then is transferred to the TES Ir/Au lattice through a thermal conductance G_K representing the thermal decoupling between the TES and its substrate. Inside the TES electrons and phonons are decoupled too and then a electron-phonon thermal conductance G_{e-p} is added. In turn, electrons can reach an excited state due to high energy flux of a-thermal phonons, thus electrons are modelled in two state e and e^* with a constant decay time τ_{ee} from the excited to normal state.

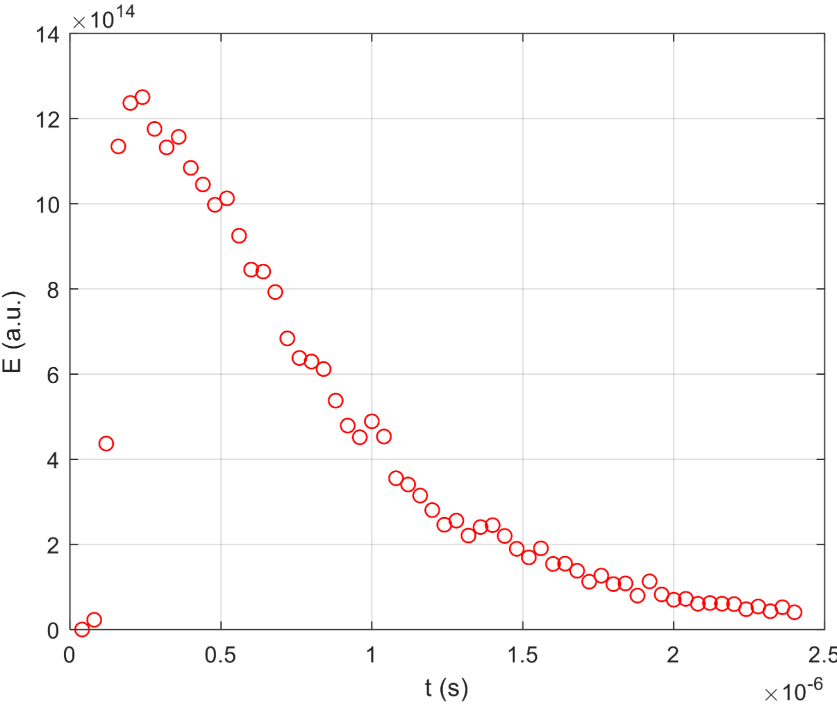

Figure 2.13: Simulation of the energy flux hitting the TESs as a function of time.

The third equation states that the hot electrons present at any instant are given by the equilibrium between those produced and those that relax to thermal states. It is also not independent of the first two, since the term with the time constant τ_{e-l} describes the generic probability of generating an excited electron by absorption of a thermal phonon.

The first two equations broadly outline the mechanism that could be used to estimate τ_{e-l}. But this would require averaging from the phonon and space spectra and the available phases of the electronic states, etc. Therefore, I will limit myself to equations involving average quantities, i.e. energies and particle numbers, and implicit quantities, i.e. densities of electron and phonon states in the film, and interaction cross sections, and so on. This is beyond the scope of this thesis, so I limit myself to this semi-quantitative description.

The energy flux hitting the TESs can be determined on a case-by-case basis by simulation, as seen in Figure 2.13, where the intensity of the energy hitting the TES in the time unit has a characteristic pattern and is significant in the first microseconds.

From the thermal point of view then, when the electrons relax it is possible

to write the thermal balance on each subsystem as:

$$\begin{cases} C_e \dfrac{dT_e(t)}{dt} = \dfrac{N_{e^*}(t)}{\tau_{e-e}} - G_{e-ph}(T_e - T_l) + P_J(T_e) \\ \\ C_l \dfrac{dT_l(t)}{dt} = G_{e-ph}(T_e - T_l) - G_K(T_l - T_{Si}) \\ \\ C_{Si} \dfrac{dT_{Si}(t)}{dt} = G_K(T_l - T_{Si}) + \dfrac{E_{ath}(t)}{\tau_K} + G(T_{Si} - T_{bath}) \end{cases} \tag{2.45}$$

where T_x and C_x are the temperature and the thermal capacitance of each x subsystem, and P_J is the power dissipated through Joule effect by the TES. Those are just an extension of the model described in Section 2.2, where the electrical part is unchanged. Solutions can be derived at the same manner by finding that the response is the sum of three pulses. It can be seen that the a-thermal spike is terminated by the first term on the right hand of first equation which is solution of Equations 2.44. Since this evolves very fast compared to the other terms, it can be concluded for simplicity that the final solution has two main terms: a fast a-thermal transient and a slower thermal decay.

In the end, looking at Figure 2.12 can be seen that the whole part on the right have not been considered because are negligible. Nb wire contacts on Ir TES are superconducting too and hot electrons and quasiparticle are blocked by Andreev's reflection [46], while phonons are contained by Kapitza resistance at the interfaces.

2.3.3 The a-thermal phonon hot-spot

Numerical simulations of the phonon transport in large volume cryogenic detectors with a radioactive event as source, have been developed for dark matter direct detection [44]. Weakly interacting massive particle (WIMP) and light dark matter (LDM) are possible constituents of the Dark Matter filling our Galactic Halo, the most advanced method for detecting these particles is based on the detection of nuclear single recoil inside a large mass absorber at very low temperatures (10-50 mK) through the phonon and ionization emission from the interaction point [47] and [48]. The detectable recoil energy from particle in 10-100 GeV/c^2 ranges from hundred eV to tens of keV of nuclear recoil [49]. This is a quite different event respect to GeV protons passing through the silicon absorber and releasing hundreds of keV, but, the basic building blocks of the numerical simulation are the same.

In our case, since the Si substrate of CryoAC detector has a thickness of 500 μm and the positron track length is equal or greater, we can neglect the anisotropy and then any phonon focusing effect. There are several reasons that support this conjecture. If, by some remote chance we suppose a large pure ballistic transport, it can be calculated that a point–like source located at

bottom side of the Si wafer produces on the top side a spot of ballistic phonons with a diameter of about 40 μm, much less than the typical TES size, 100 μm, and pitch size, 1 mm. Therefore, the probability to detect this ballistic signal is negligible. This conjecture is also in contradiction with the mean free path of tens of μm calculated from the elastic and anharmonic process rates at THz. Further, our source is the convolution of point-like source over the straight track, causing the mixing of many ballistic pulses in different directions, so that, the anisotropies are washed out. The negligible contribution of ballistic and anisotropic transport in our numerical simulation can be demonstrated exactly with the full cascade calculation of phonon emission from the primary events, that we omit here.

Within the hypothesis that the effective evolution of the heat pulse is isotropic we need to fix the initial conditions: the spectral distribution of phonons. The initial phonon population can follow a Planckian distribution with a source temperature T_S much higher than the bulk temperature T_B: let's say $T_S \approx 100$ K. However, for the sake of our simulation it is easier to fix as initial condition a monochromatic phonons density having a frequency equal to the Debye frequency $\nu_D = 15$ THz. In fact, the decay rate for high frequency phonons is so high that the majority of them downgrade well before they hit the surface. A similar approach is used also in [49].

We have tested that the monochromatic initial condition does not have significant systematic effect on the heat pulse time evolution at the time scale of our experimental signals, i.e. tens to hundreds of μs. In the following Figure 2.14 the frequency spectra after 1, 30, 1000, and 4000 ns since phonon generation. As the number of generated phonons increase the concentration in high frequency phonons disappear and the distribution represents better the Planckian at a given temperature. It can be seen that at 1 μs time scale the spectral distribution becomes similar to a Planckian at 60 K and the diffusion radius is in 100 μm spatial scale. The two possible initial condition of monochromatic phonon in a point-like source at the Debye frequency or a Planckian distribution at 60 K in a 100 μm spherical radius, are roughly equivalent in respect to the subsequent evolution of the simulation.

In Figure 2.15a we report the mean free path Λ of phonon in the frequency range 100 GHz – 10 THz for the anharmonic (in blue) and isotope (in red) processes, respectively. It is evident that for $\nu < 1$ THz, the mean free path is much larger than the thickness of the Si substrate and that the anharmonic decay is relevant only for high energy phonon. In order to generate a phonon's burst, the self-developed numerical model proceed as follows:

- a phonon with Debye frequency ν_D is generated in a given point of the Si;
- the phonon trajectory is recorded for a number K of scattering events;
- the phonon frequency, direction and polarization are calculated for every scattering event;

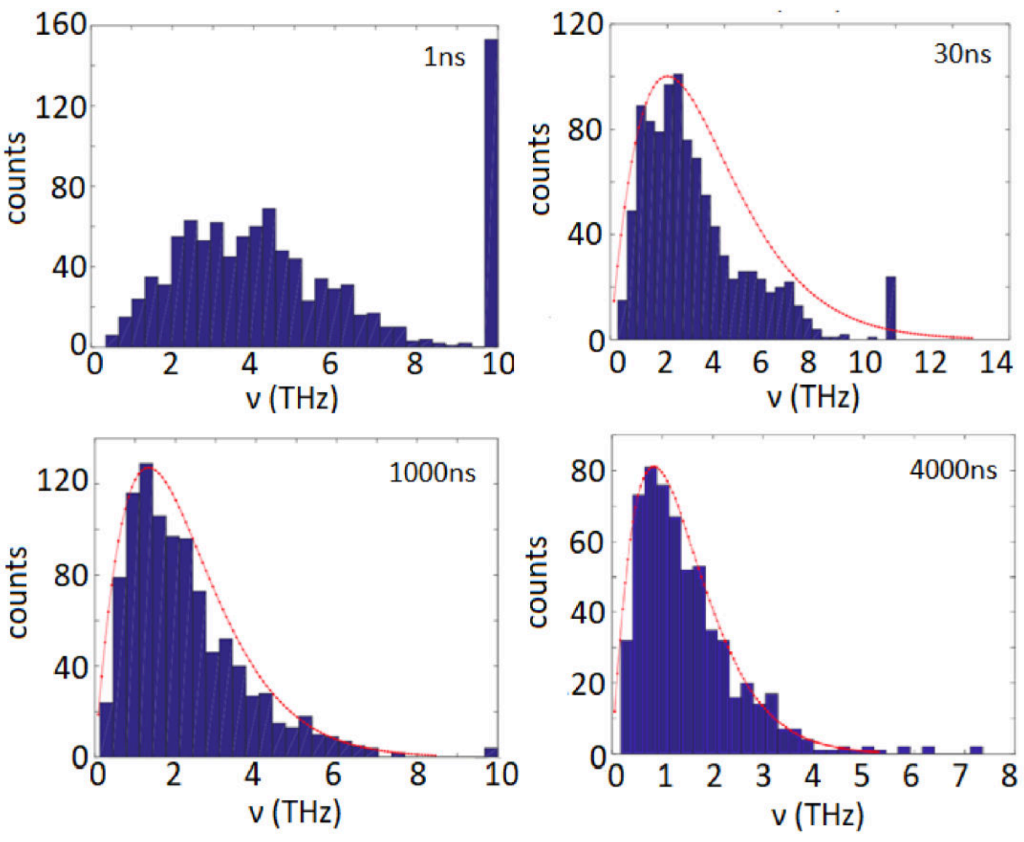

Figure 2.14: Frequency spectrum after 1, 30, 1000, and 4000 ns since phonon generation, from the initial condition of monochromatic distribution at the Debye frequency to the final one. From [43].

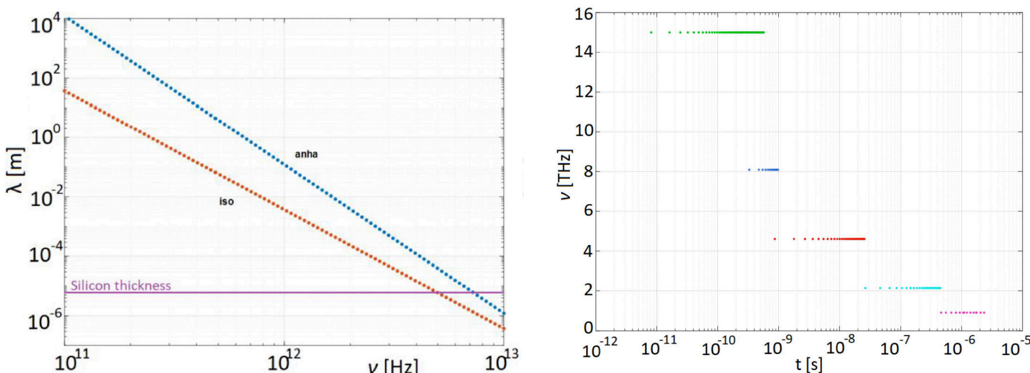

(a) Phonon mean free path vs frequency for anharmonic isotopic scattering.

(b) Frequency vs time evolution of one simulated phonon.

Figure 2.15: (a) The mean free path of phonon vs frequency for anharmonic decay (blue line -“anha”) and isotopic or elastic scattering (red line -“iso”). (b) Frequency vs time evolution of simulated phonon travel. Each dot corresponds to an elastic scattering. At each anharmonic decay, the “average” frequency halves. From [43].

- the phonon are specularly reflected from the substrate surfaces;
- the procedure is repeated for N phonon.

In Figure 2.15b is reported the time history of a simulated phonon journey: the initial Debye phonon survives for 3×10^{-10} s, then it decays to a phonon at 7 THz, after 100 μs, the phonon frequency is 300 GHz, with a huge mean free path of the order of 1 m. The typical phonon trajectory is depicted in Figure 2.16: a Debye frequency phonon is generated at the coordinates (0, 0, 50 μm). After 34 isotope scattering events (blue tracks), the phonon downgrades due to an anharmonic process. The two new phonons have now lower frequency and lower elastic scattering rate, leading to longer mean free paths (tracks in red – only one phonon is reported). The mean free path increases approximately from about 0.1 μm to 1 μm. All the path is restricted in few tens of cubic μm. After 2 more anharmonic decays (cyan and magenta tracks of Figure 2.17), the mean free path is larger than the Si thickness and the phonon starts to be reflected from the Si surfaces.

Qualification of the numerical model

To fix the level of confidence of model’s outputs, a qualification process is needed. This includes self-consistency tests and qualitative and quantitative checks of simulation results of published experiments. These qualification tests aim to evaluate the quality of the simulation, by checking the physical parameters, the evolution of the system under study, the time scale calibration, and the amplitude (energy) scale calibration.

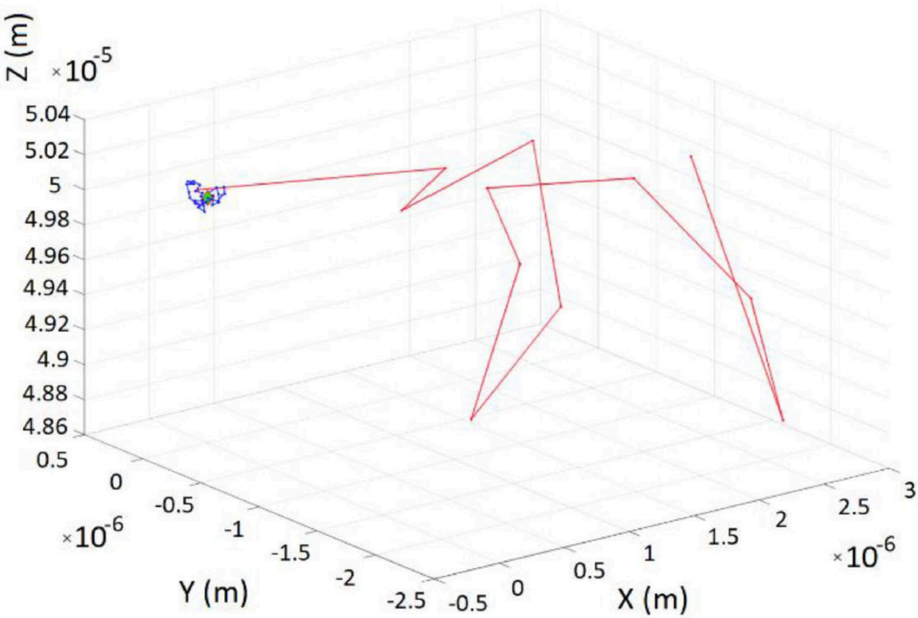

Figure 2.16: Trajectory of a phonon due to elastic scattering from isotopes. At each anharmonic decay the tack changes color: from green, to blue and red. From [43].

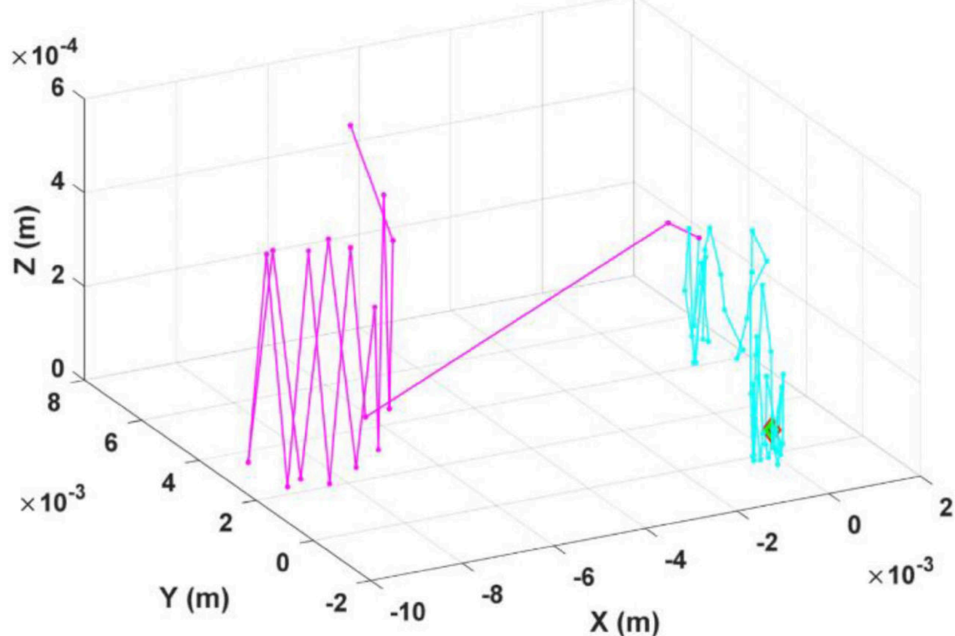

Figure 2.17: Continuation of the previous phonon trajectory after two more anharmonic decays: magenta tracks and cyan tracks. The previous track of Figure 2.16 can be seen near the origin of the axes. From [43].

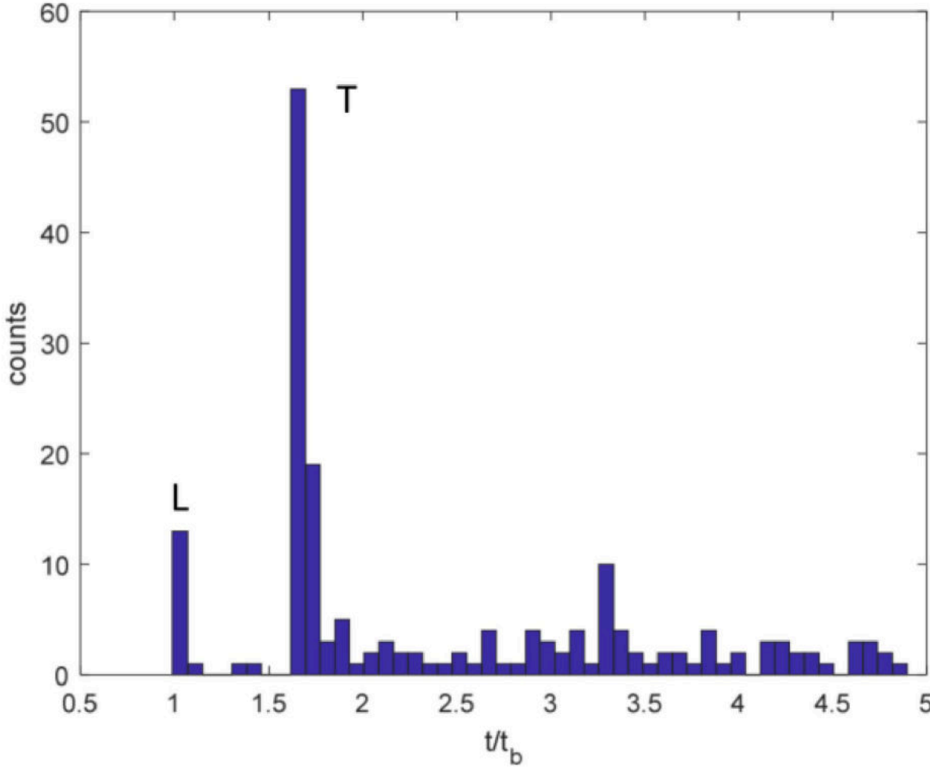

Figure 2.18: Output consistency test: arrival time distribution of LA an TA polarized phonon at $t/t_b = 1$ and 1.66 as expected. From [43].

Phonon temperature and polarization test. Starting from N Debye phonons, we check the frequency distribution after a time t, that must be Planckian as shown in Figure 2.14 in consistency with the expectations.

Propagation of ballistic phonon. We consider a Si crystal with thickness 5 mm (10 time thicker than CryoAC). We simulate a phonon source with Planck distribution at $T = 15\ K$, to produce enough sub-THz ballistic phonon. After a short initial evolution, the thermal sphere is smaller than the silicon crystal and start emitting large number of sub-THz phonon that travel without scattering towards the surfaces. Those phonons are ballistic and move at different speeds. We want to measure if the calculated velocities of simulated events are consistent with the expected ones. The phonons are collected by a detector ($1.5 \times 1.5\ mm^2$) placed in front of the source. The arrival time is normalized to the ballistic time t_b for Longitudinal wave L phonon. Then we expect 2 peaks: the longitudinal wave acoustic phonon (LA) phonon at $t/t_b = 1$ and the transverse wave acoustic phonon (TA) phonon at $t/t_b = 1.66$. As it can be seen in Figure 2.18, this correctly reproduced by the simulation.

Quasi-diffusive propagation of phonon in Si. We simulate the experiment described in the paper of S.Tamura [50]. The Si crystal has a thickness of 5 mm. The phonon are generated with a frequency of 4 THz at the bottom face. We calculate the pulse shape generated by the flux of phonon arriving

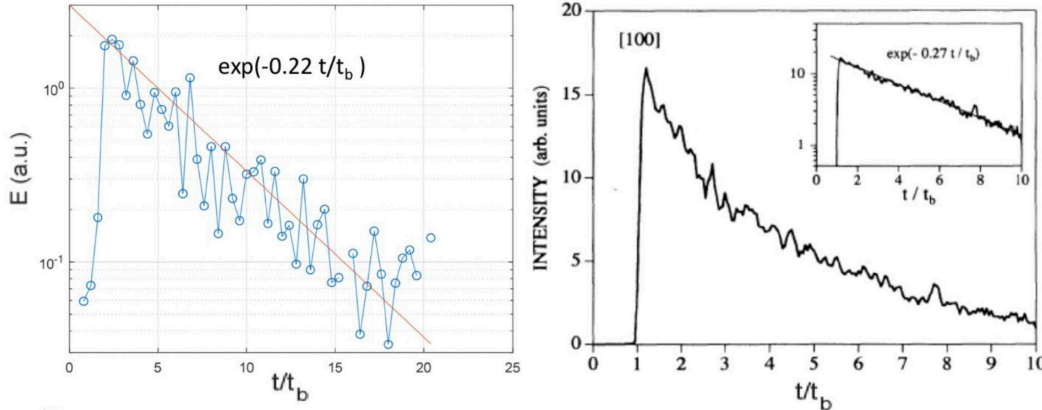

Figure 2.19: (left) Simulation of a replicated S. Tamura experiment [50]. The simulated heat pulse pulse vs t/t_b has an exponential normalized decay constant of -0.22, which is similar to the experimental value of -0.27 of S. Tamura experiment (right), with the intensity in log scale in the inset. From [43].

into the sensor on the top face. The time is normalized to the ballistic time t_b for LA phonon. In Figure 2.19, the plot of the exponential decaying heat pulse as found in the experiment of Tamura is represented. Our simulation (top plot) gives a constant decay with a slope of -0.22, similar to the result of S. Tamura of -0.27 (bottom plot).

Major outputs of the numerical model of Cryo-AC

The first important question that arises in studying the CryoAC is the size of heat spot on the TES instrumented surface for a typical event in the bulk. As we have seen in the phonon gas model, the heat sphere radius increases linearly with time (Equation 2.43). Being the CryoAC thickness (0.5 mm) very small if compared to the lateral size (10 mm), we expect a large non uniformity in the energy flux at the surface. In fact, the numerical model indicates that the phonon illumination is concentrated in a spot of few hundreds of μm and the time integration of the pulse energy flux has a peak-like shape with 1 mm FWHM (see Figure 2.20.)

The second question is related to the signal height fluctuations caused by the pitch size of the TES array on the absorber surface. In fact, if the heat spot size is much smaller than the pitch-size we expect a large number of events in which most of the a-thermal energy will be not detected by the TES array. The CryoAC has a TES array with pitch size of 1 mm. In Figure 2.21 it is shown the simulation of a linear array of TES with 1 mm spacing (left picture) and the signal amplitude plot vs the source position along the linear array (right plot). The amplitude fluctuations are acceptable, being about 20%. The signal height decreases steeply at the edge of the detector, out of the TES array.

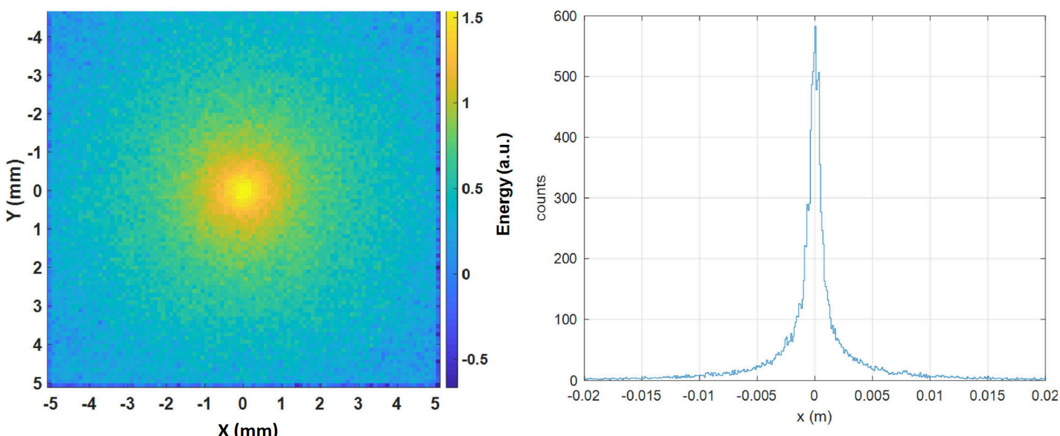

Figure 2.20: 2D plot of the integrated heat flux (arbitrary unit) at the surface (pixel size = 200 μm). (right) Integrated heat flux a the surface vs x-axis: the FWHM is about 1 mm. From [43].

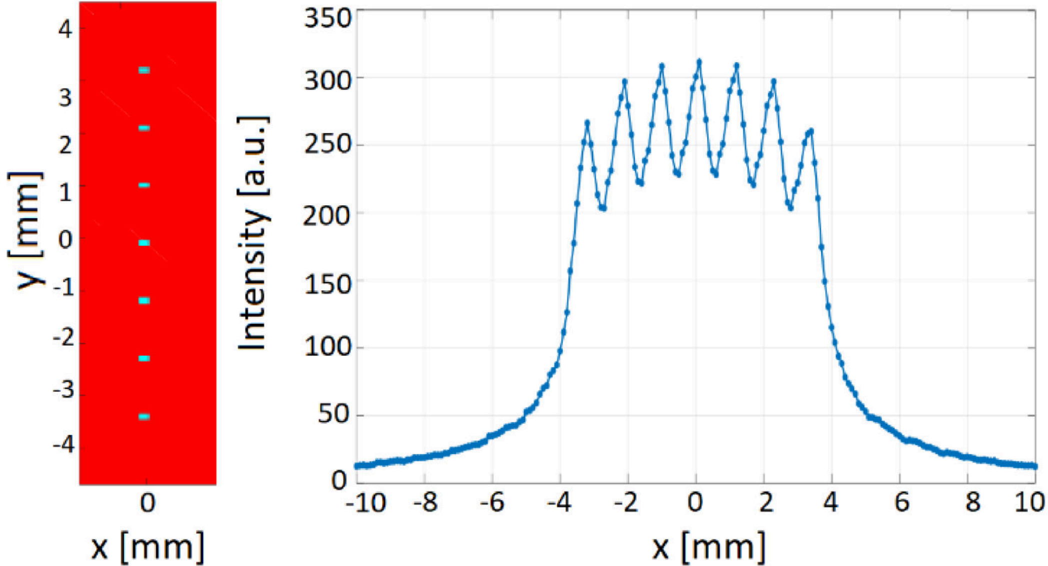

Figure 2.21: Signal height fluctuations due to the TES array pitch size: here the simulation is done for a liner TES array of 1 mm pitch size like in the actual CryoAC (left). 20% total height fluctuations are predicted moving the source along the vertical axis below the linear array (right). From [43].

2.4 The CryoAC design

To fulfill X-IFU requirements for the CryoAC detector, resumed in Table 2.1, have a detector with the 99.98% detection efficiency required, on a 4.9 cm^2 absorber, with intrinsic dead time of 1%, and being fast on coincidence tagging with the NASA TES microcalorimeter array [26]; it have been designed a detector a TES based microcalorimeter detector exploiting also the a-thermal signal generation. The absorber dimensions are needed to being able of detect the 99.5% of particles passing through the TES Array. Therefore the detector shall be hexagonal to better cover the FPA area and the big 4.9 cm^2 active area covers a wider range than the TES array to intercept grazing particles. Anyway, with the mission redefinition is possible that dimensions will be modified to reduce power loads. The hexagonal absorber is suspended through several

Parameter	Value
Geometrical rejection efficiency	98.5%
Detection efficiency	99.98%
Allocated power dissipation	$< 40\ nW$ (TBC)
Time tagging accuracy	$< 10\ \mu s$
Intrinsic dead time	1%
Energy threshold	$< 20\ keV$

Table 2.1: Current CryoAC requirements. From [51].

bridges that provide a well-controlled thermal conductance G among the pixels and a thermal sinking rim, that must be gold plated to thermal anchor the whole chip by means of gold wires ultrasonically bonded between rim and cold supporting structure. The bridges must also cope with the thermo-elastic stress of thermal cycles and launch vibration.

To effectively exploit the a-thermal phonon signal detection, and sense the absorber temperature increase produced by thermalization, the active area must be covered with a total of Ir/Au TES uniformly distributed as periodic matrix. Thus the voltage biased TESs give rise to current signal that is composed by a faster a-thermal component and a slower thermal one, see Figure 2.22. The material chosen for the absorber is high resistivity Silicon ($\rho > 10\ k\Omega cm$) and the thermal conductance the silicon bridges test structure has been fitted with the law:

$$G(T) = aT + bT^3, \tag{2.46}$$

where the a and b parameters at 50 mK are: $a = 0.046 \pm 0.09 W/K^2$ and $b = 0.96 \pm 0.05 W/K^4$.

The phonon simulations in silicon, Section 2.3.3, have been used to calcu-

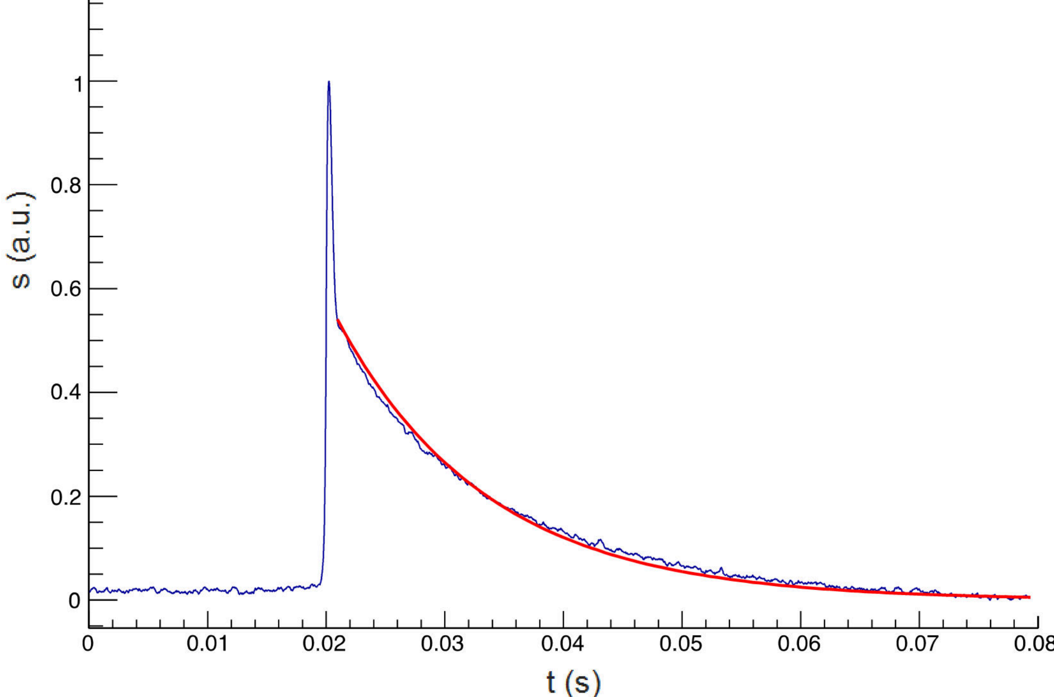

Figure 2.22: Typical pulse shape of a CryoAC model in which the a-thermal component, the fast peak, is clearly visible on top of the exponential decaying thermal pulse. the red curve fits the decay with single exponential function. (Axis unit are arbitrary)

late the pitch size of the TES periodic matrix in order to assure the required uniformity. Foreseeing a hot spot formation of energetic phonons that, at first glance, allow constraining the TES matrix pitch size in the range of 0.5-3 mm. To increment the precision on this requirement, for a-thermal phonon signal detection, have been set up a measurement of the effective hot-spot detectable area, see Section 5.4, and tune the final pitch size. Currently, CryoAC models have been designed with 480 TES on the 4.9 cm^2 active area.
The large matrix of parallel connected TES is voltage biased, then large current flows in the wiring producing a magnetic field. This magnetic field should not interfere with the TES microcalorimeter array and the maximum magnetic crosstalk requirement among the two detectors is 1 μT. Therefore, anti-inductive $Nb - SiO_x - Nb$ strip-lines, with clockwise-counterclockwise alternated neighbouring loops for TES biasing, are main ingredients of the on-chip wiring design.

Then, to work together with the spectrometer, CryoAC should provide an operating temperature of 90-100 mK (T_c of Ir/Au bilayer), a thermal conductance of 2×10^{-7} W/K, risetime $\tau_R = 30$ μs, thermal decay time $\tau_{th} = 1.5$ ms (TBC), and electro-thermal feedback decay time $\tau_{ETF} = 750 \mu s$.

In the end, the design have been completed with an innovative addition to the detector: the on chip heaters. Those heaters have been found very effective for power biasing the detector and are useful as calibrating pulse sources for monitoring purpose and full channel tests, allowing in flight test operations. Moreover, they allow to reduce power load on the shunt.

The summary of the CryoAC parameters are summarized in Table 2.2.

2.4.1 Absorber Geometry configurations

As already mentioned, the chosen geometry is a regular hexagonal (with side equal to $l = 1.819$ cm, however, the geometry inside the detector is going through a trade-off, a drawing is shown in Figure 2.23. Have been designed two different internal geometries for the detector with two absorber configurations: four 1.23 cm^2 each pixels or a single 4.92 cm^2 pixel. Design principles are based on the requirement of table 2.1 adapted to the two configurations and taking into account the mechanical simulation results of preliminary hexagonal concepts concepts [52] proposed to OHB Italy.

- 1-Pixel, Monolithic silicon absorber: the inner detector is a single hexagon of 4.92 cm^2 suspended through 12 silicon bridges.

- 4-Pixel, Segmented silicon absorber: the detector is composed of 4 distinct trapezoids absorbers, of 1.23 cm^2 and suspended through 4 silicon bridges each.

The segmented geometry has a separation between the 4 inner trapezoids of 25 μm, allowing the final detector to possess 4 completely independents

Parameter	Value	Comments
Absorber size	4.92 cm^2	CryoAC 4 pixel,
		$\sim$ 1.23 cm^2 area each pixel
Absorber Material	Silicon Ωcm	Max impurity of doping atoms
	$\rho >$ 10 k	$P,\ B,\ Al < 10^{15} atm/cm^3$
Thickness	500 μm	90% damping of fluorescenses
		up to 12 keV
		towards the TES array
Distance from X-IFU	$<$ 1 mm	CryoAC geometric Rejection
		efficiency 98.5%
Minimum energy	$\sim$ 5 keV	Measurable with:
	Threshold	^{241}Am 60 keV gamma line
	at 20 keV	(Compton edge at $\sim$ 10 keV),
		or the ^{55}Fe at $\sim$ 6 keV
Rise Time	$<$ 30 μs	transition ΔT $<$ 2% (TBC)
Effective Fall time constant	250 μ s (TBC)	It sets the CryoAC deadtime
		with τ_{TH} and GCR background
Thermal time constant	$<$ 2.5 ms	From our present evaluation
		$\sim$ 0.2 ms (TBC)
TES Material	Ir/Au bilayer	150 nm Ir / 50 nm Au
Transition temperature	90-100 mK	ΔT $<$ 2 mK (TBC)
Thermal bath temperature	50-55 mK	
TES normal resistance	$R_n = 30m\Omega$	
Shunt resistance	$R_S = 0.2m\Omega$	
On-board Pt heaters	1 each	1.2 $k\Omega$ each
	silicon bridge	parallel connected

Table 2.2: CryoAC detector main parameters.

pixels and being able to read 4 separate signals based on the arrival point of the charged particle on the detector. The thickness of thin separation between the pixels have been design in order to reduce the possibility of losing detectable particles. Thus, a thin trench minimize this problem, but is much more complex from a technological point view, because of the high aspect ratio, see section 3.7. On the other hand, the monolithic geometry was thought as an alternative, as it is much more resistant, see section 4.5, it certainly does not risk losing detectable signal, and it also presents a greater ease of production. Obviously it does not have the advantage of the 4 separate detectors, but if the thermal signal is independent from the particle interaction point, the a-thermal one is strongly dependant by the phonon generation point, as described in Section 2.3. This enables to read the TESs on the detector by 4 different circuits, and distinguish over which area of the detector the loss of energy occurred exploiting the a-thermal signal part characteristics.

Anyway, from a thermal point of view the monolithic geometry would led to a slower detector, having a single pixel. Anyway, this issue could be overcome changing the silicon bridges aspect ratio tuning the thermal conductance. In-

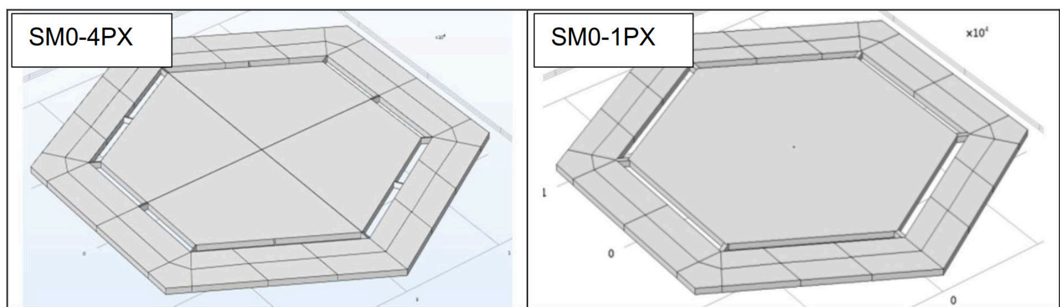

Figure 2.23: Simplified drawing of the 4-Pixel and 1-Pixel detector configuration.

stead the segmented one won't have this problem being fully fledged 4 distinct detector in one. The thermal performances of a detector prototype have been studied and are presented in Section 5.3.

In principle, from simulations both configurations would meet the technical requirements, but to verify the structural functionality have been produced structural models of both the geometry and tested to understand which of the two could best meet the technical requirements, see Chapter 4.

2.4.2 Demonstration Model

To test the operating principles and performance of the detector, and to assess its Technology Readiness Level (TRL), its Demonstration Model (DM) has been designed, produced (see Chapter 3 and tested (see Section 5.2).

A square geometry was chosen with a 1 cm^2 absorber suspended with 4 bridges, etched from a single silicon chip with a side of 1.66 cm representing one pixel of the segmented geometry. The main design characteristics of the DM are:

- the sensor array that is composed of 96 $500 \times 50 \mu m^2$ TES, parallel connected, with a pitch size of 1 mm;
- 1 cm^2 silicon absorber, 500 μm thick, that is also the substrate of the uniformly distributed TES net,
- 4 silicon bridges 1 mm long and 100 μm wide that suspend the absorber;
- the gold plated silicon rim to thermally anchor the detector to the cryostat;
- 4 Pt heaters in at the 4 silicon bridges;
- the $Nb/SiO_x/Nb$ wiring stripline, designed to produce less than 1 μT at 1 mm distance.

The complete CryoAC DM mounted in the FPA coupling bracket can be seen in Figure 2.24

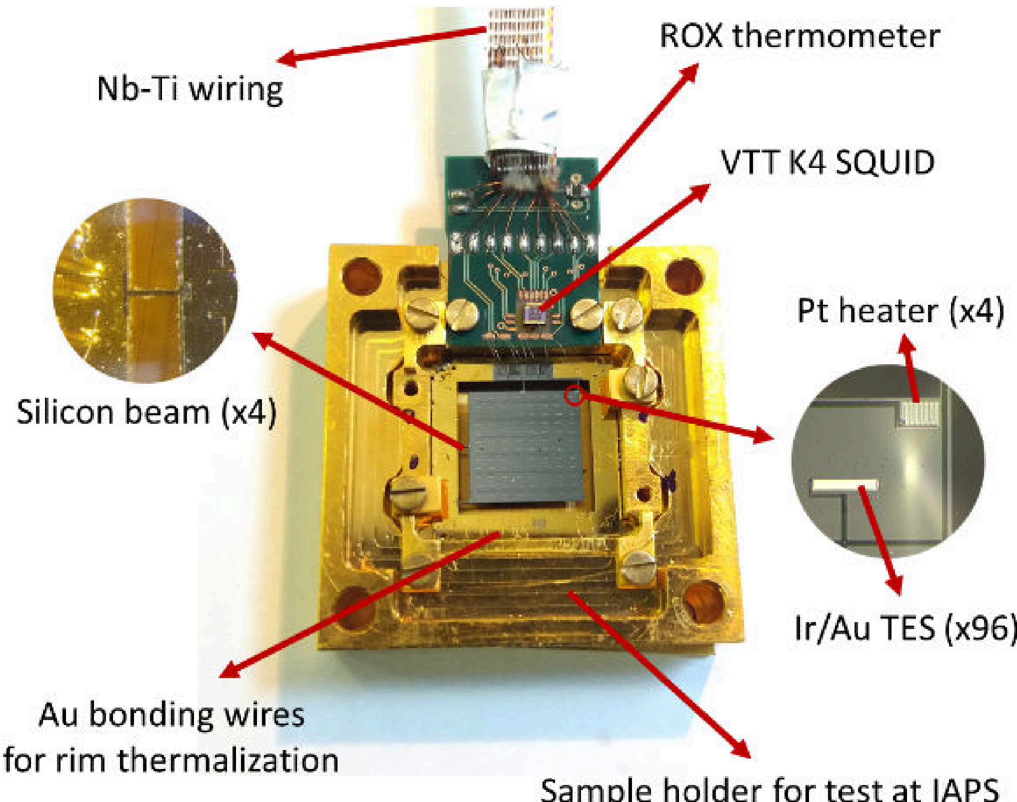

Figure 2.24: Demonstration model AC-S10 mounted on the thermal bracket for the focal plane assembly with its requirement previous than the mission redefinition. From [53].

Chapter 3

Fabrication of the CryoAC

This chapter summarizes the fabrication processes of the demonstration model of the Anticoincidence Detector that I developed during this thesis. During the fabrication of the DM, I studied the processes, and overcame several issues, according to their impact on the overall functional performance (electrical, thermal, and structural). The developed processes are in the final qualification phase, as several modifications and improvements are being made to improve the yield. Adjustments to realize the structural and engineering models in their size will be necessary and some have already been developed, see Section 4.1. Fabrication exploits micro-photo-lithography processes, plasma etching, and various deposition techniques, which will be illustrated.

3.1 Photo-lithography

Photo-lithography is a printing method by which precise patterns can be etched or deposited on a substrate with different materials. The technique exploits a photographic emulsion usually composed of Poly-methyl-methacrylate (PMMA) organic compounds called photo-resist. The resist is sensitive to UV rays and once impressed modifies its properties. Thus, quartz masks are made with the pattern to be transferred on the PMMA in chrome, so that only certain parts of the resist are exposed to UV light. I performed the exposure with a MJB4 mask aligner with 365-405 nm UV wavelength. Then the emulsion is developed to reveal the final pattern. There are two different methods of performing photo-lithography: in positive or negative. They are schematized in Figure 3.1.

3.1.1 Positive photo-lithography

Positive photo-lithography imprint the chrome pattern on the resist, as UV light makes the positive-PMMA removable by the its proper developer. Therefore, usually with this technique firstly the material is deposited, the layer of photo-resist spinned on the sample and processed, then the material not covered by the resist pattern is dry etched and finally the sample is washed

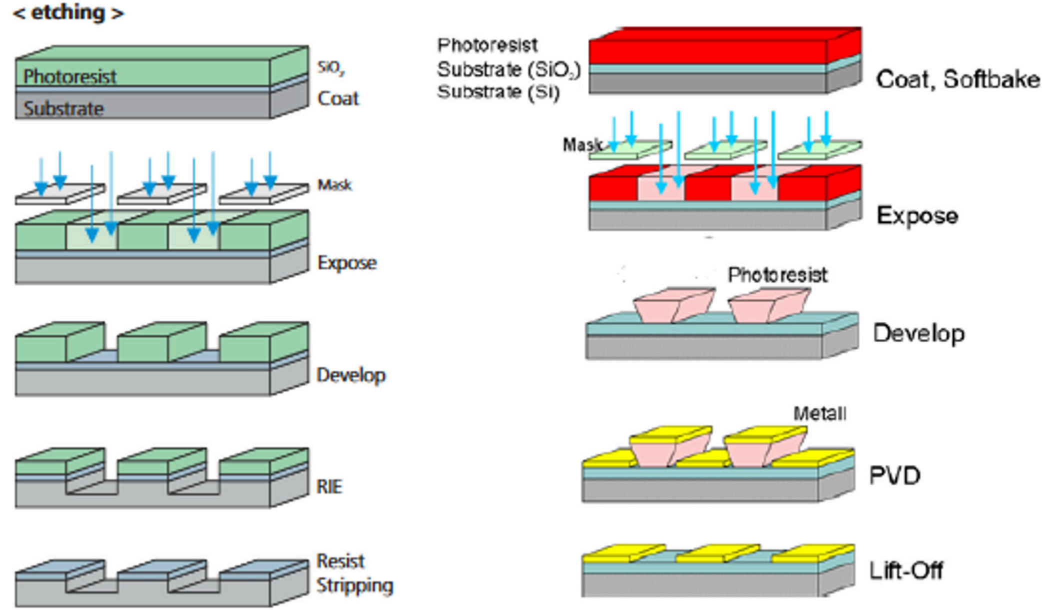

Figure 3.1: Left: Operation sequence for the positive photo-lithography. Right: Operation sequence for the negative photo-lithography.

with solvents to remove the emulsion and reveal the pattern on the material. Lithography parameters as: resist spinning, baking, UV exposure, and developing time depends by multiple factors, from environmental humidity and temperature to the resist shape wanted on the sample, some example can be found in Figure 3.2.

3.1.2 Negative photo-lithography

On the other hand, in negative photo-lithography the portions of photo-resist exposed to ultraviolet light will remain after the development step. Thus, the chrome pattern on the mask will create a trench on the PMMA leaving on the sample a pattern without resist coverings. Then, usually this technique is used depositing firstly the photo-resist and then the desired material, that will attach to the substrate only in PMMA clear parts. As before, lithography parameters are multiple and depends from many factors, in particular the developing time can be exploited to change the resist wall angle and increment the separation between the material deposited on the substrate from the one on the emulsion, see Figure 3.2.

3.2 Silicon chip preparation

The silicon substrate is a single-crystal with (100) crystallographic orientation diced into squares of $16.6 \times 16.6mm^2$ from high resistivity ($\rho > 10000\ \Omega m$) intrinsic Si wafers from Siegert Wafer. Dicing is performed by the Bruno

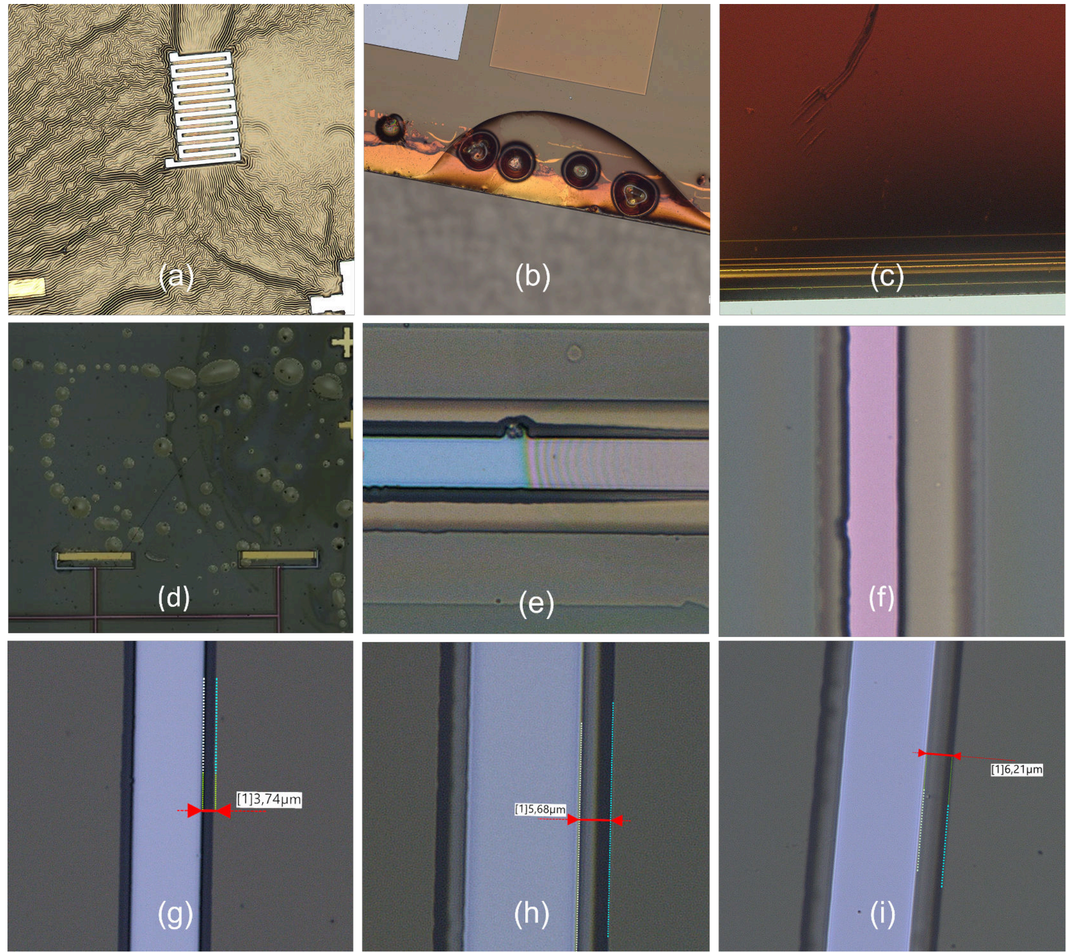

Figure 3.2: Examples of issues and results achievable tuning the lithography parameters. (a) Lithography with insufficient baking, resist remained too soft creating the observable effects after development. (b) Bubbles inside resist due to a non correct distribution. (c) Burnt resist, too aggressive baking lead to difficulties in remove the resist. (d) Lithography ruined by solvents vapours. (e) Part of the trench remained under-developed with traces of resist (the iridescent part on the right) due to a non optimal exposure. (f) Standard tuned lithography. (g) Over-developed resist to create under-etch. (h) and (i) Over-developed process where two under-etch bands are visible one lighter and one darker, under the lighter one there will be a material deposition.

Kessler Foundation (FBK, Trento, Italy) from a double side polished wafer. However, to remove any contaminants from the cutting, as the Ir film is very sensible to ferromagnetic contaminants, two cleaning processes are required to ensure good adhesion and unspoiled characteristics of the deposited films. The first cleaning process consists of three washes in an ultrasonic bath:

1. Washing in de-ionized (DI) water with Extran AP acid detergent (12 minutes)
2. Washing in de-ionized water to rinse it of detergent residue (12 minutes)
3. Washing in acetone (12 minutes)

Next, the chip is rinsed with acetone and ethanol, and shed with nitrogen. Then, left to dried in a controlled atmosphere at a temperature of 393 K for 2 hours, to remove moisture. This process of pre-cleaning is preparatory for the following chemical process and eliminates the majority of unattached organics contaminants. Subsequently it is performed a RCA[1] cleaning in order to remove organic and inorganic, including metal, contaminants. The process follows three steps:

1. Immersion of the chip in 5% NH_4OH solution for 10 minutes: by doing so the elimination of organic contamination from the surface is ensured.
2. Immersion of the chip in 10% HF solution for 30 seconds: this will act on oxides, including the native silicon dioxide on the surface to guarantee the Ir-Si interface.
3. Immersion of the chip in 5% HCl solution for 10 minutes: to remove heavy metals that can interfere with the Ir growth on the surface.

After each, and before the next bath, the sample is rinsed in abundant DI water to remove traces of the previous chemical agent. In general during rinsing procedures it is important to be care of breaking the surface tension of the liquid or perform it in a steady water flow. After the RCA the pre-cleaning with acid detergent[2], DI water and acetone is performed again. This must be done in a ISO-6 or better cleanroom environment to prevent particle deposition, see Figure 3.3, and the deposition process must be done immediately after to prevent the Silicon dioxide spontaneous growth after the RCA.

3.3 Ir/Au TES bilayer

After chip cleaning, the fabrication of the TES devices is carried out. In this step, the shape of the TESs is obtained using the positive photo-lithography

[1] The name comes from Radio Corporation of America, the company in which the inventor of such a washing worked.

[2] This step can take several minutes and an ultrasonic excitation of the chip, thus basic agents can damage the silicon surface deprived by the silicon dioxide native layer

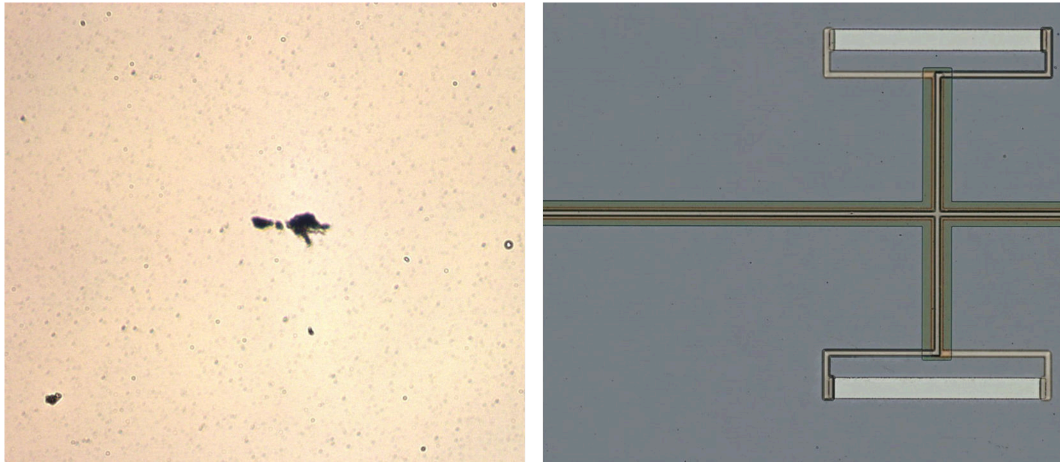

Figure 3.3: Left: Ir film deposited in a not controlled environment. Right: Same magnification and area image of a detector at the end of production inside a ISO-6 controlled environment. The difference of particulate on the surfaces is evident

technique, firstly growing the films and then shaping them via a sputter etching.

3.3.1 Ir/Au film growing

Iridium

Ir growth present several issues, in particular structural adhesion of the film to the substrate when the thickness increases over the tenth of nanometers. This problem can be addressed in several ways. The most common is to heat up the substrate to $600 - 800\ K$, but we opted for a different solution exploiting the characteristics of Pulsed laser deposition (PLD). PLD is a physical vapor-phase deposition technique that uses high-power pulsed laser beam to create an energetic plasma plume from a target; a scheme can be seen in Figure 3.4. Inside a vacuum chamber the material chosen for deposition is vaporized, therefore the plume hitting the substrate grows the film. This process must take place in ultra high vacuum (UHV) to avoid contamination, so that the plasma parameters are kept under control. The energetic plume when it hits the substrate favours the creation of iridium silicides as an interface, resulting in a very stable film [54].

There are several parameters to monitor during the process:

- the ablation laser spot on the iridium target,
- the spatial distribution of the plasma plume,
- the effective deposition rate on the substrate.

The laser ablation of the iridium target is controlled by the penetration length, which depends on the laser wavelength and the refractive index of the

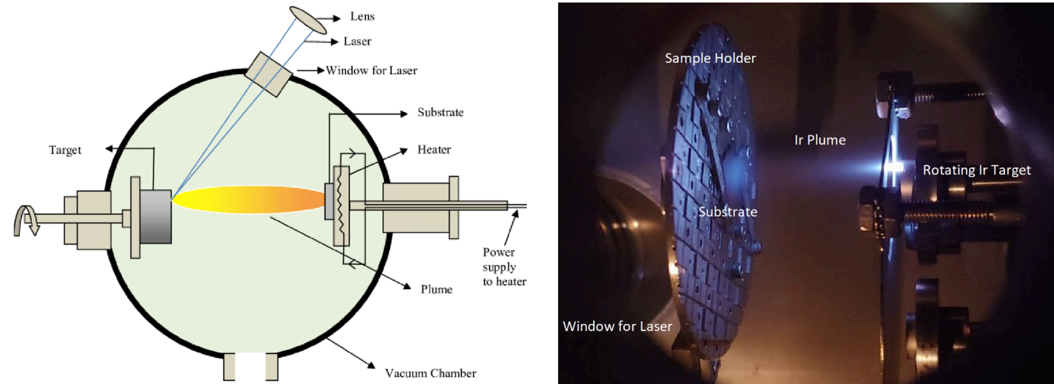

Figure 3.4: Left: Schematic of the operation of PLD. From [55]. Right: Picture of the PLD vacuum chamber for iridium film growth.

target material. The electrons of the surfaces interacts with the electromagnetic field of the laser light and collide with the material, transferring large amount of energy to the lattice, vaporizing locally the surface atoms. The Laser in use is a Q switched pulsed 1064 nm $Nd:YAG$ form Spectra Physics with a repetition rate of 10 Hz and pulse length of 10 ns and energy of 550 mJ. The spatial distribution of the plasma plume depends on the vacuum level in the chamber and on the laser focusing. Higher the vacuum and laser focusing, bigger is the cosine exponent, making more concentrated the plume (the emission form ablation has intensity proportional to cos^n). The effective deposition on the substrate is ensured as high-energy atoms from the target bombard the substrate. Particles sputtered from the substrate and atoms coming from the target form a collision zone inside the vacuum chamber. Thus, the growth of material on the substrate can take place when the plume implant atoms coming from the target rather than sputter the substrate. However, to achieve uniform growth of the deposited film, one must pay attention to several parameters such as: substrate temperature, substrate cleanliness, and vacuum level.

Gold

The deposition parameters influencing the film growth act also on the final iridium critical temperature. The bulk iridium T_c is 114 mK and stresses in the film can increase it to almost 200 mK [56]. To fix those parameters and to be able to reach the 100 mK T_c the critical temperature is adjusted by exploiting the Holm-Meissner proximity effect [35]. This phenomenon exploits the contact between a superconducting and a normal metal layer: the conduction electrons of the two layers are differently ordered. In fact, in the former case the electrons arrange themselves according to Cooper pairs [57], while in the metal the electrons arrange to fill the Fermi layer. Because of the non locality of the electrons, their properties cannot change instantaneously: the Cooper pairs of the superconductor are destroyed at the interface by Andreev's reflection [46]. Anyway, this scattering allows the non-instantaneous transition from one

configuration to another: this mechanism has as its direct consequence the lowering of the superconducting T_c having a meta-material of the two layers. Therefore, growing a gold layer above the iridium film, it is possible to obtain a critical temperature around 100 mK. A key aspect in the T_c tuning is the thickness ratio of iridium to gold [58]. Numerous transition tests with different iridium-gold thickness ratios have been performed comparing them with literature. Part of the results are shown in Figure 3.5.

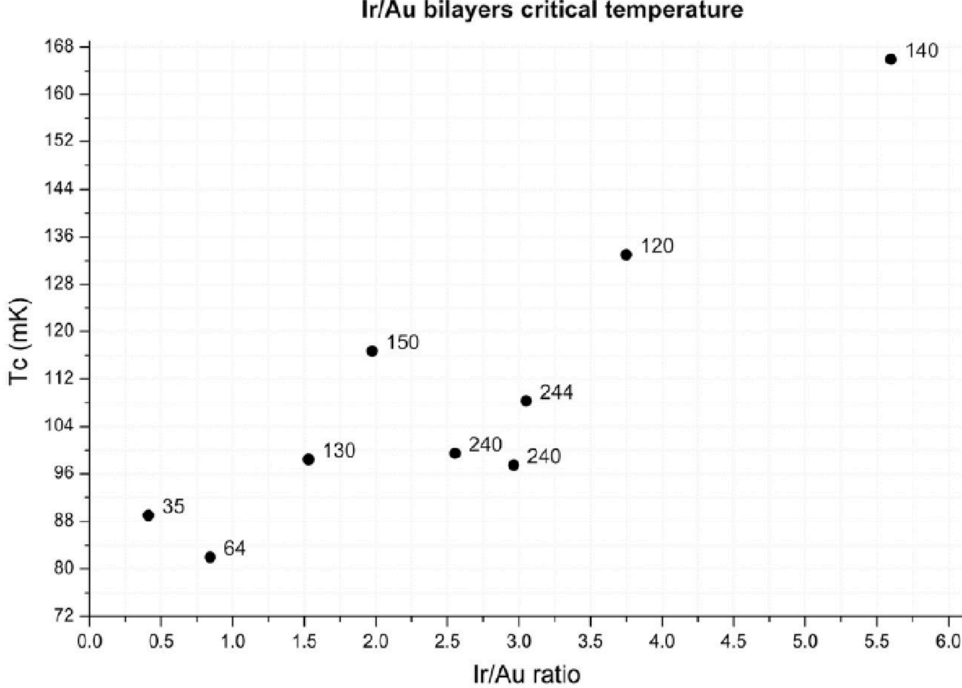

Figure 3.5: Superconducting transition temperatures with different thickness ratios of the iridium-gold films. Close to individual data the iridium thickness in nm is shown. From [59].

In the end, we fixed the thicknesses at 150 nm iridium and 50 nm of gold to obtain the 100 mK transition. The gold layer deposition is performed with an electron beam (e-Beam) placed in a different vacuum chamber inside the same cluster, visible in Figure 3.6 labelled as (C). Therefore, is possible to move the sample from one chamber to the other, without breaking vacuum ensuring an optimal interface between the two layers.

The electron gun deposition technique allows the growth of films with very high purity. The principle of operation is based on the bombardment of the material to be evaporated with an electron beam. Electrons are produced by thermoionic effect heating a tungsten filament and accelerated by a high-voltage electric field, between $5-6$ kV in our case. The electrons trajectory is conveyed in the crucible by the application of a magnetic field. The electrons will completely lose energy in the target, causing a temperature rise, melting the material and inducing its evaporation. While depositing at high rates, Gold

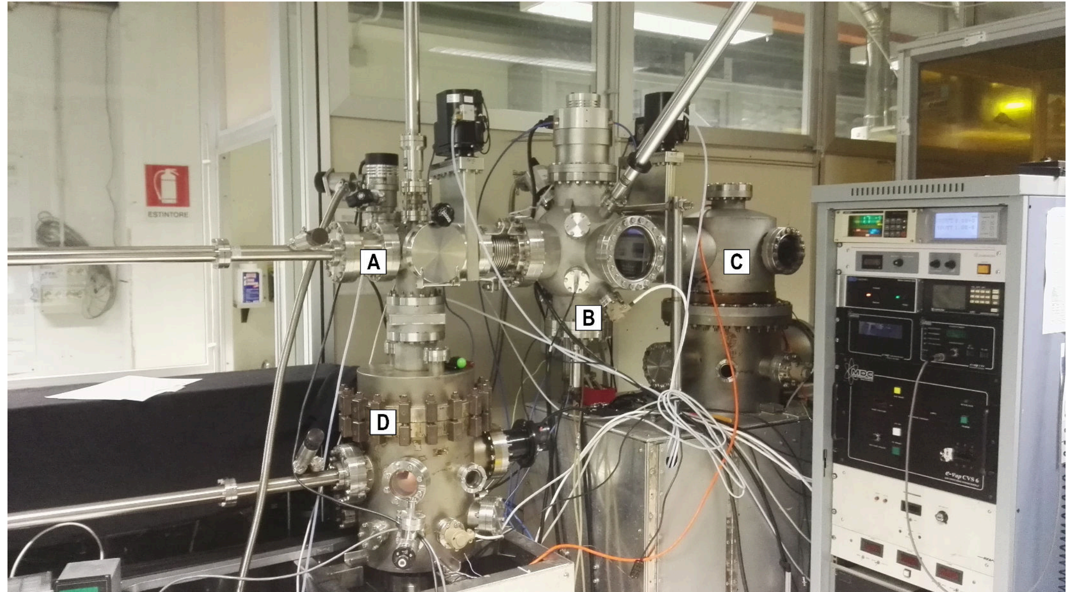

Figure 3.6: Vacuum cluster system for deposition. A: Vac-lock chamber B: RF-sputtering chamber. C: Electron beam gun chamber. D: Chamber for PLD (Pulsed Laser Deposition).

undergoes droplet emission that worsen film quality, thus to deposit smooth films the deposition rate should stay under 4 angstrom per second. Our e-Beam electron emitter current is controlled with a quartz micro-balance with a 0.1 $\AA$ sensitivity. The operating scheme is shown in Figure 3.7.

After depositing the Ir/Au bi-layer on silicon, the sample is extracted from the chambers and moved to film control. This procedure was performed with a Keyence VHX 7000 optical microscope (x6000 maximum magnification), with automatic particle sizing an counting. If the sample does not exceed the particulate concentration limit described in section 3.3.3, it is possible to etch the film and pattern the TES.

3.3.2 Ir/Au etching

To imprint the desired geometry on the film, positive photo-lithography is used. The mask and the final result are visible in Figure 3.8.

The etching is performed by a dry etching, bombarding with Argon ions the surface inside a Reactive Ion etching (RIE) machine. This technique differs from chemical dry or wet etching in that it does not interact with the material and allows for more directional etching. The deposited positive photo-resist protects areas underneath, thus TESs and desired structures remain un-etched. Finally, the remaining resist is removed with acetone and only the silicon chip with the bi-layer TESs and aligning crosses remain. The etching parameter like: the RF power, voltage bias, and the operating temperature inside the RIE are of great importance to control: the etching angle as steep walls can lead to crack films grown on them, see section 3.6, and the resist itself can

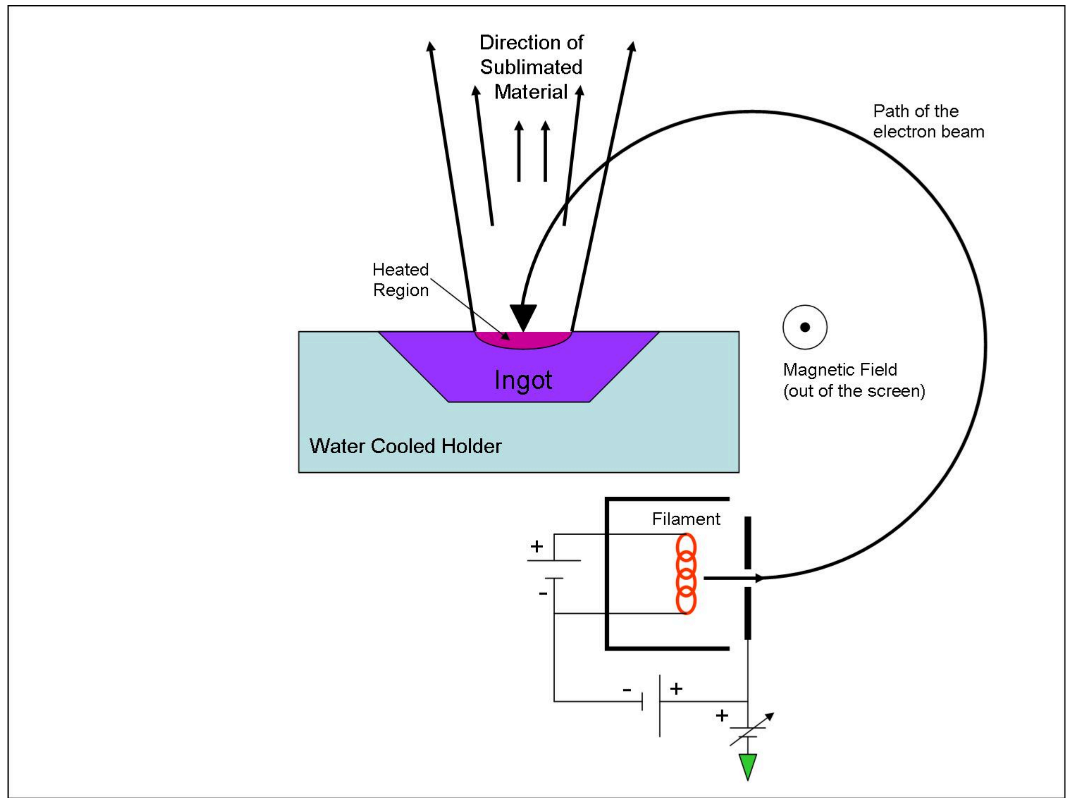

Figure 3.7: Electron beam gun deposition operation scheme. From Jatosado, eBeamScheme, CC BY-SA 3.0.

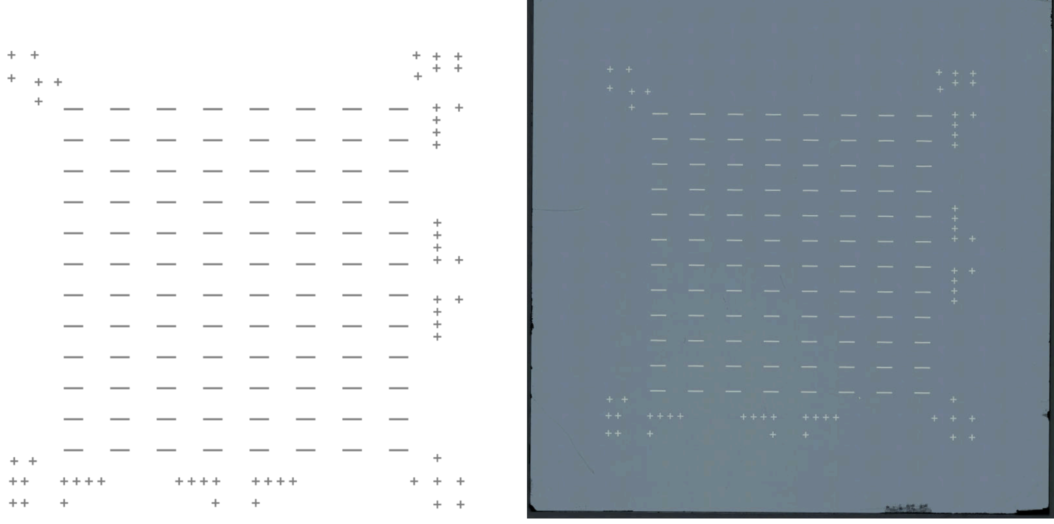

Figure 3.8: Left: CAD image of the photo-lithography mask of the TES geometry. Right: Microscope image of the chip after fabrication of the TESs. In both are visible the TES net and the cross markers for future photo-lithography alignment.

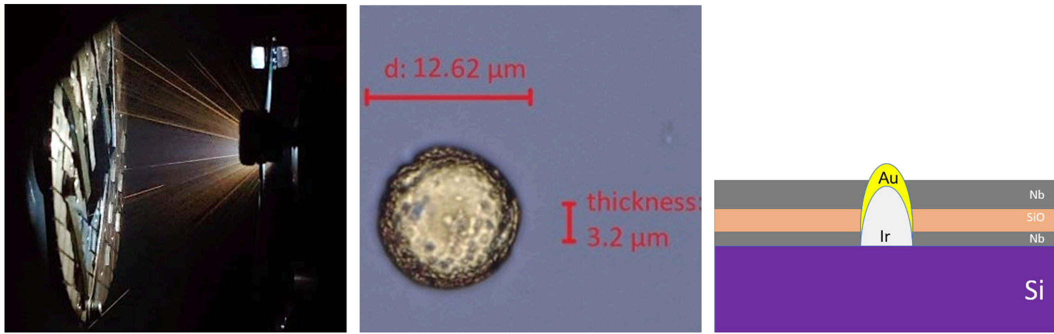

Figure 3.9: Left: PLD plume with splashing, the orange straight lines inside the plasma. Center: Ir particulate deposited by splashing effect. It has gold on top, as result of bilayer deposition and have not been fully etched as the rest of the film during TES shaping. Right: Not scaled scheme of a pinhole due to splashing particulate that cause shortcuts in superimposed wiring.

experience cracking or degradation preventing a good etching result.

Deposition and etching parameter play a key role in the quality of the films for TESs. They influence smoothness, uniformity and even films critical temperature. In the next sections, I am going to present some problems arose during the films production, in particular the critical temperature changes.

3.3.3 The splashing issue

One known issue in PLD deposition is splashing, where thermal shock under laser irradiation of target's subsurface layers lead to droplets ejection inside the plasma plume, resulting in deposition of particulates on the film. This effect is enhanced by surface irregularity and laser focusing while it can be reduced with shorter and larger laser pulses, lapping the target surface, or inserting mechanical particle velocity selector that filter slow-moving particulates. This particulate on the film is a big problem as it is embedded in the film, so it cannot be removed, and its thickness can be of 100 times higher than the film one, leading to shortcuts in multilayered structure like wiring, see Figure 3.9. To avoid this issue we need to have less than 100 particle of 5 μm diameter per cm^2.

3.3.4 Thickness uniformity

The Pulsed Laser Deposition, compared to other techniques, has the issue of a low deposition thickness uniformity. To overcome this problem can be taken several actions:

- it is possible to defocus the Laser to enlarge the spot;
- increase the sample distance from the target and perform the ablation in a controlled environment with an inert gas such He or Ar pressure

around $10^{-3} - 10^{-2}$ $mbar$,

- but the most effective technique that do not interfere with deposition parameter is moving the sample or the target.

The sample movement is easier to be implemented, but target scanning with the laser have the advantage of increasing the deposition uniformity and at the same time to uniformly ablate the target maintaining a regular target surface texture, really important to prevent splashing and consequently, the droplets. On the other hand, the target rastering have the disadvantage that, a wide target is needed to perform depositions uniformity over large areas. Our deposition parameters allows us to perform uniform depositions over a $1cm^2$ area without implementing any of the described actions. However, it is important not only the thickness uniformity, but also the repeatability. Without the target scan, Laser spot must be moved periodically in different positions on the target to prevent splashing. In addition, we rotate the target to uniformly ablate over a ring. Moreover, the movements of ablation source position causes the displacement of the center of uniformity, thus is important to have a larger area to increase also repeatability. Demonstration Models active area is 1 cm^2 and to improve our uniform depositions area we rotate the sample during deposition. For next models we are implementing a system to scan the Laser over a wider Ir target in order to achieve a 6 cm^2 uniformity area. Figure 3.10 shows the thickness of Ir on a very large substrate (55 cm^2) and its improvement with sample rotation.

3.3.5 Iridium films critical temperature distortions

The iridium superconducting critical temperature (T_c) is strongly dependant by contamination during deposition e.g. the presence of some part per million of ferromagnetic atoms suppress the superconductivity. Besides this effect we experienced that some process can similarly degrade the superconductive properties and different parameters during the deposition move the T_c as a result of crystalline stresses. After having experienced several films without the superconducting transition, see Figure 3.11, many actions have been taken to isolate and understand this effect. The Ir target was changed, the deposition environment and the focusing optics checked, and a set of films, to be tested after each process step, produced. Consequently, different effects other than the Ir/Au thickness ratio have been found to influence the iridium superconductive transition:

- stresses in the Ir crystalline structure,
- film oxidation,
- fluorides contaminants.

Stresses of the crystalline structure seems to produce rigidly shifts of the superconducting transition critical temperature, while oxidation and contamination by fluorides, in addition to ferromagnets, appear to destroy superconductivity.

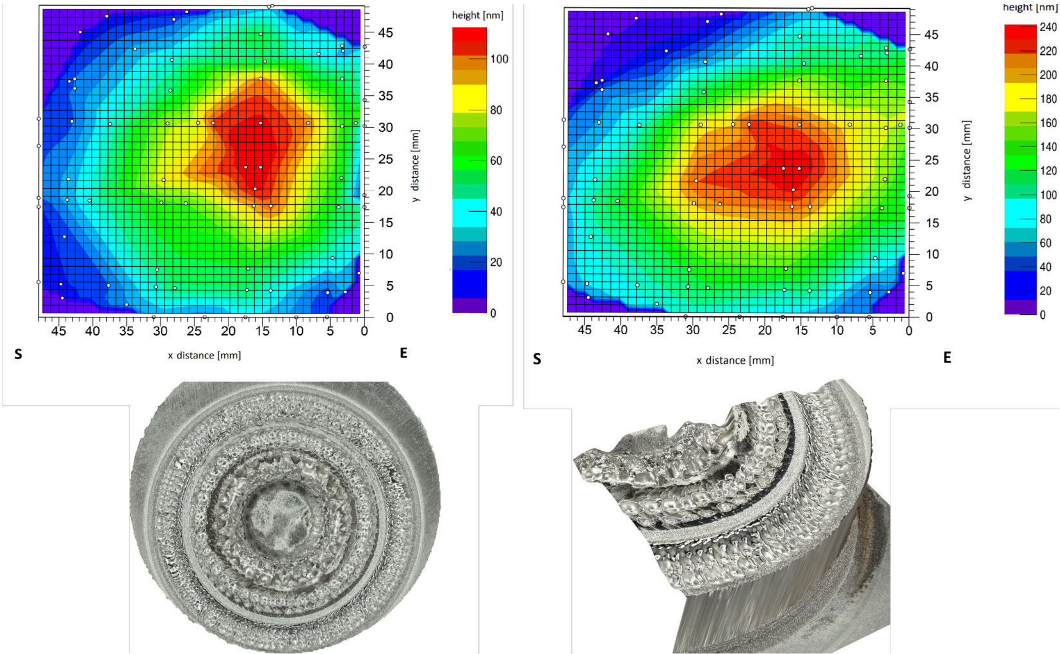

Figure 3.10: Top: Ir Thickness distribution after 1h deposition without rotating the sample at 5 cm distance from the target (left). Ir thickness distribution after 1h deposition at angle: $-20°, 0°, 20°$ respect to the Laser spot position at 5 cm distance from the target (right). Bottom: Pictures of the Ir target after several depositions, are clearly visible the ablation spots and different rings at which the ablation occurred.

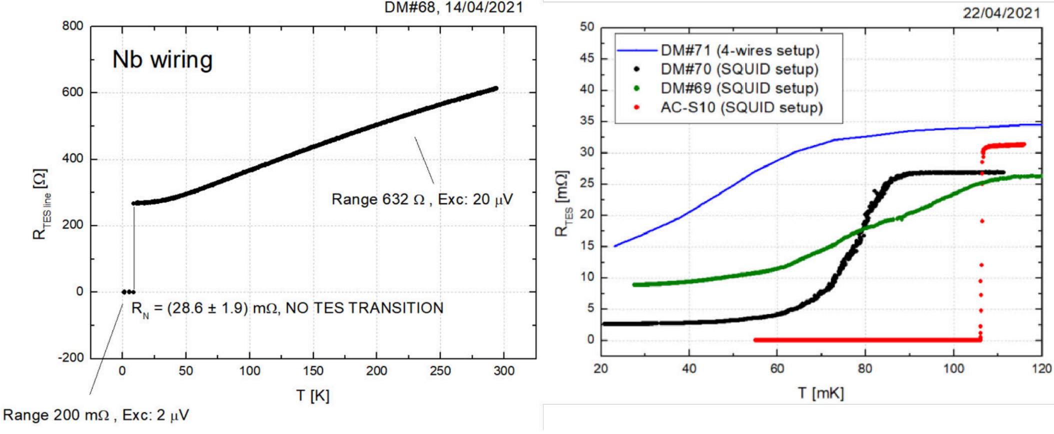

Figure 3.11: Left: Detector without the Ir superconductive transition. The Nb wiring become superconductive around 9 K but the sample resistance remain that of the TES net in the normal state down to 20 mK. Right: Detectors distorted TES transitions. The Red data refers to ACS-10, the DM of section 5.2, while the other detectors show shifted and broadened transition toward low temperatures.

Crystalline structure and T_c correlation

Hints of the critical temperature dependence from lattice stress were already observed and investigated in our lab in titanium films, [60]. Over the years, we have had evidence that samples of Ir films on Silicon (100) showed quite different T_c temperatures, difference of about 50 mK, although the growth conditions were similar. In particular, we know that the growth system experienced slight differences in deposition parameter over time, such as spot size on the Ir target and target-substrate distance. Therefore, we were interested in analyse this effect to understand if it was similar to the titanium T_c shift already experienced or could have been linked to the distorted superconducting transition observed. Consequently, the analysis of several Ir/Au bilayers with X-Ray Diffraction technique shown a systematic correlation between the size of iridium crystalline domains and the T_c of the films.

Film samples were prepared with the already described processes on the same Silicon substrate of section 3.2. At the end of deposition, the sample is extracted from the deposition systems and cut into several samples on each of which various measurements are made:

1. absolute thickness of the film with an interferometric optical profilometer,

2. resistivity at room temperature and low temperature,

3. critical temperature,

4. structural and morphological analysis.

Thickness measurements are made using the edge generated by shadowing of structures placed on chips before film deposition. We measure the height difference between the silicon substrate and the top surface of the film using a Shaeffer's optical profilometer with an overall accuracy of about 5 nm.

Resistivity measurements are performed by the 4-probe Kelvin method, via 4 aluminum wires of 25 μm diameter wedged bonded in line at the center of the large-area film. Film resistance is measured at room temperature, in liquid helium, and at 100 mK in a He-3/He-4 dilution refrigerator (Oxford Instrument Kelvinox 25).

Structural measurements are made in the Hewlett Packard XRD system that has an X-ray beam produced with copper cathode. Typical XRD spectra obtained for the bare silicon substrate and for the bilayer of Ir and Ir/Au that we grew on the same substrates are shown in Figure 3.12. The spectra show a recognizable pattern with overlapping peaks for each material: silicon (100) has the characteristic reflection line (400) doubled due to the two x-ray energy $K\alpha$ and $K\beta$ emission lines of the copper cathode; Ir films grow with a preferred structure (111), plus sub-structures (110) and (311); Au films grow over Ir with the same crystal orientation as Ir, i.e., Au(111) over Ir(111) and Au(222) over Ir (222).

Thus, we selected two Ir samples having $T_c$of 130 and 180 mK, respectively, to check whether differences in the crystal structure of the two samples

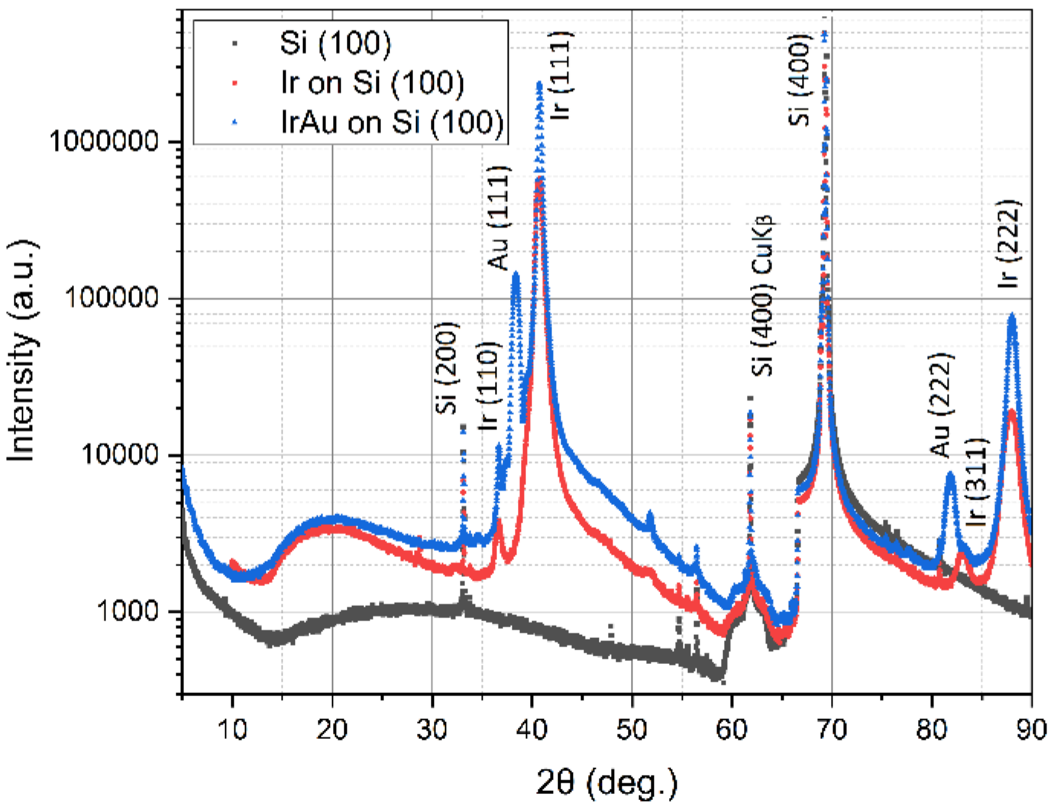

Figure 3.12: Spectra have a recognizable footprint with superimposed peaks for each material. Silicon (100) presents the characteristic (400) reflection, the Ir films grow with a preferred (111) structure plus (110) and (311) substructures, and Au films grow on top following the Ir crystalline orientation. From [56].

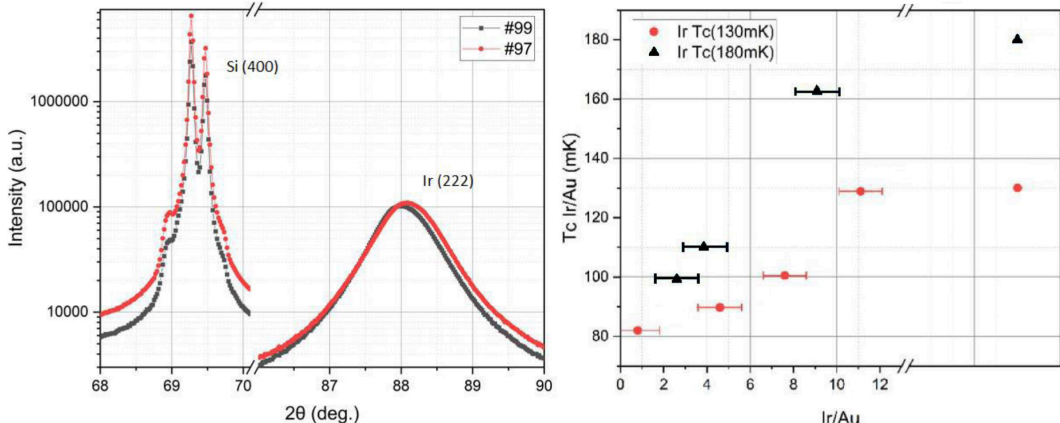

Figure 3.13: Left: Particular of the (400) Silicon peak and the (222) Ir peak for the Ir film #97 with 130 mK $T_c$and the Ir film #99 with 180 mK T_c. The (400) peaks are aligned while the (222) present a shift of the maximum. Right: Critical temperature of Ir/Au bilayer as function of the Iridium and Gold thickness ratio. The two Ir critical temperature are highlighted. From [56].

were also present. A preliminary analysis shown no significant differences between the patterns in Figure 3.12. However, by performing measurements with greater statistics and precision and focusing on individual lines, as shown in Figure 3.13, we observed a reproducible shift in the Ir (222) lines of the order of 0.08°. We verified that the shift was not due to instrumental causes, i.e., a rigid shift in the entire XRD pattern due to differences in orientation between samples, the Si (400) lines being perfectly overlapping.

We then analyzed the microscopic structure of a series of 9 bilayer samples of Ir/Au and looked for the same pattern that emerged from the line analysis shown in Figure 3.13. To uniformly calculate the magnitude of the displacement of all examined films, we have fitted with a Gaussian function to measure the line positions (maximum of the fit function θ) and the Full Width at Half Maximum (FWHM) β of each visible iridium-related line. The results are summarized in Table 3.1. The samples clustered into two sets, grA (#97, #106, #107, #108, #113) and grB (#99, #111, #112, #114), which have the relative Ir(222) line at mean values 88.079° and 88.003°, respectively, and are about 5 standard deviations apart.

In Figure 3.12 T_c measurements of the proximitized iridium samples with gold on top, as in Figure 3.5 are reported, showing that the two sets grA, red dots, and grB, black triangles, identify two T_c trends vs. the relative thickness of Ir on Au, which saturate at 130 mK and 180 mK, respectively. The right part of the plot shows the bare Ir film T_c. This means that the proximity effect generated by the gold film conforms to the T_c of the bare iridium film but does not appear to have an effect on the crystal structure, as shown in Figure 3.12 and following description.

Since it is known that the peak position and FWHM identify the crystallite

Sample	110	111	311	222	
97 (grA)	36,687	40,777		88,070	θ
T_c 130mK	0,356	0,376		0,873	β
99 (grB)	36,654	40,749		87,994	θ
T_c 180mK	0,346	0,322		0,835	β
106 (grA)	36,670	40,780		88,069	θ
T_c 130mK	0,592	0,509		1,274	β
107 (grA)	36,668	40,766		88,072	θ
T_c 130mK	0,528	0,447		1,075	β
108 (grA)	36,669	40,778	83,376	88,086	θ
T_c 130mK	0,377	0,380	0,602	0,963	β
111 (grB)	36,652	40,737	83,347	87,988	θ
T_c 180mK	0,330	0,322	0,886	0,858	β
112 (grB)	36,669	40,757		88,028	θ
T_c 180mK	0,338	0,304		0,790	β
113 (grA)	36,721	40,789		88,098	θ
T_c 130mK	0,478	0,411		0,956	β
114 (grB)	36,656	40,739		88,004	θ
T_c 180mK	0,335	0,329		0,840	β

Table 3.1: Gaussian fit of Ir and Ir/Au lines of examined films: position(maximum) θ and FWHM β are listed. Errors are on the last digit.

size, that is, the dimension of the oriented domain along the direction identified by the considered line. The crystallite size L for the main Ir (111) line was obtained through Scherrer's formula:

$$L = 0.9\frac{0.9\lambda}{\beta cos(\theta)}, \tag{3.1}$$

where $\lambda = 0.15046\ nm$ is the wavelength of Cu-Kα source, θ is the diffraction peak angle and β the FWHM of peak. It is found that the samples cluster around two average values given in Table 3.2. Those values are not completely consistent with literature for PLD depositions without substrate heating [61, 62], but appear more similar to those observed with a PLD deposition with substrate heated to 500 $°C$. Therefore, we assumed that non-uniform strain in

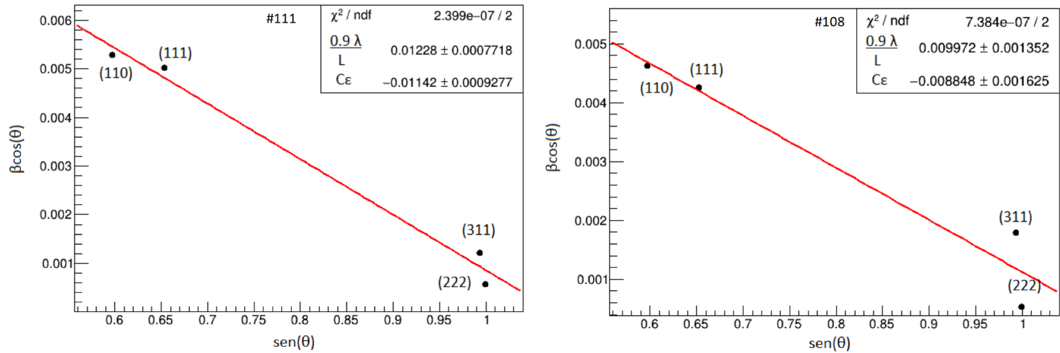

Figure 3.14: Williamson-Hall plot for the Ir/Au film sample #111 (Left) and film sample #108 (Right). L is the crystalline size and Cε the strain. From [56].

the Ir film structure can contribute to the lattice deformation. We performed an analysis according to Williamson-Hall model [63], which also takes strain into account, on samples #108 and #111, in which lines (311) are also visible. Figure 3.14 show the Williamson-Hall plots for the two samples examined. From these we were able to calculate the crystal size of the whole structure by finding values consistent with PLD deposition of Ir without substrate heating, as shown in Table 3.3, along with the average values of the two groups of samples, gr130 and gr180.

T_c	L (111) [nm]	σ(L) [nm]
grA 130 mK	25.0	1.5
grB 180 mK	32.9	0.7

Table 3.2: Average value L and related uncertainty σ(L) of the (111) crystal size for samples belonging to groups grA and grB, with critical temperatures of 130 and 180 mK. Values are calculated by means of the Scherrer formula from the data in Table 3.1.

T_c	L [nm]
#108 130 mK	10.6
#111 180 mK	13.9
grA 130 mK	9.1
grB 180 mK	12.7

Table 3.3: Crystalline size L from the Williamson-Hall model of the two samples considered and the average value of the two groups of samples at T_c of 130 and 180 mK, respectively.

To conclude, we observe evidence of two sample populations based on Ir films on Si (100) that cluster around two values of T_c, 130 and 180 mK, respectively. Structural analyses with XRD show a correlation between crystal size and T_c that are reproducible with different analyses, Scherrer and Williamson-Hall, where a larger grain size is related to a higher critical temperature. The absolute values depend on the model used, without or with strain, which suggests investigating lattice stress that should play a non-negligible role. We

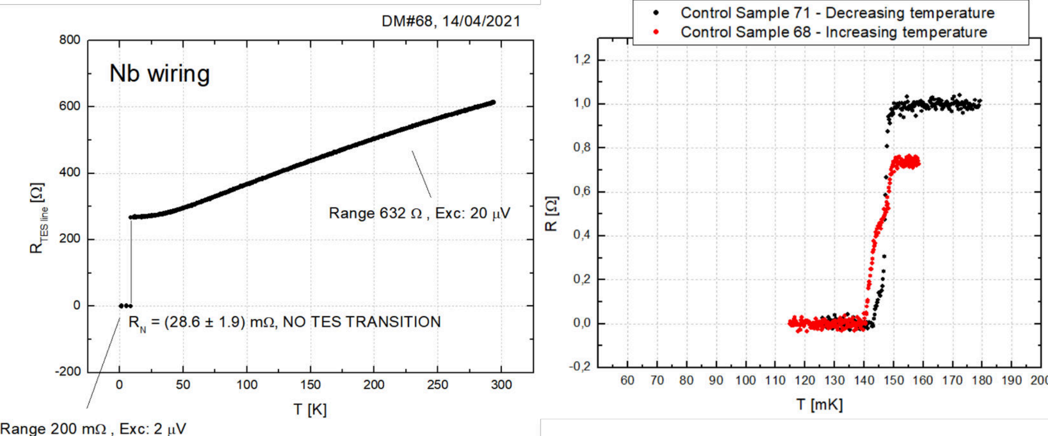

Figure 3.15: Left: Detector without the Ir superconductive transition. The Nb wiring become superconductive around 9 K but the sample resistance remain that of the TES net in the normal state down to 20 mK. Right: The red data show the superconductive transition of the same detector (#68) at the state of deposited film, thus before undergoing any process.

would therefore like to investigate this further with specific measurements on the effect of lattice stress. It should also be noted that the presence of Au in bilayer films does not seem to produce any effect on structure and appears sub-dominated and has the sole effect of decreasing T_c by proximity effect. With regard to the shaping of the superconducting transitions we didn't observe any difference in the lattice of samples with sharp and wide transitions so far. Thus, the T_c versus grain size and stress correlation seems to be related only to the superconductivity starting point as in titanium and not a suppression effect.

Oxidation

One found effect that suppressed the superconductivity in Ir films, due to processes subsequent the deposition, was oxidation, see Figure 3.15. We experienced this for Ir layers, after Oxygen plasma cleaning process but not for Ir/Au bilayers, see Figure 3.16.

To study the superficial chemical composition, possible contamination and the sample's morphology X-ray Photo-electron Spectroscopy (XPS) from Physical Electronics with an $Al-K\alpha$ monochromatic source (λ= 1486.6 eV), and Field Emission Scanning Electron Microscopy (FESEM) with a Focused Ion Beam (FIB) from CrossBeam Zeiss were respectively used. Electron spectroscopes are concerned with the study of electronic excitation of atoms, molecules and solid systems. Any experimental technique that causes a transition between two electronic states in a system can probe its electronic structure: to this is intimately linked to the chemical structure of the system (bonding, coordination, reactivity) and atomic geometry. The result of this analysis revealed that deep oxidation of iridium at ambient temperature, caused by O_2

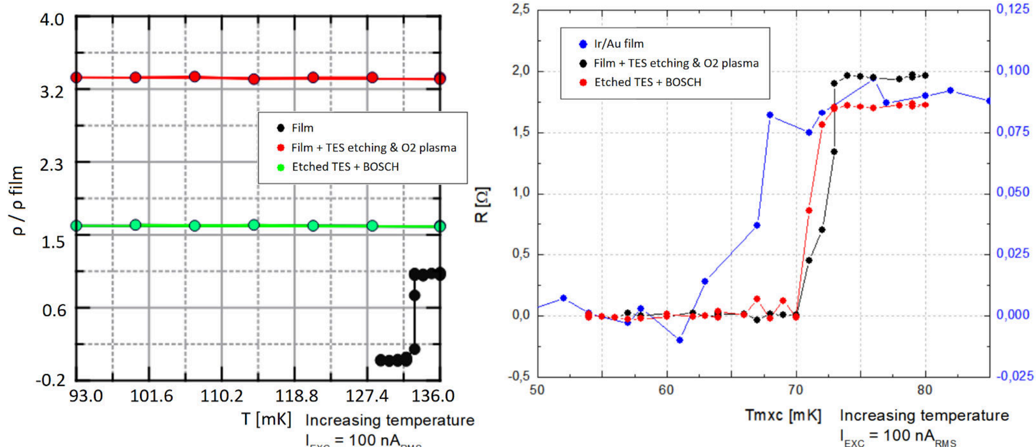

Figure 3.16: Left: Ir resistivity before and after processes. The black data are for Ir film before any process, red after deep oxygen plasma consequent to TES etching, where superconductivity is suppressed, and green after Bosch process, see section 3.7, where is experienced a relaxation towards film resistivity values. Right: Ir/Au bilayer resistance before and after processes. The blue data are for Ir/Au bilayer before any process, black after deep oxygen plasma consequent to TES etching and black after Bosch process. There's no change in the superconducting transition of the film, except for shaping effects from film to small defined geometries.

plasma and mediated by Ar etching, is possible. In particular, this is evident from the oxygen abundance increment within the superficial structure and the iridium and oxygen (IrO_2) compounds on the surface and along the edges of the excavation due etching as shown in Figure 3.17. A similar XPS study of the composition of iridium films can be found in [64].

The XPS analysis was essential to verify the superficial contamination of iridium. The iridium TESs in DMs have compounds contaminants both on the surface and on the excavated walls. Such contamination certainly adversely affects the transition of the devices. The contamination analysis, however, did not end with only the XPS measurement. In fact, to get information regarding the composition of the internal structures of the iridium deposition, the samples were analyzed by FESEM microscopy acquired in section view after FIB vertical cutting, see Figure 3.18. The images provided two fundamental observations:

1. the presence of the 10 nm iridium silicide layer at the film substrate interface,is confirmed (it is essential for good adhesion of the iridium film on Silicon the substrate),

2. the structure of the iridium film growth is columnar, possible causes for the oxygen intercalation also in the Iridium bulk.

Both phenomena are caused by the temperature during the film growth. The temperature mismatch between silicon and Ir plume during our PLD deposi-

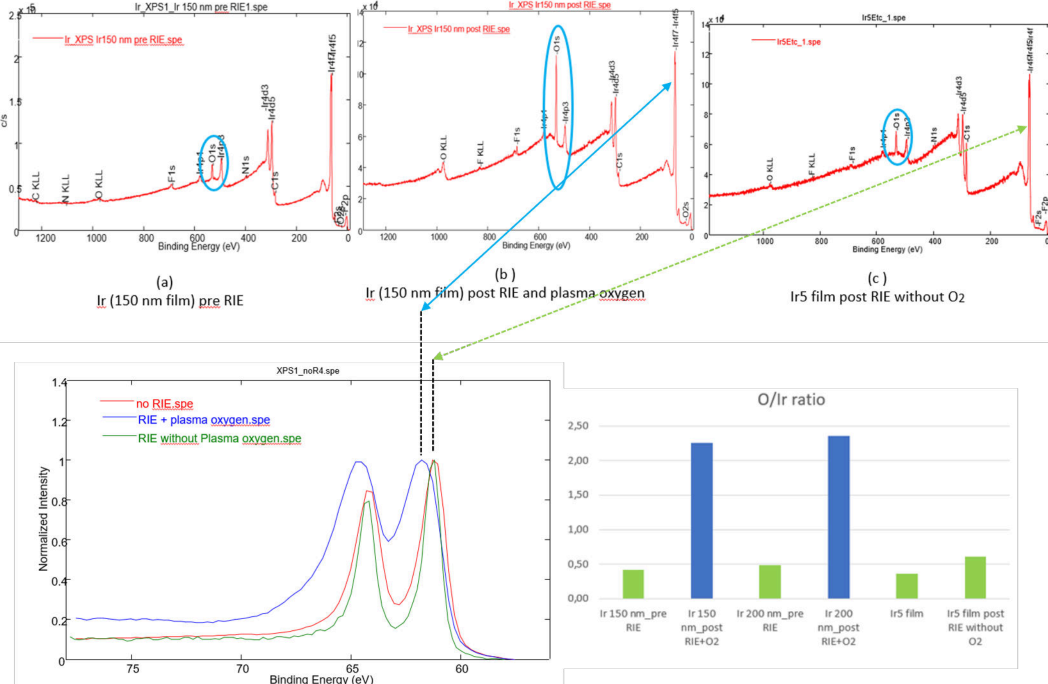

Figure 3.17: Top: XPS spectra acquired before any process (a), after O_2 plasma and etching at RIE (b) and after the new process without the Oxygen plasma. The peak related to oxygen is highlighted since it is the only peak that after the etching process (b) it is definitely increased in percentage compared to the case (a) and (c). Bottom: On the left the shift of the peak relative to iridium indicates an increase in the binding energy and thus emphasizes the formation of oxidation state. On the right the comparison between the oxygen amount in three sample before and after the process. The sample with the new process experience a negligible Oxygen increment respect the others.

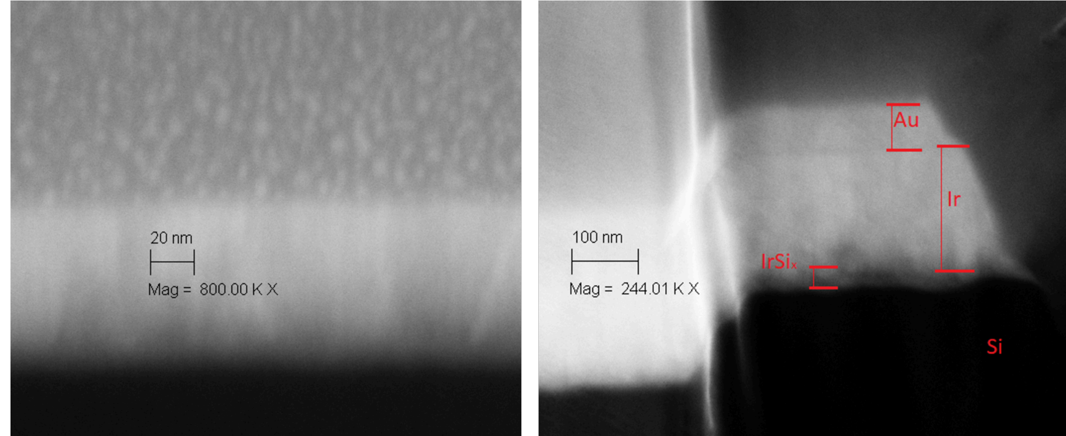

Figure 3.18: Images captured at FESEM of two Ir PLD grown films, sections are made with the in situ FIB. Left: particular of the columnar growth. Right: Ir/Au bilayer where are visible the iridium silicide interface, the iridium film and the gold one on top.

tion. Instead, while the iridium silicide at the interface is wanted to increase the film adhesion, the columnar growth can boost the iridium contamination. In fact, this type of microstructure consists of a network of low-density material surrounding a series of parallel cylindrical-shaped columns of higher density and take place when the deposited atoms have limited mobility. The presence of the columnar structure facilitates the propagation of external elements inside the structure itself. During etching by Bosch at RIE, in the various steps of the procedure, there is O_2 plasma present, so it is possible that oxygen atoms penetrate inside the iridium structure contaminating it. In conclusion, the study of contamination with XPS and FESEM provided the insight of iridium oxidation in films without the superconductive transition. To overcome this issue was reduced at minimum the use of Oxygen plasma during the the whole manufacturing process.

Fluorides contamination

Broadening of critical temperatures as in Figure 3.19 appeared to be correlated with another contamination occurred during RIE etchings, residual fluorides from Bosch processes. The RIE chamber must be carefully conditioned before any process and the radicals capture capabilities checked, in order to prevent possible cross-contamination between different processes. Fluorine gas chemical interact with Ir, as well with tungsten, and to prevent interactions that ruins the superconductivity etching with such gasses should be performed encapsulating the films to prevent interactions. After the oxidation problem overcome we continued to experience superconducting critical temperature broadening and an accurate inspection of the processes revealed some residual fluorine radicals inside the RIE chamber.

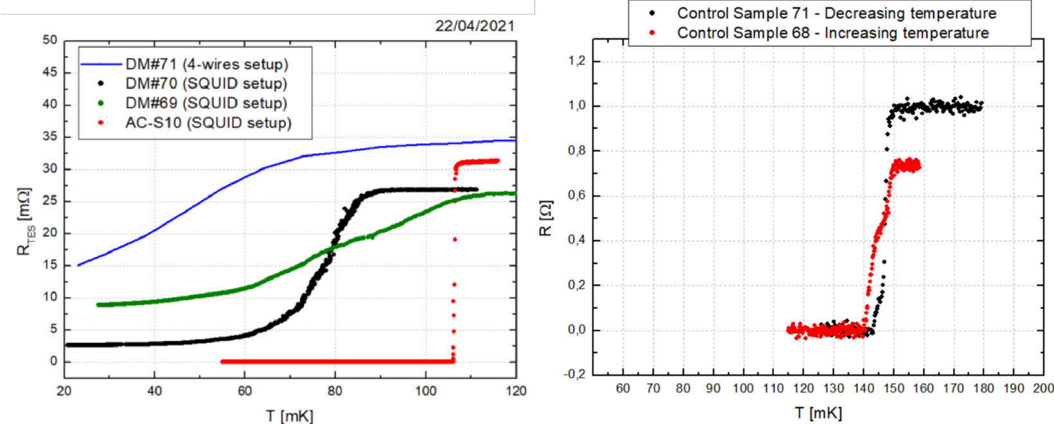

Figure 3.19: Left: Detectors distorted TES transitions. The Red data refers to ACS-10, the DM of section 5.2, while the other detectors show shifted and broadened transition toward low temperatures. Right: The black data show the superconductive transition of the detector #71 at the state of deposited film, thus before undergoing any process.

3.4 Pt Heaters

The next process in the production of the detector focuses on the fabrication of the platinum heaters, which are suitable to change the absorber working point and for calibration pulses as already pointed out in section5.2. In this step, the heaters fabrication is carried out by negative photo-lithography, so first the lithography is carried, the material deposited, the excess film removed by lift-off and the designed chosen obtained. The masks and the final result can be seen in Figure 3.20.

The deposition is carried out with the e-Beam and to improve the Pt adhesion to the silicon substrate we deposit a titanium layer. Although Ti great bonding capability are perfect to make adhesion layers they force to work at ultra high vacuum to prevent oxidation or with a gettering[3] pre-deposition and high rates. The two depositions occur in consequence, 15 nm of Ti and 80 nm of Pt.

3.5 Au thermalizing frame

After the fabrication of the heaters the thermalizing frame is deposited and its fabrication is made by negative photo-lithography with the mask in Figure 3.21.

The thickness of such a layer is about 200 nm. Again, a 20 nm adhesion layer of titanium is needed to stick the film to the silicon substrate, as the ad-

[3]residual gasses are removed by bonding them with a getter material, as titanium or niobium. A getter material is characterized by its reactivity, thus when a gas molecules hit the getter material, they combine. In this way, exploiting those characteristics is possible to boost or maintain vacuum level.

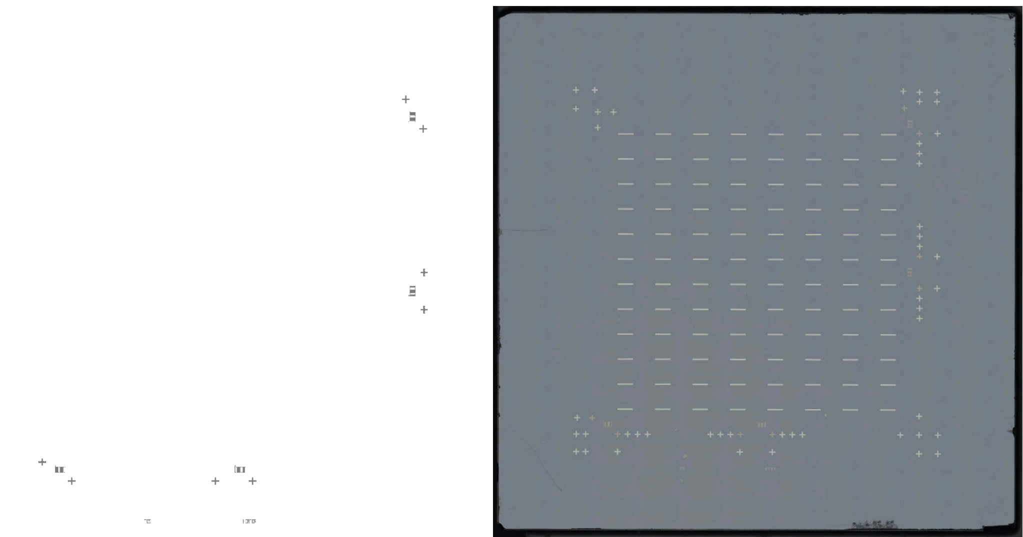

Figure 3.20: Left: CAD image of the photo-lithography mask of the Heaters. Right: Microscope image of the chip after fabrication of the Heaters.

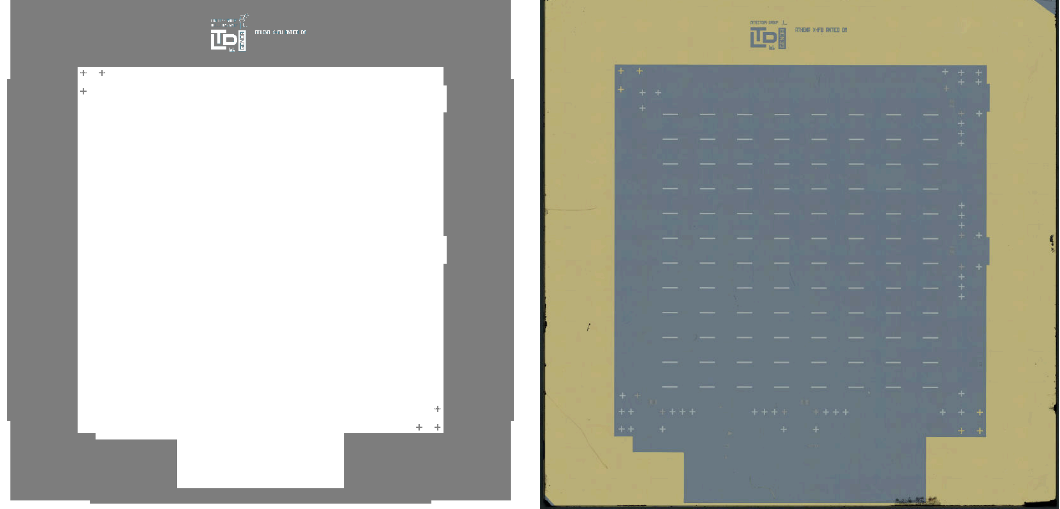

Figure 3.21: Left: CAD image of the mask for the thermalizing frame. Right: Microscope image of the chip after fabrication of the outer gold frame.

hesion of gold on silicon is extremely weak, while iridium represent an optimal growing layer for gold.

3.6 Nb superimposed striplines

After depositing the outer frame, is time to create the electrical connections for TESs and heaters. This process is divided into three parts, as the wiring is made with overlapping niobium striplines, evaporated through Radio Frequency (RF) sputtering. Thus, the lower and the upper Nb layers separated by the an insulation layer are grown. The tree step are made with negative photo-lithography and their parameters must take into account that layers will be superimposed and the first one must contact heaters and TESs. Thus, thicknesses must be scaled up to optimize step coverage as well as film walls steepness. RF sputtering consists of cathodic sputtering, a process by which there is an emission of atoms, ions, or molecular fragments from a target due to bombardment by beams of energetic particles, typically argon. The Ar is ionized and therefore an Ar+ population is formed. The target (niobium) is held at a negative potential relative to the plasma: in this way, argon ions will be accelerated toward the target. The momentum transferred by the Ar ions is such that it sputter the surface of the target. Therefore, placing the sample above the target will ensure a deposition of the sputtered material. In Figure 3.22 there is a schematic of the deposition technique operation. The possible accumulation of charges (the Ar ions) on the target surface, compromise the regular deposition and uniformity of the deposited film. For this reason The target is not held at a fix potential, but oscillating at radio frequencies. In this way the detachment of pollutant ions from the target surface is ensured. Niobium needs to be deposited in a highly controlled atmosphere so as not to be polluted by residual gases such as N_2 and O_2. Thus, the atmosphere should be formed ideally only by pure Ar. Therefore, one must work in high vacuum environment 10^{-9} $mbar$, and with Argon 5.0 (99.999% pure) flux to reach a pressures of about 10^{-2} $mbar$.

To be sure that the working conditions are suitable for the production of the Nb wiring, a test film to check the sample superconducting transition inside liquid helium. If the test film fail the deposition is repeated to reach the optimal working conditions, exploiting the niobium gettering properties. The process of making the electrical connections is highly problematic for the success of the detector. Niobium must to adhere well and have no imperfections, as it is very easy to create holes in the current passages that can lead to an open circuit. On the other hand breakage in the insulating layer could cause shortcuts between the superimposed wiring.

3.6.1 First layer of electrical connections

During this step, a 300 nm layer of niobium is deposited after lithography and the excess deposition is removed through lift-off. The first wiring thickness

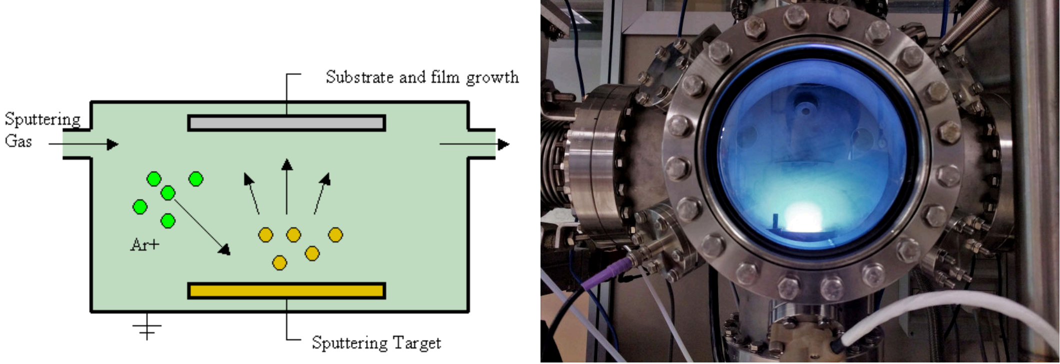

Figure 3.22: Left: Schematic of the operation of sputtering deposition. From Mattopia, SputteringProcess, CC BY-SA 3.0. Right: picture of the niobium RF sputtering deposition.

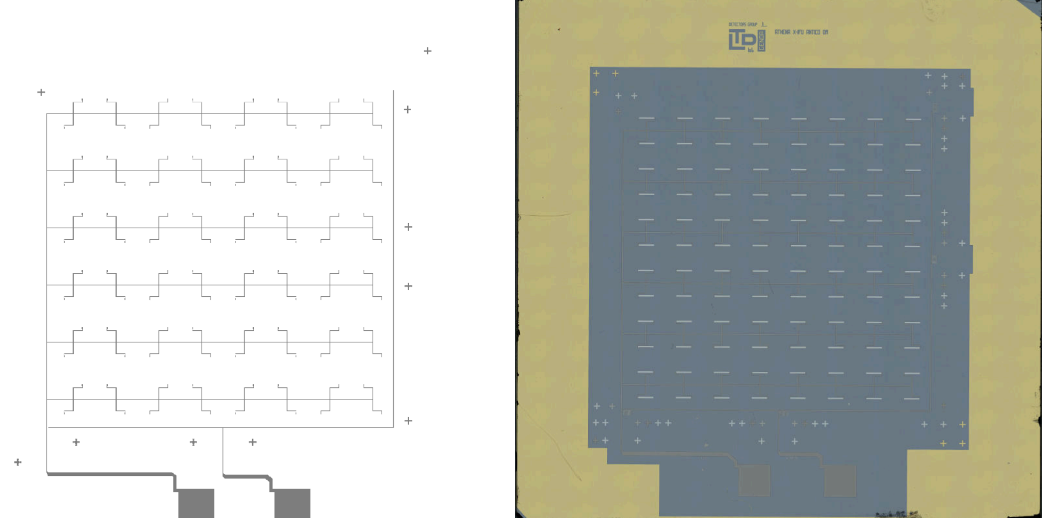

Figure 3.23: Left: CAD image of the mask for the base Nb wiring layer. Right: Microscopic image of the chip after fabrication of the first wiring layer.

have been engineered to completely cover up TESs and heaters films, but remaining a thin layer as following wiring thicknesses depends on the first one to create an optimal step coverage and stress on the films are proportional to the fourth power of the thickness. This issue will be better explained in section 3.6.4.

3.6.2 SiO insulating layer

For the insulating layer after some tests with silicon dioxide it was decided to switch to silicon monoxide. SiO_x compounds were found more robust and of greater adhesion than SiO_2. On the other hand, the deposition process has some critical issues, compared with dioxide evaporation, is to maintain at a better vacuum to limit the chemical reaction with oxygen and the formation of

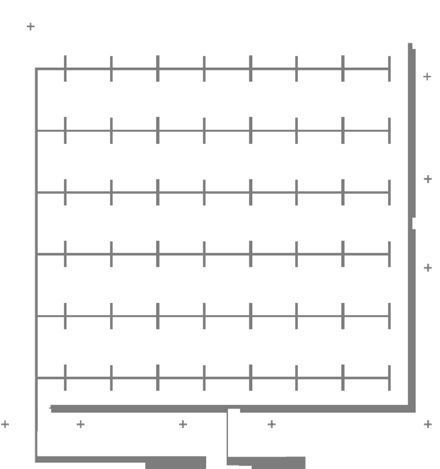

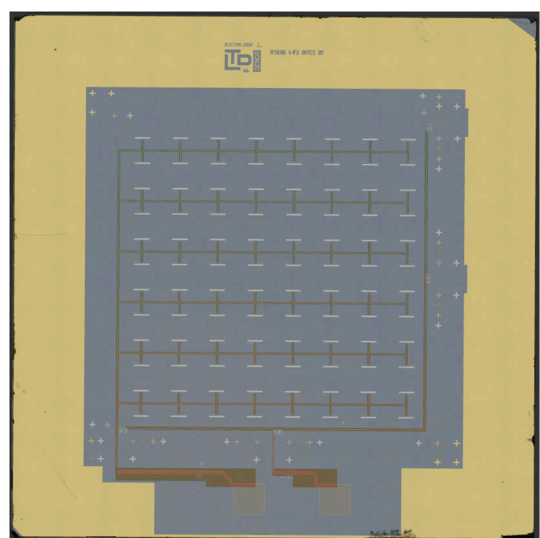

Figure 3.24: Left: CAD image of the mask for the SiO_x insulating layer. Right: Optical microscope image of the chip after fabrication of the SiO_x insulating layer.

Silicon Dioxide from the monoxide. Moreover, SiO powder sublimates then its evaporation must be carried on taking care of not placing samples in powder sight, but exploiting crucibles with baffles. To carry out the deposition, a thermal evaporation system with electrodes is used. The operation is very simple; a potential difference is applied on the two electrodes connected by a resistive crucible that will heat up causing the material evaporation. During the process, the electrodes are kept cold thanks to a water-cooling system, and the thickness deposited monitored with an oscillating quartz microbalance. The thickness of such a layer should be around 500 nm, about twice as thick as the forward connections: in this way the insulation of the lower connections with correct step coverage is ensured. After deposition, lift-off without extensive ultrasonic excitation is performed to ensure the removal of the excess material without compromising the insulation layer.

3.6.3 Second layer of electrical connections

The second line of electrical connections is carried out with exactly with the same procedure of the first one. To be sure of the insulation between the two layers of connections, the top one has smaller size, in this way it will be ensured that this layer is present only above the insulation layer. In addition, the lower line width will maintain approximately the same resistance between forward and return connections line. Since, a greater thickness will be required for the latter deposition: 700 nm. The lithographic mask of such connections and the wiring process result can be seen in Figure 3.25.

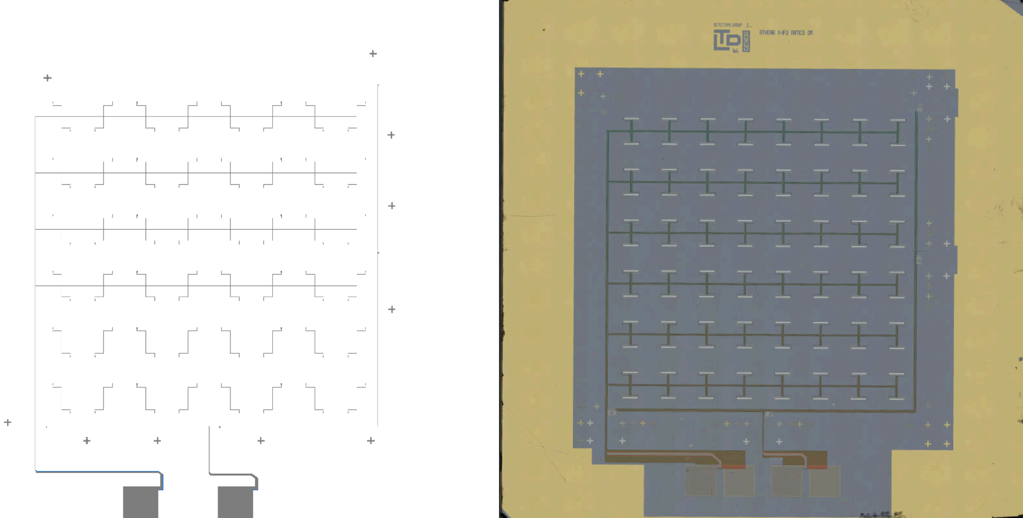

Figure 3.25: Left: CAD image of the mask for the second Nb wiring layer. Right: Optical microscope image of the chip after fabrication of the last wiring layer.

3.6.4 The current dependant parasitic resistance

During the characterization of the Demonstration Model of the detector (ACS-10), for the integration and the demonstration of the anticoincidence working principle together with the NASA DM detector (TES-array DM), was observed a current dependant parasitic resistance R_P in series at the TES network on board the detector. In Figure 3.26 can be seen the measurements that showed R_P and a FESEM image showing a breakage in the upper Nb layer that caused of the effect. The point contact inside niobium led to a resistance in series to the TES network that is superconductive for currents lower than 11 μA. The J_c calculated respect to the wiring geometry was of 0.7 $\frac{A}{cm^2}$, while at 100 mK the J_c of ACS-10 TES is 4.2 $\frac{A}{cm^2}$ and the one of our niobium films is higher than 3.9×10^5 $\frac{A}{cm^2}$ at 4.2 K.

After several analysis of the wiring production steps, investigations and tests we understood that the films breakage was due to the films wall steepness and thickness as a rapid step coverage is less mechanically stable and stress on the films are proportional to the fourth power of the thickness. Thus, all wiring layer thicknesses were reduced to the minimum optimal step coverage values and to reduce the wall film angle the first negative lithography parameters have been tuned to reach a 3 μm under-etching on the resist film, with overdevelop process, to deposit Nb under the resist. In Figure 3.26 are shown the new wiring profile without breakage in films and a comparison between the TES current and tension of ACS-10 with one of the DM#70 produced with the new wiring procedure. All the tests carried out with new wiring procedure samples highlighted the absence of the current dependant parasitic resistance.

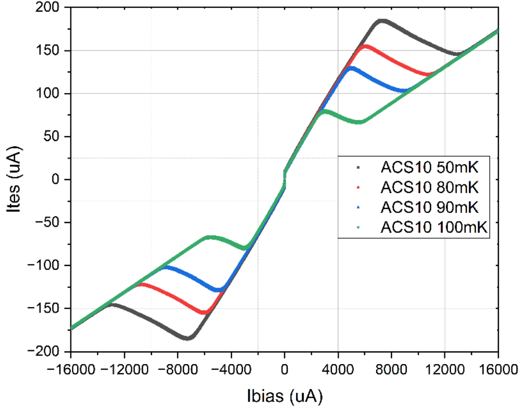

(a) ACS-10 current versus bias current.

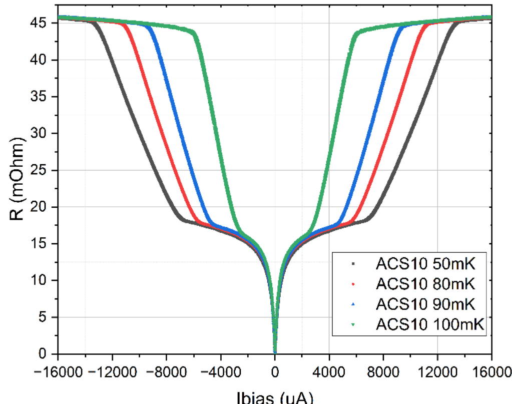

(b) ACS-10 resistance vs bias current.

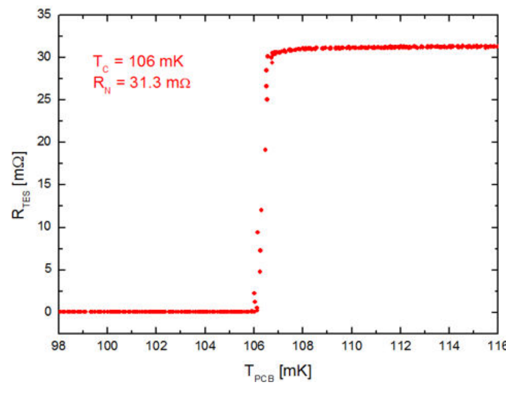

(c) Resistance vs temperature of ACS-10 with a bias current of 1 μA.

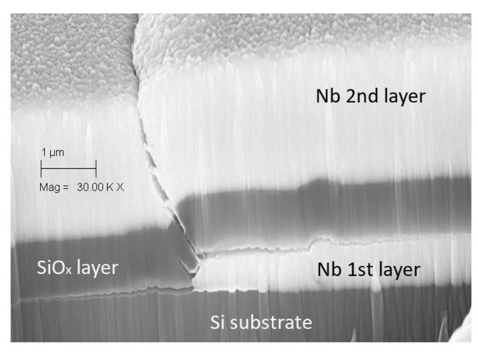

(d) FESEM image of the section of ACS-10 wiring, where the upper wiring layer have to step cover the lower Nb film.

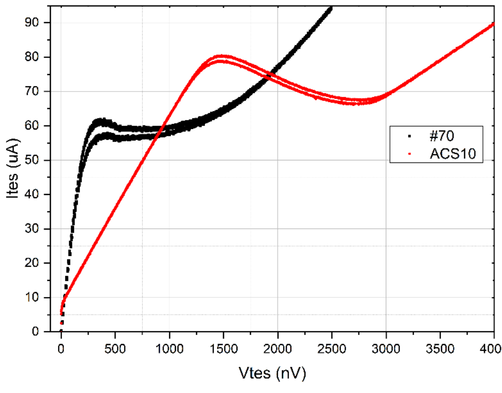

(e) Comparison between the current circulating inside the TES network of ACS-10 and DM#70 versus bias tension.

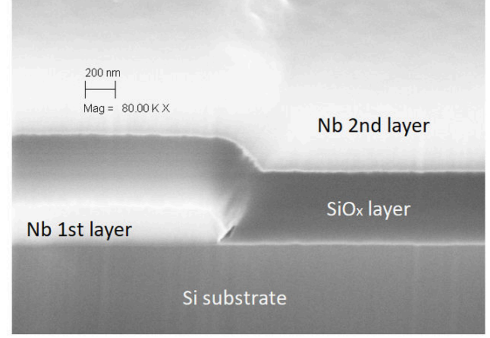

(f) FESEM image of the section of DM#70 wiring, where the upper wiring layer have to step cover the lower Nb film.

Figure 3.26: (a): An unattended slope is observed, meaning the presence of a current dependant resistance R_P in series to TESs. (b): Until the current inside the detector is lower than 11 μA TES and wiring are superconductive, then is measured a 17.9 $m\Omega$ R_P until the TESs critical current is reached. (c): The normal resistance of TESs R_N is 31.3 $m\Omega$ compatible with (b), where the total resistance was due to R_N plus R_P. (d): There is a breakage of the insulation layer that lead to point contact in Nb with a consequent low critical current and then the current dependant series resistance behaviour. (e): The DM#70 did not show the series current dependant resistance as AC-S10. (f): There is no breakage in wiring films, consequently no point contacts and R_P.

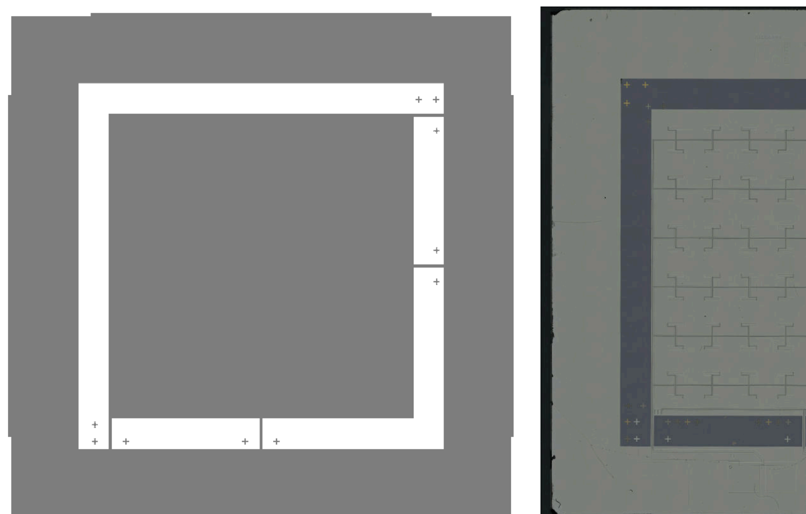

Figure 3.27: Left: CAD image of the mask for the hard-mask. Right: Optical microscope image of the chip after the hard-mask deposition.

3.7 Absorber and silicon bridges Etching

The final step, to conclude the detector fabrication and ensure the proper thermal connection between the absorber active area and the thermalizing frame, consists to suspend the absorber with respect to the outer frame by deep etching at the RIE. This will leave the absorber suspended from the silicon chip and connected to the frame through four silicon bridges that form the weak thermal bond, see Section 2.3. To proceed with the process the detector must be covered by an hard-mask, except for the trench to be etched. The hard-mask is needed as a resist soft mask cannot guarantee the desired sharpness of the walls and last for the whole etching of $500\mu m$ at 300 K with our machine. To be able of using a soft mask we upgraded our RIE and the etching process is under study, changing the working temperature and adding a breakthrough step between deposition and etching steps to reduce the resist etching time. The material chosen for the hard-mask is aluminum as it is very easy to be deposited and removed with a wet etching in $NaOH$. On the other hand, because aluminum tend to create alloys with gold, the Al layer is separated with a 5 nm SiO_x layer from the detector films. The deposition undergoes after a negative lithography according to the mask in Figure 3.27.

Both depositions are made by thermal evaporation (as for the insulation layer). Thanks to lift-off, the bi-layer will be removed from the areas to be etched. The use of a sonic bath to totally remove the films during the lift-off is not possible as the 5 nm SiO_x layer is too weak and to prevent holes in the hard mask, therefore the sample is only flushed with solvents. The deep-etch through the whole silicon chip exploits the Bosch process, an etching technique based on two continuously repeated steps: etching and passivisation of the silicon. During the etching step a SF_6 plasma is used attack silicon, while to ensure high selectivity and get a vertical etching it is spaced out by a

passivisation step that through C_4F_8 plasma polymerize the silicon creating a passivisation layer. This layer covers both the walls of the excavation and the bottom and the consequent etch step directed vertically through Inductively Coupled SF_6 Plasma (ICP), will most affect the molecules of the passivisation layer on the bottom, sputtering it completely and exposing the bottom of the excavation. On the other hand, walls will still be protected by the passivisation layer and will not be exposed to the plasma, minimizing the lateral etching of the walls achieving the most vertical and precise excavation possible. These two steps are repeated multiple times until the silicon chip has been etched through the wafer, the principle of operation is schematized in Figure 3.28.

Bosch recipe must be tuned for each machine and actual process. In the case of the DM silicon deep-etch some critical parameters are the depth of the etching (500 nm) with the end point at the etching silicon chip pass-through, and the 90°smooth wall. To overcome the notching that is experienced once the etching reach a material with a lower etch rate, e.g. a sapphire carrier or silicon oxide, see Figure 3.28F, the detector was mounted over a silicon chip, to have no interface effect at the end of the etching. On the other hand the wall angle and texture was optimized after several iterations adding a O_2 gas flux during etching to increase the wall preservation due to the passivisation layer and dividing the cycles into multiple steps to reduce the heating inside the chamber reaching a satisfactory result. This result was then overcome during the structural model manufacturing development, section 4.1 tuning the passivisation gas flow during the whole process.

At this point the detector is finished, after Bosch it is cleaned with $NaOH$ to remove Aluminum and with solvents. The final aspect together with the wall texture can be seen in Figure 3.29.

The studies that I've taken on the fabrication process allowed me to tune and change the production chain with the establishment of a manufacturing report that must be followed making the CryoAC and can be found in Appendix A.

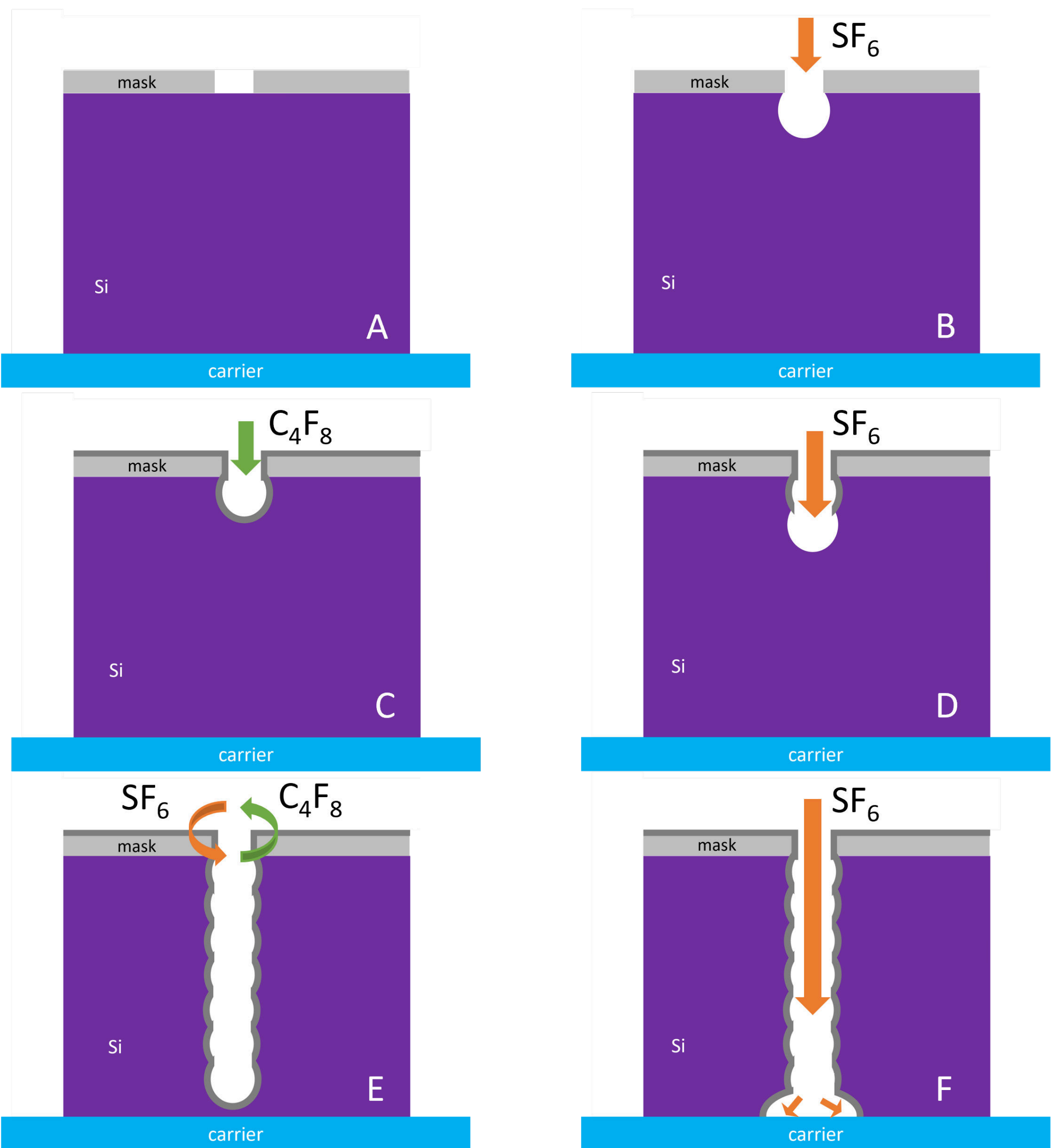

Figure 3.28: Schematic explanation of the Bosch etching process. A: Sample with the mask ready for the Bosch. B: Etching step with SF_6. C: Deposition of a passivisation layer with C_4F_8 scheme. D: The subsequent etching step etch the bottom with a higher rate than the walls starting the straight etching. E: Etching and Deposition or passivisation steps are cycled to etch the sample. F: At the end point or with an interface between silicon and silicon oxide or sapphire carrier the etching step starts to erode walls rather than the oxide or carrier.

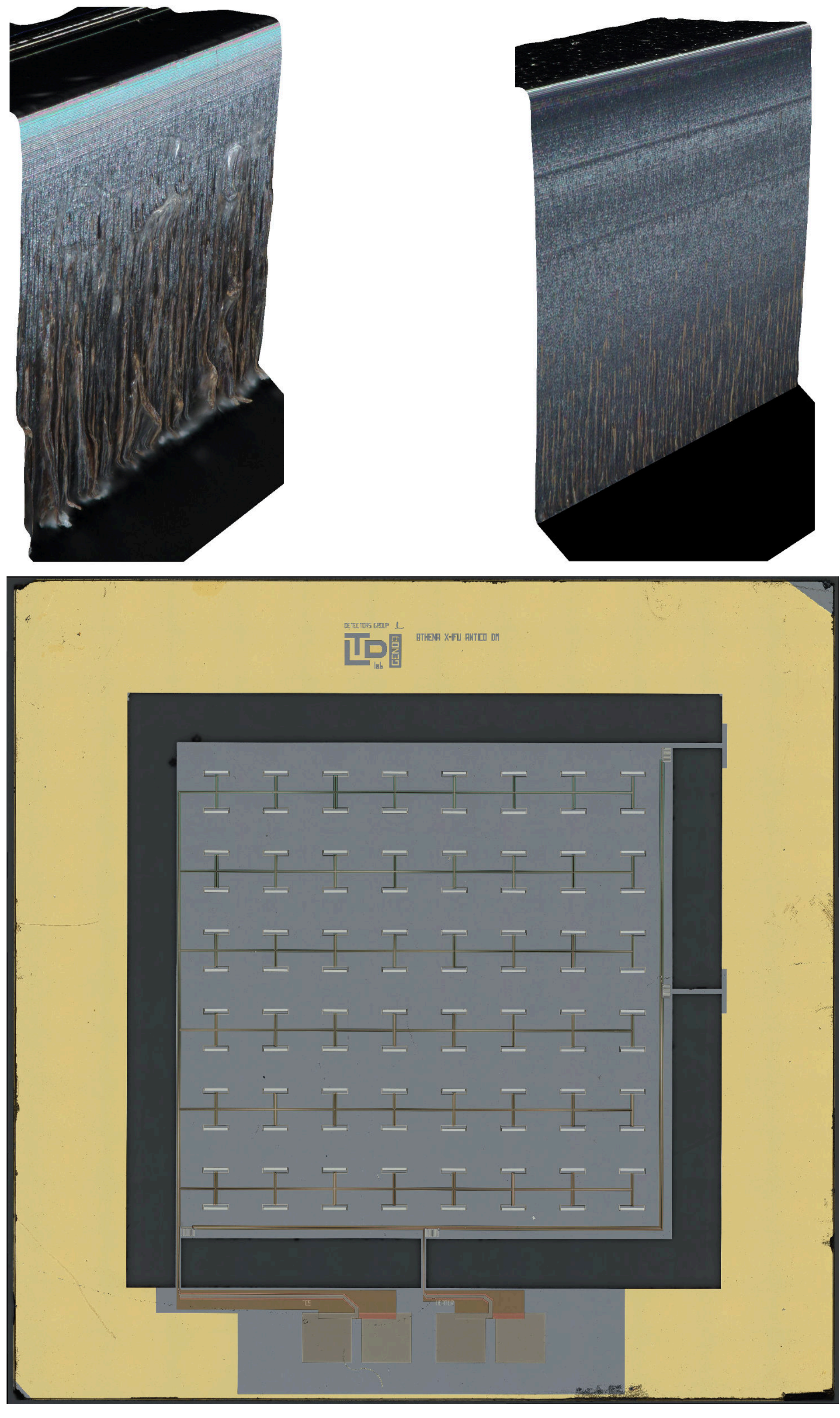

Figure 3.29: Top - left): Wall texture of the Bosch etching process there is no notching, anyway the texture is degrading with depth. Top - right): Improvement after implementing the studies of section 4.1. Down): Final aspect of the CryoAC DM.

Chapter 4

The CryoAC structural model

In the area of technology development of space components, there is a special focus on strength testing (structural, electrical and functional) of components. The failure of a component would inevitably lead to mission failure. In this sense, the space environment places particular stress on the various components due to the large temperature ranges and the background of ionizing particles. However, from a mechanical point of view, the most critical phase for all the components of a space system is the stress caused by the departure of the spacecraft on which such a system is based. In fact, the strong acceleration and vibrations transmitted to the telescope can break or irreparably damage the components. To avoid such an eventuality, it is necessary to verify that each component is able to withstand the stresses and vibrations induced by the launch. The purpose of the structural model is to verify this resistance and to identify any critical issues before proceeding with the development of engineering and flight models. Thus, in order to proceed with the development of the anticoincidence detector, it is necessary to test and verify the structural operation of the detector. In order to understand the detector's response to mechanical stress, the structural model chip will represent the geometric structure designed for the flight model. Thus, it has a larger hexagonal shape of about 4 cm^2 absorber active area.
At this stage, it was planned to divide the development by going through the realization of three sub-models: SM0, SM1 and SM2.

- SM0: Silicon-only model to simulate chip responses.
- SM1: SM0 model with the addition of the deposited electrical connections housed in the final bracket for mounting on the focal plane assembly.
- SM2: SM1 model with the addition of the TESs in a limited area of the detector and the SQUIDs on the mounting board.

During my PhD, I've developed the SM0, the tests necessary to validate its geometry and the production passages to move towards wafer-based fabrication to develop later on the SM1 and SM2, which are under study because of the mission redefinition.

4.1 The SM0 manufacturing process

Given the simplicity of the model in question, the realization process consists of few steps. The models are fabricated from silicon hexagonal chips and their preparation is the same of section 3.2 except for the hexagonal geometry, with apothem $a = 1.576\ cm$ and side $l = 1.819\ cm$. The only process such a chip undergoes is the excavation of the silicon to suspend the inner detector. To make the two different geometries, the process is the same and it's identical, in concept, to the DM one described in 3.7, but because of the larger area, and the high aspect ratio in the segmented geometries, some adjustments to the recipe are made. Therefore, we proceed with negative photo-lithography according to the masks shown in Figure 4.1. Note the differences in order to have a constant trench width to be etched in each point of the chip. In the 4-Pixel configuration, right part of Figure 4.1, the central part present a 25 μm trench; while the trench that delimit the absorber and the external rim, where the bridges are, is 1 mm wide as the DM and the 1-Pixel, visible in the left part of Figure 4.1. Thus, to have a constant etching aspect ratio the mask of the 4-Pixel have been studied to have only 25 μm trenches. So, after a

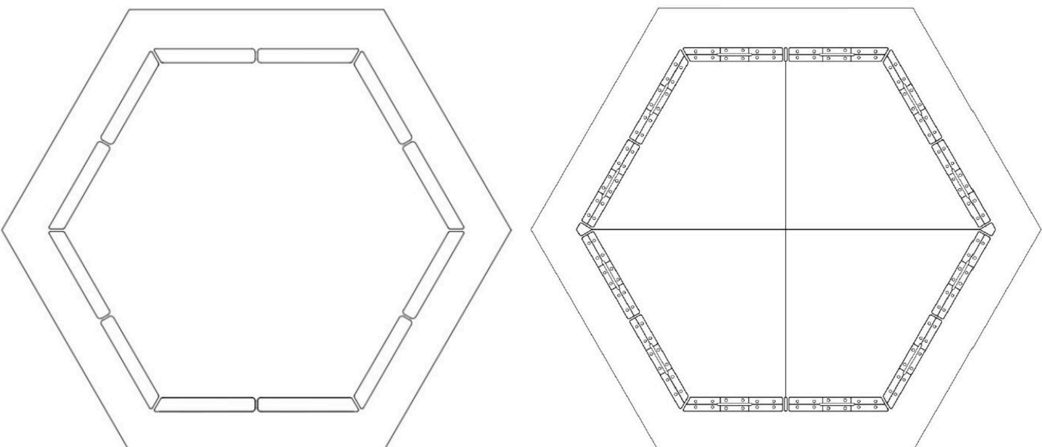

Figure 4.1: Left: Lithographic mask for negative photo-lithography of the SM0 monolithic. Right: Lithographic mask for the negative photo-lithography of segmented SM0.

negative photo-lithography of the parts to be etched, a hard mask deposition is performed: 10 nm titanium (as sticking layer) and 500 nm of aluminum. As the lift-off proceeds, the hard mask remains only in the places where you do not want the Bosch process to excavate the silicon. At this point, it is possible to mount the sample inside the RIE and proceed with the Bosch process, see Section 3.7. Because of the larger area to be excavated, the excavation time is about twice as long as for DM excavation. Initially, monolithic samples were produced by replicating the DM recipe for a larger number of Bosch cycles, because the total amount of silicon to be excavated was greater due to the larger area. Anyway, due to the non optimal features of the walls at the

bottom already described, a work around was implemented by etching half of the chip thickness on one side, and then repeating the process, and the hard mask deposition, on the other side. Later, this problem was overcome through studies of the segmented geometry; the same recipe was replicated, also on the DM, allowing $500\mu m$ deep etching on one side with uniform features across the whole chip. The production of the segmented geometry was a challenge. The recipe implemented for the monolithic did not produce satisfactory results even with the two-sided etching. Furthermore, the aligning of the two side was very difficult. After some attempt and literature studies [65], I realized that the problem of wall passivisation was improved by adding Oxygen during the etching process, but the conditions changes with the etching depth. Therefore, I developed a multi step recipe with an incremental flow of C_4F_8 gas with the etching depth to enhance the passivisation. Etching results of the original one-side etching, of the two-sided and of the one-side with an incremental flow of C_4F_8 gas are shown in Figure 4.2. At the end of the Bosch process the wall structure is analyzed with a 40° tilted optical microscope and, if the results are satisfying, the aluminum is removed by immersing the excavated sample in a basic solution. The final result of such excavation is shown in Figure 4.3.

After the fabrication, the structural tests have to be carried out: to reproduce the conditions (and therefore the vibrations) of the launch, one has to respect the so-called vibration mask provided by the launcher, which will be an Ariane 6[1]) and an experimental setup capable of reproducing this mask in terms of frequency and amplitude of vibration. Therefore, the tests carried out will be crucial in order to determine the best geometry of the structural model and to be able to proceed with the technological development of the detector. It was decided to carry out the vibration tests at a specialized company: BPS s.r.l. in Pero (Milano, Italy). This company has an electrodynamic shaker capable of reproducing the vibration mask provided by ESA. The data acquisition is carried out by means of a Doppler effect laser, which measures the frequency shift of the beam reflected by the sample excited by an electrodynamic shaker.

4.2 Sample preparation

In order to fix the samples to the shaker and to allow the laser to acquire the reflected light from the sample, we will have to undergo some preparation work before they can be tested. It was necessary to study the optical diffusivity of the sample and the mechanical arrangement that would allow simulation verification to be made.

[1]Ariane 6 is a launch system under development by the Ariane Group under the authority of the ESA. It will have a non-reusable design (different from SpaceX's launchers) but a modular type that will allow to reduce the operating costs.

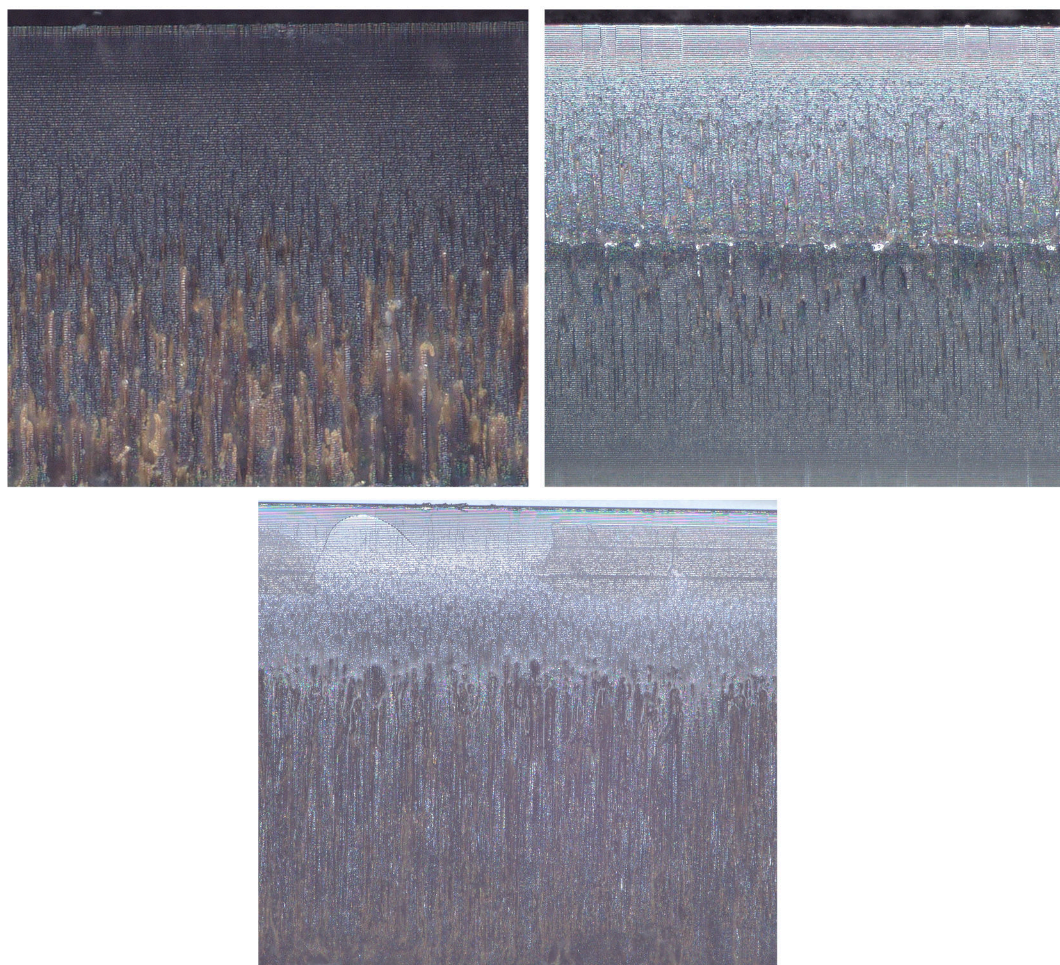

Figure 4.2: Top-Left: Bosch single sided etching process with $SF_6 + O_2$ as etch gas and C_4F_8 as passivisation gas. Bottom shows the side wall degradation due to SF_6 radicals that produce needle like structures (scars). Top-Right: Two Two sided etching of a 1-Pixel sample. The recipe is the same as the etching of the sample in the left image, but the process is done in two steps: firstly on one side and then on the other side of the chip, to prevent sidewall degradation with depth. Bottom: Bosch single sided etching process, but the flow of C_4F_8 passivisation gas is incremented during the Bosch cycles to increase the effectiveness of passivisation and prevent damages from SF_6 radicals. The sidewall texture is visibly smoother, the angle is closer to 90° and there are no notching. This recipe was then also used for new DM-like detectors.

4.2.1 The optical diffusivity of the samples

Due to the small size and low weight ($3\ g$) of the sample, it was not possible to mount an accelerometer to record the displacements of the sample due to vibrations: the size and weight of the accelerometer would have been much larger than the sample under test. For this reason, it was decided to use a Doppler shift technique, where a laser beam falls on the surface of the sample

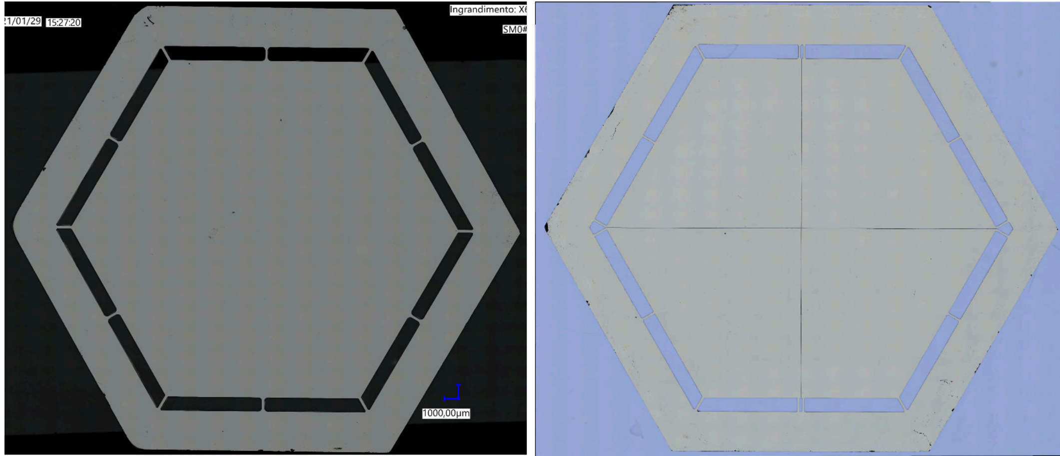

Figure 4.3: Left: Microscope image of the monolithic SM0. In that image you can see the outer frame and the suspended inner hexagonal detector. Right: Microscope image of the segmented SM0. In this case it is slightly visible the separation of the 4 suspended detectors, through a cross-shaped trench 25 μm thick.

and subsequently the reflected light is revealed. In this way, displacement, velocity and acceleration of the sample, and footings can be reconstructed by analyzing the frequency shift caused by the velocity of sample. In principle, the operation is quite simple, but due to the small area of the vibrometer (a few cm^2) and the polished silicon negligible diffusivity, loss of the reflected beam, due to overall displacement of the sample, is very likely. To overcome the problem of maintaining optical alignment during sample movements, it was necessary to devise a solution to make the surface of the samples as diffusive as possible, without altering their structural functions and avoiding distorting the measurement. For this reason, a diffusive coating was thought to ensure a greater granularity of the surface and therefore hopefully a better diffusivity. Different diffusive spray coating were considered. They were deposited on polished single-crystalline silicon samples, and the diffusivity was studied at various angles.

With the help of an optical bench, a simple setup was constructed by making the incident laser light perpendicular to sample surface. Then, the scattered radiation was detected for various angles relative to the incident normal angle. The laser used is a $HeNe$ at 543 nm (the same wavelength of the Doppler vibrometer), and to record the scattered power was used a NewPort 2930C power meter. The setup is shown in Figure 4.4.

Due to fluctuations in the power emitted by the laser it was not possible to make absolute power measurements of scattered light. Thus, the ratio of scattered power at a certain angle to incident power on the sample was acquired. At this stage, it was only a coarsely comparison of which spray had greater scattering, and therefore one was not interested in the absolute value of scattered power. Thus, while not measuring the absolute value, the data were

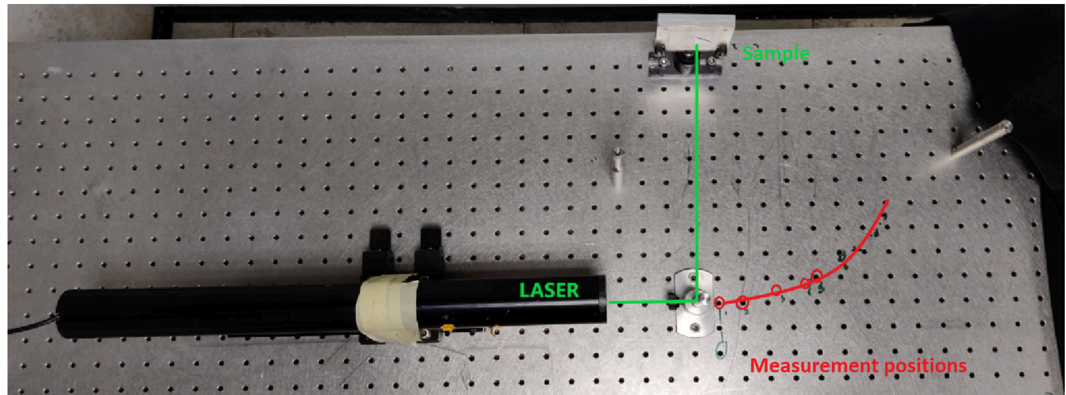

Figure 4.4: Setup of measurements by sample coating. The two distances at which measurements were taken are highlighted in red: data from the more distant ones were not found to be reliable due to the noise recorded.

fitted with a cosine function of the type $f(\theta) = a \cdot cos(b \cdot \theta)$. Measurements were made at a distance of 25 cm from the sample, and at small angles (range of 3 to 45 °). The results are shown in Figure 4.5.

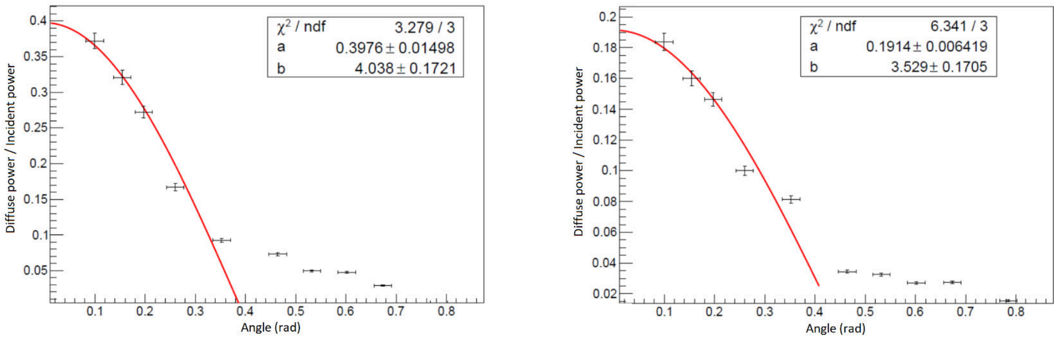

Figure 4.5: Left: Diffusivity of the Rotrivel U powder spray. Right: Diffusivity of another gypsum powder spray. The fit is performed with $f(\theta) = a \cdot cos(b \cdot \theta)$ and a larger a parameter results in higher scattering amplitude. At angles higher than 20° data are not reproducible because of background and noise. Anyway the Rotrivel U showed good performances respect to all the other available and sample compatible coatings.

The diffusive paint chosen was the Rotrivel U white, a rapidly evaporating solvent suspension powder presenting: the largest scattering amplitude, a good feather uniformity, and a zero impact on surface and bulk mechanical properties.

4.2.2 Bonding the samples to the interface flange

The electrodynamic shaker will replicate the vibration mask provided to us by SRON. The shaker interface is an oscillating plate made of a large magnesium flange to which sample must be mounted. To ensure that the vibrations are

rigidly transferred to the sample, a suitable interface flange must be made. According to the design of X-IFU, the anticoincidence detector will be anchored to the bracket structure through a 3-point structure. We chose to reproduce these 3 points as infinitely rigid constraints to study the deformations of the detector alone. Therefore, an interface aluminum alloy flange was prepared with 3 cylinders, with diameter of 2 mm, perfectly embedded in the flange itself. In this configuration, only the mechanical responses of the silicon chip were studied, as this was the goal for SM0. The next tests will cover the bracket, PCB, wire bonding, and SQuIDs. Three circular area of the detector's rim, each 2 mm in diameter, are prepared for gluing with the cylinders. This should perfectly anchor the sample to the cylinders. For this purpose, STYCAST 2850 FT epoxy glue was used, depositing about 2 mm^3 on the top end of each cylinder. After deposition of the glue, we proceeded with sample placement. This step was particularly challenging for two reasons: the possibility of breaking the sample and the care in placing it in the correct position. To be sure of the correct positioning of the sample, we used a centering mechanism using vacuum retaining 3D printed plastic flange, that can be seen in Figure 4.6. Covering the specimen and letting the glue harden at room temperature for 24 hours ensures optimal bonding. After the glue had hardened, the diffusive spray was deposited to proceed with the measurements. Some samples were initially mounted following a different curing temperature at 393 K for 30 minutes instead of curing at room temperature for 24 hours.

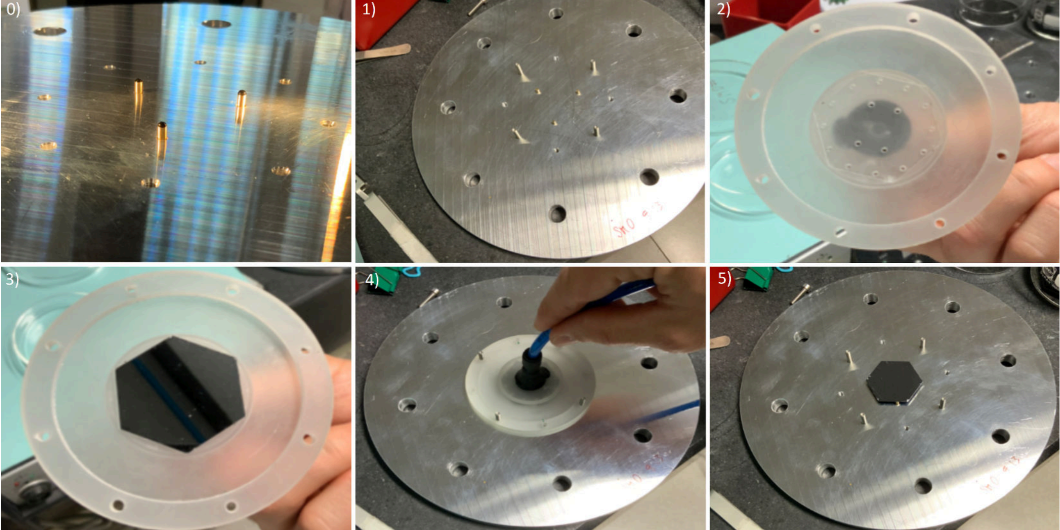

Figure 4.6: 0) Picture of the interface flange, where the 3 bonding cylinders are visible. Steps of placing a test specimen. 1) Flange ready with 4 screws for centering. 2) 3D printed mechanism with hexagonal housing and vacuum holes. 3) Test specimen held by the mechanism. 4) Centering with turning off the vacuum to place sample on cylinders. 5) Sample mounted and centered.

This curing temperature ensured good glue adhesion in short time. However, it led to cracking of the specimens, especially the 4-pixels. This was

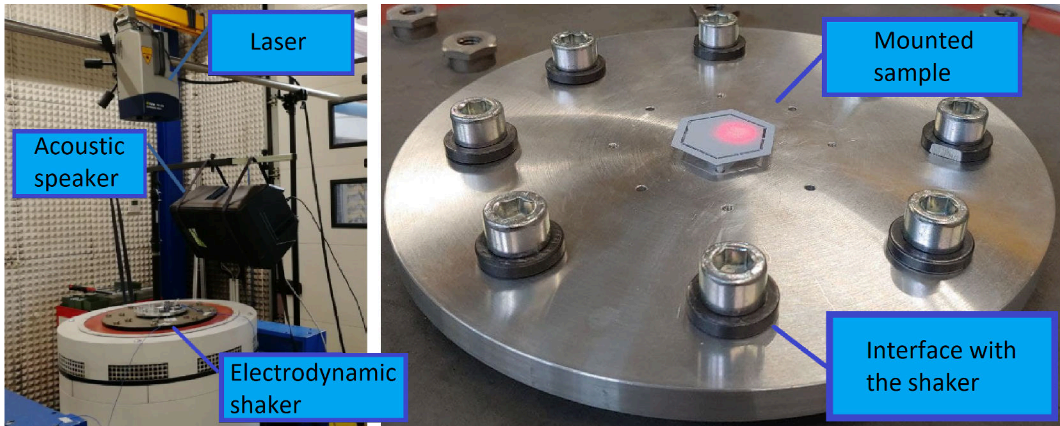

Figure 4.7: Left) The experimental setup at BPS vibration facility with the components listed above. Right) Assembly of the interface flange with the shaker. To check that the shaker exactly reproduce the desired signal, accelerometers were placed on the corner of the shaker itself, so that the control signal could be recorded.

caused by the differential expansion of the aluminum structures with respect to silicon during polymerization at 393 K. In fact, we observed that during heating, the flange expanded with respect to silicon without any problems. Returning to room temperature, the silicon is stressed by the contraction of the aluminum, up to its previous size, but being locked by the glue, it experiences high stresses. The distance between the bonding cylinders is 3 cm, and using the linear expansion coefficient with a temperature step of about 100 K, the relative expansion are about 9 μm. The accumulated stress leads to the rupture of the most brittle structures - the bridges ($L = 1\ mm$, $w = 100\ \mu m$, $t = 500\ \mu m$) - it can be inferred that such contraction can damage the specimen. For this reason, room temperature curing was chosen, avoiding the deformation of the specimen.

4.3 Experimental setup for vibration

To carry out the vibration tests, the following equipment were present at BPS vibration facility:

- electrodynamic shaker TIRA TV (59335/*-440),
- polytec Doppler scanning laser vibrometer (PSV-400-M4),
- acoustic speaker for excitation up to 20 kHz.

4.3.1 Electrodynamic shaker

The structure of an electrodynamic shaker resembles that of an acoustic speaker, presented in Figure4.8. It consists of a permanent magnet that produces a con-

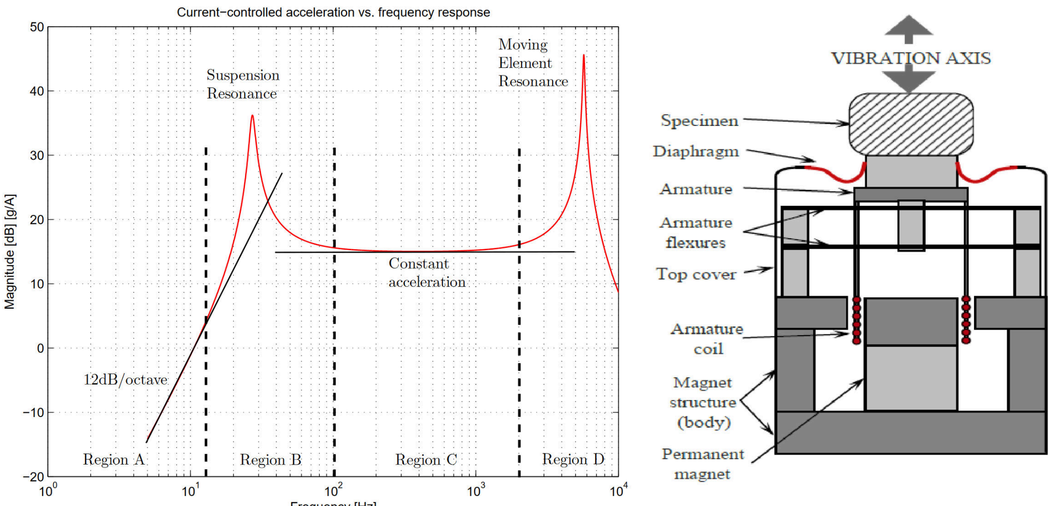

Figure 4.8: Left: Proper resonance of a shaker. At low frequencies, the displacement of the moving elements is denoted by the stiffness of the armature (Region A). As the frequency, the mass/spring/shaker system at one degree of freedom causes an increase of the acceleration of the shaker head (Region B), at this stage the armature and the coil move in unison. By increasing the frequency, the resonance of the suspension and is negligible, and there is a region of constant acceleration (region C). By increasing the frequency, the coil moves out of phase with respect to the structure and there is an increase of acceleration (region D). As the frequency increases, there is a risk of damage to the internal parts of the shaker. Right: Design of an electrodynamic shaker. From [66].

stant magnetic field in a coil, which is controlled by an AC signal source and by an armature (on which the coil) is free to move.

The coil is suspended in the permanent radial magnetic field, when a current is made to flow in it, a force proportional to the current on it, a force proportional to the current is produced, according to the Lorentz force:

$$f_{em} = B \cdot l \cdot i_a; \tag{4.1}$$

where, f_{em} is the force, i_a is the coil current, l is the length of the coil wire immersed in the field and B is the constant magnetic field. The coil is anchored to the armature, thus, the force is transferred directly to the head of the shaker and to the sample fixed on it. The structure of the shaker itself also exhibits typical resonances as explained in Figure 4.8.

4.3.2 Doppler effect Laser vibrometry

Laser Doppler vibrometry (LDV) is used for vibration measurements without need for contact with the surface under examination. The laser beam is sent to the sample surfaces, and the velocity, thus the displacement amplitude and acceleration at the test frequency, is measured through the Doppler shift. The

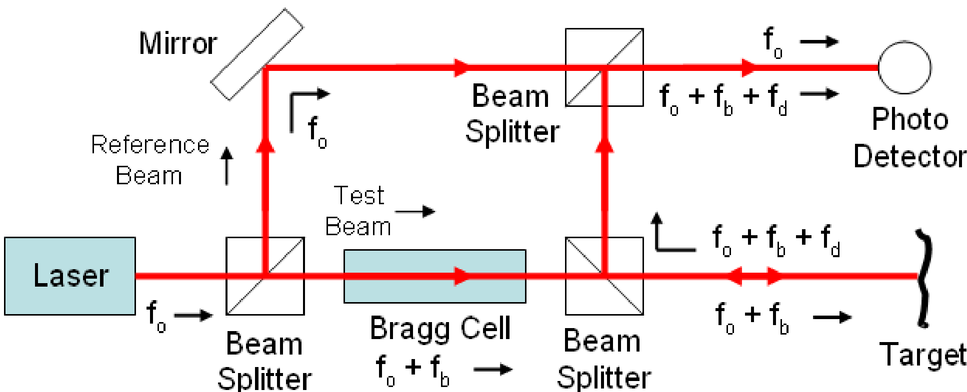

Figure 4.9: Basic schematic of a laser Doppler vibrometer. Laderaranch, LD-VSchematic, 2008.

light scattered back from the surface is detected and made to interfere with the reference beam on a photo-detector (typically a photo-diode). The operation scheme is shown in Figure 4.9.

Through a beam-splitter, the beam is split into two beams: the reference and test beam. The test one passes through a Bragg cell that adds a frequency shift f_b and is sent to the surface. The motion of the target adds a Doppler shift equal to:

$$f_d = 2\,\frac{v(t)}{\lambda}\,cos(\alpha),; \tag{4.2}$$

where $v(t)$ is the velocity of the surface, α the angle between the beam and the velocity vector, and λ the wavelength of the laser. A part of the reflected light is detected and recombined with the reference beam. Thus, the recombined signal is demodulated by the photo-detector (which is modulated with the frequency of the Bragg cell as the carrier frequency) and then is possible to trace back the frequency shift due to the Doppler effect (f_d) and consequently the speed of the surface $v(t)$. During the tests carried out, this technique was used in two different modes:

- single point: it allows the measurement of the surface motion through a single laser pointing,
- scanning: it allows the laser to move over the surface and study the displacements of multiple parts of the specimen.

4.4 Vibration test

The purpose of vibration tests is to study the response of a given structure to the accelerations to which it is subjected. This translates into looking for the typical oscillation resonances of an object and studying their modifications

upon exposure of the object to a vibrational load. If the typical resonances of the system remain unchanged, it means that the object has not undergone structural modification. As previously mentioned, the load are imposed through a vibration mask, i.e. the type of oscillation, frequency range, and associated amplitudes of vibrations. In this case, the tests were performed with two different types of excitations: sinusoidal (sinusoidal motion from an initial frequency to a final one) and random (random excitation in a predetermined frequency range). The vibrational masks reported in Table 4.1 and in Table 4.2 respectively.

Initial frequency (Hz)	Amplitude	Final frequency (Hz)	Amplitude
5 Hz	48 mm shift	11.26 Hz	48 mm shift
	0.75 $\frac{m}{s}$ velocity		1.7 $\frac{m}{s}$ velocity
	2.42 g acceleration		12.3 g acceleration
11.26 Hz	48 mm shift	21.52 Hz	48 mm shift
	1.7 $\frac{m}{s}$ velocity		1.7 $\frac{m}{s}$ velocity
	12.3 g acceleration		30 g acceleration
21.52 Hz	48 mm shift	100 Hz	1.5 mm shift
	1.7 $\frac{m}{s}$ velocity		0.47 $\frac{m}{s}$ velocity
	30 g acceleration		30 g acceleration

Table 4.1: Sinusoidal vibration mask. By construction the shaker utilized has the the structural limit of peak to peak displacement of $d = 50.8\ mm$. Therefore, at low frequency the mask was modulated for accelerations lower than the 30 g limit.

From the Power Spectral density is possible to calculate the mean square acceleration (g_{RMS}) subjected to the sample through the integral of the PSD in the frequency range:

$$g_{RMS} = \sqrt{\int_{f_i}^{f_F} PSD\ df}. \tag{4.3}$$

Summing and integrating the Power Spectral Densities in each frequency interval, given in Table 4.2, the mean square acceleration given by the electrodynamic shaker to the structural models is: 43.44 g. By setting these vibration parameters in the software present in the BPS facility could be proceeded with the tests.

4.4.1 Test procedure

The following test sequence were performed for each sample we tested:

- acoustic excitation from 500 Hz to 20 kHz for searching the resonances of the sample,
- excitation by shaker from 0 to 2 kHz for specific search of resonances of the sample,

Frequency (Hz)	Power Spectral Density ($\frac{g^2}{\sqrt{Hz}}$)
10	0.04
310	1.8
350	8.7
370	8.7
410	1.8
600	0.075
1550	0.016
1700	0.055
1820	0.055
2000	0.012

Table 4.2: Random load vibration mask. The characterization of a random vibration is usually done by the curve of power spectral density (PSD). In this way it is possibility to associate a quantity of energy in a given frequency band.

- qualification under sinusoidal excitation;
- excitation through shaker from 0 to 2 kHz for specific search of resonances of the sample, in order to check sample integrity;
- qualification under random excitation;
- excitation through shaker from 0 to 2 kHz for specific search of resonances of the sample, in order to check sample integrity;
- excitation of the first resonance until the rupture load.

Acoustic excitation

The first test is simply to study the resonances of the sample, even far beyond the upper limit of the loading frequencies provided to us by SRON. In this way it was possible to acquire information regarding the structural behavior of the samples and record the Operating Deflection Shape (ODS)[2]. The resonances and operating deflection shapes were acquired by defining a mesh of sampling points on the whole surface and scanning the laser on the specimen, to record

[2]The the Operating Deflection Shape analysis is a very versatile application for the determination of vibration trends in structures under different operating conditions. The trend of the vibrations is visualized with animated geometric models showing the dynamic properties of the structure. Through such a study, it is possible to understand the deformations of the specimen at various resonances.

the displacements of the individual parts of the surface. See Figure 4.10 for ODS and sampling points, and Figure 4.11 for the chips resonances.

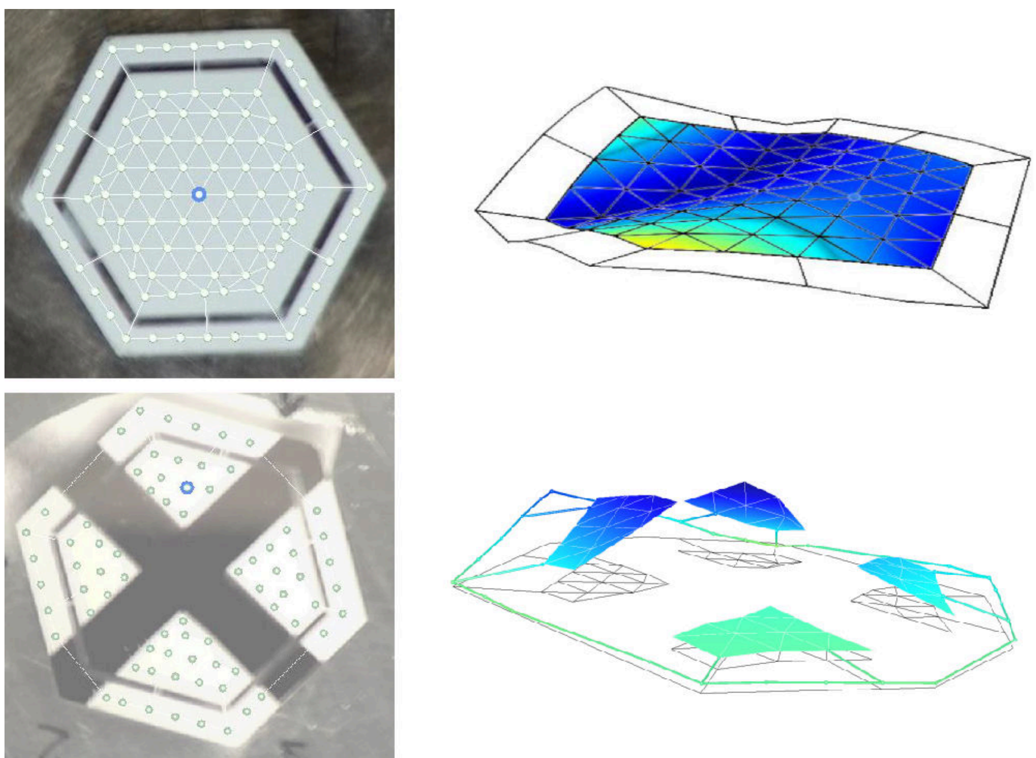

Figure 4.10: Left: Through the laser manufacturer's software, it was possible to set the points on the sample through which acquire data through the laser. Right: First resonance operational deformation. Top pictures are referred to 1-Pixel sample and bottom ones to 4-Pixels.

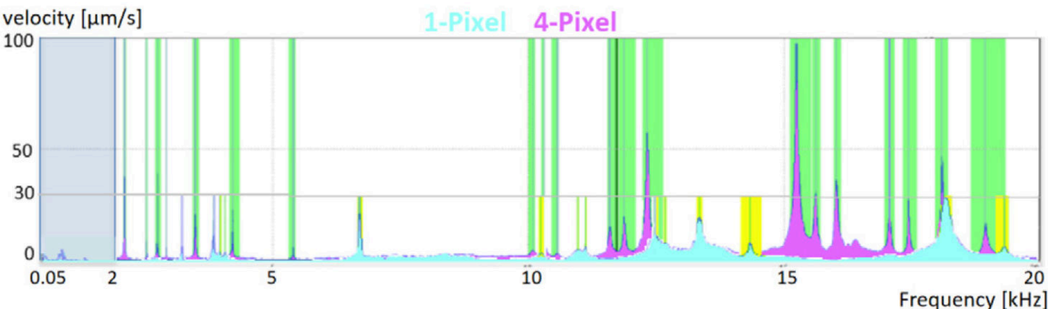

Figure 4.11: Maximal velocities of the absorbers surface with a loudspeaker excitation. The region under 2 kHz, where random load test take place, is highlighted to show the absence of any resonance. The 1-Pixel resonances are highlighted in yellow and the 4-Pixel ones in green. The differences between the two geometries are evident. From [67].

Harmonic spectra

After studying the various operational deformations and general resonances of the specimen, we moved on to a specific focus of the frequency range typical of the masks qualification loads. In this case the electrodynamic shaker is used for producing a sinusoidal signal with amplitude 0.5 g swept from 5 to 2000 Hz as seen in Figure 4.12. The signal in this case is recorded for both a single point on the sample and for the scanning of the mesh. To test the harmonic response of the system and acquire data on the resonances below 2 kHz.

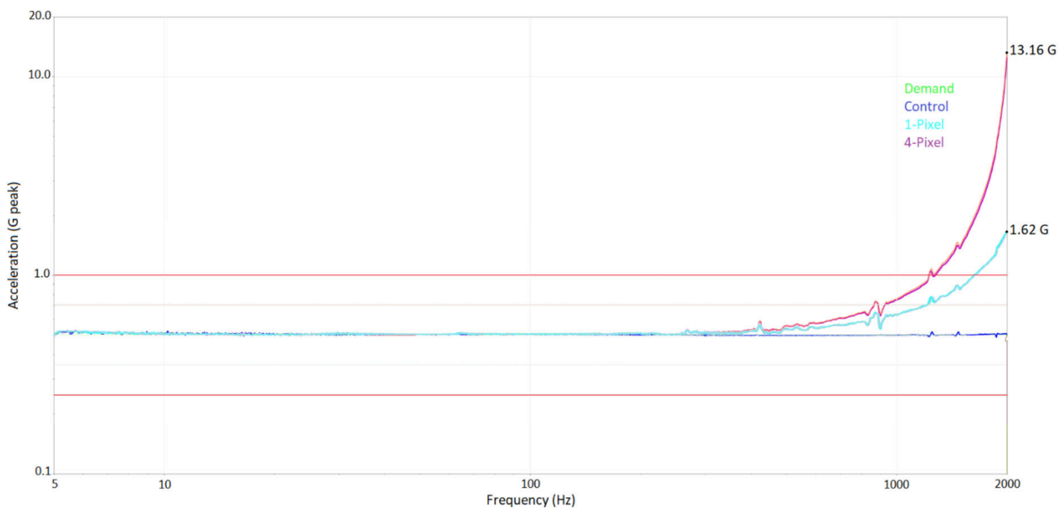

Figure 4.12: Example of resonance search using sinusoidal signal up to 2 kHz. In this example, the control (blue line) complies with the amplitude of 0.5 g. While the signal recorded by the laser (purple line), highlights the onset of a resonance around 2 kHz. The green and red lines are set by the software and correspond to the limits imposed on the shaker. As mentioned earlier, the search for resonances will be performed before and after each qualifying load to check for any frequency shifts in the typical resonances of the sample under investigation.

Sinusoidal load test

After the studies on resonances of the sample, we moved to the effective test dictated by the sinusoidal qualifying mask. The produced signal and the measured one are shown in Figure 4.13, the shape of the signal for the scanning of the mesh. Then, to check for any frequency shifts in the typical resonances of the sample under investigation, following the qualifying sinusoidal load procedure, we proceeded with the search for resonances as before.

Random load test

After the second resonance search, for checking the sample integrity we proceeded with the qualifying random load test according to the mask reported in

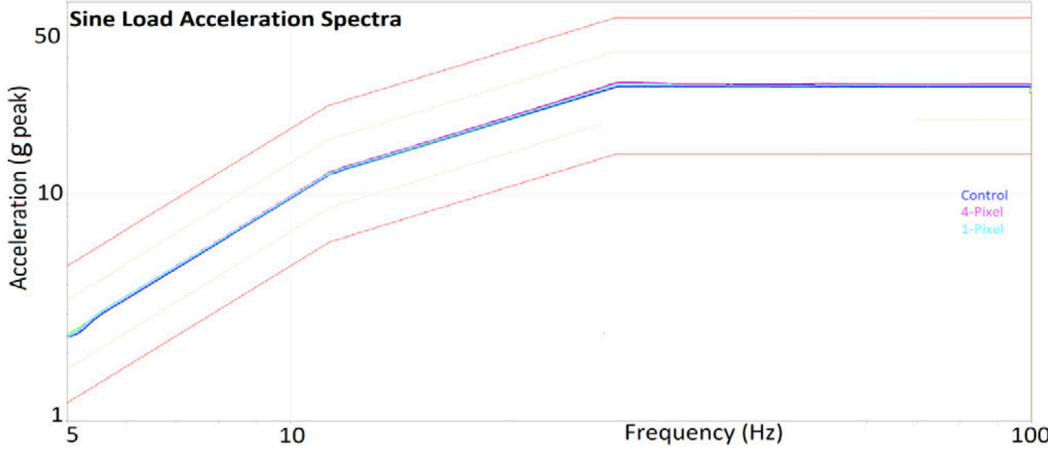

Figure 4.13: Acceleration spectra during sine load tests. The upper and lower red lines delimit the optimal signal area, the blue one is the control accelerometer response giving the shaker vibrations (equal to the mask), and in cyan and magenta the two sample group average response. From [67].

Table 4.2. The signal is detected by scanning the surface by means of the laser. An example of the measurement is shown in Figure 4.14. After the random load procedure, we searched again for typical resonances change as before.

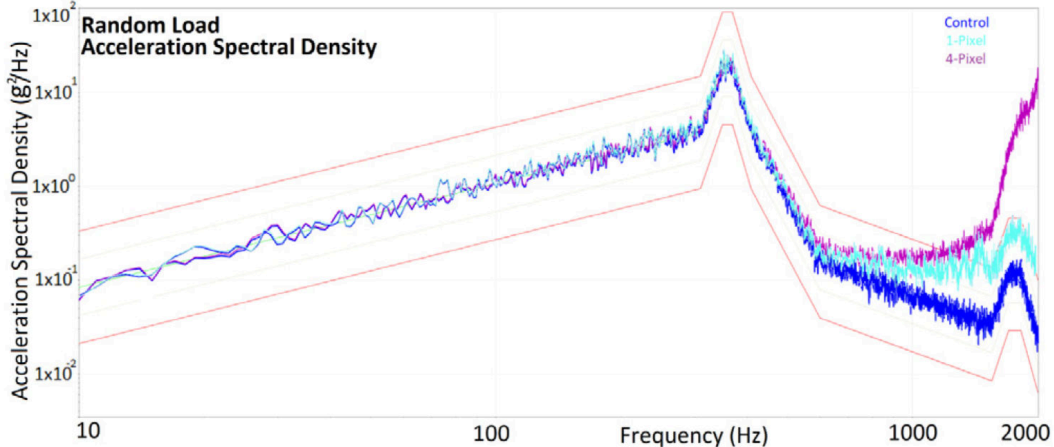

Figure 4.14: Acceleration spectral densities during random load tests. The upper and lower red lines delimit the tolerance area, the blue one is the control accelerometer response giving the shaker vibrations (equal to the mask), and in cyan and magenta the average response of the two samples. The signal measured by the laser (purple line) follows the driving signal up to 1 kHz, in fact, from that frequency the signal from the sample is amplified due to the proximity to the first resonance. From [67].

Excitation of the first resonance

After the study of resonances up to 20 kHz, the sinusoidal and random loads, and the various searches for resonances in the frequencies of interest, it was decided to subject the samples to an additional test, in order to verify the resistance to large accelerations. For this reason it was decided to excite the first detected resonance, as it is just above 2 kHz, at the upper limit of the random vibration mask. By exciting this resonance we could gather further information on the possible response to launch vibrations can excite the resonance, where high gains are possible. For the excitation of this resonance, a sinusoidal-type signal of 1.2 $\frac{mm}{s}$ peak velocity amplitude in a 500 Hz window around the resonance frequency was chosen. Such a test was performed by sweeping in frequency from the lowest to the highest and vice versa with a minute per sweep.

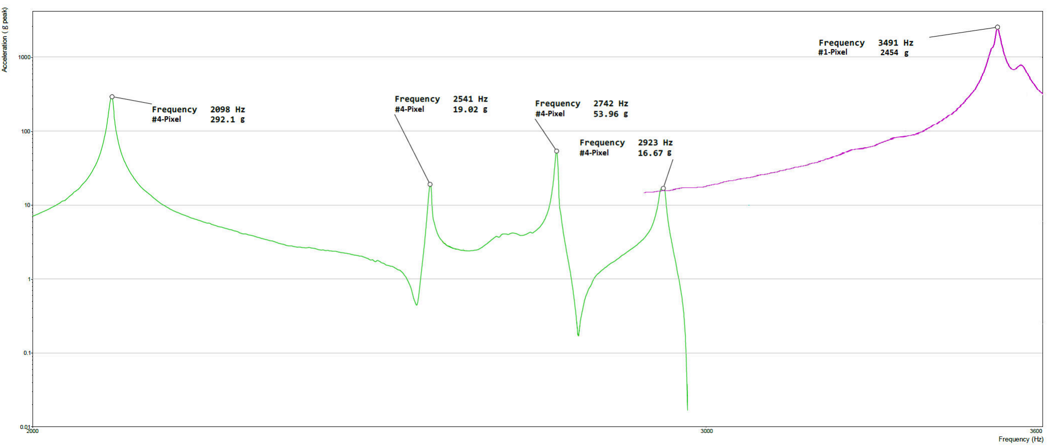

Figure 4.15: 1-Pixel geometry in green and 4-Pixel geometry in purple. The monolithic sample was excited at 1.2 $\frac{mm}{s}$ while the segmented at 0.6 $\frac{mm}{s}$, as in the subsequent sweep at 1.2 $\frac{mm}{s}$ peak velocity experienced a failure with the breakage of one of the absorbers.

4.5 Test results

Numerous samples were produced between monolithic and segmented SM0s, prepared and then tested. These samples experienced different issues during preparation or tests. The summary of all samples produced and results are given in the summary tables of monolithic (Table 4.3) and segmented specimens (Table 4.4). Regarding 1-Pixel samples, hot curing compromised the vibration tests of the SM0 #06 and SM0 #09. While the SM0 #05 and SM0 #07 samples passed the nominal vibrations and also the excitation of the first resonance without reporting ruptures or shifts in resonances. The SM0 #08 passed all testes despite the hot curing, but analysing the first resonance excitation was found a non linear modulation due to a non optimal gluing configuration that dumped vibrations. Instead in 4-Pixel samples the hot curing

1-Pixel	Sinusoidal Load	Random Load	Resonance excitation	curing
SM0 #08	Passed	Passed	Passed	393 K
SM0 #06	not performed	not performed	Broken	393 K
SM0 #09	Passed	Broken	not performed	393 K
SM0 #05	Passed	Passed	Passed	293 K
SM0 #07	Passed	Passed	Passed	293 K

Table 4.3: Summary table of monolithic samples produced and tested.

4-Pixel	Sinusoidal Load	Random Load	Resonance excitation	curing
SM0 #13	not performed	not performed	not performed	393 K Broken
SM0 #12	not performed	not performed	not performed	393 K Broken
SM0 #14	Broken	not performed	not performed	393 K
SM0 #16	Passed	Passed	Broken	293 K
SM0 #17	Passed	Passed	not performed	293 K

Table 4.4: Summary table of segmented samples produced and tested.

reported cracks during assembly as, or in case, of the SM0 #14 the breakage occurred at the beginning of the test. SM0 #16 and SM0 #17 did not suffer damages, thus were able to test: they passed both qualifying loads without resonance shift. While for the excitation of the first resonance, the first sample broke performing the $1.2\frac{mm}{s}$ excitation sweep. For this reason, the second one did not undergo to such a procedure.

Thus, the tests performed revealed the structural characteristics of the specimens produced. Both geometries, with the correct bonding process passed the qualifying loads without exhibiting cracks or changes in their structure. Therefore, both configurations are nominally qualified to proceed with the development of the structural model (SM1 and SM2). However, a fundamental issue arose during the study. The segmented configuration has a significantly larger amplitudes of the first resonance than the monolithic one (Gain = 1500). and the resonance is very close to the upper limit of the random tests frequency range, 2 kHz. The comparison of the resonances of the two configurations is shown in Figure 4.11. In the end, although both geometries withstood qualifying load tests and thus exhibit structural resistance to launch stresses, the monolithic geometry appears to be the safer one: easier to fabricate, less delicate in the assembly phase and with resonance frequencies distant from those transferred during the carrier launch. Furthermore, simulations show that the real setup should reduce the frequency of the first mode. Therefore, we are going to test both geometries in a more representative setup and to study the possibility to use the 1-Pixel configuration from a detector's performance point of view.

Chapter 5

Measurements on the CryoAC models

In addition to the various tests carried out during the fabrication of CryoAC prototypes, I performed and analyzed several measurements with full detectors, operated, set up and maintained dilution cryostats in Genoa, and designed and fabricated ad hoc prototypes to measure some thermal properties of the CryoAC. Specifically, with the AC-S10 demonstration model, shown in Figure 5.1 along with the model requirements table, the collaboration tested joint operation with the NASA-GSFC TES microcalorimeter array at the SRON-Utrecht facility. Measurements that I followed remotely due to the COVID-19 pandemy. Meanwhile, the characterization and performance tests of the produced detectors were carried out first at the facility of the University of Genoa and then at the INAF-IAPS in Rome.

5.1 The measurement setup in Genoa LTD lab

At the University of Genoa there is a wide expertise in developing and studying low-temperature detectors, particularly superconducting ones. Early developments date back to the late 1960s, in which bolometers were developed mainly for molecular beams [68], later Josephson junctions for charged particles [69] and microcalorimeters for ^{187}Re beta spectroscopy [70]. More recently, TES bolometers are being made for the microwave telescope on LSPE stratospheric balloon [71].

5.1.1 Dilution Cryostat

There are three dilution cryostat in the Genoa LTD lab. The Kelvinox 25 from Oxford Instrument was used for CryoAC measurements and tests. A dilution fridge bases its operation on the characteristic of the mixture of ^3He ^4He [72]. As can be seen in Figure 5.2, under certain conditions of temperature ($T < 0.87\ K$) and concentration of the mixture, e.g. 0.16, the fluid separates into two phases: one phase with a high concentration of ^3He, which is lighter, while

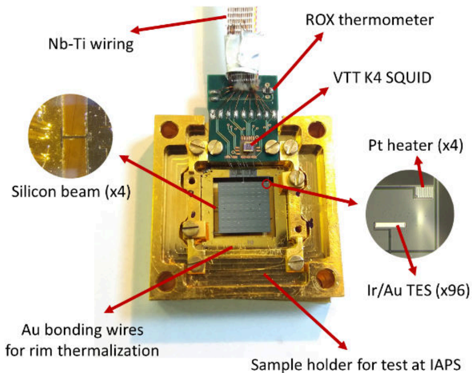

Parameter	Value
Geometrical rejection efficiency	98.5%
Detection efficiency	99.98%
Allocated power dissipation	<40 nW (CBE)
Time tagging accuracy	≤10 µs
Intrinsic dead time	1%
Energy treshold	< 20 keV

CBE current best estimate

Figure 5.1: Demonstration model AC-S10 mounted on the bracket for the focal plane assembly with its requirement previous to the mission redefinition. From [53] and [51].

the other heavier, ^4He-rich phase. In Figure 5.3 the schematic of the working principle is reported: a U shaped pipe filled by liquid mixture with a interface between two phases in the so called Mixing Chamber.

Through a pumping system, is possible to reduce the pressure on the dilute phase, causing the evaporation of ^3He. As a result of this depletion, the helium-3 will tend to pass from the concentrated phase to the dilute phase to keep the concentration constant. Then, the refrigeration power is:

$$\dot{Q} = \dot{n}_3(95T_{mx}^2 - 11T_{ex}^2), \tag{5.1}$$

where T_{mx} is the mixing chamber temperature, T_{ex} the temperature of last heat exchanger entering the mixing chamber, and n_3 is molar quantity of ^3He. The equation 5.1 states that, under steady-state conditions, in which n_3 moles per time unit are circulated through the system, the cooling power is proportional to the change in enthalpy for the dilution process from the concentrated phase to the dilute phase, minus the amount of heat required to cool them at constant pressure from the last exchanger to the mixing chamber. Both terms depend on the square of the temperature, and at zero heat input the ratio of the last exchanger to mixing chamber temperatures is about 3. To make a cycle, helium-3 is constantly evaporated from the mixture and then condensed in it, maintaining the steady-state between the phases in the mixing chamber. It is then possible to increase the cooling power by boosting the circulation rate by applying power to the still and increasing the evaporation rate, i.e. the flux, of ^3He.

To operate the fridge, a thermal bath at 4.2 K is filled with liquid ^4He. This chamber is isolated from the outside through the Outer Vacuum Chamber (OVC), so as to minimizes heat load from the 300 K environment. Inside the 4 K bath the Inner Vacuum Chamber (IVC) is located, in which the dilution unit, with the three main cooling stages is placed, Figure 5.3.

At the beginning of operations, to facilitate 4 K cooling of the dilution unit, heat exchange gas is fed into the IVC He. When necessary, ^3He gas from a

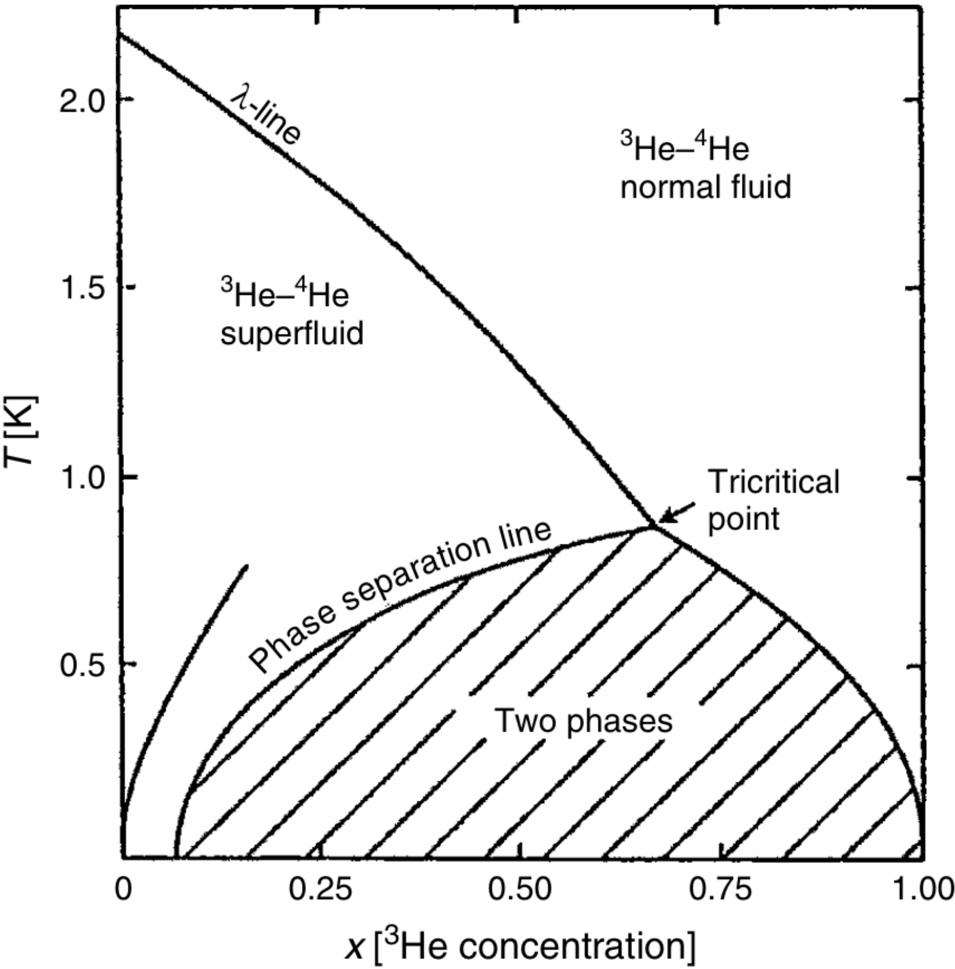

Figure 5.2: Liquid $^3He - 4^He$ phase diagram as function of the ^3He concentration. Below the tricritical point (0.87 K) the phase separation occurs. From [73].

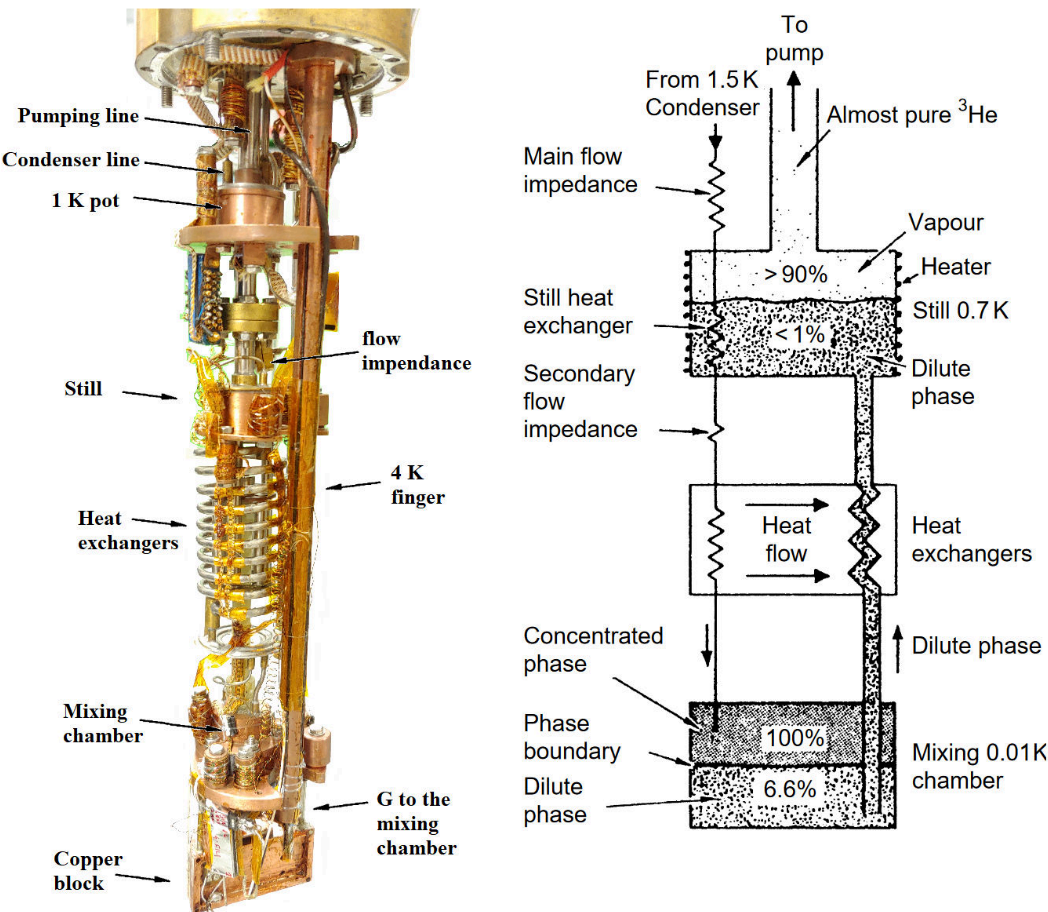

Figure 5.3: Left, photo of the interior of the IVC of one of the dilution cryostats in use in the Genoa laboratory (Kelvinox-25 Oxford Instruments), where the various cooling stages are highlighted. Right, schematic diagram of a dilution cryostat, showing the system for circulation of the mixture, the mixing chamber, heat exchanger, still.

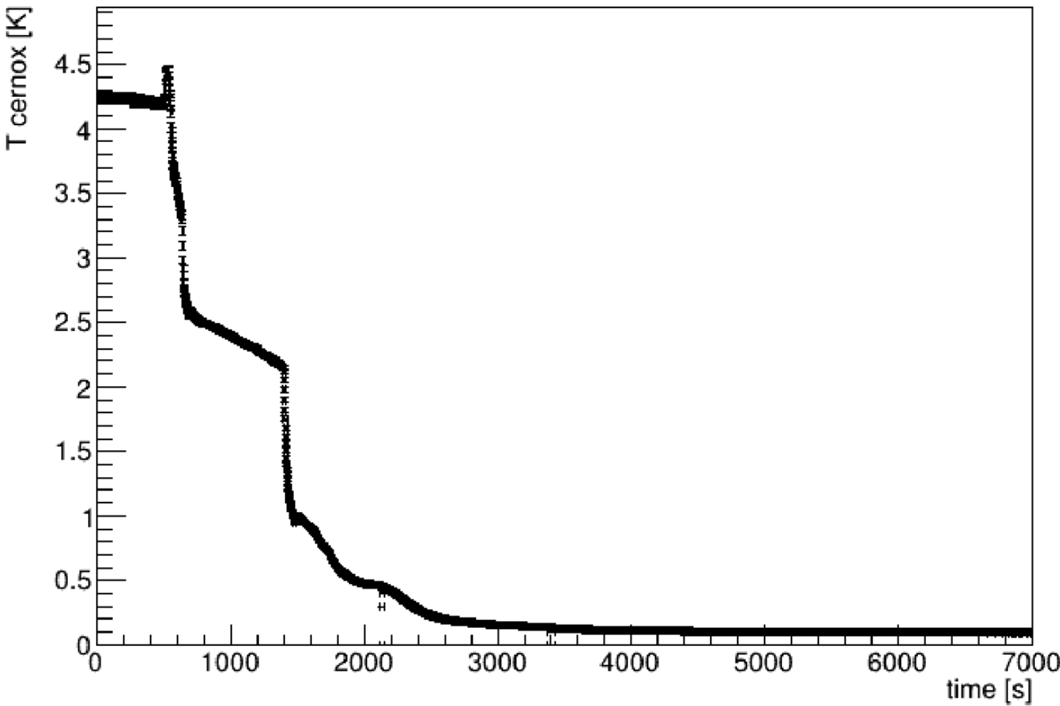

Figure 5.4: Measurement of the mixing chamber temperature during the cool down. Is possible to appreciate the different steps of the refrigeration process: constant temperature of LHe 4.2 K till 500 s, then condensation of the ^3He-^4He mixture, at 1400 s the start of circulation process of the mixture, with at 0.7 K a the start of ^3He and ^4He phase separation inside the mixing chamber.

closed circuit is used. Although designed for ^4He exchange gas, ^3He is preferred to ensure that thermal conductances in bolometer and microcalorimeter tests are not altered by residual ^4He gas that forms superfluid films. Once 4 K is reached, the gas is pumped to decouple the IVC from the helium bath and begin the cooling process below 4 K. The gaseous mixture of $^3He -^4 He$ is liquefied, through filters at 77 and 4 K, by means of heat exchangers in the 1 K pot stage. Thereafter, the now liquid mixture proceeds through several heat exchangers to arrive at the mixing chamber, where the separation between the two phases takes place, once the temperature is lower than 0.87 K depending by the ^3He concentration, Figure 5.2, and the process of dilution of ^3He from one phase to the other takes place. This is the coldest point in the cryostat. The typical cool down profile is shown in Figure 5.4

A copper cold finger, simply called “block", was mounted on the mixing chamber with a controlled thermal conductance. The functionality of this setup is to dump the mixing chamber fast thermal fluctuations and have a better control of the samples temperature mounted on it. Sample mounting can be made by applying a bonding layer that enhance the thermal coupling [72] (usually GE7031) and then mechanically fixed (by spring or screws), to maximize the thermal conductance with the "block" depending on the sample

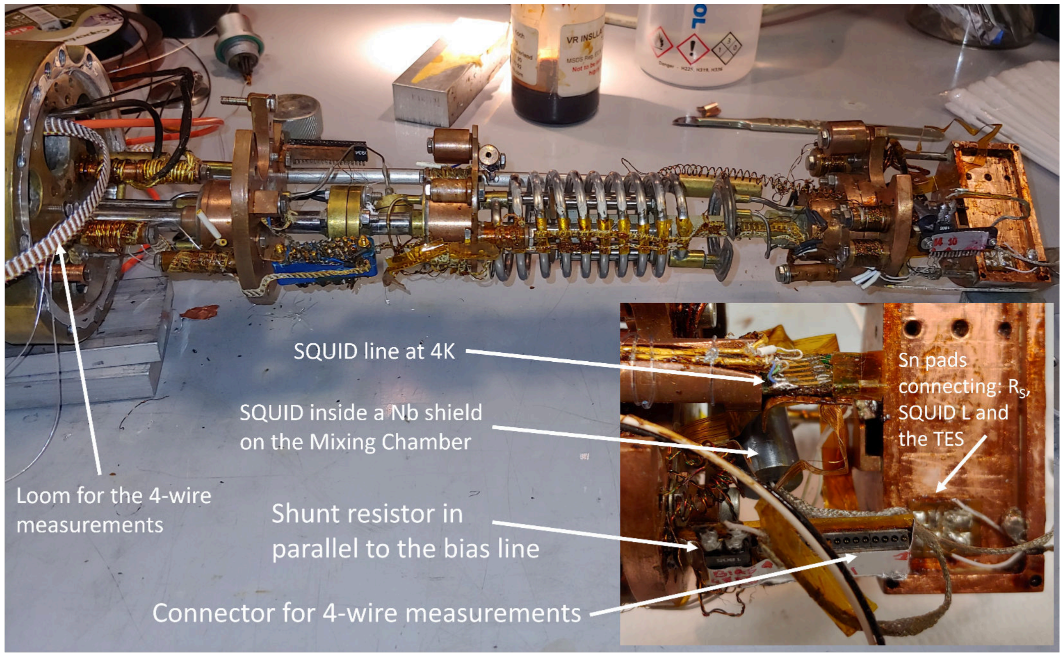

Figure 5.5: Kelvinox 25 in the process of wiring. In the inset a zoom of the copper "block" with the SQUID readout.

holder used. In our case, a thin layer of GE (10-100 μm) is inserted between the specimen holder and the "block", and assured via a screw.

Especially in Kelvinox 25, which does not have an intermediate thermal shield from 4 K walls, care is taken to have the sample temperature under control. Samples must be covered and shielded from the external radiation at 4 K. The "block" can then be thermostated using a Germanium thermometer and a heater with stability better than 10 μK.

5.1.2 Instrumental apparatus

The cryostat have been rewired, see Figure 5.5, to perform 4-wire measurements with 4 different channels, with a DC SQUID and a bias line connected to the input coil of the SQUID. The DC SQUID is used as a current to voltage amplifier through a Flux Locked Loop (FLL) electronic from Magnicon GmbH. In Figure 5.6 it is shown the bias line circuit connected with the SQUID.

TES measurement circuit

To measure TES response, the circuit in Figure 5.6 is used. Through a voltage divider formed by a load resistor of R_L and a shunt resistor R_{sh} of the order of 5 $m\Omega$ the bias voltage is supplied to the TES. While the series between the TES (R_x) and the SQuID input inductance L, about 4.5 nH, that behaves like an ammeter. In this way, it is possible to measure the TES current. Since the circuit, including the connections, is completely superconductive at the operating temperature, it is possible to make an accurate determination of

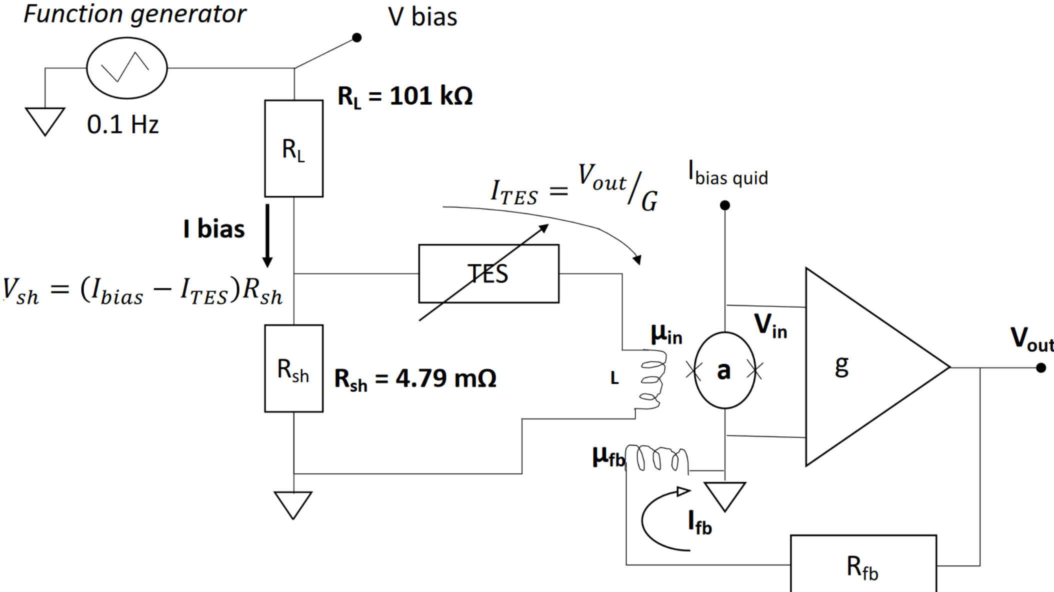

Figure 5.6: Electrical diagram of the measurement system. The TES is powered through a voltage generator so as to provide a constant bias voltage. A divider is inserted, formed by R_L on the hot side and a shunt resistor R_S on the cold side, ($R_L \gg R_X \gg R_S$)to reduce noise from the outside, and have a voltage generator. To measure the changes in current IX passing through the TES (due to the change in R_X) we couple the system to a SQuID via an input inductance L. Then, the SQUID is used as a current-voltage amplifier with a FLL Magnicon electronics.

current I_x. In addition, this arrangement makes possible exploit the negative electro-thermal feedback, as already explained in Section 2.2. The SQuID we have mounted in the cryostat is the K3B model from VTT and controlled with electronics from Magnicon GmbH.

DC SQuID

SQuID DC-based current-to-voltage amplifiers are the most suitable for reading the signal of TESs because of the large parameter space available for the best noise matching. [74]. This is a device composed of a superconducting ring interrupted by two Josephson junctions, i.e. Superconducting-Isolating-Superconducting (SIS) junctions, named after the physicist who first studied them. Going to study the properties of these types of junctions, it is possible to observe how by passing a current, through the junction, which exceeds the critical value I_c, a difference of potential is generated at its ends. While for lower current values this is zero. The current when passing through a junction is also modulated by the phase difference of the Cooper pairs of the two superconducting half-rings 1 and 2:

$$I = I_c sen(\Phi_1 - \Phi_2). \tag{5.2}$$

In contrast, by applying a magnetic field, the current is modulated according to the flux Φ applied on the ring:

$$I_c(\Phi) = I_c(0) \left| \frac{\Phi_0}{\pi\Phi 0} sen\left(\frac{\pi\Phi}{\Phi_0}\right) \right|, \tag{5.3}$$

Where Φ_0 is a quantum of magnetic flux (fluxon) corresponding to $h/2e = 2.07 \times 10^{15} Wb$.

Then by applying an external magnetic field flux and biasing the SQuID with a constant current, it is possible to observe a periodic signal of the output voltage with period Φ_0. As described by Equation 5.3. SQUIDs are not linear devices, in Figure 5.7 SQUIDs voltage versus flux and voltage versus current characteristics. We are using an array of 6 SQUID from VTT, K3B model, visible in Figure 5.8 together with its voltage-current and voltage-flux characteristics.

It is then possible to use the SQuID as a current to voltage amplifier. The current signal generated by the TES produces a change in magnetic flux concatenated with the loop of the SQuID. In order to produce a linear response, a feedback that generates a flux equal to the flux entered by TES keeps the flux in the loop of the SQuID-FLL (Fluxed Locked Loop) fixed. The output of the SQuID is then the voltage required to produce the current that feeds the feedback inductance.

The scheme of a typical SQuID readout electronic is reported in Figure 5.6 where we call g the voltage amplifier gain, it is usually a big number, while a is due to SQuID $V - \Phi$ characteristic (a=dV/$d\Phi$). For small variations of Φ

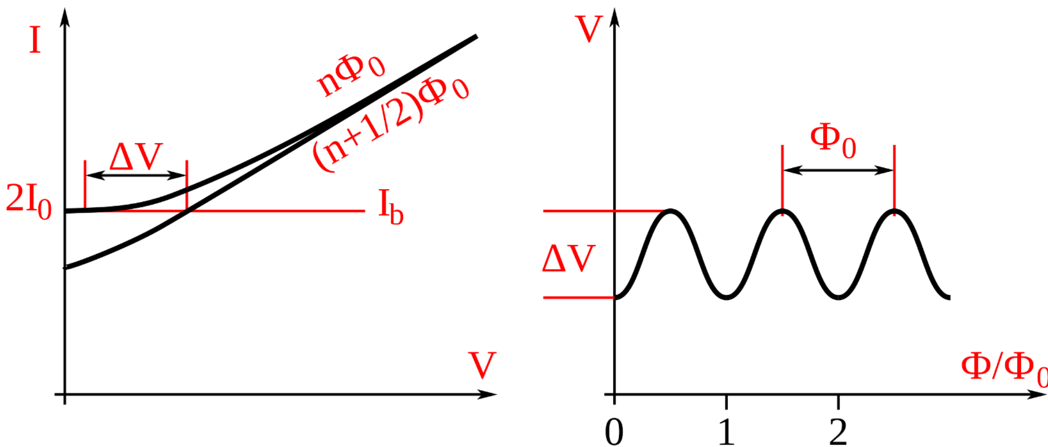

Figure 5.7: Left: Voltage-Flux characteristic of an SQuID, it is periodic with Φ_0. Right: Voltage-current characteristic dependence on the magnetic flux in the SQuID (integer or semi-integer). It is clear the non-Ohmic behavior of the device, which has zero resistance for bias currents below the critical current. The voltage-flux characteristic is the oscillation between the two states at integer and semi integer flux at a given bias current. From Janolaf30 IVcurve, CC BY-SA 3.0.

in the linear region, we can consider a constant (not depending by Φ but only function as SQuID working point and device geometry, linear region of the sinusoid). Since the feedback forces total Φ close to zero this approximation is right:

$$V_{out} = gV_{in} \qquad V_{in} = a\Phi. \tag{5.4}$$

Then, if we write the magnetic flux into SQuID sensor as sum of input and feedback coil and develop calculation we obtain:

$$V_{in} = a(\Phi_{in} - \Phi_{fb}) = a(\mu_{in}I_{in} - \mu_{fb}I_{fb}) = a(\mu_{in}I_{in} - \mu_{fb}\frac{V_{out}}{R_{fb}}) \tag{5.5}$$

$$V_{out} = ga(\mu_{in}I_{in} - \mu_{fb}\frac{V_{out}}{R_{fb}}) = \frac{ga\mu_{in}}{1 + ga\frac{\mu_{fb}}{R_{fb}}}I_{in}, \tag{5.6}$$

where μ is the, input or feedback, coil mutual induction to the SQuID ring. Thus, the general expression for SQuID gain is the closed loop gain:

$$G = \frac{ga\mu_{in}}{1 + ga\frac{\mu_{fb}}{R_{fb}}} \tag{5.7}$$

The voltage amplifier gain g usually is a large value, thus we can consider the limit to infinite of the product between g and SQuID sensor responsivity a.

$$\lim_{ga\to\infty} G = R_{fb}\frac{\mu_{in}}{\mu_{fb}} \tag{5.8}$$

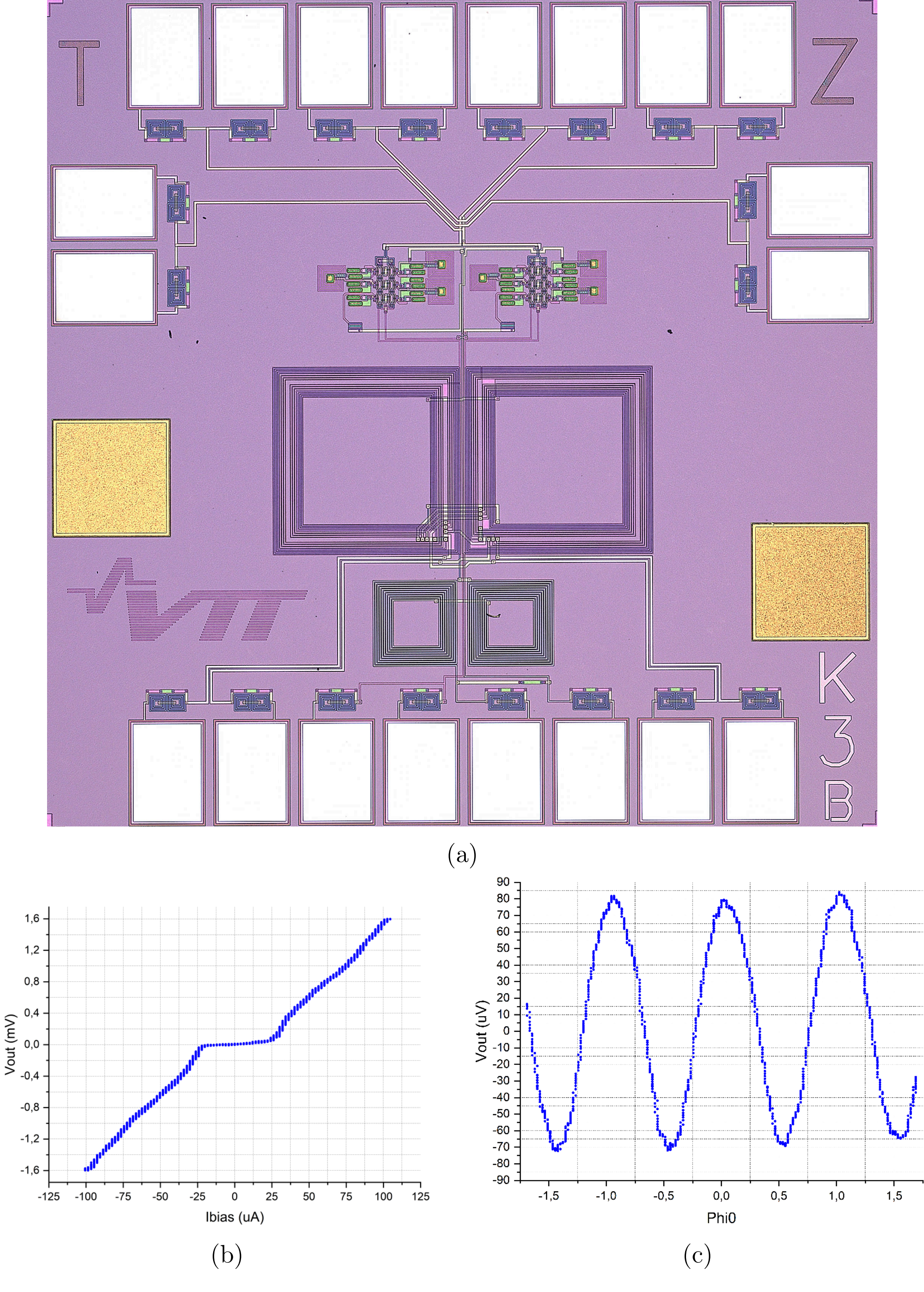

Figure 5.8: (a): K3B SQUID array from VTT mounted on the cryostat. (b): V-I characteristic at zero magnetic flux applied. (c): V-Phi characteristic with 32 μA of bias current.

5.2 Operating the Demonstration Model

At the beginning of my thesis work, the first Demonstration Model we have delivered was the AntiCoincidence sample named AC-S10. It was used to complete phase A of the project and to define the procedures and to test the operation of the detector as an anticoincidence, while also performing compatibility tests with the spectrometer.

5.2.1 Demonstration Model characterization

The ACS-10 DM characterization was carried out in Rome at INAF-IAPS, by Claudio Macculi, Matteo D'Andrea and Guido Torrioli, with tests from the thermo-electric characterization, to the pulse response from 6 keV to 12.7 MeV [53].

Thermo-electric characterization

The sample has shown a narrow superconducting transition Figure 5.9a, with a critical temperature $T_C = 106\ mK$ and a normal resistance $R_N = 31.3\ m\Omega$. To evaluate the thermal conductance of the system it has been used the Pt heaters, measuring the thermal power needed to drive the unbiased TES inside the transition ($T = T_C$) as a function of the thermal bath temperature 5.9b. Then data have been fitted with a power-law model describing the power flow to the heat bath as described in Section 2.2:

$$P_H = k(T_C^n - T^n), \tag{5.9}$$

where k and n are constants determined by the nature of the thermal link. The best-fit parameters are reported in the plot in Figure 5.9b. Note the $n \sim 4$, as expected for a phonon-mediated material [26], indicating that the power measured flows through the absorber silicon beams.

The measured thermal conductance G is:

$$G = knT^{n-1} = 34\ nW/K\ @\ 106\ mK \tag{5.10}$$

The characteristic I-V curves of the sample at different thermal bath temperatures are reported in Figure 5.10a. The current flowing through the TES (I_{TES}) is measured as a function of the current injected to the bias circuit (I_{BIAS}), where the TES is connected in parallel with a $R_S = 0.5\ m\Omega$ shunt resistor. The slope of the curves in the TES superconducting region is affected by a current-dependent parasitic resistance ($R_P \sim 20\ m\Omega$ at maximum) appearing in series with the TES for $I_{TES} > \sim 10\ \mu A$. That has been already discussed in Section 3.6.4. Thanks to the on-board heater, it has been possible to acquire another family of characteristic curves, injecting different amounts of power on the absorber while keeping fixed the bath temperature at $T_{bath} = 50\ mK$, see Figure 5.10b. These curves define a large set of points where it is possible to operate the detector with the bath at 50 mK. Note

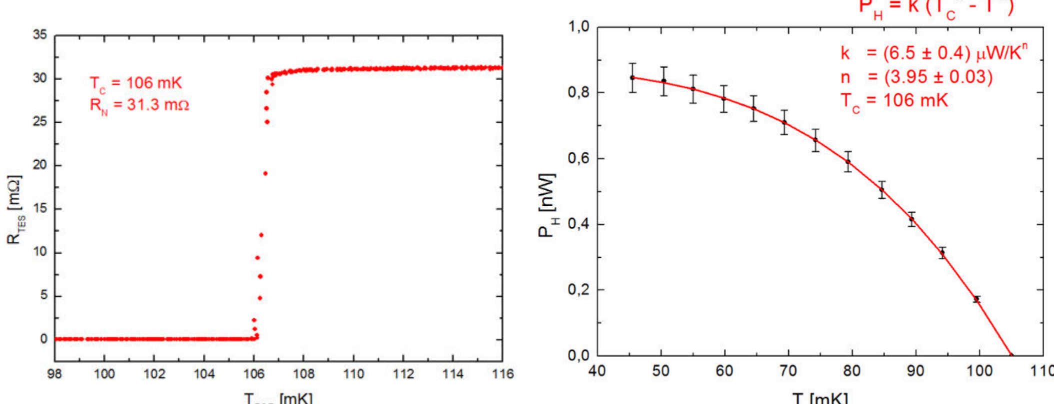

(a) Resistance versus temperature of ACS-10 with a bias current of 1 μA.

(b) Power injected on the absorber versus thermal bath temperature.

Figure 5.9: (a): The detector TES network has a normal resistance R_N of 31.3 $m\Omega$ and sharp transition at 106 mK. (b): Injected power injected on the absorber to bring the unbiased TES into the transition as a function of the thermal bath temperature to find out the Detector Thermal conductance toward the thermal bath. From [53].

that the use of the heaters allows a reduction in the current needed to bias the TES within the transition: the more power injected by the heaters, the less current is required to bias the TES. This has the advantage of reducing also the current flowing through the shunt resistor, and consequently its power dissipation, which is a dominant contribution to the total power dissipated on the cold stage. This is really important, especially with the mission redefinition and the need to reduce power loads. The cost for this is to reduce the loop gain of the system, slowing down the detector.

Table 5.1 shows, as examples, the specification of three analogous working point of the detector ($R_{TES} = 10\% R_N \sim 3m\Omega$), obtained at different heater powers. Note that with higher injected power by the heater, the result is lower total power dissipation and lower loop gain.

Operation at 50 mK thermal bath and low energy threshold

The detector has been operated in the third working point in Table 5.1, with a total power dissipation $P_{TOT} = 2.6nW$ at 50 mK, fully compliant with the DM requirement ($P_{TOT} < 40\ nW$). To probe the low energy threshold, the sample has been illuminated by a ^{55}Fe source (6 keV photons), with a count rate of $\sim$ 10 cts/s. Simultaneously, the sample has been also stimulated injecting fast (1 μs) rectangular current pulses into the on-board heaters (I_H = 4.3 μA), generating thermal pulses with an energy $E = 35\ keV$ at the rate of 2 cts/s as in Figure 5.11a.

The acquired pulses show a rise time $\tau_R \sim 30\ \mu s$ and a thermal decay time $\tau_D \sim 5\ ms$. The energy spectrum is shown in Figure 5.11b. It has been

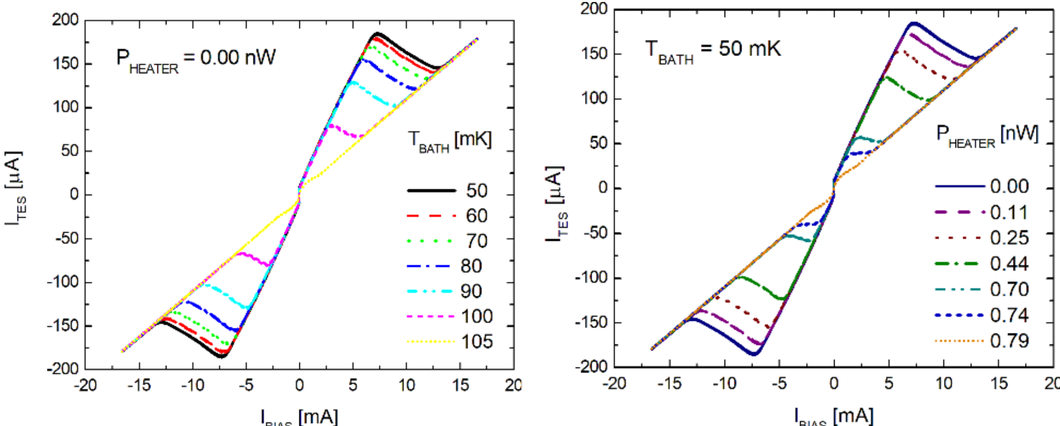

(a) TES current over the TES Bias current at different bath temperature.

(b) I_{TES} vs I_{BIAS} at $T_{bath} = 50\ mK$ with different powers dissipated by the heaters.

Figure 5.10: Characteristic I-V curves of the sample. (a): "Standard I-V" at different T_{bath}. (b): "Operative I-V": sweeping the power injected by the heaters. It is shown the parasitic resistance effect discussed in Section 3.6.4. The "Operative I-V" shows how the dissipation through the heaters allows to set different working points without affecting the detector characteristics. From [53].

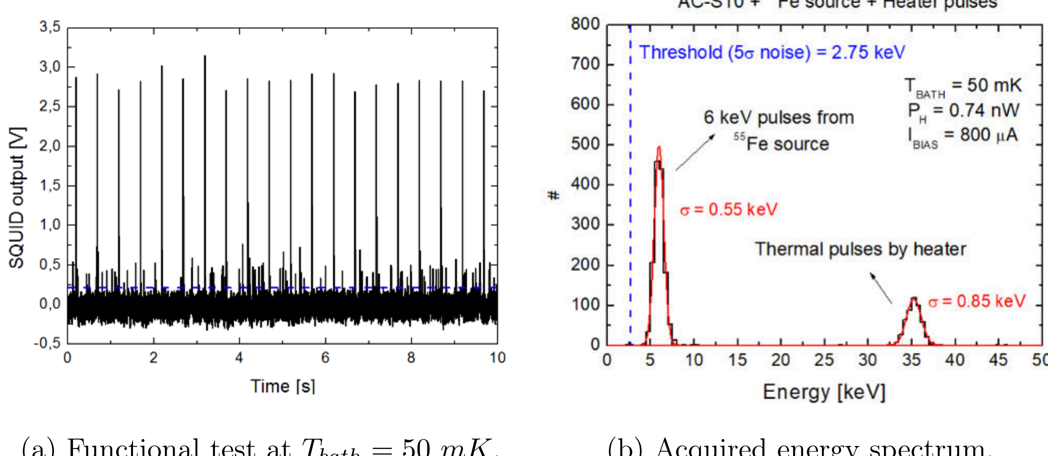

(a) Functional test at $T_{bath} = 50\ mK$.

(b) Acquired energy spectrum.

Figure 5.11: CryoAC performances (a): Functional test of AC-S10 operated at $T_B = 50\ mK$. Response to 35 keV Heater pulses and 6 keV from ^{55}Fe. The blue dashed line is the low energy threshold level (5 sigma noise). (b): Acquired energy spectrum fitted by gaussian functions (red line). From [53].

#	P_H (nW)	I_{BIAS} (mA)	I_{TES} μA	P_{R_S} (nW)	P_{TES+R_P} (nW)	P_{SQUID} (nW)	P_{TOT} (nW)	$\mathscr{L}$
1	0.00	8.10	181	30.1	0.76	1.5	32.3	195
2	0.25	6.75	150	20.7	0.51	1.5	23.0	135
3	**0.74**	**0.80**	**39**	**0.29**	**0.02**	**1.5**	**2.6**	**9**

Table 5.1: Specifications of three possible working points of the detector at $T_{bath} = 50\ mK$. In each point $R_{TES} = 10\% RN \sim 3m\Omega$. P_H is the power injected by the heater and P_{R_S}, P_{TES+R_P}, and P_{SQUID} are the power dissipated by the shunt resistor, by the TES plus the parasitic resistance, and by the SQUID. P_{TOT} is the total power dissipation at 50 mK. The third line (in bold) corresponds to the working point used for the measurements reported in Sections 5.2.1 and 5.2.1. From [53].

obtained from the Pulse Height spectrum, calibrating the energy scale to the 6 keV line. Note that the heater pulses line is properly centered around the energy of 35 keV, demonstrating the use of the heater as a calibration pulse generator and probing the linearity of the detector response in this energy range. The measured low energy threshold is $E_{threshold} = 2.75\ keV$, fully compatible with the DM requirement of $E_{threshold} < 20\ keV$. It corresponds to the 5 sigma level over the noise, which has been evaluated from the baselines of the acquired pulses. The sample shows also some spectroscopic capability with energy resolution of $\Delta E_{FWHM} = 1.30\ keV$ at 6 keV. Although the CryoAC is not aimed to perform spectroscopy, and there is not a related requirement on the DM, this could provide some scientific return for the X-IFU in the hard X-ray detection [75].

Pulse response up to the saturation regime

At this point the on-board heaters were used to stimulate the detector across its whole band, in order to test the response up to the saturation regime. Also for this measurement the detector has been operated in the third working point in Table 5.1. The acquired pulses are shown in Figure 5.12a. For each pulse it has been measured the pulse height PH in Figure 5.12c and the recovery time t_{REC} in Figure 5.12d. The recovery time is here defined as the sum of the pulse decay time, i.e. the characteristic time at which the signal is reduced to $1/e$ times its maximum value, and the time in which the pulse is saturated, shown in Figure 5.12b. The study of the detector behavior in saturation is important since it is related to its Dead Time, which is one of the main requirement driving the CryoAC design ($D_T < 1\%$). From the plots in Figure 5.12 is possible to evaluate for the CryoAC DM a detector saturation threshold of $\sim$ 1.3 MeV, and assess that the recovery time in saturation grows roughly logarithmic with the deposited energy.
Although the DM does not have requirements related to these aspects, these kind of studies are useful in view of the CryoAC Flight Model design.

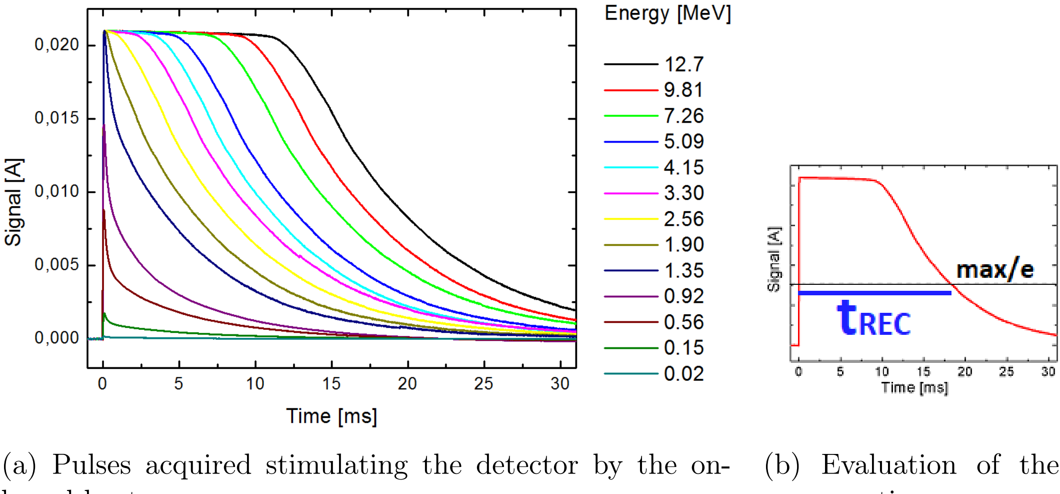

(a) Pulses acquired stimulating the detector by the on-board heaters

(b) Evaluation of the recovery time.

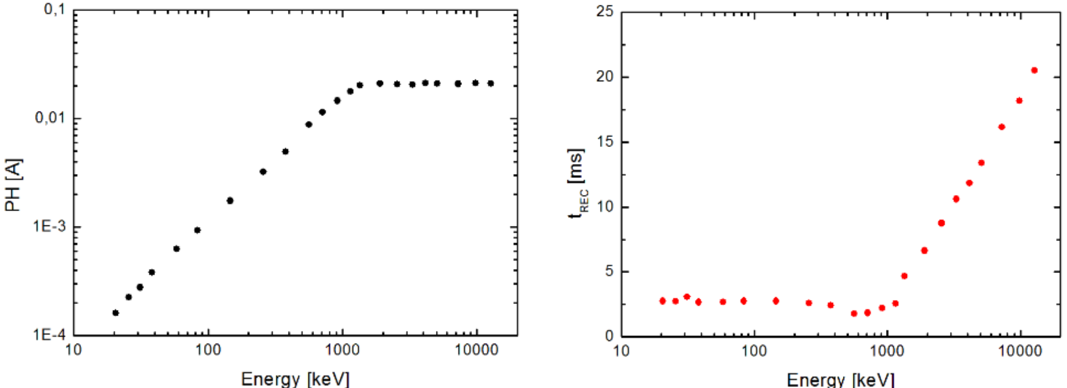

(c) Pulse Height as a function of the energy.

(d) Recovery time as a function of the energy.

Figure 5.12: CryoAC DM saturation threshold and recovery time. (a): Pulses acquired stimulating the detector with the on-board heaters up to 12.7 MeV. Saturation starts at $\sim$ 1.3 MeV. (b): Evaluation of the recovery time for saturated pulses. (c): Pulse Height as a function of the energy. Saturation starts at $\sim$ 1.3 MeV. (d): Time as a function of the energy. Once the detector is in the saturation regime the recovery time grows logarithmic with the deposited energy. From [53].

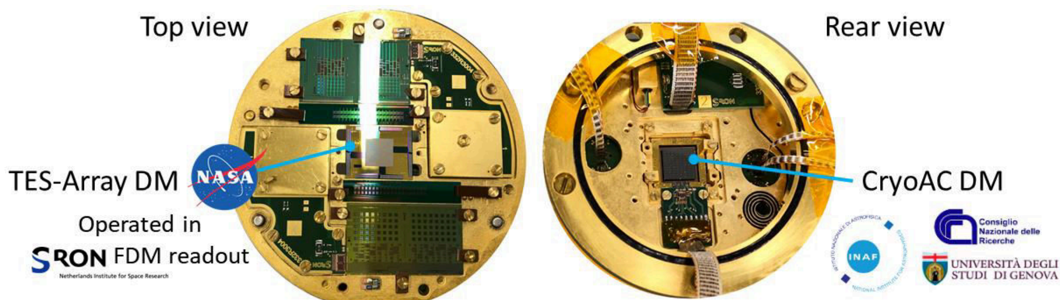

Figure 5.13: The detectors plate inside the SRON 40-pixel-B setup, showing both TES array DM (Top view) and CryoAC DM (Rear view). From [30].

5.2.2 Joint tests of AC-S10 and the NASA TES-array DM

First joint test of X-IFU TES array and CryoAC Demonstration Models were performed mounting them in the SRON FDM 40-pixel-B setup setup, 0.5 mm each other in Utrecht at SRON. The setup, visible in Figure 5.13, was representative of the one in the X-IFU FPA and was operated by Matteo D'Andrea and SRON team during the COVID-19 limitations. Several tests, from compatibility tests of the two detectors to anticoincidence capability demonstration were performed [30]. I am currently participating to the final measurements in the full Demonstration Model setup with the NASA TDM readout.

The microcalorimeter TES Array Demonstration Model

The microcalorimeter TES array DM is a 32×32 pixels array fabricated at NASA/GSFC [26]. The main characteristics of the chip are summarized in Table 5.2. The detector has been operated connecting simultaneously 20 pixels of the array.

Component	Characteristics
TESs	Mo/Au bilayer (35 nm/108 nm thick), 100×100 μm^2, $T_C \sim 87$ mK, $R_N \sim 51$ $m\Omega$
Absorbers	Au/Bi (2.50 μm/3.39 μm thick), 240×240 μm^2, 250 μm pitch
Membranes	SiN (0.5 μm thick)
Leads	Nb (bottom)/$SiO2$/Nb (top) (154 nm/260 nm/212 nm thick), width: 6 μm (bottom)/3 μm (top)

Table 5.2: TES Array Demonstration Model chip (ATH-1 G) characteristics. From [30].

Compatibility tests

First, it has been verified that the microcalorimeter TES array pixels show similar performance before and after the introduction of the CryoAC in the

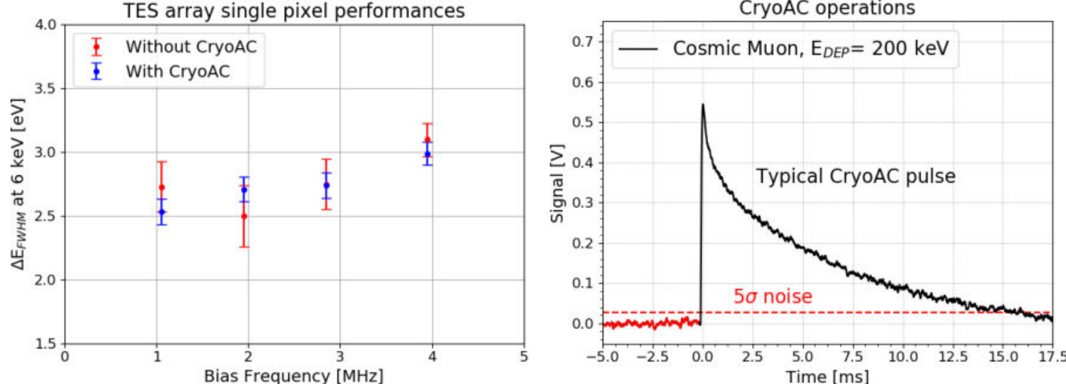

(a) TES array performances before and after CryoAC integration.

(b) Typical pulse generated by a cosmic muon on the CryoAC.

Figure 5.14: TES array and CryoAC DMs operations. (a): TES array single pixel energy resolution FWHM before and after the integration of the CryoAC in the experimental setup. (b): Typical pulse generated by a cosmic muon interacting with the CryoAC with its 5σ noise. From [30].

setup. In Figure 5.14a are shown the ΔE_{FWHM} measured on $Mn-k\alpha$ complex at 6 keV of 4 reference pixels operated at different FDM bias frequencies, from 1 MHz to 4 MHz, measured in the 40-pixel-B setup with and without the CryoAC to have a first evaluation the performances. No significant degradation has been observed in the two configurations, within a statistical accuracy around 0.3 eV.

On the CryoAC side, it has been verified the detector compliance with the functional requirements of Figure 5.1. In the integrated setup the detector has been operated at $T_{bath} = 50\ mK$, with an assessed total power dissipation $P_{TOT} = 3.3\ nW$ and a first trigger joint test between ATHENA X-IFU TES Array and CryoAC threshold $E_{threshold} = 8\ keV$, fulfilling the DM requirements. The typical pulse detected by the CryoAC after the interaction with a cosmic muon can be seen in Figure 5.14b.

To assess the impact of CryoAC operations on the magnetic environment at TES array level, it has been performed a magnetic field scans on the microcalorimeter TES array pixels visible in Figure 5.15. These measurements consist in varying the magnetic field normal to the TES array via a magnetic coil in the setup, and monitoring its biased pixels baseline level. Typically, this level shows a maximum in correspondence of the optimal magnetic field value, i.e. the value that cancels the residual magnetic field at the pixel level. The magnetic field scans have been performed while operating the CryoAC at different bias current corresponding to different colors in Figure 5.15. As already pointed out the CryoAC wiring has been designed with anti-inductive niobium striplines to limit the electromagnetic coupling with the microcalorimeter TES array. The scans have not highlighted any change in the magnetic environment

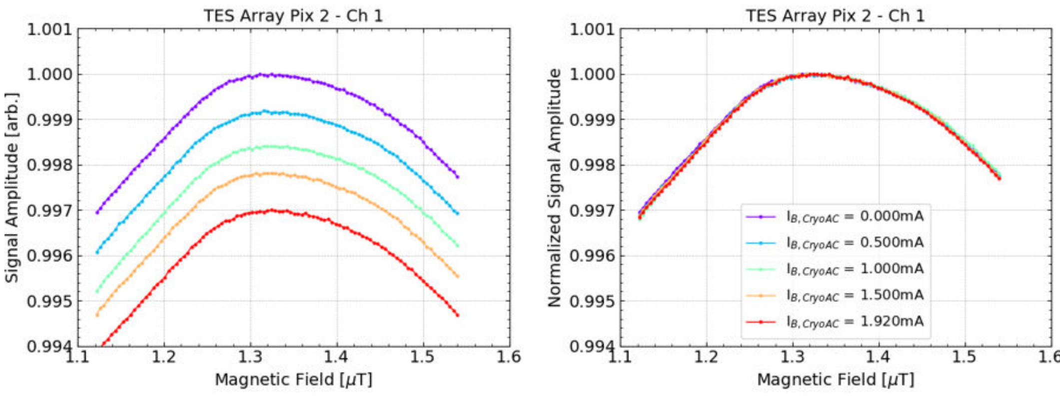

(a) : Signal vs normal magnetic field. (b) : Normalized signals of (a)

Figure 5.15: Magnetic scan performed on a TES array pixel for different CryoAC bias currents. (a): Baseline level of the pixel as a function of the magnetic field. (b): Same plot with the signal amplitude normalized at maximum level for each curve. From [30].

at TES array level induced by the CryoAC, since the parabolic shape and the maximum position remain the same for each acquired curve. Differences in the absolute signal amplitude are due to slow thermal effects related to the change of the CryoAC power dissipation. Measurements have been repeated for different pixels, obtaining similar results. Then, is possible to conclude that the typical CryoAC DM bias currents do not have a significant magnetic impact on the TES array.

From the performance point of view, it has been also performed the dynamic cross talk measurement, visible in Figure 5.16. In this case, it has been injected high-energy thermal pulses on the CryoAC via its on-board heaters, higher than 1 MeV with 10 Hz frequency. Looking simultaneously at the signal on TES array blind pixels, using a trigger generated by the CryoAC via a dedicated custom electronics. The results on averaged signal shown no evidence of significant cross talk on the TES array down to the level of 0.1 eV, when the CryoAC develops a pulse. In addition, the measurement has been repeated for different pixels and CryoAC bias currents without noticing significant differences.

AntiCoincidence measurements

In the end, long time joint measurements were performed joint long measurements with both detectors to detect coincidence signals due to cosmic muons as visible in Figure 5.17. The setup hosted a ^{55}Fe source to test the TES array response at 6 keV. 19 pixels of TES microcalorimeter array were operated in multiplexing mode for 890 ks (around 10 days) acquiring the signals from the ^{55}Fe source together with the CryoAC, collecting 286 coincidence events from cosmic muons. The observed count rate is 1.6 $cts/cm^2/min$, in agreement with the expectations for cosmic muons [76].

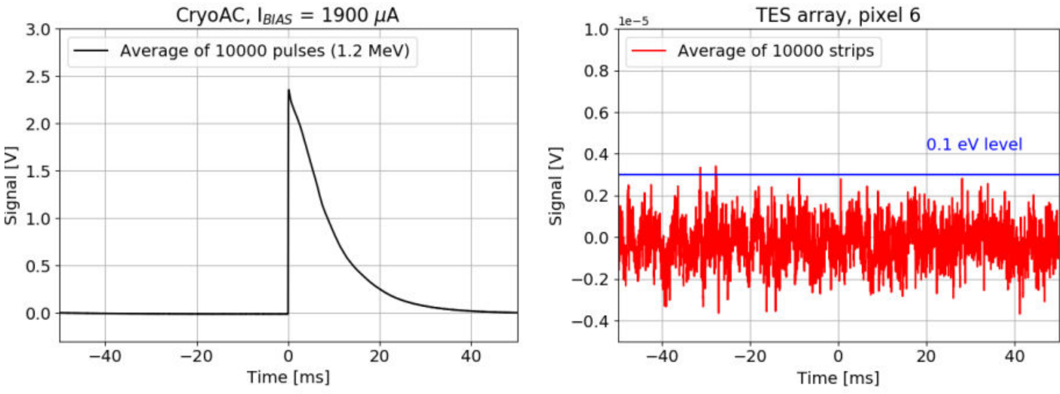

(a) Average CryoAC thermal pulse. (b) Average signal on the TES array

Figure 5.16: Dynamic cross talk measurement. (a): Average of 10000 thermal pulses of 1.2 MeV generated in the CryoAC by the on-board heater. (b): Average of the 10000 simultaneous triggered strips of signal on a TES array pixel, while measuring the thermal pulses on the CryoAC. It has been found no signal cross talk down to 0.1 eV. From [30].

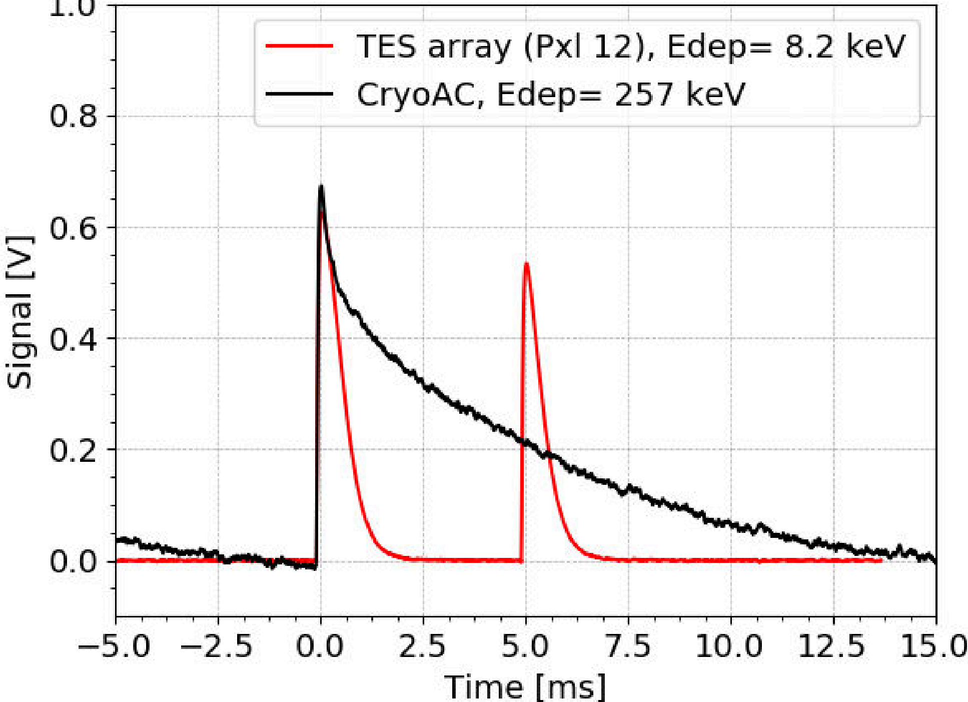

Figure 5.17: Pulses detected simultaneously by TES microcalorimeter array (red line) and CryoAC (black line). On TES array, the first pulse is due to a background particle (detected also by the CryoAC), while the second one is due to an X-ray photon from the ^{55}Fe source that is correctly detected only by the TES array. From [30].

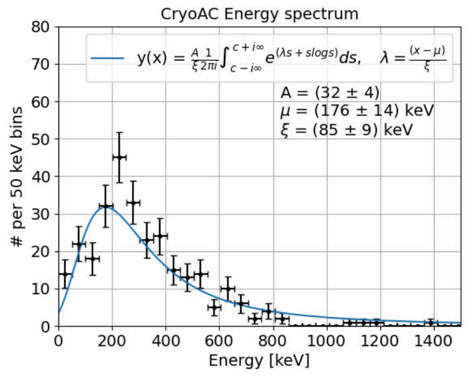

(a) Energy depositions on CryoAC.

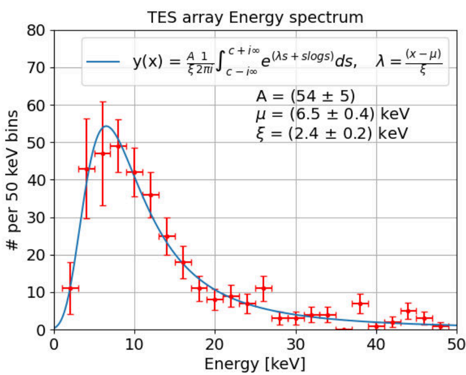

(b) Energy depositions on TES array.

Figure 5.18: Muons detecting events spectra fitted by Landau Distributions. Plots are referred to Energy depositions on CryoAC (a), and on TES array (b). From [30].

For all collected events, both the energy deposition on the CryoAC and on the TES array were analyzed. The acquired spectra are shown in Figure 5.18. The spectra are consistent with the expectations for Minimum Ionizing Particles (MIPs), showing Landau distribution shapes and peaking energies of $\sim 7\ keV$ for the TES array and $\sim 200\ keV$ for the CryoAC.

5.2.3 DM measurements conclusions

The detector is compliant with its requirements, showing a total power dissipation of $2.6\ nW$ at $50\ mK$ and a low energy threshold $< 3\ keV$. The on-board heaters are a useful option to optimize the detector operation, by reducing the total power dissipation at low temperature. They also enable numerous calibration measurements on the detector that could be repeated during the flight, e.g. thermal conductance, and detector response in linear and saturation regime. The first joint operation between the X-IFU TES microcalorimeter array and CryoAC Demonstration Models, performed in a FDM setup, shows that the detectors can properly operate together. No significant magnetic coupling or cross talk have been measured. The performed tests represents an important step towards the FPA development. In particular, the simultaneous detection of cosmic muons on TES array and CryoAC has provided a first demonstration of the anticoincidence capabilities of the system, representing a milestone for the X-IFU project. Anyway, these measurements would be repeated in a more representative setup of the mission with a TDM based readout with DC biased pixels as it is the most mature technology for X-IFU aims [77]. However, pixels operated under AC bias (FDM) suffer a lower magnetic field sensitivity than pixels operated under DC bias (TDM). Since the TES array and CryoAC interaction is strongly related to the magnetic coupling between the detectors, the new compatibility measurements that we are currently taking at SRON with the DC-bias setup are of great importance

to fix a the whole system, considering the mission redefinition.

5.3 Measurements of the detector thermal properties

5.3.1 Review of TES-substrate thermal coupling measurements

To have full control over the operational parameters of the detector, it is important to the evaluate the thermal conductance between the electrons in the TES and phonons in the substrate.

A first measurement of the electron-phonon coupling inside iridium was done in 2008 in Genoa LTD lab [78] where it was found $g_{e-p} = 5.4{\times}10^4\ W/Km^3$. The value was found by fitting the decay time of the pulse signal at a very low *alpha* working point, thus with negligible G_{ETF} (0.1% estimated error).

A second measurement was made in 2021 [79], where we obtained $g_{e-p} = 8.8 \times 10^5\ W/Km^3$. In this measurement the method followed was different: G was calculated from the power on the TES as function of its temperature, at different thermal bath temperatures.

The two values are quite distant, a factor 16, anyway there are several differences in the two measurements:

- materials, 2008 measurement is done on a Ir TES while 2021 one on Ir/Au (Ir thermal capacity is $\sim$ 10 times higher than gold one). Also wiring where different, aluminum the first and niobium the second;
- analysis, 2008 measurement was obtained by fitting the pulse signal decay time at a very low *alpha* working point, while 2021 was obtained by calculating the Joule power dissipated by the TES as a function of its temperature;
- volumes, TES used in the two measurement were $75 \times 75 \times 0.06\ \mu m^3$ in 2008 and $50 \times 50 \times 0.15\ \mu m^3$ in 2021;

Furthermore, the 2021 measurement need more data with low α working points and could be improved with more thermal bath temperatures to fit the range and the power law.

Anyway, the two setup are very similar. Both measurements were done with the Genoa LTD measurement setup described in Section 5.1 illuminating the two TES with an optical laser at 439 nm (2.824 eV) PLP-10-044, Hamamatsu Photonics K.K. with 100 ps pulse-length, through an optical fiber in the cryostat. The setup is shown in Figure 5.19a. This because the only possibility to directly excite electrons inside the TES is through an electromagnetic field.

From these considerations our g_{e-ph} value should be for sure higher than the 2008 one and could be between the two values. To check and have a more accurate measurement for our detector, considering that is not possible to

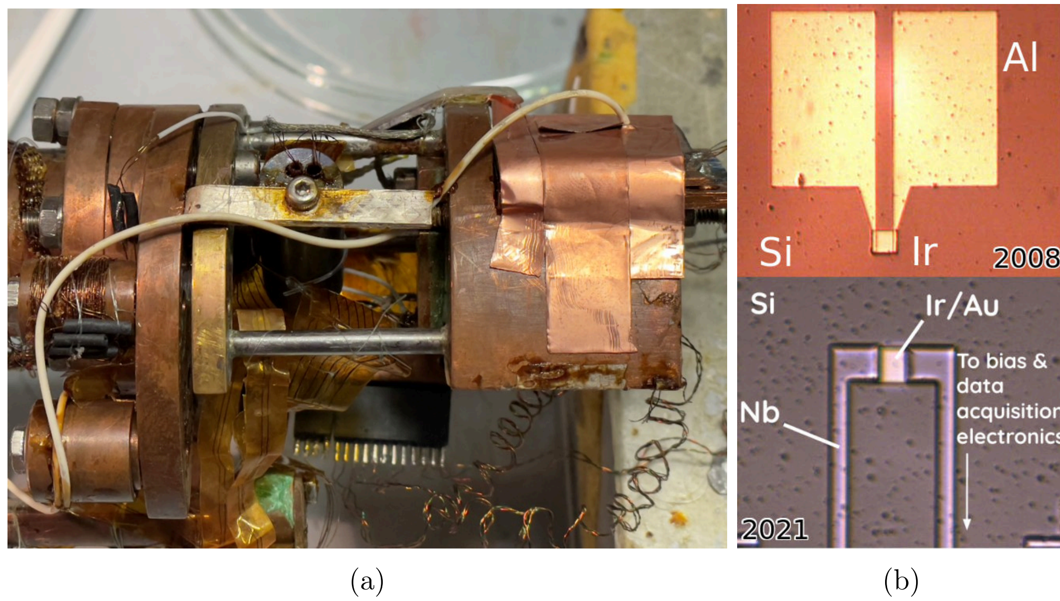

(a) (b)

Figure 5.19: (a): Optical fiber fixed to the readout system inside the Kelvinox 25. The fiber is thermalized at several stages in the fridge, then coupled to the shield for the 4 K radiation on the detector. (b): Top, 75×75 μm Ir TES of 2008 measurement. Bottom, 50×50 μm Ir/Au TES of 2021 measurement.

disentangle the electron phonon coupling from the Kapitza component due to the coupling between TES and substrate phonon[1], we have prepared a CryoAC prototype with a single TES to measure its thermal properties and deepen our knowledge on $Ir/Au - Si$ thermal conductance and Ir/Au thermal capacity. In the next Section the first measurements with this detector are presented. Unfortunately we did not already measured accurately those two properties.

5.3.2 Pure thermal detector measurements

To test the pure thermal performance of the CryoAC detector was designed and fabricated a detector inspired by the DM visible in Figure 5.20. The main difference is the single TES of 2×1 mm^2, 80 times the DM's single TES area. A single TES, with total area equal to that of the array of 96 TESs, makes it possible to illuminate the detector at a point on the absorber several millimeters away from the sensor and detect only the thermal part of the signal, according to the explanation of signal generation seen in Section 2.3, and at the same time keep the volume of the TES, thus its heat capacity, similar. The detector has only a gold heater and simplified Nb wiring with two parallel lines.

The complete analysis and measurements are in progress and we are prepar-

[1]The Kapitza thermal conductance power law has exponent 3 and is proportional to the contact area [72], so the total thermal conductance between TES electrons and substrate phonon is dominated by the electron-phonon coupling inside the TES at low temperature and small contact areas

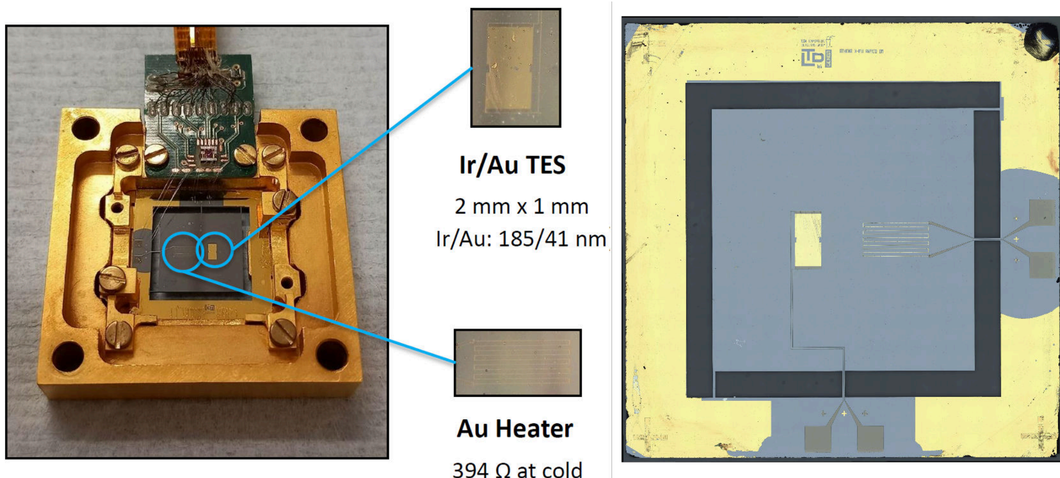

Figure 5.20: The pure thermal prototype to study the CryoAC performances. Is visible the single Ir/Au TES area equal to 80 CryoAC DM TES, the single heater with resistance comparable to the 4 CryoAC DM heaters, and the simplified wiring that is composed by two parallel lines.

ing a paper on it. In any case, I will present the first results based on the first measurements at INAF conducted by Claudio Macculi, Matteo D'Andrea and Guido Torrioli.

From the operational point of view, the peculiarity of this model is its broad resistive transition, visible in Figure 5.21. We have taken advantage of the problems caused by etching processes on the Ir/Au superconducting transition to cover a wide temperature range of the working points of the detector and to study its characteristics with temperature. However, this will leads to a low α.

The first measured parameter was the thermal conductance towards the thermal bath. This was already measured on AC-S10 and we compared the two results, see Figure 5.22. The two conductances are fully compatible with each other and with a phonon mediated transport model. The differences could be related to the position of the heaters, one in the middle for the thermal prototype and 4 in correspondence of the silicon bridges for AC-S10.

Then, the sample have been illuminated with a ^{55}Fe source from the backside, in a corner, far from the TES to highlight the thermal response. Results are visible in Figure 5.23 which shows a high spectral resolution (173 eV FWHM) compared with AC-S10 (1.3 keV FWHM), where the signal is dominated in the first μs by the a-thermal component. While as visible in Figure 5.24 on this prototype the response is basically thermal. 5.24 Instead, in Figure 5.25 is shown a comparison between the two spectra, obtained from the raw pulse heights of the thermal prototype and AC-S10 for ^{55}Fe and thermal heaters calibrating pulses. The spectra have been normalized referring to acquisition time as the cont rate were the same for both, and is appreciable the 6 keV peak broadening due to the a-thermal signal.

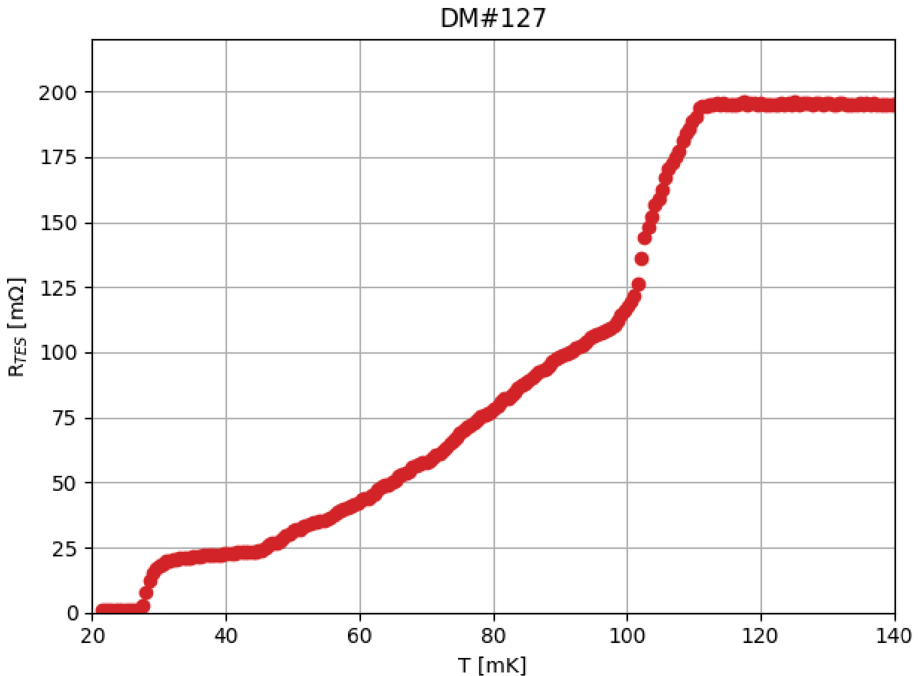

Figure 5.21: Resistance of the TES in function of the absorber temperature (bias current 1 μA). The superconducting transition covers about 80 mK from 30 to 110 mK.

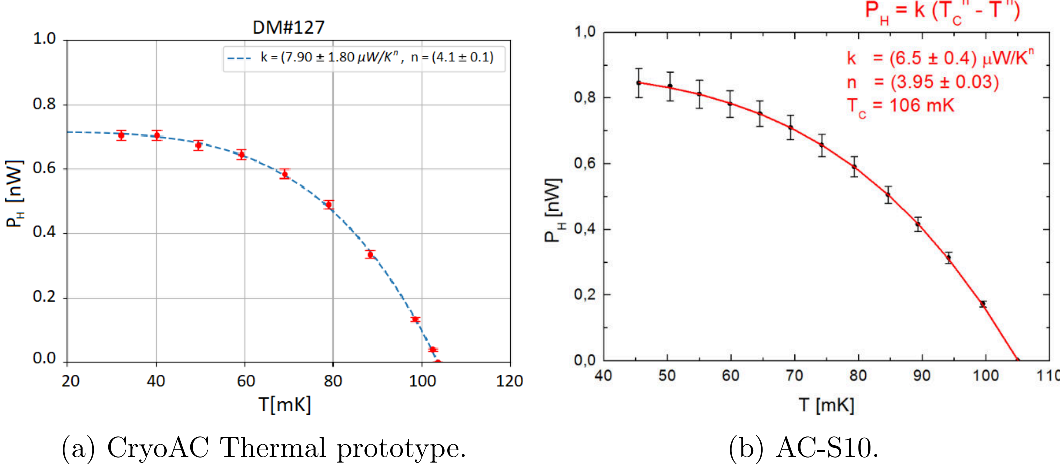

(a) CryoAC Thermal prototype. (b) AC-S10.

Figure 5.22: Power injected on the absorber to bring the unbiased TES into the transition as a function of the thermal bath temperature to find out the Detector Thermal conductance toward the thermal bath. (a): Power curve for the CryoAC thermal prototype. (b) same measurement done on AC-S10, [53]. The two conductivity values for the silicon bridges are fully compatible with each other.

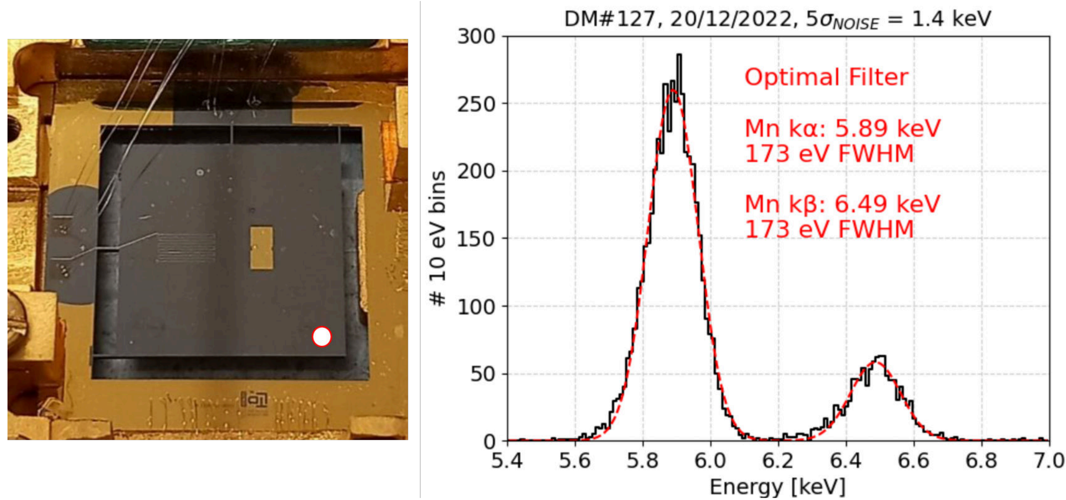

Figure 5.23: ^{55}Fe spectra with a 173 eV spectral resolution (AC-S10 ΔE_{FWHM} = 1.3 keV) both $Mn\ k\alpha$ and $k\beta$ are visible. The improvement in ΔE_{FWHM} is due to the signal that is essentially just thermal.

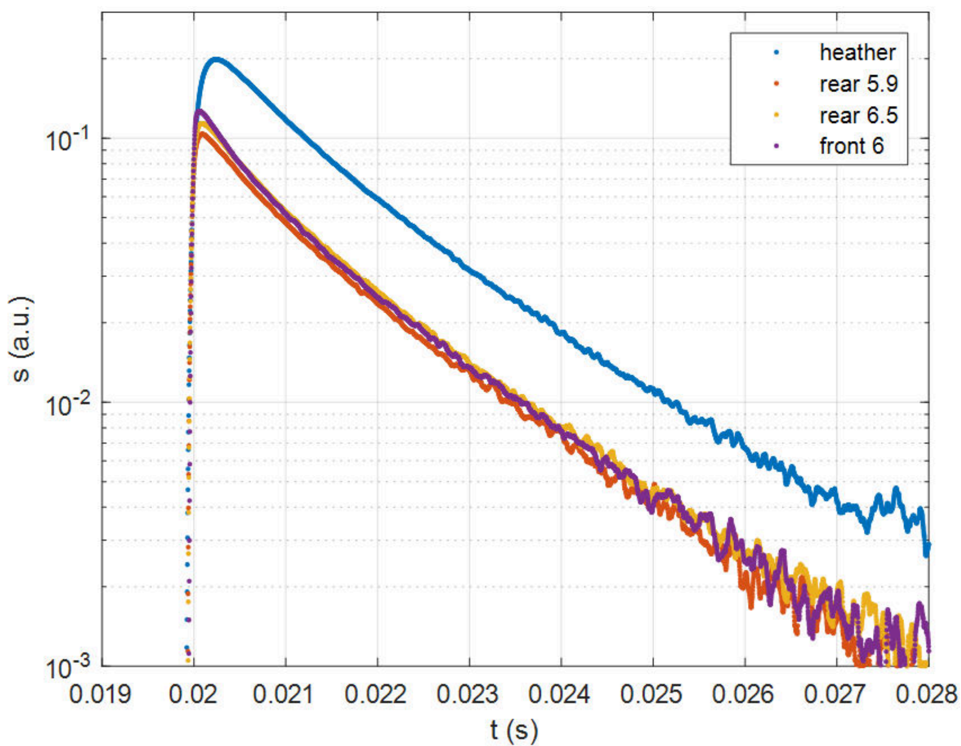

Figure 5.24: Thermal pulse response of the prototype. Are compared the 12 keV from Heater in blue, together with signals from ^{55}Fe from the back, aligned with the absorber corner (orange and yellow) and from the front nearer to the TES in purple. The purple signal is the one with the higher a-thermal component.

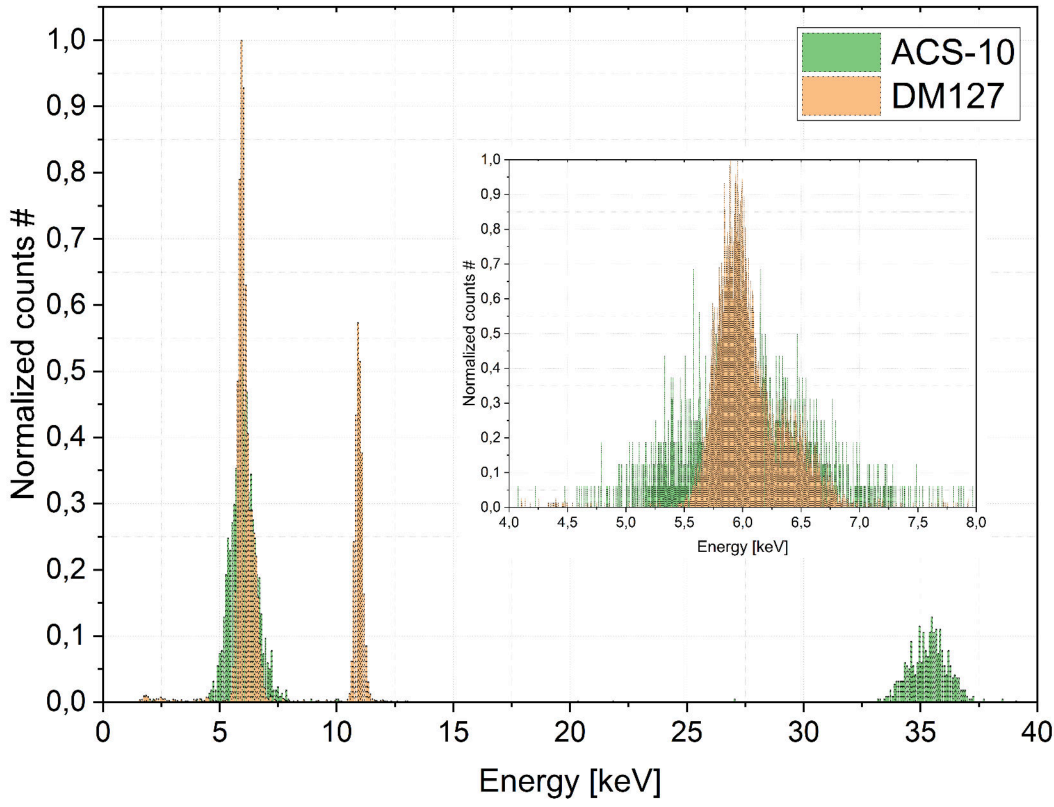

Figure 5.25: Acquired energy spectrum by raw pulse heights. are visible at 6 keV the spectra from ^{55}Fe and the 12 keV, for the thermal prototype, and the 35 keV, for AC-S10, heaters calibrating pulses. In the inset a zoom around the ^{55}Fe peak.

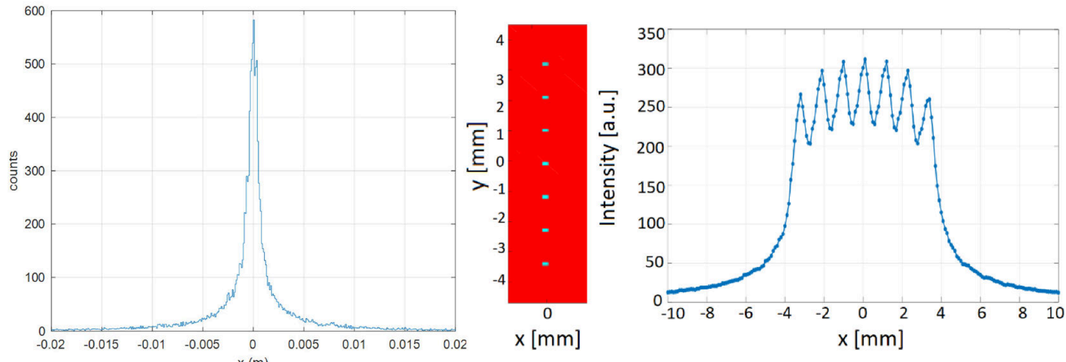

Figure 5.26: left) Integrated a-thermal flux at the surface vs x-axis: the FWHM is about 1 mm. right) Signal height fluctuations due to the TES array pitch size: here the simulation is done for a liner TES array of 1 mm pitch size like in the actual CryoAC. 20% total height fluctuations are predicted moving the source along the vertical axis below the linear array. From [43].

In Table 5.3 are summarized some parameter of the thermal prototype together with AC-S10 one and CryoAC requirements.

Parameter	DM#127 ($P_H = 0\ nW$)	AC-S10 ($P_H = 0\ nW$)	CryoAC requirement	Note
Low Energy Threshold	1.4 keV	$\sim 3\ keV$	$< 6\ keV$	
Bias current	1 mA	8 mA		$< \sim 3\ mA$ requested by FPA
Power dissipation @ 50 mK	9 nW	30 nW	$< 9\ nW$ / pixel	Possible reduction tuning heaters and R_S
Rise Time	25 μs	15 μs	$< 15\ \mu s$	max 30 μs for time tagging
ETF Decay Time	1.3 ms	700 μs	$< 250\ \mu s$	tunable with α and silicon bridge aspect ratio
Thermal decay time	2.4 ms	$\sim 3\ ms$	$< 2.5\ ms$	
ΔE_{FWHM} @ 6 keV	170 eV	1.3 keV	$< 2.5\ keV$	

Table 5.3: Parameters of the thermal prototype (DM#127) compared to AC-S10 and CryoAC requirements. Some notes on the values are necessary: (a) the Bias current and power dissipation for AC-S10 are very high due to the current-dependant parasitic resistance, (b) the rise time is influenced by the a-thermal part of the signal that makes it faster, (c) the ETF decay time is lower in the thermal prototype due to the wide superconducting transition.

5.4 Measurement of the a-thermal phonon hotspot

In Section 2.3.3 I've presented the size of the phononic hot-spot on the TES instrumented surface for a typical event simulated in the bulk. The actual pitch size for TES should be defined by a direct measurement of this hot-spot, replicated in Figure 5.26.

The method we have proposed, of measuring the phonon hot-spot profile consists in exciting the detector with a movable source of collimated gamma ray

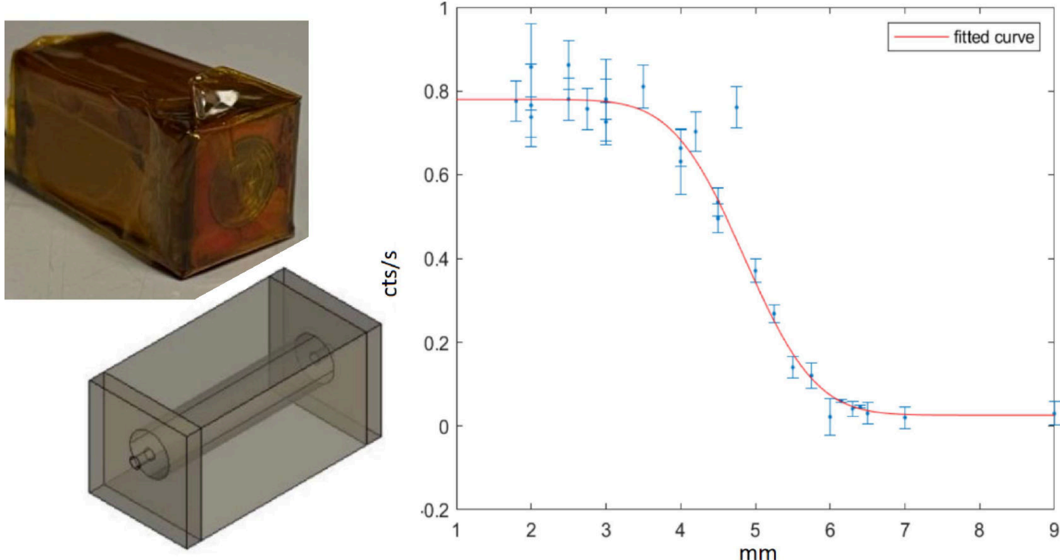

Figure 5.27: left) CAD drawing of collimator for ^{241}Am - 60 keV source and "shaped" plastic capsule aligned and glued on backside of collimator and covered with Kapton adhesive tape. right) 60 keV integrated beam profile measured with Ge detector of two aligned beam collimators considered in text. From [43].

radiation and measuring the energy associated with the a-thermal component of the generated pulses. The reference position for the hot-spot profile is that of the TES. The model predicts that the maximum a-thermal contribution occurs in the position of the TES and that its amplitude decays to 1/2 in about 1 mm.

We have investigated what technique could be used to create well collimated beams, available at 100 mK, using low intensity sources, that can be integrated in a $^3He -^4 He$ dilution cryogenic system and in a limited amount of space. The reliable solution based on our experience of using radioactive sources in a cryogenic environment is to use the ^{241}Am gamma source in a passive collimator. Among the simulated solutions that included a tungsten pore collimator and a two-hole aligned lead collimator, we selected the latter for the best compromise between beam width and throughput. The pore collimator also had feasibility problems as lead does not resist precision laser drilling and tungsten on the contrary was too hard to drill about 2 mm as required by the simulations. It has a half-height width of about 1.3 mm and allows a rate of one range per second. Since the beam width of the optimized collimator cannot be much smaller than the expected hot-spot size, an appropriate data analysis based on the deconvolution methods is required to account for this.

The integrated linear count rate of the 60 keV beam as a function of distance from the knife-edge screen for the beam width measurement is shown in Figure 5.27 together with the collimator.

We have verified that under these conditions a technique of deconvolution of the measured hot-spot profile with the beam intensity function, can allow

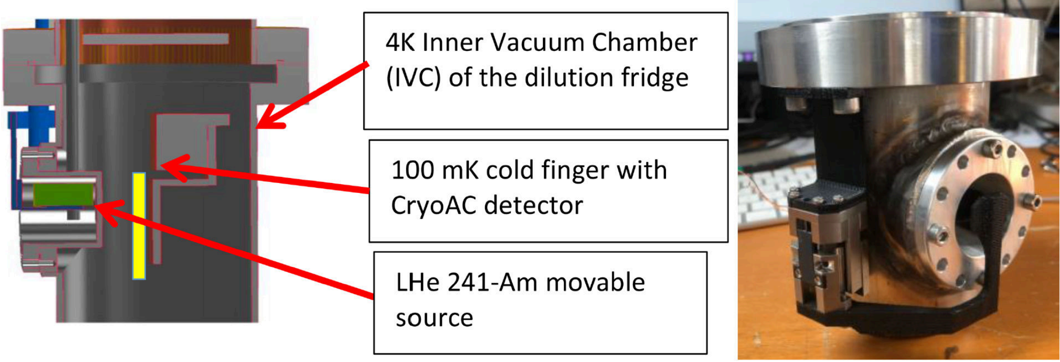

Figure 5.28: left) Vertical section of the source (green), window (brown) and CryoAC detector (yellow) in the dilution fridge. right) Assembly of cryogenic 60 keV ^{241}Am piezo-moto movement in its final position. From [43].

us to derive a profile very close to the genuine hot-spot profile.

The experimental set-up was defined and manufactured. The ^{241}Am source with collimator is mounted on a stand that can be moved freely in a vertical direction. This will be placed in the liquid helium outside the inner vacuum chamber (IVC) of the dilution fridge. The inner vacuum chamber wall has been duplicated and modified to accommodate an aluminum window thin enough to have no significant impact on the 60 keV beam, but strong enough to hold the vacuum at 4.2 K.

The window fits into the hole in the wall to approach the detector mounted on the cold finger of the mixing chamber. The window can be removed at 300 K to carry out the fine alignment operation of the beam on the detector.

In the latest version, the ^{241}Am source with the collimator is moved vertically with a piezo cryogenic motor that has a travelling distance of about 2 cm, which is greater than the size of the detector itself, therefore covering it. Figure 5.28 shows the new drawings and the set-up of the source assembly on the outside of the IVC chamber.

The assembly was tested at 77 K in a glass Dewar at which almost the entire linear thermal expansion of the materials is experienced. The glass Dewar allows any unexpected behavior to be visually measured. We have seen that the complete system works as expected, the piezo motor allows the entire travel distance to be covered. It was observed that a small horizontal displacement due to thermal contraction must be compensated.

Data taking has not yet been carried out because the detector is waiting to be manufactured with the new procedures, but the lithographic masks for the fabrication of the detector with only one TES and a row of TESs and the set-up are ready. The duration of the experiment and data analysis is expected to be about 3 months.

Conclusions

In my Ph.D. thesis, I developed the first demonstration model that was integrated into the SRON facility. I worked on the production process and its impact on performance, studying modifications and methods to mitigate issues. I contributed to the development of the model of the a-thermal hot-spot generation and to the study of a method to measure its characteristics. I performed full characterizations and measurements of electro-thermal parameters on several prototypes of the CryoAC. I made the first structural models that were undergone to the vibration loads expected for the mission.

- The studies carried out during these years have allowed us to improve our understanding of how the detector works both from the thermal and mechanical point of view.
- The work on the fabrication process gave us a better understanding and control of the manufacturing technologies and overcoming issues such as the current-dependent parasitic resistance of AC-S10;
- Experimental data and developed models allow us to better understand and control all detector parameters in order to carefully tune the CryoAC characteristics within the mission requirements.

Few points still open are:

1. the fine tuning of the thermal model with dedicated measurement of thermal parameters such as actual thermal capacity and electron-phonon conductance,
2. the sizing of the phonon hot-spot for the a-thermal signal contribution,
3. a final trade-off between the absorber configuration, 1-pixel or 4-pixel.

However, starting from my work, it is possible to make a provisional design of the Engineering Model despite these open points, to be refined in a short time.

Appendix A

Manufacturing report

In this Appendix I've reported the Manufacturing Report prepared to take note and guide operators in the CryoAC fabrication.

Title **DM#00 Logbook**

Prepared by : Lorenzo Ferrari Barusso, Manuela Rigano Date :

Inputs by : Lorenzo Ferrari Barusso, Flavio Gatti Date :

Checked by : Date :

Agreed by : Date :

Authorized by: Flavio Gatti Date :

DISTRIBUTION LIST

POS.	NAME	DEPT.	N° OF COPIES	FULL COPY

DOCUMENT CHANGE RECORD

Issue	Date	Changed Section	Description of Change

Abbreviations and acronyms

Item	Meaning
AIT	Assembly Integration and Test
ASI	Agenzia Spaziale Italiana
ASW	Application Software
CADM	Configuration and Data Management
CNR	Consiglio Nazionale delle Ricerche
CPO	Central Project Office
CryoAC	Cryogenic Anticoincidence
FA	Funding Agency
FEE	Front End Electronics
FPA	Focal Plane Assembly
GSE	Ground Segment
ICU	Instrument Control Unit
INAF	Istituto Nazionale di Astrofisica
LPO	Local Project Office
MP	Management Plan
OBS	Organization Breakdown Structure
PA	Product Assurance
PBS	Product Breakdown Structure
PS	Project Scientist

SM	System Manager
UniGE	University of Genova
UniPA	University of Palermo
WBEE	Warm Back End Electronics
WBS	Work Breakdown Structure
WEE	Warm Electronics
X-IFU	X-ray Integral Field Unit

Applicable Documents

[AD#]	Doc. Reference	Issue	Title
[AD1]			
[AD2]			

Reference Documents

[RD#]	Doc. Reference	Issue	Title
[RD1]	XIFU-UNGE-CRA-LI-0001		Declared Material List
[RD2]	XIFU-UNGE-CRA-LI-0002		Declared Process List
[RD3]			CryoAC_Chip_ Manufacturing_Flow
[RD4]			Cs test procedure

Table Of Contents

1 INSTRUMENT DESCRIPTION 6
2 DM CONFIGURATION DESCRIPTION 6
2.1 Elements composing DM 7
2.1.1 Fabrication process phases diagram 7
2.1.2 Material on DM 8
3 OPERATING LOG 8
3.1.1 Chip preparation 8
3.1.2 TES Fabrication 14
3.1.3 Pt Heaters 24
3.1.3.1 00-00-202x Negative Micro Photo Lithography (Procedure: XIFU-UNGE-CRA-PR-0001) Mask 2.0 24
3.1.3.2 Ti sticking layer deposition (Procedure: XIFU-UNGE-CRA-PR-0004) 27
3.1.3.3 00-00-202x Pt heater growth by e-beam evaporation (Procedure: XIFU-UNGE-CRA-PR-0004) 28
3.1.3.4 00-00-202x Lift-off 1 (Procedure: XIFU-UNGE-CRA-PR-0013-r00) 29
3.1.4 Thermal contact 30
3.1.4.1 00-00-202x Negative Micro Photo Lithography (Procedure: XIFU-UNGE-CRA-PR-0001) Mask 3.0A 31
3.1.4.2 00-00-202x Ti Sticking Layer (Procedure: XIFU-UNGE-CRA-PR-0004) 33
3.1.4.3 00-00-202x Au growth e-beam (Procedure: XIFU-UNGE-CRA-PR-0004) 34
3.1.4.4 00-00-202x Lift-off 1 (Procedure: XIFU-UNGE-CRA-PR-0013-r00) 35
3.1.5 Nb Wire Lower Strip line 37
3.1.5.1 00-00-202x Negative Micro Photo Lithography (Procedure: XIFU-UNGE-CRA-PR-0001) Mask 3.0B 37
3.1.5.2 00-00-202x Nb sample deposition by RF sputtering (XIFU-UNGE-CRA-PR-0005) 39
3.1.5.3 00-00-202x Lift-off 1 (Procedure: XIFU-UNGE-CRA-PR-0013-r00) 41
3.1.6 SiO Insulation 42
3.1.6.1 00-00-202x Negative Micro Photo Lithography (Procedure: XIFU-UNGE-CRA-PR-0001) 42
3.1.7.2 00-00-202x Silicon Oxide Deposition by thermal evaporator (Procedure: XIFU-UNGE-CRA-PR-0004) 45

3.1.6.2 00-00-202x Lift-off 2 (Procedure: XIFU-UNGE-CRA-PR-0014-r00) 46

3.1.6 Nb Wire Upper Strip line 47

3.1.6.4 00-00-202x Negative Micro Photo Lithography (Procedure: XIFU-UNGE-CRA-PR-0001) Mask 3.0A 48

3.1.7.3 00-00-202x Nb Deposition by RF Sputtering (Procedure XIFU-UNGE-CRA-PR-0005-r00) 50

3.1.7.4 00-00-202x Lift-off 2 (Procedure XIFU-UNGE-CRA-PR-0014-r00) 51

3.1.7.5 00/00/20xx TES Tested at room temperature. 61

3.1.8 RIE Final Etching; Deep Rie Etching with Bosch process 53

3.1.8.2 00-00-202x Negative Micro Photo Lithography (Procedure: XIFU-UNGE-CRA-PR-0001) Mask 3.0 A 53

3.1.8.3 00-00-202x Silicon Oxide Deposition by thermal evaporator (Procedure: XIFU-UNGE-CRA-PR-0004) 55

3.1.8.4 00-00-202x Al Evaporation - Frontside (Procedure: XIFU-UNGE-CRA-PR-0015-r00) 57

3.1.8.5 00-00-202x Lift-off 2 (Procedure XIFU-UNGE-CRA-PR-0014-r00) 57

3.1.8.6 Bosch etching process (Procedure XIFU-UNGE-CRA-PR-0016-r00) 58

3.1.8.7 Aluminum Hard mask Stripping (Procedure: XIFU-UNGE-CRA-PR-0008-r00) ... 60

1 Instrument description

Working principle

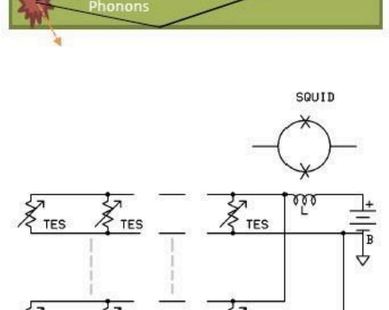

- Particles release energy inside the silicon substrate
- The energy produces phonons
- Phonons hit the TES network and increase its temperature
- TES network read in parallel as a single object

2 DM configuration description

«Planar design»

2.1 Elements composing DM.

Fabrication process

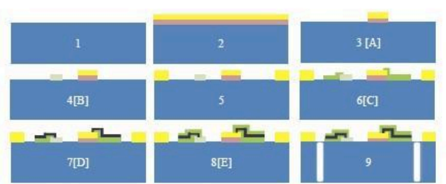

1. Silicon wafer
2. Ir:Au bilayer deposition by PLD
3. TES by Ir:Au bilayer etching
4. Pt heaters fabrication
5. Au thermalization layer deposition on rim
6. Niobium wiring (lower strip) fabrication
7. Silicon oxide insulation
8. Niobium wiring (upper strip) fabrication
9. Deep RIE:
   I. Al Hard-mask deposition
   II. Etching using bosch process
   III. Removal aluminum mask

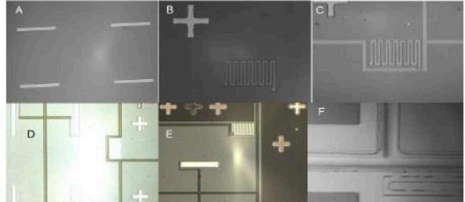

2.1.1 Fabrication process phases diagram

CryoAC -Chip Manufacturing Process Flow

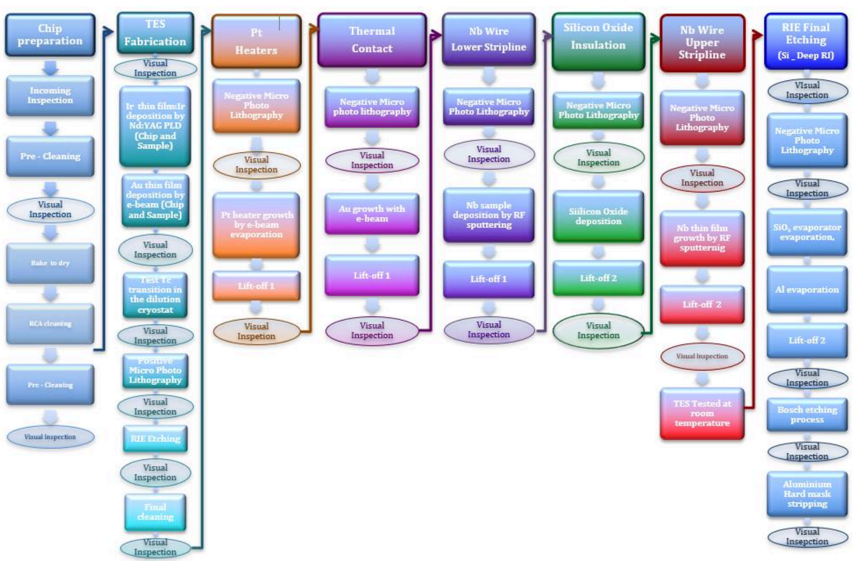

Reference documents for the processes are XIFU-UNGE-CRA-LI-0002 and CryoAC_Chip_ Manufacturing_Flow

2.1.2 Material on DM

All the materials present on SM are included in the DML [XIFU-UNGE-CRA-LI-0001]

3 Operating log

3.1 Chip preparation

3.1.0 **00-00-202x Incoming Inspection (Procedure: XIFU-UNGE-CRA-PR-0006-r00)**

Made in Clean Room under Optical microscope and camera CCD Wafer cut using dicing saw to nominally chip dimension: 16.6x16.6 $mm^{2.}$ **FBK slice "x";** Supplier FBK Foundation

3.1.1 **00-00-202x Pre – Cleaning (Procedure: XIFU-UNGE-CRA-PR-0007-r00)**

STEP	Description	Expected Value	Measured value	Remarks
1.	Prepare the ultrasonic cleaner: put DI water in it	Ok		
2.	Put in a beaker 60 ml of DI water and 2 ml of Extran AP 22 solution	60 ml 2 ml		
3.	Place the chip in the beaker and hold it with reverse action tweezers	Ok		
4.	Put the beaker with the sample in the grid container inside the ultrasonic bath	Ok		
5.	Make sure the water level is equal to or greater than that of the sample; if necessary, add water, making sure that the beaker remains in contact with the grid so that it does not start to float, thus risking tipping over	Ok		
6.	Start the ultrasonic cleaner timer and set for a time > 10 min	> 10 min		
7.	Withdraw the chip with reverse tweezers during sonication to avoid the deposition of contaminants when the sonication is finished	Ok		
8.	Wash the chip under the DI water flow to remove Extran AP 22 residues from the sample before passing the solvent wash	Ok		
9.	Prepare the ultrasonic cleaner: put DI water in it	Ok		
10.	Put in a beaker 60 ml of DI water	Ok		

11.	Place the chip in the beaker and hold it with reverse action tweezers	Ok		
12.	Put the beaker with the sample in the grid container inside the ultrasonic bath	Ok		
13.	Make sure the water level is equal to or greater than that of the sample; if necessary, add water, making sure that the beaker remains in contact with the grid so that it does not start to float, thus risking tipping over	Ok		
14.	Start the ultrasonic cleaner timer and set for a time > 10 min	> 10 min		
15.	Withdraw the chip with reverse tweezers during sonication to avoid the deposition of contaminants when the sonication is finished	Ok		
16.	Make a clean with solvent:			
16.1	Prepare the ultrasonic cleaner: put DI water in it	Ok		
16.2	Put in a beaker 50 ml of acetone	Ok		
16.3	Place the chip in the beaker and hold it with reverse action tweezers	Ok		
16.4	Put the beaker with the sample in the grid container inside the ultrasonic bath	Ok		
16.5	Make sure the water level is equal to or greater than that of the sample; if necessary, add water, making sure that the beaker remains in contact with the grid so that it does not start to float, thus risking tipping over	Ok		
16.6	Start the ultrasonic cleaner timer and set for a time > 10 min	>10 min		
16.7	Withdraw the chip with reverse tweezers during sonication to avoid the deposition of contaminants when the sonication is finished	Ok		
16.8	Rinse with 5 ml of acetone flush	Ok		
16.9	Rinse with 5 ml of Ethanol flush	Ok		
16.10	Dry with Nitrogen	Ok		
17.	Check the cleanliness of the chip surface under the microscope	Ok	Ok	

18.	If the chip is clean go on to the next procedure in the process flow or store in a vacuum box sample holder (VR tray gel pack);		Ok	
19.	If particles or another type of contaminants are detected, proceed with another solvent cleaning step with direct flow or spinner and/or subsequent passage in oxygen plasma			
Date: 00/00/202x	**Operator:**	**PA/QA:**		

3.1.2 00-00-202x Visual inspection (Procedure XIFU-UNGE-CRA-PR-0008-r00)

STEP	Description	Expected Value	Measured value	Remarks
1.	If the sample does not meet the acceptance criteria repeat the pre-cleaning procedure	Ok		
2.	FOTO			
3.	Go to the next process or store in a closed capsule	Ok		
Date: 00/00/202x	**Operator:**	**PA/QA:**		

3.1.3 00-00-202x Bake to dry (Procedure: XIFU-UNGE-CRA-PR-0010-r00)

STEP	Description	Expected Value	Measured value	Remarks
1.	Set the hot plate to 120°C	120 °C		
2.	use a glass slide as carrier	Ok		
3.	insert the chip on the hot plate, use the tweezers to slide the sample from the glass slide to the hot plate.	Ok		
4.	start the chronometer	Ok		
5.	Cover the chip with an half of glass petri and wait for a time >120 min	>120 min		
6.	After 120 minutes remove the chip from the cooking plate using the tweezers to slide it over the glass slide.	Ok		
	Operator:	**PA/QA:**		

Date: 00/00/202x		

3.1.4 00-00-202x RCA Clean (Procedure: XIFU-UNGE-CRA-PR-0009-r00)

STEP	Description	Expected Value	Measured value	Remarks
2.	Prepare one beaker and one crystallizer for each type of solution to use:			
2.1	PFTE for HF solution	Ok		
2.2	Pyrex/PFTE for ammonia hydroxide solution and for Hydrochloric solution	Ok		
3.	Reset chronometer	Ok		
4.	Put about 40 ml of every solution in his apposite beaker	Ok		
5.	Prepare a bottle of DI water to wash the chip after/before each step and pour 100 ml in each crystallizer	Ok		
6.	Have the waste containers of the solution used ready for use	Ok		
7.	RCA-1. **Organic Clean**: Removal of insoluble organic contaminants with a 5% H2O:NH4OH solution:			
7.1	Put the chip in the solution start the chronometer and wait 10 min	10 min		
7.2	After 10 minutes, gently take the chip with the tweezers, possibly holding it in a corner and rinse it with DI water flush in a dedicated crystallizer	Ok		
8.	RCA-2. **Oxide Strip**: Removal of a thin silicon dioxide layer where metallic contaminants may accumulate because of Organic-clean (RCA-1) using a diluted 10% H2O:HF solution.			
8.1	Put the chip in the solution start the chronometer and wait 30 sec	30 s		
8.2	After 30 sec, gently take the chip with the tweezers, possibly holding it in a corner and rinse it with DI water flush in a dedicated crystallizer	Ok		
9.	RCA-3. **Ionic Clean**: Removal of ionic and heavy metal atomic contaminants using a solution of 5% H2O: HCl.			
9.1	Put the chip in the solution, start chronometer and wait 10 min	10 min		
9.2	After 10 minutes, gently take the chip with the tweezers, possibly holding it in a corner	Ok		

	and rinse it with DI water flush in a dedicated crystallizer			
10.	Move the sample in a beaker with DI water	Ok		
11.	Rinse one more time in DI water flux	Ok		
12.	Dry with Nitrogen	Ok		
13.	Check the cleanliness of the chip surface under the microscope	Ok		
14.	Make a cleaning with solvents: **Repeat the Pre – Cleaning (Procedure: XIFU-UNGE-CRA-PR-0007-r00)**	Ok		
15.	Check the cleanliness of the chip surface under the microscope	Ok		
16.	If the chip is clean go on to the next procedure in the process flow or store in a vacuum box sample holder (VR tray gel pack);			
17.	If particles or another type of contaminants are detected, proceed with another solvent cleaning step with direct flow or spinner			
Date: **00/00/202x**	**Operator:**	**PA/QA:**		

3.1.5 00-00-202x Pre – Cleaning (Procedure: XIFU-UNGE-CRA-PR-0007-r00)

STEP	Description	Expected Value	Measured value	Remarks
1.	Prepare the ultrasonic cleaner: put DI water in it	Ok		
2.	Put in a beaker 60 ml of DI water and 2 ml of Extran AP 22 solution	60 ml 2 ml		
3.	Place the chip in the beaker and hold it with reverse action tweezers	Ok		
4.	Put the beaker with the sample in the grid container inside the ultrasonic bath	Ok		
5.	Make sure the water level is equal to or greater than that of the sample; if necessary, add water, making sure that the beaker remains in contact with the grid so that it does not start to float, thus risking tipping over	Ok		

6.	Start the ultrasonic cleaner timer and set for a time > 10 min	> 10 min		
7.	Withdraw the chip with reverse tweezers during sonication to avoid the deposition of contaminants when the sonication is finished	Ok		
8.	Wash the chip under the DI water flow to remove Extran AP 22 residues from the sample before passing the solvent wash	Ok		
9.	Prepare the ultrasonic cleaner: put DI water in it	Ok		
10.	Put in a beaker 60 ml of DI water	Ok		
11.	Place the chip in the beaker and hold it with reverse action tweezers	Ok		
12.	Put the beaker with the sample in the grid container inside the ultrasonic bath	Ok		
13.	Make sure the water level is equal to or greater than that of the sample; if necessary, add water, making sure that the beaker remains in contact with the grid so that it does not start to float, thus risking tipping over	Ok		
14.	Start the ultrasonic cleaner timer and set for a time > 10 min	> 10 min		
15.	Withdraw the chip with reverse tweezers during sonication to avoid the deposition of contaminants when the sonication is finished	Ok		
16.	Make a clean with solvent:			
16.1	Prepare the ultrasonic cleaner: put DI water in it	Ok		
16.2	Put in a beaker 50 ml of acetone	Ok		
16.3	Place the chip in the beaker and hold it with reverse action tweezers	Ok		
16.4	Put the beaker with the sample in the grid container inside the ultrasonic bath	Ok		
16.5	Make sure the water level is equal to or greater than that of the sample; if necessary, add water, making sure that the beaker remains in contact with the grid so that it does not start to float, thus risking tipping over	Ok		

16.6	Start the ultrasonic cleaner timer and set for a time > 10 min	>10 min		
16.7	Withdraw the chip with reverse tweezers during sonication to avoid the deposition of contaminants when the sonication is finished	Ok		
16.8	Rinse with 5 ml of acetone flush	Ok		
16.9	Rinse with 5 ml of Ethanol flush	Ok		
16.10	Dry with Nitrogen	Ok		
17.	Check the cleanliness of the chip surface under the microscope	Ok		
18.	If the chip is clean go on to the next procedure in the process flow or store in a vacuum box sample holder (VR tray gel pack);			
19.	If particles or another type of contaminants are detected, proceed with another solvent cleaning step with direct flow or spinner and/or subsequent passage in oxygen plasma			
Date: 00/00/202x	**Operator:**	**PA/QA:**		

3.1.6 00-00-202x Visual inspection (Procedure XIFU-UNGE-CRA-PR-0008-r00)

STEP	Description	Expected Value	Measured value	Remarks
1.	If the sample does not meet the acceptance criteria repeat the pre-cleaning procedure	Ok		
2.	FOTO			
3.	Go to the next process or store in a closed capsule	Ok		
Date: 00/00/202x	**Operator:**	**PA/QA:**		

3.2 TES Fabrication

00-00-202x

Ir/Au bilayer: Ir deposition by Nd:YAG PLD and Au by ebeam (Chip and Control Sample- CS)

3.2.1 00-00-202x Ir Deposition (Procedure: XIFU-UNGE-CRA-PR-0011-r00)

STEP	Description	Expected Value	Measured value	Remarks
1.	Mount the chip and the control sample on the sample holder with the clamps and screws in Clean Room	Ok		
2.	Make a visual inspection in clean room with optical microscope and check for particles and residual of metal films	Ok		
3.	In case of presence of deposited contaminant caused by the mounting process clean with Nitrogen flux or, if necessary, flush with solvent: acetone and then ethanol, and dry with nitrogen			
4.	Close in a clean capsule in clean room	Ok		
5.	Open the vac lock chamber, The vac lock chamber must be flushed with clean nitrogen until its closure.	Ok		
7.	Insert the sample holder in vac lock chamber on the metal forks on the maneuvering arm	Ok		
8.	Stop flush nitrogen, close the chamber and start vacuum with rotative pump and turbo pump when the vacuum is below 4 10^{-1} mbar	Ok		
9.	Wait till the pressure arrive to < 5 10^{-6} mbar	< 5 10^{-6} mbar		
10.	Check the level of vacuum of PLD chamber	Ok		
11.	If vacuum is in order of magnitude of 10^{-8} start process:	~ 10^{-8} mbar		
12.	Open Gate Valve number 3. Insert sample holder in the PLD chamber maneuvering the vertical and the horizontal arms:			
12.1	Transfer the sample holder from the vertical to the horizontal arm and check that the sample holder is correctly fixed to the fork	Ok		
12.2	Remove the vertical arm from the PLD chamber, closed Gate Valve number 3 and wait that vacuum goes back to starting value.	Ok		

13.	**Ir thin film growth by Nd:YAG PLD:**			
	Vacuum	~ 10^{-8} mbar		
	Laser energy (nom.)	750 mJ, Max. Q-switched		
	Laser frequency	10 Hz		
13.1	Move and rotate the arm until the chip is in the correct position with respect to the iridium target to deposit correctly on the whole chip			
13.2	Wear with the safety eyeglass for class IV laser	Ok		
13.3	Prepare a chronometer	Ok		
13.4	Fix the angular position to +40° to the reference point.			
13.5	Switch on the laser and wait for the warm ap at least fifteen minutes with the pumping lamp power at minimum	Ok		
13.6	Set the modality “Sngl Shot” and check the laser spot on photographic paper at the enter flange. If it is not like in figure stop the procedure and check the optics alignment.			
13.7	Set the modality “Rep” and start the Deposition process by rotating laser power knob to the already settled value and check that the laser light signal in operation is on and start the chronometer	Ok		
13.8	Check to the power monitor that the reference settled value is reached and stable	Ok		
13.9	Check the monitor during all the process and note for all changes or drift	Ok		
	Distance from target	~ 3.6 cm -360° (nominal 0°)		
	Angular Positions	Centered		

	Deposition time	30 min.: 10 min. @ 40° 10 min. @ 0° 10 min. @ 20°		Reference monitor at mW
	Thickness Expected:	***150 nm***		
14.	Once deposition is complete move the sample holder from PLD into the insertion chamber: repeat the procedure used to bring the chip from the insertion chamber to that of the PLD, as described in steps 12., for the subsequent deposition operation. of a thin Au film with e-beam	Ok		
Date: **00/00/202x**	**Operator:**	**PA/QA:**		

FIGURE
Fig 3.1.2.1 Ir plume with very low content of clusters from Ir target.

Move sample carrier with arm from PLD to e-beam chamber closing the gates valve on PLD chamber and opening step by step the two gates valves towards the e-beam chamber.

3.2.2 00-00-202x Gold deposition by e-beam (Procedure: XIFU-UNGE-CRA-PR-0004)

STEP	Description	Expected Value	Measured value	Remarks
1.	Check the pressure of the e-beam chamber: should be lower than 5-10 x10^{-8} mbar for 1-10 Ang/s deposition rate, respectively	Ok		
2.	Turn on the e-beam, set the voltage previously fixed for the material and open the water cooling circuits “eBeam” and “eBeam monitor” input and output.	Ok		
2.1.	Rotate the 4-pocket stage to the one containing Au	Ok		
3.	Select process “Au_TES” in the thickness monitor.	Ok		

4.	Start the system so check voltage and deposition rate, and eventually, make the needed parameter's adjustment then stop the system.	Ok		
5.	Move the chip inside the chamber:			
5.1.	Transfer the sample holder from the vertical to the horizontal arm and check that the sample holder is correctly fixed to the fork	Ok		
5.2.	Open gate valve 4 and, as the arm moves forward, open gate valve 5;	Ok		
5.3.	Move the sample from the download chamber to that of the e-beam chamber by mean of the transfer arm;	Ok		
5.4.	Move and rotate the arm until the carrier is in the reference position (vertical axis to the crucible center)	Ok		
6.	Reset to ZERO the value of thickness monitor.	Ok		
7.	Start the system with the thickness monitor.	Ok		
8.	Check that spot is at the center of the crucible and that the process stops at 500 Angstrom	50 nm		
9.	Close the water circuit, turn off the eBeam system and move the sample holder from e-beam into the insertion chamber: repeat inversely the procedure used to bring the chip from the vac-lock chamber to the e-beam chamber, as described in steps 5.2 to 5.4. Gently remove the SS UHV carrier from the fork and pull it out of the chamber	Ok		
Date: 00/00/202x	**Operator:**	**PA/QA:**		

3.2.3 00-00-202x Visual inspection (Procedure XIFU-UNGE-CRA-PR-0008-r00)

STEP	Description	Expected Value	Measured value	Remarks
1.	Measure thickness with profilometer:			
2.	FOTO			

3.	Sonicate in acetone for 10 minutes	10m		
4.	If the sample does not meet the acceptance criteria NCR and NRB	Ok		
5.	FOTO			
6.	Go to the next process or store in a closed capsule	Ok		
Date: 00/00/202x	**Operator:**	**PA/QA:**		

3.2.4 00-00-202x Test Tc transition in dilution cryostat (Control Sample)

Reference CS-Test procedures and Test Report

Tc = ... mK measured on CS

3.2.5 00-00-202x Positive Micro Photo Lithography (Procedure XIFU-UNGE-CRA-PR-0002) Mask: "DM HEATERS 2.0"

STEP	Description	Expected Value	Measured value	Remarks
1.	Set the hot plate to 100 °C	100 °C		
2.	Resist coating with spinner:			
2.1.	Put the chip in spinner and fix it with vacuum (-0,75 bar)	Ok		
2.3.	Spin at 3000 rpm and wash with Acetone 10 ml	10 ml 3000 rpm		
2.4.	Puddle the ma-p1275 resist onto the chip using a dispenser pipe [RD4][RD5][RD6]	Ok		
2.5.	Spin at 3000 rpm maximum acceleration for 30 second	30 s 3000 rpm		
3.	Move the sample from spinner to hotplate be careful do not clamp the chip to avoid resist coating damage, use a slide as carrier	Ok		
4.	Bake on hot plate for 5 min at 100°C	5 min 100°		
5.	Alignment and Exposure:			
5.1.	Clean the mask with 10 ml acetone flush at 4 ml/s, rinse with ethanol and dry with argon. Then load lithographic mask into mask aligner: chrome plated side below to contact with chip.	Ok		

5.2.	Check the correct WEC, Wedge Error Compensation, regulation and in case adjust it (SUSS mask aligners are equipped with a WEC head system that allows reaching the parallelism between substrate and mask with a micrometric precision, training is needed).	Ok		
5.3.	Put chip on mask aligner sample holder using same caution of point 3	Ok		
5.4.	Align sample to mask using the micromanipulator: every draw in the mask has its apposite collimators (crosses) to make the best alignment (training is needed)	Ok		
5.5.	Check exposition conditions (time and number of cycles) and in case adjust them: usually 5 second for 2 cycles, but they may change with UV lamp power emission (training is needed)	5s 5 cycles		
5.6.	Activate automatic UV exposition cycles	Ok		
5.7.	When the exposure process is finished, release the chip by lifting the locking lever	Ok		
6.	Develop:			
6.1.	Workbench preparation:			
6.1.1.	Stopwatch	Ok		
6.1.2.	More than 50 ml DI water in a beaker	Ok		
6.1.3.	More than 40 ml ma-D331 developer in a beaker	Ok		
6.2.	Put the chip inside in developer bath for 2:10 min.	2:10 min		
6.3.	Stop develop by moving the chip in the DI water bath	Ok		
6.4.	Dry with Nitrogen	Ok		
6.5.	Check the completion of development process under the microscope (coaxial light 20%): The exposure to light causes a chemical change that allows to the photoresist to be removed by a special solution (developer). Positive photoresist becomes soluble in the developer when exposed. The edges of the	Ok		

	resist must be defined and without erosion (over develop) while the exposed area must be clean and free from resist.			
6.6.	In case of incomplete process, repeat form 6.2 for 10-20 s and check again under the microscope			
7.	Hashing resist residuals in O2 Plasma:			
7.1.	Put the chip onto a glass slide, then place them with the chip on the appropriate metal plate	Ok		
7.2.	Insert it into the O2 plasma generator, switch ON pumping valve, then switch ON O2 valve	Ok		
7.3.	Wait for O2 flux stabilization at 200 sccm	200 sccm		
7.4.	Turn on the RF generator at 100 W	100 W		
7.5.	Stop process after 5 minutes	5 min		
Date: 00/00/202x	**Operator:**	**PA/QA:**		

3.2.6 00-00-202x Visual inspection (Procedure XIFU-UNGE-CRA-PR-0008-r00)

STEP	Description	Expected Value	Measured value	Remarks
1.	If the sample does not meet the acceptance repeat the photolithography process	Ok		
2.	FOTO			
3.	Go to the next process or store in a closed capsule	Ok		
Date: 00/00/202x	**Operator:**	**PA/QA:**		

3.2.7 00-00-202x RIE Etching (Procedure XIFU-UNGE-CRA-PR-0003)

STEP	Description	Expected Value	Measured value	Remarks

1.	Glue the "back" chip to sapphire carrier wafer with 3 µl of Santovac 5 with Hamilton syringe:			
1.1	place the sapphire carrier wafer on the hotplate at 120 °C and open pumping valve to fix the wafer	120 °C		
1.2	put 3 µl of Santovac 5 with Hamilton syringe to center of the carrier wafer	Ok		
1.3	as soon as the Santovac is fluid, lean on the chip and cover with the vacuum cup and apply 700 -900 mbar for about 2 min.	Ok		
1.4	switch off the pumping valve and remove the cover and the carrier wafer from the hot plate by dragging it on the cold edge	Ok		
1.5	check with visual inspection if chip is aligned and remove excess of Santovac 5	Ok		
2.	Start RIE:			
2.1.	Open the gas lines of Ar, He and N2 "RIE" and "purge RIE"	Ok		
2.2.	Open the water circuit "ICP RIE IN", "ICP RIE OUT" and the output "Turbo RIE"	Ok		
2.3.	Start the chiller, set 20°C and run	Ok		
2.4.	Push start RIE button and then start the program Open PC 2000	ok		
3.	Close the vac-lock aperture and start the automatic procedure for sample loading	Ok		
4.	Load the RIE-ICP recipe "Ir Etch2" and wait for the execution: ICP pow. PE pow. Press. Ar flux time 500 W 50 W 5 mbar 50 sccm	20 min.		
5.	Load the sample with the automatic RIE-ICP procedure and process check.	Ok		
5.1	Check at microscope (see Acceptance Criteria §5 points 1 and 2) in case of partial iridium removal reload sample into RIE machine (step 2) and repeat the procedure, adjust properly time of step 3.			
6.	Remove chip from sapphire wafer:			
6.1	Put the sapphire carrier wafer on the hot plate at 120° and switch on the pumping valve	120° C		
6.2	As soon as the <santovac 5 is fluid, gently drag chip outside the wafer with tweezers	Ok		

6.3	Wash chip with acetone to remove Santovac 5 from the backside.	Ok		
7.	Remove photoresist:			
7.1	Sonicate in acetone for few seconds;	Ok		
7.2	Rinse in ethanol bath;	Ok		
7.3	Dry with nitrogen;	Ok		
8.	Turn off the pumps, when the turbo is at 0 rpm switch off the RIE, the chiller and close water circuit and gasses	Ok		
Date: 00/00/202x	**Operator:**	**PA/QA:**		

3.2.8 00-00-202x Verification Surface Resistance test = x,x MΩ

3.2.9 00-00-202x Final cleaning (Procedure: XIFU-UNGE-CRA-PR-0012-r00)

STEP	Description	Expected Value	Measured value	Remarks
1.	Prepare the ultrasonic cleaner: put DI water in it	Ok		
2.	Put in a beaker 20 ml of Remover rm-700	20 ml		
4.	Place the chip in the beaker and hold it with reverse action tweezers during sonication.	Ok		
5.	Put the beaker with the sample in the grid container inside the ultrasonic bath	Ok		
6.	Make sure the water level is equal to or greater than that of the sample; if necessary, add water, making sure that the beaker remains in contact with the grid so that it does not start to float, thus risking tipping over	Ok		
7.	Start the ultrasonic cleaner timer and set for a time> 10 min	Ok		
8.	Withdraw the chip with reverse tweezers during sonication to avoid the deposition of contaminants when the sonication is finished and rinse in DI water	Ok		
9.1	Rinse with 5 ml of acetone flush	Ok		
9.2	Rinse with 5 ml of Ethanol flush	Ok		
10.	Dry with Nitrogen	Ok		
11.	Make a cleaning with Oxygen Plasma:			
11.1	Turn-on Oxygen Plasma Generator	Ok		

11.2	Put the chip onto a glass slide, then place them with the chip on the appropriate metal plate	Ok		
11.3	Insert it into the O2 plasma generator, switch ON pumping valve, then switch ON O2 valve	Ok		
11.4	Wait for O2 flux stabilization at 200 sccm	200 sccm		
11.5	Turn on the RF generator at 100 W	100 W		
11.6	Stop the process after 8 minutes and 20 seconds	8 min 20s		
12.	Check the cleanliness of the chip surface under the microscope	Ok		
13.	If the chip is clean switch to the next procedure in the process flow or store in a close capsule			
14.	If necessary, repeat the passage in oxygen plasma, proceeding 2 minutes at a time and checking under a microscope before repeating the procedure			
Date: 00/00/202x	**Operator:**	**PA/QA:**		

3.2.10 **00-00-202x Visual inspection (Procedure XIFU-UNGE-CRA-PR-0008-r00)**

STEP	Description	Expected Value	Measured value	Remarks
1.	If the sample does not meet the acceptance criteria NCR and NRB	Ok		
2.	FOTO			
3.	Go to the next process or store in a closed capsule	Ok	Ok	
Date: 00/00/202x	**Operator:**			

3.3 Pt Heaters

3.3.1 **00-00-202x Negative Micro Photo Lithography (Procedure: XIFU-UNGE-CRA-PR-0001) Mask: “DM HEATERS 3.0 A”**

STEP	Description	Expected Value	Measured value	Remarks

1.	Set the hot plate to 95 °C	95 °C		
2.	Resist coating with spinner:			
2.1.	Put the chip in spinner and fix it with vacuum (-0,75 bar)	Ok		
2.3.	Spin at 2000 rpm and wash with Acetone 10 ml	10 ml 2000 rpm		
2.4.	Puddle the ma-N440 resist onto the chip using a dispenser's pipe [RD4][RD5][RD6]	Ok		
2.5.	Spin at 3000 rpm maximum acceleration for 30 second	30 s 3000 rpm		
3.	Move the sample from spinner to hotplate be careful do not clamp the chip to avoid resist coating damage, use a slide as carrier	Ok		
4.	Bake on hot plate for 5 min at 95°C	5 min 95°C		
5.	Alignment and Exposure:			
5.1.	Clean the mask with 10 ml acetone flush at 4ml/s, rinse with ethanol and dry with Nitrogen. Then load lithographic mask into mask aligner: chrome plated side below to contact with chip.	Ok		
5.2.	Check the correct WEC, Wedge Error Compensation, regulation and in case adjust it (SUSS mask aligners are equipped with a WEC head system that allows reaching the parallelism between substrate and mask with a micrometric precision, training is needed).	Ok		
5.3.	Put chip on mask aligner sample holder using same caution of point 3	Ok		
5.4.	Align sample to mask using the micromanipulator: every draw in the mask has its apposite collimators (crosses) to make the best alignment (training is needed)	Ok		
5.5.	Check exposition conditions (time and number of cycles) and in case adjust them: usually 5 second for 2 cycles, but they may change with UV lamp power emission (training is needed)	5 cycles 5 s		

5.6.	Activate automatic UV exposition cycles	Ok		
5.7.	When the exposure process is finished, release the chip by lifting the locking lever	Ok		
6.	Develop:			
6.1.	Workbench preparation:			
6.1.1.	Stopwatch	Ok		
6.1.2.	More than 50 ml DI water in a beaker	Ok		
6.1.3.	More than 40 ml ma-D332s/ma-D532s developer a beaker	Ok		
6.2.	Put the chip inside in developer bath for 2:10 min.	2 min 10 s		
6.3.	Stop develop by moving the chip in the DI water bath	Ok		
6.4.	Dry with Nitrogen	Ok		
6.5.	Check the completion of development process under the microscope (coaxial light 20%): The exposure to light causes a chemical change that allows to the photoresist to be removed by a special solution (developer), with negative photoresist, unexposed regions are soluble in the developer. The edges of the resist must be defined and without erosion (over develop) while the unexposed area must be clean and free from resist.	Ok		
6.6.	In case of incomplete process, repeat form 6.2 for 10-20 s and check again under the microscope			
7.	Hashing resist residuals in O2 Plasma:			
7.1.	Put the chip onto a glass slide, then place them with the chip on the appropriate metal plate	Ok		
7.2.	Insert it into the O2 plasma generator, switch ON pumping valve, then switch ON O2 valve	Ok		
7.3.	Wait for O2 flux stabilization at 200 sccm	200 sccm		
7.4.	Turn on the RF generator at 100 W	100 W		

7.5.	Stop process after 5 minutes	5 min		
Date: **00/00/202x**	**Operator:**	**PA/QA:**		

3.3.2 00-00-202x Visual inspection (Procedure XIFU-UNGE-CRA-PR-0008-r00)

STEP	Description	Expected Value	Measured value	Remarks
1.	If the sample does not meet the acceptance criteria repeat the photolithography process	Ok		
2.	FOTO			
3.	Go to the next process or store in a closed capsule	Ok		
Date: **00/00/202x**	**Operator:**			

3.3.3 00-00-202x Ti sticking layer deposition (Procedure: XIFU-UNGE-CRA-PR-0004)

STEP	Description	Expected Value	Measured value	Remarks
1.	Check the pressure of the e-beam chamber: should be lower than 5-10 x10^{-8} mbar for 1-10 Ang/s deposition rate, respectively	Ok		
2.	Turn on the e-beam, set the voltage previously fixed for the material and open the water cooling circuits “eBeam” and “eBeam monitor” input and output.	Ok		
2.1.	Rotate the 4-pocket stage to the one containing the Ti	Ok		
3.	Select process “Pt_Heaters” in the thickness monitor. Film number 1.	Ok		
4.	Start the system so check voltage and deposition rate, and eventually, make the needed parameter’s adjustment then stop the system.	Ok		7 ang/s
5.	Insert chip in Insert chamber:			
5.1.	Mount the chip in metal sample holder and fix it with metal clamps/springs;	Ok		

5.2.	Close the rotary vane pump of the vac-lock chamber, turn off the turbo pump, equalize the pressure filling with nitrogen;	Ok		
5.3.	Open the door of vac-lock chamber;	Ok		
5.4.	Fix the SS UHV carrier with chip on forks mounted at the end of the insertion arm;	Ok		
5.5.	Close the vac-lock chamber;	Ok		
5.6.	Open valve of rotary vane pump and switch on the turbo pump of the vac-lock at Insert chamber pressure lower than $4x10^{-2}$ mbar;	< $4x10^{-2}$ mbar		
5.7.	When pressure, in the Insert chamber, is lower than $5x10^{-6}$ mbar, open gate valve 4 and, as the arm moves forward, open gate valve 5;	< $5x10^{-6}$ mbar		10^{-8}mbar
5.8	Move the sample from the download chamber to that of the e-beam chamber by mean of the transfer arm;	Ok		
5.9	Move and rotate the arm until the carrier is in the reference position (vertical axis to the crucible center)	Ok		
6.	Ti sticking layer (monitor)			
6.1	Reset to ZERO the value of thickness monitor.	Ok		
6.2	Start the system with the thickness monitor.	Ok		
6.3	Check that the process stops at 150 Angstrom.	15 nm		
Date: 00/00/202x	**Operator:**	**PA/QA:**		

3.3.4 **00-00-202x Pt heater growth by e-beam evaporation (Procedure: XIFU-UNGE-CRA-PR-0004)**

STEP	Description	Expected Value	Measured value	Remarks
1.	Set the voltage previously fixed for the material.	Ok		10^{-8}mbar
1.1.	Rotate the 4-pocket stage to the one containing the Pt	Ok		

2.	Select process “Pt_Heaters” in the thickness monitor. Film number 2.	Ok		
3.	Check voltage and deposition rate, and eventually, make the needed parameter’s adjustment then stop the system.	Ok		4 ang/s
4.	Pt layer (monitor)			
4.1	Reset to ZERO the value of thickness monitor.	Ok		
4.2	Start the system with the thickness monitor.	Ok		
4.3	Check that the process stops at 800 Angstrom.	80 nm		
5.	Close the water circuit, turn off the eBeam system and move the sample holder from e-beam into the insertion chamber: repeat inversely the procedure used to bring the chip from the vac-lock chamber to the e-beam chamber, as described in steps 5.5 to 5.8. in Ti sticking layer process. Gently remove the SS UHV carrier from the fork and pull it out of the chamber	Ok		
Date: **00/00/202x**	**Operator:**	**PA/QA:**		

3.3.5 00-00-202x Lift-off 1 (Procedure: XIFU-UNGE-CRA-PR-0013-r00)

STEP	Description	Expected Value	Measured value	Remarks
1.	Prepare the ultrasonic cleaner: put DI water in it	Ok		
2.	Put in a beaker 40 ml of Acetone	40 ml		
3.	Insert a slide into the beaker, placing it tilted and firm against the bottom	Ok		
4.	Place the chip in the beaker so that it rests on the slide and that it is easier to extract it from the beaker during sonication.	Ok		
5.	Leave the chip in Acetone bath for a time > 10 min	Ok		
6.	Put the beaker with the sample in the grid container inside the ultrasonic bath	Ok		

7.	Make sure the water level is equal to or greater than that of the sample; if necessary, add water, making sure that the beaker remains in contact with the grid so that it does not start to float, thus risking tipping over	Ok		
8.	Start the ultrasonic cleaner and chronometer: leave the chip in sonication for 1 m then stop the ultrasonic cleaner.	1 m		
9.1	Rinse with 5 ml of acetone flush	Ok		
9.2	Rinse with 5 ml of Ethanol flush	Ok		
10.	Dry with Nitrogen	Ok		
11.	Check the cleanliness of the chip surface under the optical microscope with CCD camera	Ok		
12.	If the chip is clean go on to the next procedure in the process flow or store in a vacuum box sample holder (VR tray gel pack);			
13.	If the lift-off process is not finished and part of sacrificial layer are detected, repeat steps 5. To 10. If necessary, proceed with solvent cleaning step: Acetone, then Ethanol with direct flow or spinner and/or subsequent passage in oxygen plasma			
Date: 00/00/202x	**Operator:**	**PA/QA:**		

3.3.6 00-00-202x Visual inspection (Procedure XIFU-UNGE-CRA-PR-0008-r00)

STEP	Description	Expected Value	Measured value	Remarks
1.	If the sample does not meet the acceptance criteria NCR and NRB	Ok		
2.	FOTO			
3.	Go to the next process or store in a closed capsule	Ok	Ok	
Date: 00/00/202x	**Operator:**	**PA/QA:**		

3.4 Thermal contact

3.4.1 00-00-202x Negative Micro Photo Lithography (Procedure: XIFU-UNGE-CRA-PR-0001) Mask: "DM HEATERS 3.0 A"

STEP	Description	Expected Value	Measured value	Remarks
1.	Set the hot plate to 95 °C	95 °C		
2.	Resist coating with spinner:			
2.1.	Put the chip in spinner and fix it with vacuum (-0,75 bar)	Ok		
2.3.	Spin at 2000 rpm and wash with Acetone 10 ml	10 ml 2000 rpm		
2.4.	Puddle the ma-N440 resist onto the chip using a dispenser pipe [RD4][RD5][RD6]	Ok		
2.5.	Spin at 3000 rpm maximum acceleration for 30 second	30 s 3000 rpm		
3.	Move the sample from spinner to hotplate be careful do not clamp the chip to avoid resist coating damage, use a slide as carrier	Ok		
4.	Bake on hot plate for 5 min at 95°C	5 min 95 °C		
5.	Alignment and Exposure:			
5.1.	Clean the mask with 10 ml acetone flush at 4 ml/s, rinse with ethanol and dry with nitrogen. Then load lithographic mask into mask aligner: chrome plated side below to contact with chip.	Ok		
5.2.	Check the correct WEC, Wedge Error Compensation, regulation and in case adjust it (SUSS mask aligners are equipped with a WEC head system that allows reaching the parallelism between substrate and mask with a micrometric precision, training is needed).	Ok		
5.3.	Put chip on mask aligner sample holder using same caution of point 3	Ok		
5.4.	Align sample to mask using the micromanipulator: every draw in the mask has its apposite collimators (crosses) to make the best alignment (training is needed)	Ok		

5.5.	Check exposition conditions (time and number of cycles) and in case adjust them: usually 5 second for 2 cycles, but they may change with UV lamp power emission (training is needed)	5 cycles 5 s		
5.6.	Activate automatic UV exposition cycles	Ok		
5.7.	When the exposure process is finished, release the chip by lifting the locking lever	Ok		
6.	Develop:			
6.1.	Workbench preparation:			
6.1.1.	Stopwatch	Ok		
6.1.2.	More than 60 ml DI water in a beaker	Ok		
6.1.3.	More than 40 ml ma-D332s/ma-D532s developer in a beaker	Ok		
6.2.	Put the chip inside in developer bath for 2:20 min.	2 min 20s		
6.3.	Stop develop by moving the chip in the DI water bath	Ok		
6.4.	Dry with Nitrogen	Ok		
6.5.	Check the completion of development process under the microscope (coaxial light 20%): The exposure to light causes a chemical change that allows to the photoresist to be removed by a special solution (developer), with negative photoresist, unexposed regions are soluble in the developer. The edges of the resist must be defined and without erosion (over develop) while the unexposed area must be clean and free from resist.	Ok		
6.6.	In case of incomplete process, repeat form 6.2 for 10-20 s and check again under the microscope			
7.	Hashing resist residuals in O2 Plasma:			
7.1.	Put the chip onto a glass slide, then place them with the chip on the appropriate metal plate	Ok		

7.2.	Insert it into the O2 plasma generator, switch ON pumping valve, then switch ON O2 valve	Ok		
7.3.	Wait for O2 flux stabilization at 200 sccm	200 sccm		
7.4.	Turn on the RF generator at 100 W	100 W		
7.5.	Stop the process after 5 minutes	5 min		
Date: 00/00/202x	**Operator:**	**PA/QA:**		

3.4.2 00-00-202x Visual inspection (Procedure XIFU-UNGE-CRA-PR-0008-r00)

STEP	Description	Expected Value	Measured value	Remarks
1.	If the sample does not meet the acceptance criteria repeat the photolithography process	Ok		
2.	FOTO			
3.	Go to the next process or store in a closed capsule	Ok		
Date: 00/00/202x	**Operator:**			

3.4.3 00-00-202x Ti Sticking Layer (Procedure: XIFU-UNGE-CRA-PR-0004)

STEP	Description	Expected Value	Measured value	Remarks
1.	Check the pressure of the e-beam chamber: should be lower than 5-10 x10^{-8} mbar for 1-10 Ang/s deposition rate, respectively	Ok		
2.	Turn on the e-beam, set the voltage previously fixed for the material and open the water cooling circuits “eBeam” and “eBeam monitor” input and output.	Ok		
2.1.	Rotate the 4-pocket stage to the one containing the Ti	Ok		
3.	Select process “Au_RIM” in the thickness monitor. Film number 1.	Ok		
4.	Start the system so check voltage and deposition rate, and eventually, make the	Ok		7 ang/s

	needed parameter's adjustment then stop the system.			
5.	Insert chip in Insert chamber:			
5.1.	Mount the chip in metal sample holder and fix it with metal clamps/springs;	Ok		
5.2.	Close the rotary vane pump of the vac-lock chamber, turn off the turbo pump, equalize the pressure filling with nitrogen;	Ok		
5.3.	Open the door of vac-lock chamber;	Ok		
5.4.	Fix the SS UHV carrier with chip on forks mounted at the end of the insertion arm;	Ok		
5.5.	Close the vac-lock chamber;	Ok		
5.6.	Open valve of rotary vane pump and, when pressure inside the Insert chamber is lower than $4x10^{-2}$ mbar, switch on the turbo pump of the vac-lock;	< $4x10^{-2}$ mbar		
5.7.	when pressure inside the Insert chamber is lower than $5x10^{-6}$ mbar, open gate valve 4 and, as the arm moves forward, open gate valve 5;	< $5x10^{-6}$ mbar		10^{-8} mbar
5.8	Move the sample from the download chamber to that of the e-beam chamber by mean of the transfer arm;	Ok		
5.9	Move and rotate the arm until the carrier is in the reference position (vertical axis to the crucible center)	Ok		
6.	Ti sticking layer (monitor):			
6.1	Reset to ZERO the value of thickness monitor.	Ok		
6.2	Start the system with the thickness monitor.	Ok		
6.3	Once deposition is complete stop the thickness monitor.	40 nm		
Date: 00/00/202x	**Operator:**	**PA/QA:**		

3.4.4 **00-00-202x Au growth e-beam (Procedure: XIFU-UNGE-CRA-PR-0004)**

STEP	Description	Expected Value	Measured value	Remarks
1.	Set the voltage previously fixed for the material.	Ok		2.1x10^{-8} mbar
1.1.	Rotate the 4-pocket stage to the one containing the Au	Ok		
2.	Select process "Au_RIM" in the thickness monitor. Film number 2.	Ok		
3.	Check voltage and deposition rate, and eventually, make the needed parameter's adjustment then stop the system.	Ok		
4.	Au layer (monitor):			
4.1	Reset to ZERO the value of thickness monitor.	Ok		
4.2	Start the system with the thickness monitor.	Ok		
4.3	Once deposition is complete stop the thickness monitor.	200 nm		
6.	Close the water circuit, turn off the eBeam system and move the sample holder from e-beam into the insertion chamber: repeat inversely the procedure used to bring the chip from the vac-lock chamber to the e-beam chamber, as described in steps 5.5 to 5.8. in Ti sticking layer process. Gently remove the SS UHV carrier from the fork and pull it out of the chamber	Ok		
Date: 00/00/202x	**Operator:**	**PA/QA:**		

3.4.5 **00-00-202x Lift-off 1 (Procedure: XIFU-UNGE-CRA-PR-0013-r00)**

STEP	Description	Expected Value	Measured value	Remarks
1.	Prepare the ultrasonic cleaner: put DI water in it	Ok		
2.	Put in a beaker 40 ml of Acetone	40ml		
3.	Insert a slide into the beaker, placing it tilted and firm against the bottom	Ok		

4.	Place the chip in the beaker so that it rests on the slide and that it is easier to extract it from the beaker during sonication.	Ok		
5.	Leave the chip in Acetone bath for a time> 10 min	Ok		
6.	Put the beaker with the sample in the grid container inside the ultrasonic bath	Ok		
7.	Make sure the water level is equal to or greater than that of the sample; if necessary, add water, making sure that the beaker remains in contact with the grid so that it does not start to float, thus risking tipping over	Ok		
8.	Start the ultrasonic cleaner and chronometer: leave the chip in sonication for 1 m then stop the ultrasonic cleaner.	1 m		
9.1	Rinse with 5 ml of acetone flush	Ok		
9.2	Rinse in 5 ml of Ethanol flush	Ok		
10.	Dry with Nitrogen	Ok		
11.	Check the cleanliness of the chip surface under the optical microscope with CCD camera	Ok		
12.	If the chip is clean go on to the next procedure in the process flow or store in a vacuum box sample holder (VR tray gel pack);			
13.	If the lift-off process is not finished and part of sacrificial layer are detected, repeat steps 5. To 10. If necessary, proceed with solvent cleaning step: Acetone, then Ethanol with direct flow or spinner and/or subsequent passage in oxygen plasma			
Date: **00/00/202x**	**Operator:**	**PA/QA:**		

3.4.6 00-00-202x Visual inspection (Procedure XIFU-UNGE-CRA-PR-0008-r00)

STEP	Description	Expected Value	Measured value	Remarks
1.	If the sample does not meet the acceptance criteria NCR and NRB	Ok		
2.	FOTO			
3.	Go to the next process or store in a closed capsule	Ok		
Date: **00/00/202x**	**Operator:**	**PA/QA:**		

3.5 Nb Wire Lower Strip line

3.5.1 00-00-202x Negative Micro Photo Lithography (Procedure: XIFU-UNGE-CRA-PR-0001) Mask: "DM HEATERS 3.0 B"

STEP	Description	Expected Value	Measured value	Remarks
1.	Set the hot plate to 95 °C	95 °C		
2.	Resist coating with spinner:			
2.1.	Put the chip in spinner and fix it with vacuum (-0,75 bar)	Ok		
2.3.	Spin at 2000 rpm and wash with Acetone 10 ml	10 ml 2000 rpm		
2.4.	Puddle the ma-N440 resist onto the chip using a dispenser pipe [RD4][RD5][RD6]	Ok		
2.5.	Spin at 3000 rpm maximum acceleration for 30 second	30 s 3000 rpm		
3.	Move the sample from spinner to hotplate be careful do not clamp the chip to avoid resist coating damage, use a slide as carrier	Ok		
4.	Bake on hot plate for 5 min at 95°C	5 min 95 °C		
5.	Alignment and Exposure:			
5.1.	Clean the mask with 10 ml acetone flush at 4 ml/s, rinse with ethanol and dry with nitrogen. Then load lithographic mask into mask aligner: chrome plated side below to contact with chip.	Ok		
5.2.	Check the correct WEC, Wedge Error Compensation, regulation and in case adjust it (SUSS mask aligners are equipped with a WEC head system that allows reaching the parallelism between substrate and mask with a micrometric precision, training is needed).	Ok		
5.3.	Put chip on mask aligner sample holder using same caution of point 3	Ok		

5.4.	Align sample to mask using the micromanipulator: every draw in the mask has its apposite collimators (crosses) to make the best alignment (training is needed)	Ok		
5.5.	Check exposition conditions (time and number of cycles) and in case adjust them: usually 5 second for 2 cycles, but they may change with UV lamp power emission (training is needed)	5 cycles 5 s		
5.6.	Activate automatic UV exposition cycles	Ok		
5.7.	When the exposure process is finished, release the chip by lifting the locking lever	Ok		
6.	Develop:			
6.1.	Workbench preparation:			
6.1.1.	Stopwatch	Ok		
6.1.2.	More than 50 ml DI water in a beaker	Ok		
6.1.3.	More than 40 ml ma-D332s/ma-D532s developer in a beaker	Ok		
6.2.	Put the chip inside in developer bath for 4:00 min.	4 min		Overdeveloped to have good under etching (twice the time needed to delete newton rings)
6.3.	Stop develop by moving the chip in the DI water bath	Ok		
6.4.	Dry with Nitrogen	Ok		
6.5.	Check the completion of development process under the microscope (coaxial light 20%): The exposure to light causes a chemical change that allows to the photoresist to be removed by a special solution (developer), with negative photoresist, unexposed regions are soluble in the developer. The edges of the resist must be defined and without erosion (over develop) while the unexposed area must be clean and free from resist.	Ok		

6.6.	In case of incomplete process, repeat form 6.2 for 10-20 s and check again under the microscope			
7.	Hashing resist residuals in O2 Plasma:			
7.1.	Put the chip onto a glass slide, then place them with the chip on the appropriate metal plate	Ok		
7.2.	Insert it into the O2 plasma generator, switch ON pumping valve, then switch ON O2 valve	Ok		
7.3.	Wait for O2 flux stabilization at 200 sccm	200 sccm		
7.4.	Turn on the RF generator at 100 W	100 W		
7.5.	Stop the process after 5 minutes	5 min		
Date: 00/00/202x	**Operator:**	**PA/QA:**		

3.5.2 00-00-202x Visual inspection (Procedure XIFU-UNGE-CRA-PR-0008-r00)

STEP	Description	Expected Value	Measured value	Remarks
1.	If the sample does not meet the acceptance criteria repeat photolithography process	Ok		
2.	FOTO			
3.	Go to the next process or store in a closed capsule	Ok		
Date: 00/00/202x	**Operator:**	**PA/QA:**		

3.5.3 00-00-202x Nb sample deposition by RF sputtering (XIFU-UNGE-CRA-PR-0005)

STEP	Description	Expected Value	Measured value	Remarks
1.	Check the level of vacuum of RF Sputtering chamber	Ok		
2.	If vacuum chamber is not conditioned wait for pressure < 3x 10^{-8} mbar and start the reconditioning process and check the Nb film transition.			

2.1.	Sample upload in the Sputtering Chamber:			
2.1.1	Mount the sample in metal sample holder and fix it with metal clamps;	Ok		
2.1.2	turn off the turbo pump of the vac-lock camber, close pumping valve and equalize the pressure to the atmosphere opening valve of nitrogen input line;	Ok		
2.1.3	open vac-lock door;	Ok		
2.1.4	fix metal sample holder with chip on the fork of the maneuvering arm in a specific position: 1 pay attention that the fork must be in right mode, with the bend downwards 2-fix the sample holder on the fork using the interlock near the disk surface 3- the sample holder must be with the chip facedown;	Ok		
2.1.5	closed vac-lock door;	Ok		
2.1.6	close valve of input nitrogen line, open pumping valve and switch ON the turbo pump;	Ok		
2.1.7	wait for pressure < $5x10^{-6}$ mbar;	< $5x10^{-6}$ mbar		
2.1.8	open gate valve 4;	Ok		
2.1.9	move the sample from the vac-lock chamber to the sputtering chamber;	Ok		
2.1.1 0	Transfer the carrier to the sputtering arm and check if the carrier is correctly fixed to the new fork; pull back the transfer arm to the parking position in the vac-lock;	Ok		
2.1.1 2	close gate 4;	Ok		
2.2.	Wait the pressure goes down to < $3x\ 10^{-8}$ mbar.	< $3\cdot10^{-8}$ mbar		
2.3	Set the material parameters in the thickness monitor.	Ok		
2.4	Open Argon valve then set flux at 3.0 10^{-2} mbar, rotate the shutter and wait for 5 min.	Ok		
2.5	Open the water circuit “Sput Nb” Input and output	3 atm		

2.6	Turn on the RF sputtering facility and the impedance controller, check the values to have maximum 20% of reflected power	Ok		
2.7	Start and reset to ZERO the value of thickness monitor	Ok		
2.8	Start Nb deposition: P=3.0x10^{-2} mbar with10% tolerance, RF power = 300 W.	1500 ang monitor		
2.9	Once deposition is complete turn-off the system with RF off, stop the thickness monitor and close the water circuit	300 nm expected		
2.10	Sample download in the Sputtering Chamber:			
2.11.	Repeat in reverse order the upload procedure 2.1.	Ok		
Date: **00/00/202x**	**Operator:**	**PA/QA:**		

3.5.4 00-00-202x Lift-off 1 (Procedure: XIFU-UNGE-CRA-PR-0013-r00)

STEP	Description	Expected Value	Measured value	Remarks
1.	Prepare the ultrasonic cleaner: put DI water in it	Ok		
2.	Put in a beaker 60 ml of mr-Rem 700	60 ml		
3.	Insert a slide into the beaker, placing it tilted and firm against the bottom	Ok		
4.	Place the chip in the beaker so that it rests on the slide and that it is easier to extract it from the beaker during sonication.	Ok		
5.	Leave the chip in Remover bath for a time> 10 min	>10m		
6.	Put the beaker with the sample in the grid container inside the ultrasonic bath	Ok		
7.	Make sure the water level is equal to or greater than that of the sample; if necessary, add water, making sure that the beaker remains in contact with the grid so that it does not start to float, thus risking tipping over	Ok		
8.	Start the ultrasonic cleaner and chronometer: leave the chip in sonication for 10 m then stop the ultrasonic cleaner.	10 m		

9.1	Rinse with 5 ml of acetone flush	Ok		
9.2	Rinse with 5 ml of Ethanol flush	Ok		
10	Dry with Nitrogen	Ok		
11.	Check the cleanliness of the chip surface under the optical microscope with CCD camera	Ok		
12.	If the chip is clean go on to the next procedure in the process flow or store in a vacuum box sample holder (VR tray gel pack);			
13.	If the lift-off process is not finished and part of sacrificial layer are detected, repeat steps 5. To 10 with mr-Rem700. If necessary, proceed with solvent cleaning step: Acetone, then Ethanol with direct flow or spinner and/or subsequent passage in oxygen plasma			
Date: 00/00/202x	**Operator:**	**PA/QA:**		

3.5.5 00-00-202x Visual inspection (Procedure XIFU-UNGE-CRA-PR-0008-r00)

STEP	Description	Expected Value	Measured value	Remarks
1.	If the sample does not meet the acceptance criteria NRB and NCR	Ok		
2.	FOTO			
3.	Go to the next process or store in a closed capsule	Ok		
Date: 00/00/202x	**Operator:**	**PA/QA:**		

3.6 SiO Insulation

3.6.1 00-00-202x Negative Micro Photo Lithography (Procedure: XIFU-UNGE-CRA-PR-0001) Mask: "DM HEATERS 3.0 B"

STEP	Description	Expected Value	Measured value	Remarks
1.	Set the hot plate to 95 °C	95 °C		
2.	Resist coating with spinner:			

2.1.	Put the chip in spinner and fix it with vacuum (-0,75 bar)	Ok		
2.3.	Spin at 2000 rpm and wash with Acetone 10 ml	10 ml 2000 rpm		
2.4.	Puddle the ma-N440 resist onto the chip using a dispenser pipe [RD4][RD5][RD6]	Ok		
2.5.	Spin at 3000 rpm maximum acceleration for 30 second	30 s 3000 rpm		
3.	Move the sample from spinner to hotplate be careful do not clamp the chip to avoid resist coating damage, use a slide as carrier	Ok		
4.	Bake on hot plate for 5 min at 95°C	5 min 95°C		
5.	Alignment and Exposure:			
5.1.	Clean the mask with 10 ml acetone flush at 4 ml/s, rinse with ethanol and dry with nitrogen. Then load lithographic mask into mask aligner: chrome plated side below to contact with chip.	Ok		
5.2.	Check the correct WEC, Wedge Error Compensation, regulation and in case adjust it (SUSS mask aligners are equipped with a WEC head system that allows reaching the parallelism between substrate and mask with a micrometric precision, training is needed).	Ok		
5.3.	Put chip on mask aligner sample holder using same caution of point 3	Ok		
5.4.	Align sample to mask using the micromanipulator: every draw in the mask has its apposite collimators (crosses) to make the best alignment (training is needed)	Ok		
5.5.	Check exposition conditions (time and number of cycles) and in case adjust them: usually 5 second for 2 cycles, but they may change with UV lamp power emission (training is needed)	5 cycles 5 s		
5.6.	Activate automatic UV exposition cycles	Ok		
5.7.	When the exposure process is finished, release the chip by lifting the locking lever	Ok		
6.	Develop:			
6.1.	Workbench preparation:			
6.1.1.	Stopwatch	Ok		

6.1.2.	More than 50 ml DI water in a beaker	Ok		
6.1.3.	More than 40 ml ma-D332s/ma-D532s developer in a beaker	Ok		
6.2.	Put the chip inside in developer bath for 3:00 min.	3 min		
6.3.	Stop develop by moving the chip in the DI water bath	Ok		
6.4.	Dry with Nitrogen	Ok		
6.5.	Check the completion of development process under the microscope (coaxial light 20%): The exposure to light causes a chemical change that allows to the photoresist to be removed by a special solution (developer), with negative photoresist, unexposed regions are soluble in the developer. The edges of the resist must be defined and without erosion (over develop) while the unexposed area must be clean and free from resist.	Ok		
6.6.	In case of incomplete process, repeat form 6.2 for 10-20 s and check again under the microscope			
7.	Hashing resist residuals in O2 Plasma:			
7.1.	Put the chip onto a glass slide, then place them with the chip on the appropriate metal plate	Ok		
7.2.	Insert it into the O2 plasma generator, switch ON pumping valve, then switch ON O2 valve	Ok		
7.3.	Wait for O2 flux stabilization at 200 sccm	200 sccm		
7.4.	Turn on the RF generator at 100 W	100 W		
7.5.	Stop the process after 5 minutes	5 min		
Date: 00/00/202x	**Operator:**	**PA/QA:**		

3.6.2 **00-00-202x Visual inspection (Procedure XIFU-UNGE-CRA-PR-0008-r00)**

STEP	**Description**	**Expected Value**	**Measured value**	**Remarks**
1.	If the sample does not meet the acceptance criteria repeat photolithography process	Ok		
2.	FOTO			
3.	Go to the next process or store in a closed capsule	Ok		

Date: 00/00/202x	Operator:	PA/QA:

3.6.3 00-00-202x Silicon Oxide Deposition by thermal evaporator (Procedure: XIFU-UNGE-CRA-PR-0004)

STEP	Description	Expected Value	Measured value	Remarks
1.	Open the evaporator chamber:			
1.1	disconnect the rotary pump from the turbo by turning the control knob counterclockwise	Ok		
1.2	switch-off turbo pump power	Ok		
1.3	open the valve for nitrogen to inject the gas in the evaporator chamber	Ok		
1.4	open for a few seconds the control for nitrogen in chamber to slowdown the rotary pump	Ok		
1.5	after slow downing pump re-open nitrogen control and insert the nitrogen in the evaporator chamber	Ok		
1.6	when is possible open the chamber, pull-up the cover and closed nitrogen	Ok		
2.	Mount the chip in metal sample holder and fix it with metal clamps/springs;	Ok		
3.	Position the chip near the balance control and above the evaporator sources (note down the angular position for each source and a shutter position) and place the chip in the shutter position	Ok		
4.	Close the evaporator chamber, connect the rotary pump with the turbo turning the control clockwise	Ok		
5.	When pressure is less than 5 $x10^{-1}$ mbar start turbo pump	Ok		
6.	Set the material parameters in the thickness monitor.	Ok		
7.	When the pressure is < 4 $x10^{-6}$ mbar start the evaporation procedure:	< $4x10^{-6}$ mBar		
7.1.	Open the water circuit “monitor evap” “electrode evap” input and output	Ok		

7.2.	Set the lever for the second evaporation source (right) to evaporate Silicon Oxide film:	Ok		
7.3.	Set the material parameters in the thickness monitor.	Ok		
8.	Start Silicon Oxide evaporation: Turn ON the emission current.	Ok		
8.1	Visually check on the viewport flange and see the thickness monitor: when starting the thickness counter, adjust the current to have a constant rate of about 3 ang / s then rotate the sample in the deposition position.	3 ang/s		
8.2	Once deposition is complete turn-off the emission current, stop the thickness monitor and close the water circuit	5000 ang		
9.	Repeat the procedure as described at point 1 to open the chamber and take out the glass slide with the sample	Ok		
Date: 00/00/202x	**Operator:**	**PA/QA:**		

3.6.4 00-00-202x Lift-off 2 (Procedure: XIFU-UNGE-CRA-PR-0014-r00)

STEP	Description	Expected Value	Measured value	Remarks
1.	Put in a beaker 40 ml of Acetone or Remover mr-Rem 700	40 ml		
2.	Insert a slide into the beaker, placing it tilted and firm against the bottom	Ok		
3.	Place the chip in the beaker so that it rests on the slide and that it is easier to extract it from the beaker during sonication.	Ok		
4.	Leave the chip in Acetone bath for a time > 1h	t > 1h		
5.1	Flush 20ml Acetone at 3 ml/s inside the beaker on the chip	Ok		
5.2	Rinse with 5 ml of acetone flush	Ok		
5.3	Rinse in 5 ml of Ethanol flush	Ok		
6.	Dry with Nitrogen	Ok		
7.	Check the cleanliness of the chip surface under the optical microscope with CCD camera	Ok		

8.	If the chip is clean go on to the next procedure in the process flow or store in a vacuum box sample holder (VR tray gel pack);			
9.	If the lift-off process is not finished and part of sacrificial layer are detected, repeat steps 5. To 10 with Acetone or remover ma-Rem700 for a time > 1h or to all night or proceed with sonication.			
10.	In case of sonication: Prepare the ultrasonic cleaner: put DI water in it			recommended
10.1	Put the beaker with the sample in the grid container inside the ultrasonic bath			
10.2	Make sure the water level is equal to or greater than that of the sample; if necessary, add water, making sure that the beaker remains in contact with the grid so that it does not start to float, thus risking tipping over			
10.3	Start the ultrasonic cleaner and chronometer: leave the chip in sonication for time < 30 s then stop the ultrasonic cleaner.			
10.5	Check the cleanliness of the chip surface under the optical microscope with CCD camera, If the lift-off process is not finished and part of sacrificial layer are detected, repeat the process			
Date: **00/00/202x**	**Operator:**	**PA/QA:**		

3.6.5 00-00-202x Visual inspection (Procedure XIFU-UNGE-CRA-PR-0008-r00)

STEP	Description	Expected Value	Measured value	Remarks
1.	If the sample does not meet the acceptance criteria repeat photolithography process	Ok		
2.	FOTO			
3.	Go to the next process or store in a closed capsule	Ok		
Date: **00/00/202x**	**Operator:**	**PA/QA:**		

3.7 Nb Wire Upper Strip line

3.7.1 00-00-202x Negative Micro Photo Lithography (Procedure: XIFU-UNGE-CRA-PR-0001) Mask: "DM HEATERS 3.0 A"

STEP	Description	Expected Value	Measured value	Remarks
1.	Set the hot plate to 95 °C	95 °C		
2.	Resist coating with spinner:			
2.1.	Put the chip in spinner and fix it with vacuum (-0,75 bar)	Ok		
2.3.	Spin at 2000 rpm and wash with Acetone 8 ml	10 ml 2000 rpm		
2.4.	Puddle the ma-N440 resist onto the chip using a dispenser pipe [RD4][RD5][RD6]	Ok		
2.5.	Spin at 3000 rpm maximum acceleration for 30 second	30 s 3000 rpm		
3.	Move the sample from spinner to hotplate be careful do not clamp the chip to avoid resist coating damage, use a slide as carrier	Ok		
4.	Bake on hot plate for 5 min at 95°C	5 min 95°C		
5.	Alignment and Exposure:			
5.1.	Clean the mask with 10 ml acetone flush at 4 ml/s, rinse with ethanol and dry with nitrogen. Then load lithographic mask into mask aligner: chrome plated side below to contact with chip.	Ok		
5.2.	Check the correct WEC, Wedge Error Compensation, regulation and in case adjust it (SUSS mask aligners are equipped with a WEC head system that allows reaching the parallelism between substrate and mask with a micrometric precision, training is needed).	Ok		
5.3.	Put chip on mask aligner sample holder using same caution of point 3	Ok		
5.4.	Align sample to mask using the micromanipulator: every draw in the mask has its apposite collimators (crosses) to make the best alignment (training is needed)	Ok		
5.5.	Check exposition conditions (time and number of cycles) and in case adjust them: usually 5 second for 2 cycles, but they may change with UV lamp power emission (training is needed)	5 cycles 5 s		

5.6.	Activate automatic UV exposition cycles	Ok		
5.7.	When the exposure process is finished, release the chip by lifting the locking lever	Ok		
6.	Develop:			
6.1.	Workbench preparation:			
6.1.1.	Stopwatch	Ok		
6.1.2.	More than 50 ml DI water in a beaker	Ok		
6.1.3.	More than 40 ml ma-D332s/ma-D532s developer in a beaker	Ok		
6.2.	Put the chip inside in developer bath for 3:00 min.	3 min 00 s		
6.3.	Stop develop by moving the chip in the DI water bath	Ok		
6.4.	Dry with Nitrogen	Ok		
6.5.	Check the completion of development process under the microscope (coaxial light 20%): The exposure to light causes a chemical change that allows to the photoresist to be removed by a special solution (developer), with negative photoresist, unexposed regions are soluble in the developer. The edges of the resist must be defined and without erosion (over develop) while the unexposed area must be clean and free from resist.	Ok		
6.6.	In case of incomplete process, repeat form 6.2 for 10-20 s and check again under the microscope			
7.	Hashing resist residuals in O2 Plasma:			
7.1.	Put the chip onto a glass slide, then place them with the chip on the appropriate metal plate	Ok		
7.2.	Insert it into the O2 plasma generator, switch ON pumping valve, then switch ON O2 valve	Ok		
7.3.	Wait for O2 flux stabilization at 200 sccm	200 sccm		
7.4.	Turn on the RF generator at 100 W	100 W		
7.5.	Stop the process after 5 minutes	5 min		
Date: 00/00/202x	**Operator:**	**PA/QA:**		

3.7.2 00-00-202x Visual inspection (Procedure XIFU-UNGE-CRA-PR-0008-r00)

STEP	Description	Expected Value	Measured value	Remarks
1.	If the sample does not meet the acceptance criteria repeat photolithography process	Ok		
2.	FOTO			
3.	Go to the next process or store in a closed capsule	Ok		
Date: **00/00/202x**	**Operator:**	**PA/QA:**		

3.7.3 00-00-202x Nb Deposition by RF Sputtering (Procedure XIFU-UNGE-CRA-PR-0005-r00)

STEP	Description	Expected Value	Measured value	Remarks
1.	Check the level of vacuum of RF Sputtering chamber	Ok		
2.	If vacuum chamber is not conditioned wait for pressure < 3x 10-8 mbar and start the reconditioning process and check the Nb film transition.			
2.1.	Sample upload in the Sputtering Chamber:			
2.1.1	Mount the sample in metal sample holder and fix it with metal clamps;	Ok		
2.1.2	turn off the turbo pump of the vac-lock camber, close pumping valve and equalize the pressure to the atmosphere opening valve of nitrogen input line;	Ok		
2.1.3	open vac-lock door;	Ok		
2.1.4	fix metal sample holder with chip on the fork of the maneuvering arm in a specific position: 1 pay attention that the fork must be in right mode, with the bend downwards 2- fix the sample holder on the fork using the interlock near the disk surface 3- the sample holder must be with the chip facedown;	Ok		
2.1.5	closed vac-lock door;	Ok		
2.1.6	close valve of input nitrogen line, open pumping valve and switch ON the turbo pump;	Ok		

2.1.7	wait for pressure < $5x10^{-6}$ mbar:	< $5x10^{-6}$ mbar		
2.1.8	open gate valve 4;	Ok		
2.1.9	move the sample from the vac-lock chamber to the sputtering chamber;	Ok		
2.1.10	Transfer the carrier to the sputtering arm and check if the carrier is correctly fixed to the new fork; pull back the transfer arm to the parking position in the vac-lock;	Ok		
2.1.12	close gate 4;	Ok		
2.2.	Wait the pressure goes down to < 3x 10-8 mbar.	< $3{\cdot}10^{-8}$ mbar		
2.3	Set the material parameters in the thickness monitor.	Ok		
2.4	Open Argon valve then set flux at 3.0 10^{-2} mbar, rotate the shutter and wait for 5 min.	Ok		
2.5	Open the water circuit "Sput Nb" Input and output	3 atm		
2.6	Turn on the RF sputtering facility and the impedance controller, check the values to have maximum 20% of reflected power	Ok		
2.7	Start and reset to ZERO the value of thickness monitor	Ok		
2.8	Start Nb deposition: P=$3.0x10^{-2}$ mbar with10% tolerance, RF power = 300 W.	3500 ang monitor		
2.9	Once deposition is complete turn-off the system with RF off, stop the thickness monitor and close the water circuit	700 nm expected		
2.10	Sample download in the Sputtering Chamber:			
2.10.1	Repeat in reverse order the upload procedure 2.1.	Ok		
Date: 00/00/202x	**Operator:**	**PA/QA:**		

3.7.4 00-00-202x Lift-off 2 (Procedure XIFU-UNGE-CRA-PR-0014-r00)

STEP	Description	Expected Value	Measured value	Remarks

1.	Put in a beaker 40 ml of Acetone or Remover ma-Rem 700	40 ml		
2.	Insert a slide into the beaker, placing it tilted and firm against the bottom	Ok		
3.	Place the chip in the beaker so that it rests on the slide and that it is easier to extract it from the beaker during sonication.	Ok		
4.	Leave the chip in Acetone bath for a time> 1h	T > 1h		
5.1	Flush 20ml Acetone at 3 ml/s inside the beaker on the chip	Ok		
5.2	Rinse with 5 ml of acetone flush	Ok		
5.23	Rinse in 5 ml of Ethanol flush	Ok		
6.	Dry with Nitrogen	Ok		
7.	Check the cleanliness of the chip surface under the optical microscope with CCD camera	Ok		
8.	If the chip is clean go on to the next procedure in the process flow or store in a vacuum box sample holder (VR tray gel pack);			
9.	If the lift-off process is not finished and part of sacrificial layer are detected, repeat steps 5. To 10 with Acetone or remover ma-Rem700 for a time>1h or to all night or proceed with sonication.			
10.	In case of sonication: Prepare the ultrasonic cleaner: put DI water in it			recommended
10.1	Put the beaker with the sample in the grid container inside the ultrasonic bath			
10.2	Make sure the water level is equal to or greater than that of the sample; if necessary, add water, making sure that the beaker remains in contact with the grid so that it does not start to float, thus risking tipping over			
10.3	Start the ultrasonic cleaner and chronometer: leave the chip in sonication for time < 30 s then stop the ultrasonic cleaner.			
10.5	Check the cleanliness of the chip surface under the optical microscope with CCD camera, If the lift-off process is not finished and part of sacrificial layer are detected, repeat the process			
Date: **00/00/202x**	**Operator:**	**PA/QA:**		

3.7.5 00-00-202x Visual inspection (Procedure XIFU-UNGE-CRA-PR-0008-r00)

STEP	Description	Expected Value	Measured value	Remarks
1.	If the sample does not meet the acceptance criteria NRB and NCR	Ok		
2.	FOTO			
3.	Go to the next process or store in a closed capsule	Ok		
Date: 00/00/202x	**Operator:**	**PA/QA:**		

3.8 RIE Final Etching; Deep Rie Etching with Bosch process

3.8.1 00-00-202x Negative Micro Photo Lithography (Procedure: XIFU-UNGE-CRA-PR-0001) Mask: "DM HEATERS 2.0"

STEP	Description	Expected Value	Measured value	Remarks
1.	Set the hot plate to 95 °C	95 °C		
2.	Resist coating with spinner:			
2.1.	Put the chip in spinner and fix it with vacuum (-0,75 bar)	Ok		
2.3.	Spin at 2000 rpm and wash with Acetone 10 ml	10 ml 2000 rpm		
2.4.	Puddle the ma-N440 resist onto the chip using a dispenser pipe [RD4][RD5][RD6]	Ok		
2.5.	Spin at 3000 rpm maximum acceleration for 30 second	30 s 1500 rpm		
3.	Move the sample from spinner to hotplate be careful do not clamp the chip to avoid resist coating damage, use a slide as carrier	Ok		

4.	Bake on hot plate for 6 min at 95°C	6 min 95°C		
5.	Alignment and Exposure:			
5.1.	Clean the mask with 10 ml acetone flush at 4 ml/s, rinse with ethanol and dry with nitrogen. Then load lithographic mask into mask aligner: chrome plated side below to contact with chip.	Ok		
5.2.	Check the correct WEC, Wedge Error Compensation, regulation and in case adjust it (SUSS mask aligners are equipped with a WEC head system that allows reaching the parallelism between substrate and mask with a micrometric precision, training is needed).	Ok		
5.3.	Put chip on mask aligner sample holder using same caution of point 3	Ok		
5.4.	Align sample to mask using the micromanipulator: every draw in the mask has its apposite collimators (crosses) to make the best alignment (training is needed)	Ok		
5.5.	Check exposition conditions (time and number of cycles) and in case adjust them: usually 5 second for 2 cycles, but they may change with UV lamp power emission (training is needed)	5 cycles 5 s		
5.6.	Activate automatic UV exposition cycles	Ok		
5.7.	When the exposure process is finished, release the chip by lifting the locking lever	Ok		
6.	Develop:			
6.1.	Workbench preparation:			
6.1.1.	Stopwatch	Ok		
6.1.2.	More than 50 ml DI water in a beaker	Ok		
6.1.3.	More than 30 ml ma-D332s/ma-D532s developer in a beaker	Ok		
6.2.	Put the chip inside in developer bath for 4:00 min.	4 min		
6.3.	Stop develop by moving the chip in the DI water bath	Ok		
6.4.	Dry with Nitrogen	Ok		
6.5.	Check the completion of development process under the microscope (coaxial light 20%): The exposure to light causes a chemical change that allows to the photoresist to be removed by a special solution (developer), with negative photoresist, unexposed regions are soluble in	Ok		

	the developer. The edges of the resist must be defined and without erosion (over develop) while the unexposed area must be clean and free from resist.			
6.6.	In case of incomplete process, repeat form 6.2 for 10-20 s and check again under the microscope			
7.	Hashing resist residuals in O2 Plasma:			
7.1.	Put the chip onto a glass slide, then place them with the chip on the appropriate metal plate	Ok		
7.2.	Insert it into the O2 plasma generator, switch ON pumping valve, then switch ON O2 valve	Ok		
7.3.	Wait for O2 flux stabilization at 200 sccm	200 sccm		
7.4.	Turn on the RF generator at 100 W	100 W		
7.5.	Stop the process after 5 minutes	5 min		
Date: 00/00/202x	**Operator:**	**PA/QA:**		

3.8.2 00-00-202x Visual inspection (Procedure XIFU-UNGE-CRA-PR-0008-r00)

STEP	Description	Expected Value	Measured value	Remarks
1.	If the sample does not meet the acceptance criteria repeat photolithography process	Ok		
2.	FOTO			
3.	Go to the next process or store in a closed capsule	Ok		
Date: 00/00/202x	**Operator:**	**PA/QA:**		

3.8.3 00-00-202x Silicon Oxide Deposition by thermal evaporator (Procedure: XIFU-UNGE-CRA-PR-0004)

STEP	Description	Expected Value	Measured value	Remarks
1.	Open the evaporator chamber:			

1.1	disconnect the rotary pump from the turbo by turning the control knob counterclockwise	Ok		
1.2	switch-off turbo pump power	Ok		
1.3	open the valve for nitrogen to inject the gas in the evaporator chamber	Ok		
1.4	open for a few seconds the control for nitrogen in chamber to slowdown the rotary pump	Ok		
1.5	after slow downing pump re-open nitrogen control and insert the nitrogen in the evaporator chamber	Ok		
1.6	when is possible open the chamber, pull-up the cover and closed nitrogen	Ok		
2.	Mount the chip in metal sample holder and fix it with metal clamps/springs;	Ok		
3.	Position the chip near the balance control and above the evaporator sources (note down the angular position for each source and a shutter position) and place the chip in the shutter position	Ok		
4.	Close the evaporator chamber, connect the rotary pump with the turbo turning the control clockwise	Ok		
5.	When pressure is less than 5 $x10^{-1}$ mbar start turbo pump	Ok		
6.	Set the material parameters in the thickness monitor.	Ok		
7.	When the pressure is < 4 $x10^{-6}$ mbar start the evaporation procedure:	< $4x10^{-6}$ mBar		
7.1.	Open the water circuit “monitor evap” “electrode evap” input and output	Ok		
7.2.	Set the lever for the second evaporation source (right) to evaporate Silicon Oxide film:	Ok		
7.3.	Set the material parameters in the thickness monitor.	Ok		
8.	Start Silicon Oxide evaporation: Turn ON the emission current.	Ok		
8.1	Visually check on the viewport flange and see the thickness monitor: when starting the thickness counter, adjust the current to have a constant rate of about 3 ang / s then rotate the sample in the deposition position.	3 ang/s		

8.2	Once deposition is complete turn-off the emission current and stop the thickness monitor.	50 ang		
Date: 00/00/202x	**Operator:**	**PA/QA:**		

3.8.4 00-00-202x Al Evaporation - Frontside (Procedure: XIFU-UNGE-CRA-PR-0015-r00)

STEP	Description	Expected Value	Measured value	Remarks
9.	Set the lever for the first evaporation source (left) to evaporate Aluminum film:	Ok		
10.	Set the material parameters in the thickness monitor.	Ok		
11.	Rotate the sample in the right position and then start Aluminum evaporation: Turn ON the emission current.	Ok		
11.1	Visually check on the viewport flange and see the thickness monitor: when starting the thickness counter, adjust the current to have a constant rate of about 20 ang/s.	20 ang/s		
11.2	Once deposition is complete turn-off the emission current, stop the thickness monitor and close the water circuit	> 4500 ang		
12.	Repeat the procedure as described at point 1 to open the chamber and take out the glass slide with the sample	Ok		
Date: 00/00/202x	**Operator:**	**PA/QA:**		

3.8.5 00-00-202x Lift-off 2 (Procedure XIFU-UNGE-CRA-PR-0014-r00)

STEP	Description	Expected Value	Measured value	Remarks
1.	Put in a beaker 40 ml of Acetone or Remover ma-Rem 700	40 ml		
2.	Insert a slide into the beaker, placing it tilted and firm against the bottom	Ok		
3.	Place the chip in the beaker so that it rests on the slide	Ok		
4.	Leave the chip in Acetone bath for a time> 1h	T > 1h		

5.1	Flush 20ml Acetone at 3 ml/s inside the beaker on the chip	Ok		
5.2	Rinse with 5 ml of acetone flush	Ok		
5.23	Rinse in 5 ml of Ethanol flush	Ok		
6.	Dry with Nitrogen	Ok		
7.	Check the cleanliness of the chip surface under the optical microscope with CCD camera	Ok		
8.	If the chip is clean go on to the next procedure in the process flow or store in a vacuum box sample holder (VR tray gel pack);			
9.	If the lift-off process is not finished and part of sacrificial layer are detected, repeat steps 1. to 9.			
Date: 00/00/202x	**Operator:**	**PA/QA:**		

3.8.6 00-00-202x Visual inspection (Procedure XIFU-UNGE-CRA-PR-0008-r00)

STEP	Description	Expected Value	Measured value	Remarks
1.	If the sample does not meet the acceptance criteria repeat remove aluminum with ma-D 532/s or equivalent and restart from the 3.8.1 process (check for SiOx)	Ok		
2.	FOTO			
3.	Go to the next process or store in a closed capsule	Ok		
Date: 00/00/202x	**Operator:**	**PA/QA:**		

3.8.7 00-00-202x Bosch etching process (Procedure XIFU-UNGE-CRA-PR-0016-r00)

STEP	Description	Expected Value	Measured value	Remarks
1.	Glue the “back” chip to sapphire carrier wafer with 3 µl of Santovac 5 with Hamilton syringe:			
1.1	place the sapphire carrier wafer on the hotplate at 120 °C and open pumping valve to fix the wafer	120 °C		
1.2	put 3 µl of Santovac 5 with Hamilton syringe to center of the carrier wafer	3 µl		

1.3	as soon as the Santovac is fluid, lean on the chip and cover with the vacuum cup and apply 700 -900 mbar for about 2 min. Break the vacuum and apply gently a small pressure with tweezers.	Ok		
1.4	put 3 µl of Santovac 5 with Hamilton syringe to the back chip (support chip) and cover it with the second chip, the one that must be etched	3 µl		
1.5	as soon as the Santovac is fluid, lean on the chip and cover with the vacuum cup and apply 700 -900 mbar for about 2 min.	Ok		
1.6	switch off the pumping valve and remove the cover and the carrier wafer from the hot plate by dragging it on the cold edge	Ok		
1.8	check with visual inspection if chip is aligned and remove excess of Santovac 5	Ok		
2.	Start RIE:			
2.1	Open the gas lines of N_2 “RIE” and “RIE purge”, C_4F_8, SF_6, Ar, O_2 and He	Ok		
2.2	Open the water circuit “ICP RIE IN”, “ICP RIE OUT” and “Turbo RIE”	Ok		
2.3	Start the chiller, set 20°C and run	Ok		
2.4	Push start RIE button and then start the program Open PC 2000	ok		
3.	open the vac-lock and place the carrier wafer on the transfer arm	Ok		
4.	close the vac-lock aperture and start the automatic procedure for sample loading	Ok		
5.	Load the RIE-ICP recipe for Bosch Process and wait for the execution at 20 °C. Recipe name: “Bosch DM” ICP pow. PE pow. GAS. gas flux time etch 300 W 30 W SF_6+O_2 80+8 sccm dep 300 W 3 W C_4F_8 80 sccm 6 cycles of: 40, 40, 60, 60, 80, 80 repetition of dep and etch process (with an increment of 1.2% in C_4F_8 flux each time)	Ok		
6.	Unload the sample with the automatic RIE-ICP procedure and process check.	Ok		
7.	Bring the sapphire carrier with the two chips in the vac-lock aperture, then check it visually with the vac-lock camera.	Ok		

8.	Check at optical microscope with CCD camera in clean room (see Acceptance Criteria §5 points 1 and 2) in case of etched is only partial and does not pass through of the silicon, reload sample into RIE machine (step 2) and repeat the procedure, adjust properly the number of cycles.			
9.	Remove chip from sapphire wafer:			
9.1	put the sapphire carrier wafer on the hot plate at 120° and switch on the pumping valve	Ok		
9.2	as soon as the Santovac is fluid, gently drag chip outside the wafer with tweezers	Ok		
9.3	put the two chips inside the beaker with 30 ml of acetone and leave it for 10-20 min to remove Santovac 5.	Ok		
9.4	Sonicate in acetone for few seconds;	Ok		
9.5	Rinse in ethanol bath;	Ok		
9.6	Dry with nitrogen;	Ok		
10.	Turn off the pumps, when the turbo is at 0 rpm switch off the RIE, the chiller and close water circuit and gasses	Ok		
Date: **00/00/202x**	**Operator:**	**PA/QA:**		

3.8.8 00-00-202x Aluminum Hard mask Stripping (Procedure: XIFU-UNGE-CRA-PR-0008-r00)

STEP	Description	Expected Value	Measured value	Remarks
1.	Put in a beaker ~80 ml of Developer ma-D 532/S (or 332/S)	Ok		
2.	Place the beaker on the stirrer and select velocity between 3 and 4.	Ok		
3.	Hold the chip with reverse tweezers and put it inside in developer bath.	Ok		
4.	Leave the chip in Developer bath until Aluminum is visibly vanished.	Ok		
5.	Stop develop by moving the chip in the DI water bath	Ok		
6.	Rinse in ~ 50 ml of DI water	Ok		
7.	Dry with Nitrogen	Ok		

8.	Check the cleanliness of the chip surface under the optical microscope with CCD camera	Ok		
9.	If the chip is clean store in a vacuum box sample holder (VR tray gel pack);	Ok		
10.	If the hard-mask stripping process is not finished and part of aluminum layer is detected, repeat steps 1. To 7.			
Date: 00/00/202x	**Operator:**	**PA/QA:**		

3.8.9 00-00-202x Visual inspection (Procedure XIFU-UNGE-CRA-PR-0008-r00)

STEP	Description	Expected Value	Measured value	Remarks
1.	If the sample does not meet the acceptance criteria NCR and NRB	Ok		
2.	FOTO			
3.	Go to the next process or store in a closed capsule	Ok	Ok	
Date: 00/00/202x	**Operator:**	**PA/QA:**		

3.8.10 00-00-202x TES Tested at room temperature after bonding.

1 Test at Room Temperature R = xxx Ω TES, xxx Ω Heaters

Bibliography

[1] R. Giacconi et al. "Evidence for x Rays From Sources Outside the Solar System". In: *Phys. Rev. Lett.* 9 (11 Dec. 1962), pp. 439–443. DOI: 10.1103/PhysRevLett.9.439.

[2] F. Nicastro et al. "Observations of the missing baryons in the warm–hot intergalactic medium". In: *Nature* 558.7710 (2018), pp. 406–409. DOI: 10.1038/s41586-018-0204-1.

[3] R. Giacconi. "The Dawn of X-Ray Astronomy". In: 2003. DOI: 10.1002/3527608966.ch1.

[4] X. Barcons et al. "Athena (Advanced Telescope for High ENergy Astrophysics) Assessment Study Report for ESA Cosmic Vision 2015-2025". In: (2012). DOI: 10.48550/arXiv.1207.2745.

[5] K. Nandra et al. "Athena : The Advanced Telescope for High-Energy Astrophysics". In: (Volker Springel/MPA-Chandra/CXC-NASA). URL: https://www.cosmos.esa.int/documents/400752/400864/Athena+Mission+Proposal/18b4a058-5d43-4065-b135-7fe651307c46.

[6] D. Barret et al. "The Athena X-ray Integral Field Unit: a consolidated design for the system requirement review of the preliminary definition phase". In: *Experimental Astronomy* (2023). DOI: 10.1007/s10686-022-09880-7.

[7] N. Meidinger et al. "The Wide Field Imager Instrument for Athena". In: *arXiv* (2017). DOI: 10.48550/ARXIV.1702.01079.

[8] *XMM - Newton X-ray Observatory*. URL: https://www.cosmos.esa.int/web/xmm-newton/home.

[9] *Chandra X-ray Observatory - NASA's flagship X-ray telescope*. URL: https://chandra.harvard.edu/.

[10] S. Wen et al. "Mass, Spin, and Ultralight Boson Constraints from the Intermediate-mass Black Hole in the Tidal Disruption Event 3XMM J215022.4–055108". In: *The Astrophysical Journal* 918.46 (2021). DOI: 10.3847/1538-4357/ac00b5.

[11] *MS 0735.6+7421: Monstrous Black Hole Blast in the Core of a Galaxy Cluster*. ref.: B. McNamara et al 2005, Nature. DOI: 10.1038/nature03202. URL: https://chandra.harvard.edu/photo/2006/ms0735/.

[12] T. Tuominen et al. "An EAGLE view of the missing baryons". In: *A&A* 646 (2021). DOI: 10.1051/0004-6361/202039221.

[13] J. P. Dietrich et al. "A filament of dark matter between two clusters of galaxies". In: *Nature* 487.7406 (2012), pp. 202–204. DOI: 10.1038/nature11224.

[14] S. Ando et al. "Decaying dark matter in dwarf spheroidal galaxies: Prospects for x-ray and gamma-ray telescopes". In: *Phys. Rev. D* 104 (2 2021), p. 023022. DOI: 10.1103/PhysRevD.104.023022.

[15] N. Aghanim et al. "Planck 2018 results, I. Overview and the cosmological legacy of Planck". In: *Astronomy & Astrophysics* 641 (2020). DOI: 10.1051/0004-6361/201833880.

[16] N. Aghanim et al. "Planck 2018 results, VI. Cosmological parameters". In: *Astronomy & Astrophysics* 641 (2020). DOI: 10.1051/0004-6361/201833910.

[17] "Tracing the Universe: X-ray survey supports standard cosmological model". In: (ESA 2018). URL: http://sci.esa.int/jump.cfm?oid=60686.

[18] R. Yao et al. "Revealing the source of Jupiter's x-ray auroral flares". In: *Science Advances* 7.28 (2021). DOI: 10.1126/sciadv.abf0851.

[19] G. Branduardi-Raymont et al. "X-rays from Saturn: a study with XMM-Newton and Chandra over the years 2002-05". In: *Astronomy and Astrophysics* 510 (2010), A73. DOI: 10.1051/0004-6361/200913110.

[20] *Jupiter: Solar Storms Ignite 'Northern Lights' on Jupiter*. ref.: Dunn, W. et al, 2016, JGR. DOI: 10.1002/2015JA021888. URL: https://chandra.harvard.edu/photo/2016/jupiter/.

[21] L. Piro et al. "Athena synergies in the multi-messenger and transient universe". In: *Experimental Astronomy* 54 (2022). DOI: 10.1007/s10686-022-09865-6.

[22] E. Troja et al. "The X-ray counterpart to the gravitational-wave event GW170817". In: *Nature* 551.7678 (2017). DOI: 10.1038/nature24290.

[23] B. P. Abbott et al. "GW170817: Observation of Gravitational Waves from a Binary Neutron Star Inspiral". In: *Phys. Rev. Lett.* 119 (16 2017). DOI: 10.1103/PhysRevLett.119.161101.

[24] M.G. Aartsen et al. "Extending the Search for Muon Neutrinos Coincident with Gamma-Ray Bursts in IceCube Data". In: *The Astrophysical Journal* 843.2 (2017). DOI: 10.3847/1538-4357/aa7569.

[25] E. Wille et al. "Development of the ATHENA mirror". In: *SPIE 2018: Ultraviolet to Gamma Ray*. Ed. by Jan-Willem A. den Herder, Kazuhiro Nakazawa, and Shouleh Nikzad. SPIE, July 2018. DOI: 10.1117/12.2313296.

[26] S. J. Smith et al. "Performance of a Broad-Band, High-Resolution, Transition-Edge Sensor Spectrometer for X-ray Astrophysics". In: *IEEE TAS* 31.5 (2021). DOI: 10.1109/TASC.2021.3061918.

[27] L. Ravera et al. "The X-ray Integral Field Unit (X-IFU) for Athena". In: *SPIE 2014: Ultraviolet to Gamma Ray*. Ed. by Tadayuki Takahashi, Jan-Willem A. den Herder, and Mark Bautz. Vol. 9144. Society of Photo-Optical Instrumentation Engineers (SPIE) Conference Series. July 2014, 91442L, p. 91442L. DOI: 10.1117/12.2055884.

[28] M. Durkin et al. "Mitigation of Finite Bandwidth Effects in Time-Division-Multiplexed SQUID Readout of TES Arrays". In: *IEEE TAS* 31.5 (2021). DOI: 10.1109/TASC.2021.3065279.

[29] H. Akamatsu et al. "Demonstration of MHz frequency domain multiplexing readout of 37 transition edge sensors for high-resolution x-ray imaging spectrometers". In: *Applied Physics Letters* 119.18 (2021). DOI: 10.1063/5.0066240.

[30] M. D'Andrea et al. "ATHENA X-IFU Demonstration Model: First Joint Operation of the Main TES Array and its Cryogenic AntiCoincidence Detector (CryoAC)". In: *Journal of Low Temperature Physics* 209.3-4 (2022). DOI: 10.1007/s10909-022-02786-w.

[31] K.D. Irwin and G.C. Hilton. "Transition-Edge Sensors". In: *Cryogenic Particle Detection*. Ed. by Christian Enss. Vol. 99. 2005. DOI: 10.1007/10933596_3.

[32] S. Lotti et al. "Review of the Particle Background of the Athena X-IFU Instrument". In: *ApJ* 909.2 (2021). DOI: 10.3847/1538-4357/abd94c.

[33] F. Chiarello et al. "Study on the trigger logic for the X-IFU Athena anticoincidence system". In: *SPIE 2022: Ultraviolet to Gamma Ray*. Ed. by Jan-Willem A. den Herder, Shouleh Nikzad, and Kazuhiro Nakazawa. Vol. 12181. International Society for Optics and Photonics. SPIE, 2022. DOI: 10.1117/12.2630034.

[34] S. Seltzer. *XCOM-Photon Cross Sections Database, NIST Standard Reference Database 8*. 1987. DOI: 10.18434/T48G6X.

[35] N.R. Werthamer. "Theory of the Superconducting Transition Temperature and Energy Gap Function of Superposed Metal Films". In: *Physical Review* 132.2440 (1963). DOI: 10.1103/PhysRev.132.2440.

[36] K.D. Irwin. "An application of electrothermal feedback for high resolution cryogenic particle detection". In: *Appl. Phys. Lett.* 66.15 (1995). DOI: 10.1063/1.113674.

[37] D.H. Andrews et al. "Attenuated Superconductors I. For Measuring Infra-Red Radiation". In: *Review of Scientific Instruments* 13.7 (1942). DOI: 10.1063/1.1770037.

[38] D. McCammon. "Thermal Equilibrium Calorimeters – An Introduction". In: *Topics in Applied Physics*. Springer Berlin Heidelberg, 2005. DOI: 10.1007/10933596_1.

[39] Dario Corsini. "The Anticoincidence Detector onboard the Athena X-Ray observatory". In: (2018). DOI: 10.15167/CORSINI-DARIO_PHD2018-03-26.

[40] M. Galeazzi and D. McCammon. "Microcalorimeter and bolometer model". In: *Journal of Applied Physics* 93.8 (2003). DOI: 10.1063/1.1559000.

[41] Matteo D'Andrea. "Opening the low-background and high-spectral-resolution domain with the ATHENA large X-ray observatory: Development of the Cryogenic AntiCoincidence Detector for the X-ray Integral Field Unit". In: (2019). DOI: 10.48550/ARXIV.1904.03307.

[42] M.E. Msall and J.P. Wolfe. "Ballistic phonon production in photoexcited Ge, GaAs, and Si". In: *Physical Review B* 65.19 (2002). DOI: 10.1103/physrevb.65.195205.

[43] L. Ferrari Barusso et al. "First Configurational Study of the CryoAC Detector Silicon Chip of the Athena X-Ray Observatory". In: *IEEE Transactions on Applied Superconductivity* 33.1 (2023). DOI: 10.1109/tasc.2022.3222959.

[44] D. Brandt et al. "Monte Carlo Simulation of Massive Absorbers for Cryogenic Calorimeters". In: *Journal of Low Temperature Physics* 167.3-4 (2012). DOI: 10.1007/s10909-012-0480-3.

[45] F. Pröbst et al. "Model for cryogenic particle detectors with superconducting phase transition thermometers". In: *Journal of Low Temperature Physics* 100.1-2 (1995). DOI: 10.1007/bf00753837.

[46] W. Falci, W. Feinberg, and F.W.J. Hekking. "Correlated tunneling into a superconductor in a multiprobe hybrid structure". In: *Europhysics Letters* 54.2 (2001). DOI: 10.1209/epl/i2001-00303-0.

[47] I. Alkhatib et al. "Light Dark Matter Search with a High-Resolution Athermal Phonon Detector Operated above Ground". In: *Physical Review Letters* 127.6 (2021). DOI: 10.1103/physrevlett.127.061801.

[48] K. Alfonso et al. "CUPID: The Next-Generation Neutrinoless Double Beta Decay Experiment". In: *Journal of Low Temperature Physics* (2022). DOI: 10.1007/s10909-022-02909-3.

[49] Steven W. Leman. "Invited Review Article: Physics and Monte Carlo techniques as relevant to cryogenic, phonon, and ionization readout of Cryogenic Dark Matter Search radiation detectors". In: *Review of Scientific Instruments* 83.9 (2012). DOI: 10.1063/1.4747490.

[50] Shin-ichiro Tamura. "Quasidiffusive propagation of phonons in silicon: Monte Carlo calculations". In: *Physical Review B* 48.18 (1993). DOI: 10.1103/physrevb.48.13502.

[51] C. Macculi et al. "The Cryogenic AntiCoincidence Detector for ATHENA X-IFU: The Project Status". In: *Journal of Low Temperature Physics* 199.1-2 (2020). DOI: 10.1007/s10909-019-02314-3.

[52] D. Corsini et al. "The mechanical and EM simulations of the CryoAC for the ATHENA X-IFU". In: *SPIE 2016: Ultraviolet to Gamma Ray*. Ed. by Jan-Willem A. den Herder, Tadayuki Takahashi, and Marshall Bautz. Vol. 9905. International Society for Optics and Photonics. SPIE, 2016. DOI: 10.1117/12.2232499.

[53] M. D'Andrea et al. "The Demonstration Model of the ATHENA X-IFU Cryogenic AntiCoincidence Detector". In: *Journal of Low Temperature Physics* 199.1-2 (2019). DOI: 10.1007/s10909-019-02300-9.

[54] S. Petersson et al. "Formation of iridium silicides from Ir thin films on Si substrates". In: *J. Appl. Phys.* 50.5 (1979). DOI: 10.1063/1.326325.

[55] J. Mittra et al. "Role of Substrate Temperature in the Pulsed Laser Deposition of Zirconium Oxide Thin Film". In: *Materials Science Forum* 710 (2012). DOI: 10.4028/www.scientific.net/msf.710.757.

[56] L. Ferrari Barusso et al. "Ir film structural properties for TES application". In: *IEEE TAS* 33 (5 2023). DOI: 10.1109/TASC.2023.3257822.

[57] L.N. Cooper. "Bound Electron Pairs in a Degenerate Fermi Gas". In: *Phys. Rev.* 104.1189 (1956). DOI: 10.1103/PhysRev.104.1189.

[58] U. Nagel et al. "Proximity effect in iridium-gold bilayers". In: *J. Appl. Phys.* 76.7 (1994). DOI: 10.1063/1.357310.

[59] M. Biasotti et al. "The Phonon-Mediated TES Cosmic Ray Detector for Focal Plane of ATHENA X-Ray Telescope". In: *Journal of Low Temperature Physics* 199.1-2 (2020). DOI: 10.1007/s10909-020-02348-y.

[60] B. Siri et al. "Impact of Annealing on T_C and Structure of Titanium Thin Films". In: *IEEE Transactions on Applied Superconductivity* 31.5 (2021). DOI: 10.1109/tasc.2021.3071997.

[61] M. A. El Khakani, B. Le Drogoff, and M. Chaker. "Effect of the deposition temperature on the properties of iridium thin films grown by means of pulsed laser deposition". In: *Journal of Materials Research* 14.8 (1999). DOI: 10.1557/jmr.1999.0438.

[62] Y. Gong et al. "Low-temperature deposition of iridium thin films by pulsed laser deposition". In: *Vacuum* 82.6 (2008). DOI: 10.1016/j.vacuum.2007.09.003.

[63] D. Nath, Fouran Singh, and Ratan Das. "X-ray diffraction analysis by Williamson-Hall, Halder-Wagner and size-strain plot methods of CdSe nanoparticles- a comparative study". In: *Materials Chemistry and Physics* 239 (2020). DOI: 10.1016/j.matchemphys.2019.122021.

[64] N.V. Gelfond et al. "An XPS study of the composition of iridium films obtained by MO CVD". In: *Surface Science* 275.3 (1992). DOI: 10.1016/0039-6028(92)90804-f.

[65] T. Xu et al. “Effects of deep reactive ion etching parameters on etching rate and surface morphology in extremely deep silicon etch process with high aspect ratio”. In: *Advances in Mechanical Engineering* 9.12 (2017). DOI: 10.1177/1687814017738152.

[66] L. Martini. “Real-time control of an Electrodynamic Shaker”. PhD thesis. 2016. URL: http://amslaurea.unibo.it/10080/.

[67] L. Ferrari Barusso et al. “First structural tests of the CryoAC Detector silicon chip of the Athena X-ray observatory”. In: *NIM-A* 1047 (2023). DOI: https://doi.org/10.1016/j.nima.2022.167862.

[68] M. Cavallini, G. Gallinaro, and G. Scoles. “Notizen: High Sensitivity Bolometer Detector for Molecular Beams”. In: *Zeitschrift für Naturforschung A* 22.3 (1967). DOI: 10.1515/zna-1967-0319.

[69] A. Barone et al. “Superconducting Nb-NbxOy-Pb tunnel junctions as high resolution detectors for nuclear spectroscopy: Preliminary results”. In: *Nuclear Instruments and Methods in Physics Research Section A: Accelerators, Spectrometers, Detectors and Associated Equipment* 234.1 (1985). DOI: 10.1016/0168-9002(85)90809-5.

[70] F. Gatti et al. “Detection of environmental fine structure in the low-energy β-decay spectrum of 187Re”. In: *Nature* 397.6715 (1999). DOI: 10.1038/16414.

[71] G. Addamo et al. “The large scale polarization explorer (LSPE) for CMB measurements: performance forecast”. In: *Journal of Cosmology and Astroparticle Physics* 2021.08 (2021). DOI: 10.1088/1475-7516/2021/08/008.

[72] O.V. Lounasmaa. *Experimental principles and methods below 1 Kelvin.* en. San Diego, CA: Academic Press, Sept. 1974.

[73] Frank Pobell. *Matter and methods at low temperatures.* en. 1992nd ed. Berlin, Germany: Springer, 1992.

[74] J. Clarke and A.I. Braginski. *The SQUID handbook.* en. Weinheim, Germany: Wiley-VCH Verlag, Mar. 2006.

[75] M. D’Andrea et al. “The Cryogenic AntiCoincidence detector for ATHENA X-IFU: a scientific assessment of the observational capabilities in the hard X-ray band”. In: *Experimental Astronomy* 44.3 (May 2017), pp. 359–370. DOI: 10.1007/s10686-017-9543-4. URL: https://doi.org/10.1007/s10686-017-9543-4.

[76] S. Eidelman et al. (Particle Data Group). “Chapt. 24. Cosmic Rays””. In: *Phys. Lett. B* 592.1 (2004 and 2005 partial update for the 2006 edition). URL: http://pdg.lbl.gov/.

[77] L. Gottardi and K. Nagayashi. “A Review of X-ray Microcalorimeters Based on Superconducting Transition Edge Sensors for Astrophysics and Particle Physics”. In: *Applied Sciences* 11.9 (2021). DOI: 10.3390/app11093793.

[78] D. Bagliani et al. “Ir TES Electron-Phonon Thermal Conductance and Single Photon Detection”. In: *Journal of Low Temperature Physics* 151.1-2 (2008). DOI: 10.1007/s10909-007-9641-1.

[79] M. Fedkevych et al. “An Examination of Thermal Coupling of an Ir/Au TES for TORIO-229 Experiment”. In: *Journal of Low Temperature Physics* 209.3-4 (2022). DOI: 10.1007/s10909-022-02901-x.

[80] C. Done and M. Gierliński. “Observing the effects of the event horizon in black holes”. In: *Monthly Notices of the Royal Astronomical Society* 342.4 (July 2003), pp. 1041–1055. ISSN: 0035-8711. DOI: 10.1046/j.1365-8711.2003.06614.x.

[81] M. Ozaki and V. Fioretti. 2018. URL: https://indico.esa.int/event/249/contributions/4195/attachments/3262/4235/Hitomi-related_Geant4_activities.pdf.